ELECTRONIC STRUCTURE OF TWO-DIMENSIONAL NANOMATERIALS: TRANSPORT AND OTHER PROPERTIES

THESIS SUBMITTED FOR THE DEGREE OF
DOCTOR OF PHILOSOPHY (SCIENCE)
IN
PHYSICS (THEORETICAL)

by

D'SOUZA RANSELL RICHARD

DEPARTMENT OF PHYSICS
UNIVERSITY OF CALCUTTA
JULY, 2018

Acknowledgment

I would like to express my sincere appreciation to my supervisors, Prof. Sugata Mukherjee and Prof. Tanusri Saha-Dasgupta for their affection and constant support during the course of my research. Their patience, motivation and immense knowledge in the field of condensed matter physics is what made it possible for me to submit my thesis within five years. I genuinely consider myself to be extremely lucky to have worked under their supervision. Apart from my supervisors, I would like to thank my thesis committee, Dr. Manoranjan Kumar, Dr. Sakuntala Chatterjee and Dr. Gour Prasad Das for their insightful comments during past evaluations.

My honest thanks goes out to Dr. Sajeev Chacko, Dr. Niharika Singh and Sagar S. De for teaching me shell scripting and Mathematica, both of which I have used extensively in my research. I would also like to thank Dr. Georg K. H. Madsen, Dr. Jesús Carrete Montaña and Dr. Peter Kratzer for giving me the opportunity to present my work at TU Wien, Austria and University of Duisburg-Essen, Germany.

Moreover, I would like to thank my group members and friends here in SNBose, Poonam, Dhani, Chandreyee, Shaili, Ritam, Ravi, Subrata, Debasish for making my hostel life a beautiful memory. Special thanks to Kartik and Sagar for their suggestions. My friends back in Mumbai (WAY too many to name separately) have supported me in various ways and I couldn't imagine a life without them. Special thanks to Rossi and my friends from Pune, Dinesh and Suyog for all the help required in Pune during my stay in Kolkata. A warm thank you to Florian and Eloïse for being marvelous hosts during my trip to Europe.

Finally, a heartfelt thank you to Yishi Chakrabarty for making her home like my second home and helping me with all of the official paper work around Kolkata.

My family has been extremely supportive during my entire Ph.D. process. My Dad has been discussing physics with me from a very young age till today and is undoubtedly the main reason for my interest in physics. Thanks to my siblings, Rossi, Rinaldo and Deepika, even though being so far, have been of great help and motivation. I have been extremely fortunate to have been raised with such a supportive and loving family.

It has been an amazing 5 years!

Ransell D'Souza

List of Publications

All papers have been published during the course of the author's Ph.D. and are discussed in this thesis.

1. **Ransell D'Souza** and Sugata Mukherjee,
   Length dependent lattice thermal conductivity of single & multi layered hexagonal boron nitride: A first-principles study using the Callaway-Klemens & real space super cell methods
   Physical Review B **96**, 205422 (2017)
   DOI: https://doi.org/10.1103/PhysRevB.96.205422

2. **Ransell D'Souza**, Sugata Mukherjee and Tanusri Saha-Dasgupta
   Influence of interface geometry on phase stability and bandgap engineering in boron nitride substituted graphene: A combined first-principles and Monte Carlo study
   Journal of Alloys and Compounds **708**, 437-443 (2017)
   DOI: https://doi.org/10.1016/j.jallcom.2017.03.006

3. **Ransell D'Souza** and Sugata Mukherjee
   First-principles study of the electrical and lattice thermal transport in monolayer and bilayer graphene
   Physical Review B **95**, 085435 (2017)
   DOI: https://doi.org/10.1103/PhysRevB.95.085435

4. **Ransell D'Souza** and Sugata Mukherjee
   Thermoelectric transport in graphene/h-BN/graphene heterostructures: A computational study
   Physica E: Low-dimensional Systems and Nanostructures **81**, 96-101 (2016)
   DOI: https://doi.org/10.1016/j.physe.2016.03.006

5. **Ransell D'Souza** and Sugata Mukherjee
   Electronic structure, phase stability and resistivity of hybrid hexagonal $C_x(BN)_{1-x}$ two-dimensional nanomaterial: A first-principles study
   Physica E: Low-dimensional Systems and Nanostructures **69**, 138-144 (2015)
   DOI: https://doi.org/10.1016/j.physe.2015.01.026

6. **Ransell D'Souza** and Sugata Mukherjee
   First principles calculation of thermoelectric parameters of Monolayer- and Bilayer-Graphene and Heterostructures of Graphene and h-BN
   Journal of Physics: Conference Series **759**, 012040 (2016)
   DOI: 10.1088/1742-6596/759/1/012040

7. **Ransell D'Souza** and Sugata Mukherjee
   Enhancement of thermoelectric figure-of-merit of Graphene upon BN-doping and sample length reduction.(Manuscript submitted)

Résumé

Carbon, an element discovered before history itself, is one of the most ubiquitous and fourth most abundant element in the universe. A.L. Lavoisier proposed the name carbon in 1789 from the Latin *carbo* meaning "charcoal." It plays an important role in biological and technological applications because of the many ways it forms chemical bonds, giving birth to a number of pure elemental allotropes such as diamond, graphite, fullerenes, graphene, *etc.*, each having distinct physical properties. Diamond is an insulator and is a colourless, transparent, crystalline solid and the hardest known material. Graphite is black and shiny but soft and has the highest thermodynamic stability as compared to the other allotropes is a good electrical conductor. A single layer of graphite, graphene, has phenomenal electronic and optoelectronic applications due to which it is one of the most studied two-dimensional (2D) material. Optical and electronic properties differ due to confinement of electrons and in the case of 2D materials, also due to the absence of interlayer interactions. These play an important role in determining band structure. Graphene has zero band gap and is a semi-metal. This limits its usefulness in electronic applications which require a finite bandgap. The need to introduce a tunable band gap has brought many other 2D materials into the lime light. Among these, hexagonal boron nitride (h-BN) is an insulator with a band gap exceeding 5eV, and the family of transition-metal dichalcogenides (TMDs) includes several semiconductors with bandgaps ranging from 0.4eV to 3eV.

Boron and nitrogen have masses close to that of carbon and boron-boron, nitrogen-nitrogen bonds are weaker than the carbon-nitrogen, carbon-boron bonds making it relatively easy to dope boron and nitrogen into the lattice of

graphene. These doped materials are perfect candidates for bandgap engineering.

Layered materials, *i.e.*, stacking of such single layers to form heterostructures have physical properties which are unique to the number of layers. For example, bi-layer graphene can be used as a tunable band gap semiconductor. Graphene-*h*-boron nitride heterostructures are promising candidates for solid states devices.

Organic-Inorganic hybrid perovskites, unlike layered materials, do not have a simple physical mixture. Their inorganic and organic components mix at the microscopic limit and hence have traits which are not typical of either organic nor inorganic materials. Organic-Inorganic hybrid perovskites, which when made into atomically thin 2D sheets, have also proved to be excellent semiconductor materials for photovoltaic applications.

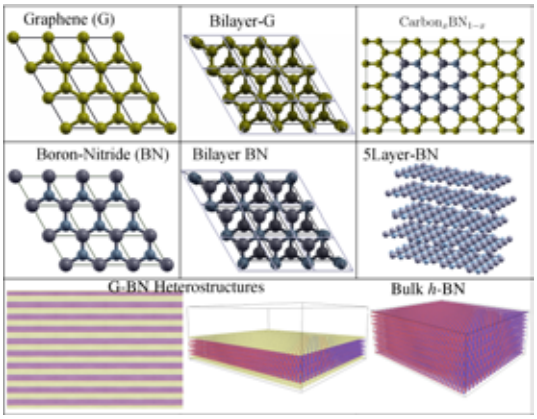

Figure 1: A schematic figure of all the materials studied in this thesis.

The materials studied in the thesis are shown in Fig. 1. The thesis embodies the work carried out by me over the last five years. In order to understand the electronic, magnetic and thermal properties of these materials, *ab-initio* computational calculations using Density Functional Theory were carried out. Electrical (thermal) transport properties are then calculated from the electronic bandstructure (phonon dispersion) by solving the Boltzmann transport equations.
The thesis is organized in seven chapters as as follows;

Chapter 1: Introduction

Chapter 1 presents a brief introduction to two-dimensional materials. The basic concepts, the current status of the subject, and the fascinating applications of these materials in basic and applied science are briefly discussed, thus providing the motivation for the work carried out in the subsequent chapters. We also review some of the experimental procedures in producing and synthesizing these nanomaterials.

Chapter 2: Theoretical Framework

Chapter 2 provides detail discussions on Density functional theory, Density functional perturbation theory, Boltzmann transport theory for electrons and phonons, Molecular dynamics, Regular solution model and Monte Carlo simulation used in the theoretical and computational investigations of the transport, electrical and thermal properties of the materials taken up in the present study.

Chapter 3: Thermoelectric transport properties of monolayer (MLG) and bilayer graphene (BLG)

Chapter 3 presents a discussion on the thermal and electronic properties of monolayer and bilayer graphene. The computational details used by us are mentioned in the chapter. The electrical properties studied are electrical- conductivity, resistivity, mobility, Seebeck coefficient and the power factor. Properties due to phonons which have been considered are phonon dispersion, Grüneisen parameters and the lattice thermal conductivity. We device a method to enchance the figure of merit by doping graphene with one and two dimers of boron nitride.
Results from this Chapter have been published in
(i) First-principles study of the electrical and lattice thermal transport in monolayer and bilayer graphene (Phys. Rev. B 95, 085435 (2017))
(ii) Enhancement of thermoelectric figure-of-merit of Graphene upon BN-doping and sample length reduction.(Manuscript submitted)

Chapter 4: First-principles calculations of lattice thermal conductivity of multi-layered hexagonal boron nitride and comparison to experiments

Chapter 4 calculates the mode, length and temperature dependence lattice thermal conductivity using two methods, the Callaway-Klemens method and a real space super cell iterative method. The materials studied in this chapter are single-, bi-, multi- layered hexagonal boron nitride and bulk boron nitride.
Results from this Chapter have been published in
(i) Length-dependent lattice thermal conductivity of single-layer and multilayer

hexagonal boron nitride: A first-principles study using the Callaway-Klemens and real-space supercell methods (Phys. Rev. B 96, 205422 (2017))

Chapter 5: Thermoelectric transport properties of graphene/boron-nitride/graphene heterostructure nanomaterials

Chapter 5 deals with the transport properties of graphene/boron-nitride layered heterostructures. The materials examined here are single, bi- and 5 - layered hexagonal boron nitride and Graphene-*h*-BN heterostructures,*viz*, three-,four- and five- layered boron nitride sandwiched between graphene layers. The lattice thermal conductivity for each system was calculated using molecular dynamic simulations. We also calculated the electrical transport properties of Graphene-*h*-BN heterostructures. Finally, combining the electrical transport properties along with lattice thermal conductivity, we calculated the figure of merit of Graphene-*h*-BN heterostructures.

Results from this Chapter have been published in

(i) Thermoelectric transport in graphene/h-BN/graphene heterostructures: A computational study (Physica E 81, 96 (2016))

Chapter 6: Thermodynamic, Electronic Structure and resistivity of Hybrid Hexagonal $C_{2x}(BN)_{1-x}$ Two-dimensional Nanomaterial

In chapter 6, we study the electronic structure, thermodynamic properties and resistivity of hybrid hexagonal $C_{2x}(BN)_{1-x}$ two dimensional nanomaterials. The electron bandstructures are examined by varying the carbon concentration, x, for different interfaces between graphene and h-BN, *viz*, zigzag, armchair and mixture of both zigzag and armchair interfaces. The thermodynamic properties were calculated using two methods, the mean free approach or regular solution model and classical Monte Carlo method. The goal was to uncover the role of the interface geometry formed between the interfaces. We extended our studies by reducing the dimensionality, *i.e.*, studied the thermodynamic properties of nanoribbons. Lastly, using the Boltzmann transport theories on band electrons, we calculated the electrical resistivity of hexagonal $C_{2x}(BN)_{1-x}$.

Results from this Chapter have been published in

(i) Electronic structure, phase stability and resistivity of hybrid hexagonal

$C_x(BN)_{1-x}$ two-dimensional nanomaterial: A first-principles study (Physica E, 69, 138 (2015))
(ii) Influence of interface geometry on phase stability and bandgap engineering in boron nitride substituted graphene: A combined first-principles and Monte Carlo study (Journal of Alloys and Compounds 708, 437 (2017))

Chapter 7: Conclusion and Outlook

The main results of our work are summarized in this Chapter. Further, we discuss the future scope of our present formalisms.

List of Figures

List of Tables

Contents

Chapter 1

Introduction

"What could we do with layered structures with just the right layers?", asked Richard Feynman prophetically in his famous lecture, *There's Plenty of Room at the Bottom*, at an American Physical Society meeting at Caltech on December 29, 1959 [32]. Even though he made no formal contribution to the field, Feynman's talk has been credited with having given the impetus to the study of nanomaterials and nanotechnology. The past several years have seen amazing development that has brought us close to answering that question.

1.1 What are 2D materials?

Nanomaterials are materials with at least one dimension in the nanometer scale. If only one dimension is restricted, we have atomically thin planar crystalline materials, termed as two-dimensional (2D) materials or single layer materials. If two dimensions are limited in size, we will have nanowires or 1D materials. If all dimensions are in the range of a few nanometers we usually talk of 0D materials.

2D materials are largely classified as either 2D allotropes of different elements and compounds, normally found having two or more covalently bonding elements. A beautiful example made popular by a couple of Nobel Prizes to their discoverers [33, 34, 35, 36, 37] is the family of sp^2 carbon materials, where

0D fullerenes, 1D nanotubes, 2D graphene and 3D graphite exhibit very different (See Fig. 1.1)properties. The 2D materials consisting of a single type of atom typically bear the '-ene' suffix in their names; for *eg.*, graphene is named after graphite "+ene", Silicene is the combination of silicon "+ene", Germanene is germanium "+ene" and so on. In 1962, the term Graphene was termed by Hanns-Peter Boehm *et al.* who fabricated and observed single-layer carbon foils [38].

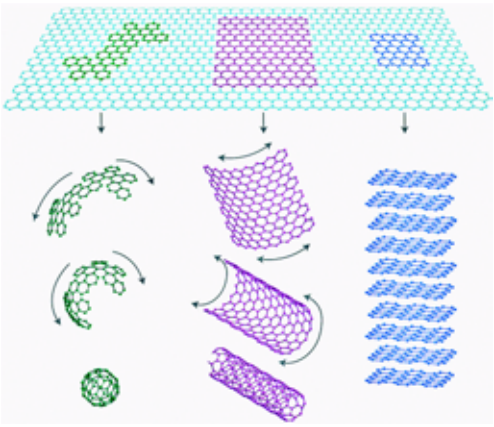

Figure 1.1: Mother of all graphitic form. Graphene is a 2D material for carbon materials of all dimensionality. It can be wrapped up into 0D fullerenes, rolled into 1D nanotubes or stacked into 3D graphite. Figure adapted from Ref. [1].

Materials consisting of compounds generally have the "-ane" or "-ide" suffixes. An example is Hexagonal boron nitride. At the nanometer scale one of the most essential parameter that defines the properties of the material is its dimensionality. Optical, electronic and thermal properties differ due to confinement of electrons and in the case of 2D materials, also due to the absence of interlayer interactions. These play an important role in determining band structure. Changes in mechanical and chemical properties are mainly due to geometry effects and to the high (even infinite in the thinnest materials) surface-bulk ratio [39, 40].

Following the seminal paper by Novoselov and Geim [41], graphene has become one of the most studied 2D material because of its exceptional electronic and optoelectronic applications [42]. It is one of the most attractive 2D material due to its uncommon band structure and phenomenal high carrier mobilities. It has thus created an immense interest in the condensed matter community and in the media since its isolation in 2004. Pristine graphene, though extremely interesting, suffers from a draw back; it is a zero band gap semi-metal, which makes it uninteresting from a device application point of view. Development of graphene-based electronics depends on our ability to open a tunable band gap. Fortunately, there are a large number of 2D materials that cover the entire range of electronic properties shown in Fig. 1.2. Hence large efforts have been made to functionalize graphene by engineering a controllable bandgap. Hexagonal Boron Nitride (h-BN) was theoretically predicted to produce a bandgap in graphene

when it was deposited on graphene[43]. The family of single-layered transition-

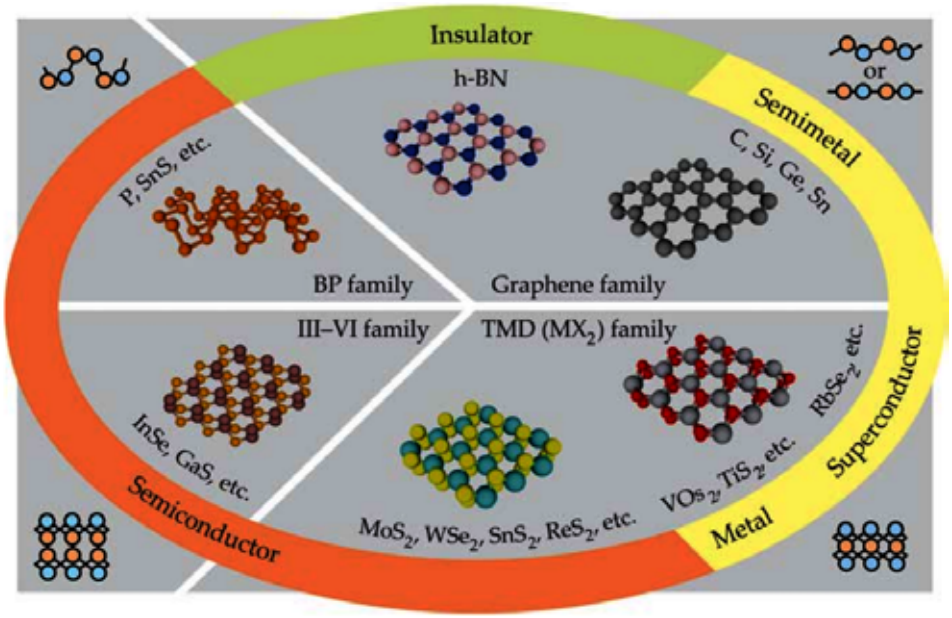

Figure 1.2: The 2D world of materials than stretch over the entire range of electronic properties. Schematic diagrams of the cross sectional area of the materials are shown at the four corners. These materials include graphene and its analogues, for *eg.*, *h*-BN, the III-VI calcifications of semiconductors and transition-metal dichalcogenides. Figure adapted from Ref. [2]

metal dichalcogenides (TMDs)- whose generalized formula is MX_2, where M is a transition metal of such as Mo, W, Ti, Zr, Hf, V, Nb, Hf, Fe, Co, Ni, Zn and X is a chalcogen such as S, Se, or Te include several semiconductors with band gaps in the range $\sim$ 0.5 eV to 3 eV.

There are essentially two approaches to synthesis 2D materials: The top-down approach and the bottom-up approach (see Fig. 1.3). The top-down approach involves the peeling off say a layer of graphene from the already existing structure in the form of graphite. Graphite is composed of layers of graphene. Individual graphene sheets were first exfoliated from graphite in 2004 by Andre Geim and Konstantine Novoselov isolated graphene in 2004 [41]. They stuck scotch tape to a block of highly oriented pyrolytic graphite and peeled off many layers. A second piece of tape was used to peel a few more graphite layers off of the first piece of tape. This process was continued about a dozen times. When the last piece of tape was stuck to a flat silicon wafer and peeled it away, some of the layers remaining on the

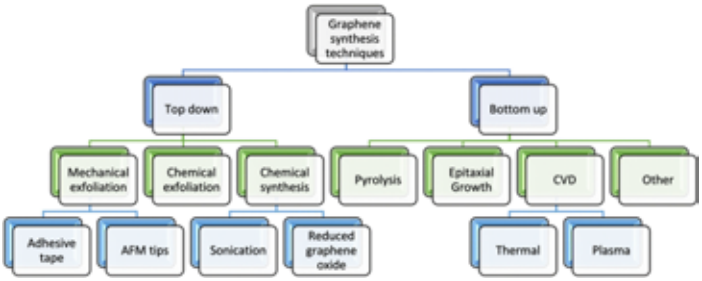

Figure 1.3: A process flow chart of Graphene synthesis. Figure adapted from Ref. [3].

wafer were a single atom thick. This method is therefore also known as "scotch tape" method. Examples of this approach are micro-mechanical cleavage or exfoliation, chemical exfoliation, electrolytic exfoliation, and thermal exfoliation and reduction. In the bottom-up approach, graphene layer is deposited on a substrate using hydrocarbon as the source of carbon. Examples of this approach are chemical vapour deposition (CVD), chemical conversion of CO_2, unzipping of carbon nanotube, arc discharge, self assembly of surface surfactant, epitaxial growth on SiC and solvo-thermal methods.

1.2 2D materials from layered Materials

In layered materials, the planar structures are held together by strong in-plane covalent bonds, whereas the layers are coupled by the relatively weaker out-of-plane van der Waals forces. Such layered materials are therefore also referred to as van der Waals materials. Each layer in these materials can be separated easily with little or no defects since it only involves breaking the van der Waals bonds. For example, by exfoliating bulk graphite, layers of graphene are constructed.

It is not only graphite that responds to the idea of pulling out a layer from a three dimensional material. Many such 2D nanomaterials have been discovered during the last few years. Hexagonal boron nitride and TMDs are examples of such materials. However, each TMD monolayer is three atom thick consisting of a transition metal layer sandwiched between two chalcogen layers. Layered materials are atomically very stable and hence can be relocated to any substrate with relative ease.

1.3 Van der Waal structures

The expanding range of van de Waals materials has turned the attention of the material science community to the question of designing new materials by stacking two or more 2D crystals of dissimilar materials. Such designer materials would have strong covalent bonds to provide in-plane stability of the 2D crystals, whereas

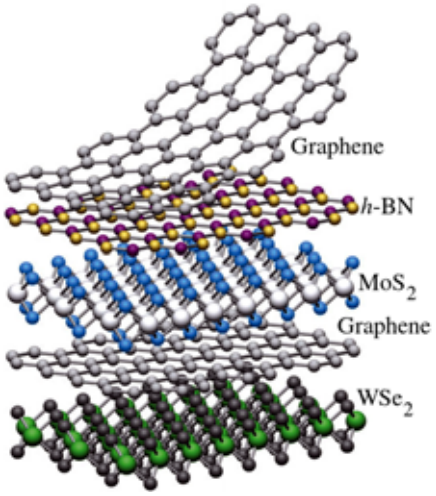

Figure 1.4: Building van der Waals heterostructures. Figure adapted from Ref. [4]

the stacks would be held together by the relatively weak the van-der-Waals-like forces. The resulting stack, called van der Waals heterostructure (vdWH) (see Fig. 1.4) exhibits absolutely novel physics besides opening a new era in integrated flexible technology.

1.4 Motivation

1.4.1 Basic physics in 2D

Reduced dimensions confines charge and heat transport to a plane. This leads to quantum confinement and a decrease in the bulk dielectric screening which results in exceptional electrical, optical, mechanical and magnetic properties. In

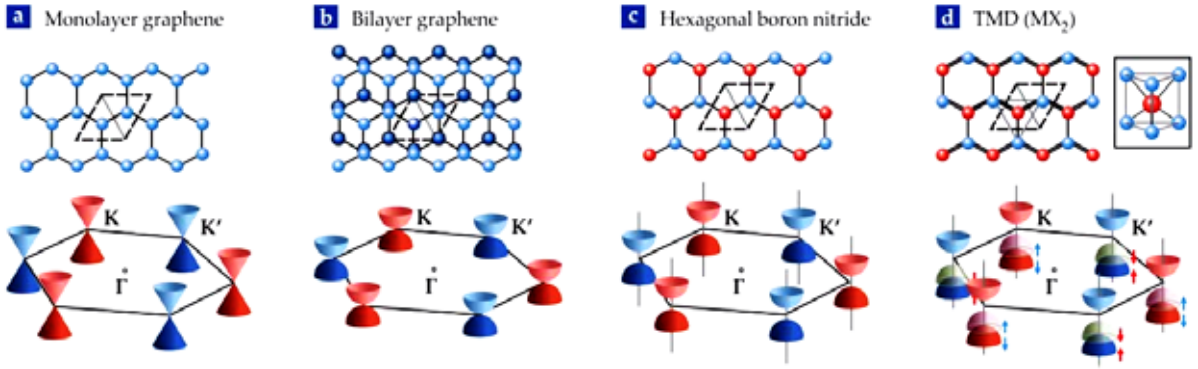

Figure 1.5: Lattice structure and schematic band structures at the corners of the first Brillouin zone for (a)monolayer graphene, (b) bilayer graphene, (c) hexagonal boron nitride, and (d) the transition-metal dichalcogenides (TMDs). The dashed lines in the lattice diagrams indicate unit cells. Because of their inversion symmetry, monolayer and bilayer graphene have no bandgap. Due to spin–orbit coupling, the TMDs' valence band is split into two spin-polarized bands, marked by the red and blue arrows. Figure adapted from Ref. [2].

graphene's band structure, the valence and conduction bands meet in conical valleys at two of the high-symmetry points, conventionally labelled $\mathbf{K}$ and $\mathbf{K}'$, in the Brillouin zone, as shown in Fig. 1.5 a. Thus the valence- and conduction band energies are linear functions of momentum. This property implies that the speed of electrons in graphene is a constant, much like the speed of photons, though the effective speed is 300 times less than the speed of light in vacuum. The quantum mechanical description can thus be simplified by introducing quasi-relativistic spin-$\frac{1}{2}$ particles with a vanishingly small mass and governed by Dirac equation and are therefore called Dirac Fermions (See Appendix A). Graphene's relativistic behaviour arises from the symmetry of the honeycomb lattice rather

from the requirement of Lorentz invariance. This gives rise to novel phenomena, such as the anomalous room-temperature quantum Hall effect [44, 45], and has opened up a new category of "Fermi-Dirac" physics.

Fig. 1.5 b shows bilayer graphene which consists of two graphene layers stack together to form a staggered honeycomb lattice. Its quasi-particles gain mass, and the energy dispersion becomes parabolic. However, since the inversion symmetry is maintained the energy at the $\mathbf{K}^{'}$ and $\mathbf{K}$ is still degenerate thus preventing an opening of a bandgap. This energy degeneracy can be lifted by breaking the lattice's inversion symmetry. In h-BN shown in Fig. 1.5 c, this is achieved by replacing two carbon atoms in the graphene's unit cell by boron and nitrogen.This results in a large energy gap, making h-BN an extremely good insulator and dielectric. A similar symmetry breaking takes place in TMDs (see Fig. 1.5 d) giving rise to a family of semiconductors with a full bandgap range, from visible to infrared.

1.4.2 Applications

As shown in Fig. 1.2, since ultrathin 2D nanomaterials encompasses a complete range of electronic properties they can be integrated in a variety of applications in electronics/optoelectronics, catalysis, energy storage and conversion, sensors, biomedicine, *etc.*

2D monolayers which are semiconducting in nature, having direct band gaps, are suitable for producing and detecting photons at wave lengths which are function of the band gaps. They can be tuned through quantum confinement, which are achieved by changing the number of layers. Synthesis of various 2D circuit elements into 2D memory devices can be an interesting way to produce low-power, flexible electronics. It is encouraging to device 2D logic circuits from a starting layered material sheet, for *eg.*, graphene, which can be tuned from a semi-metal into a semiconductor. This can be done either by doping with other elements and thus lessen the need for external contacts. Integrating 2D memory layers, logic circuits with 2D sensors, optics, and components needed for energy storage can be used to design energy-effective, ultrathin solid state devices.

Due to the latest breakthroughs in experiments, graphene monolayers can be

grown on metallic as well as non metallic substrates. Many other 2D materials, for *eg.*, MoS_2 or in general TMDs, can also be synthesized by CVD methods. Development in 2D materials has been backed by developments in characterization techniques, such as Raman spectroscopy to understand how layered materials are piled up together and to establish the number of layers in a system. It is possible to avoid vapor-phase synthesis by exfoliating materials having layers which are atomically stable, for *eg.*, graphene, *h*-BN, TMDs, *etc.* to obtain mono- and few layers which have useful application for energy storage. However, for atomically unstable materials that do not have corresponding layered materials, such as silicene, stanene, phosphorene, germanene and borane, which are atomically stable only in particular isomeric structures, still remains a challenge to grow.

1.4.3 Review of the materials studied in the thesis

1.4.3.1 Mono- and Multi- layer graphene

There are six electrons in the atomic orbitals of carbon, $1s^2\ 2s^2\ 2p^2$. However, the $1s$ electrons do not contribute to the chemical bonds as they are typically inert. The $2s$, $2p_x$ and $2p_y$ orbitals in graphene hybridize to shape the new planar orbitals called sp^2 orbitals. These orbitals are along lines making an angle of 120° with each other, which are responsible for the hexagonal lattice structure and contain one electron each.

A single layer of graphite was first studied theoretically in 1947, by Philip Russel Wallace [46]. Using the tight binding approximation he showed the unusual semimetallic behavior in this material. As discussed earlier the conduction and the valence bands are not separated by a gap, and do not overlap either. In fact they intersect in two inequivalent points, called Dirac points in the first Brillouin zone. The electron dispersion in the vicinity of the Dirac points is conical and not parabolic, as in most semiconductors. At that time, the thought of a purely 2D structure was not reality and Wallace's studies of graphene served him as a starting point to study graphite, an important material for nuclear reactors in the post–World War II era. However, in 2004, Andre Geim's group, at Manchester University [41] produced a single layer of graphite using micromechanical exfoliation (Microexfoliation). Further, they studied

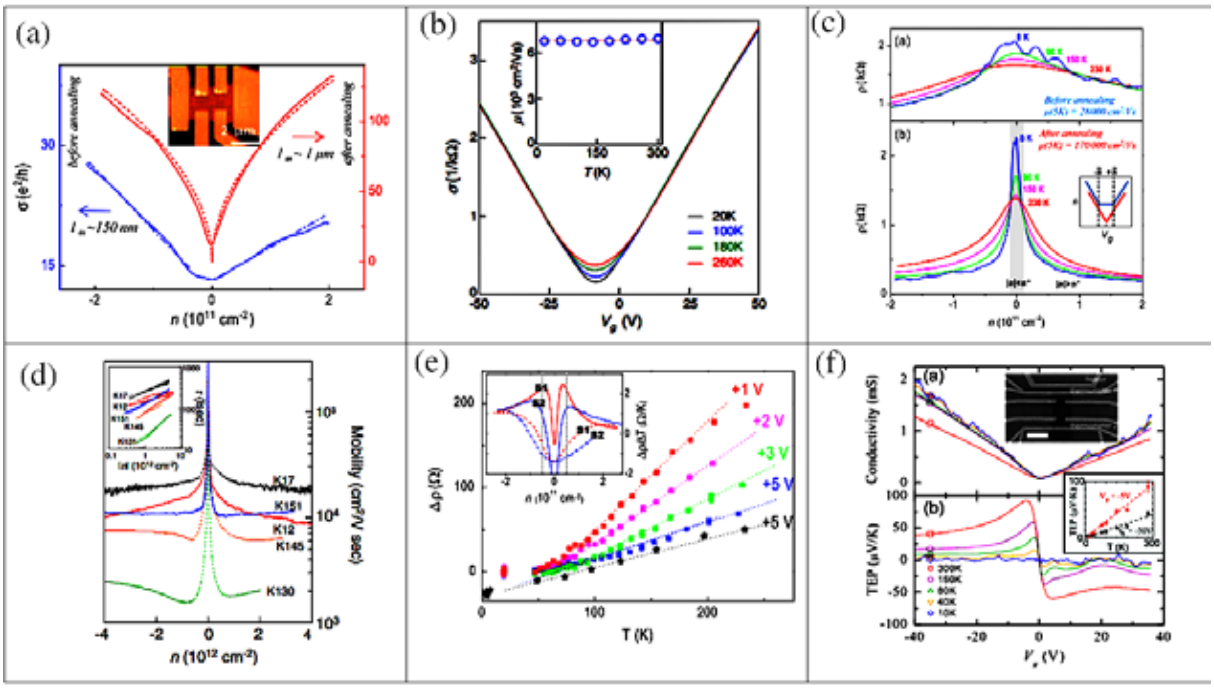

Figure 1.6: Experimentally measured electron transport coefficients of MLG and BLG. (a) The electrical conductivity of graphene as a function of charge carriers before (blue) and after (red) annealing the sample. (b) The electrical conductivity of bilayer graphene at various temperature as a function of gate voltage. (c) The resistivity of graphene as a function of charge carriers before (top) and after (below)annealing the sample. (d) The mobility of graphene as a function charge carriers. (e) The Bloch-Grüneisen behavior of graphene at various gate voltages. (f) The Seebeck coefficients of graphene as a function of gate voltage at various temperatures. Figures adapted from references [5, 6, 7, 8]

the electric field effect and carried out a series of successful experiments on the produced graphene, thus dispelling the earlier hypothesis [36, 37]. Andre Geim and Konstantine Novoselov were awarded the Nobel Prize in Physics in 2010 "for groundbreaking experiments regarding the two dimensional material graphene".

It has been shown that the electronic structure of graphene rapidly evolves with the number of layers, approaching the 3D limit of graphite at 10 layers [43]. Moreover, only graphene and, to a good approximation, its bilayer has simple electronic spectra: they are both zero-gap semiconductors with one type of electron and one type of hole. For three or more layers, the spectra become increasingly complicated: several charge carriers appear [47, 45] and the conduction and valence bands start to overlap [43, 47]. This allows single-, double- and a few - (3 to <10) layer graphene to be distinguished a three different types of 2D crystals (“graphenes”). Thicker structures should be considered, to all intents and purposes, as thin films of graphite [45]. The strength and specificity of its covalent bonds makes graphene one of the strongest materials

(tensile strength of about $\sim$ 130 gigapascals) in nature, albeit one of the softest (0.77 mg/m^2($\sim$ 1000 times lighter than paper)), with literally no extrinsic substitutional impurities, leading to the highest electronic mobilities among metals and semiconductors. It has extraordinary thermal, mechanical, electrical and many other properties. The most intriguing aspects of graphene are its unique electronic properties such as ballistic transport, longest free path ($\sim$ 300 μm) and high electron mobility ($\sim 20 \times 10^3$cm^2/Vs.) at room temperature, quantum Hall effects and massless Dirac ferminons [45]. Therefore, graphene is being considered for a plethora of applications that range from conducting paints, and flexible displays, to high speed electronics. In fact, it can be said that perhaps, not since the invention of the transistor out of germanium in the 1950's, a material has had this kind of impact in the solid state literature.

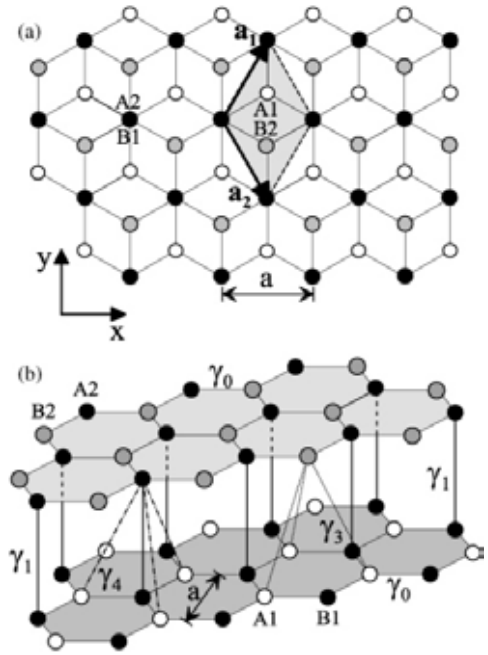

Figure 1.7: (a) Top and (b) side view of the crystal structure of bilayer graphene. Atoms A1 and B1 on the lower layer are shown as white and black circles, A2, B2 on the upper layer are black and grey, respectively. The shaded rhombus in (a) indicates the conventional unit cell. Figure reproduced from [9].

Bilayer graphene consists of two monolayers, with four atoms in the unit cell, labelled A1, B1 on the lower layer and A2, B2 on the upper layer (see Fig. 1.7). The layers are arranged such that atom B1 from the lower layer is directly below atom A2 from the upper layer. The other two atoms, A1 and B2, do not have a counterpart on the other layer that is directly above or below them [9]. This stacking type is known as the Bernal-stacked or AB-stacked and is the most thermodynamically stable configuration in comparison to the other types of stacking, the AA-stacked or twisted graphene. Many of the properties of bilayer graphene are comparable to that of monolayer graphene such as exceptional electrical conductivity [48]; tuning the electrical properties by doping or altering the carrier density through gating [41, 49, 50], high room temperature lattice thermal conductivity [51, 52], Young's modulus for bilayer graphene is about 0.8 TPa [53, 54], the transparency is about 95% with transmittance of white light [55], impermeable to gases [56] and lastly,

the capability of being chemically fabricated [57]. Therefore, just at monolayer graphene, bilayer graphene has promising application in areas such as transparent and flexible electrodes for touch screen display [58], high-frequency transistors [59], thermoelectric devices [60], photo-detectors [61], energy storage devices like super-capacitors [62, 63] and composite materials [64, 65]. However, bilayer graphene has characteristics that make it unique as compared to monolayer graphene. More specifically, the low-energy band structure is distinct. Unlike monolayer graphene having a linear low-energy dispersion, bilayer graphene has a quadratic electronic energy dispersion and hence bilayer graphene has chiral quasiparticles [49, 66] instead of massless one as in the case of monolayer graphene.

Bilayer graphene is the thinnest possible limit for an intercalated material [62, 63] since it constitutes only two layers of monolayer graphene. Bilayer graphene can be used as a tunable band gap semiconductor. One can focus on each of the layers separately making way to new characteristics in bilayer graphene which include the potential to control the energy band gap up to ~ 300 meV by doping or gating [66, 67, 50]. Moreover, by electrostatic confinement with gates, the band gap in bilayer graphene has been used to build devices, constrictions and dots [68]. When there is the need to use more material for increased strength [64, 65] or optical signatures [69], bilayer or multilayer graphene can be more favorable as compared to monolayer graphene. The fundamentals to electronic transport properties of graphene is to understand the mechanism which causes the scattering of its charge carriers. [70, 71]. Scattering might result from the following reasons, (i) due to charged impurities from the bottom substrate or the impurities in the graphene sheets [72, 70, 71], (ii) wrinkles in the graphene sheet [6], (iii) phonons in graphene [73, 74, 75, 76], (iv) puddle formation of hole and electron at low carrier density [77, 78].

Bolotin *et. al.* [5] have found a decline carrier scattering for suspended graphene. They reported that, after an annealing treatment to get rid of the residual impurities, the graphene sample mobility surpassed 2×10^5cm^2/Vs, an order of magnitude enhancement as compared to graphene devices on a substrate [79]. This allowed them to probe transport regimes which are now made accessible due to remarkable cleanliness of suspended graphene. They show that

the resistivity is greatly dependent on temperature. For *eg.*, at low temperature, $T \sim 5$K, the electron mobility is $\sim 1.7 \times 10^5$cm^2/Vs which is nearly ballistic. For larger carrier densities, the resistivity increases with T having a linear dependence above 50K suggesting that the carrier scattering is from acoustic phonons. The highest measured mobility was also recorded by them for their most pure sample having a value of 1.2×10^5cm^2/Vs at T =240 K. The low temperature regime electrical conductivity on the suspended sample showed a linear behavior of n before the annealing treatment. This linearity of electrical conductivity suggests that the scattering is primarily due to charge impurities A dozen of graphene sample specimens were investigated to measure the conductivity by Tan *et.al.* [7] with different levels of disorder with mobility in the range from 1×10^3cm^2/Vs - 20×10^3cm^2/Vs.

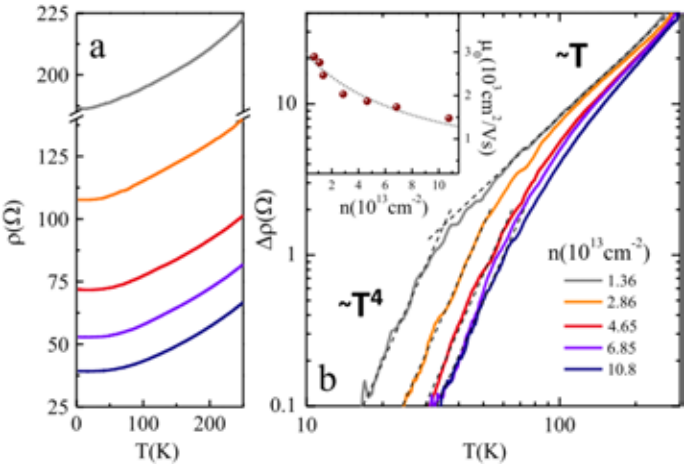

Figure 1.8: (a)Resistivity as a function of temperature for different charge carrier densities of graphene samples. (b) The temperature dependent resistivity scales as T^4 in the low T range to a linear T range for temperature larger than the Bloch-Grüneisen temperature, Θ_{BG}. Figure adapter from reference [10]

They estimated that the impurity concentration showed values in the range 2×10^{11}cm^{-2}-15×10^{11}cm^{-2}. The conductivity of these specimens in the low carrier density limit are linked to residual density effected by the inhomogeneous charge distribution in the graphene samples having values in the range $2\frac{e^2}{h} - 12\frac{e^2}{h}$. Temperature dependence of electron transport were also done by Morozov *et. al.* [6] for both mono- and bi- layer graphene and concluded that if extrinsic disorders were eliminated, mobilities higher than 2×10^5cm^2/Vs are achievable. The resistivity depends greatly on the electron-phonon scattering in the material. For temperatures above the Debye temperature Θ_D, the resistivity varies linearly with temperature which reflects the classical behavior of phonons. The bosonic behavior of phonons are seen below Θ_D which results in a swift decrease in resistivity, *i.e.*, the temperature dependent resistivity is $\rho \sim T^5$ for a normal 3D conductor. However, for 2D systems, such as graphene, a new characteristic temperature scale for the low-density electron-phonon scattering

is define known as the Bloch-Grünesien (BG) regime. The BG temperature is given $\Theta_{BG} = \frac{2v_{ph}k_F}{k_B} < \Theta_D$. Here v_{ph} and k_F are the phonon group velocity and Fermi momentum, respectively. It was theoretically predicted [73] and experimentally observed [10] that in 2D systems the smooth transition from the classical behavior to the rapidly decreasing regime will have the temperature dependence as $\rho \sim T^4$. Electrical conductivity and Seebeck coefficient were also calculated for the first time by Zuev *et. al.* [8] using a microfabricated heating system. These experimental works carried out by various groups [8, 10, 73, 6, 7] on electron transport coefficients for MLG and BLG have motivated us to carry out computational studies based on first-principles calculations.

1.4.3.2 Single- and multi- layer Hexagonal boron nitride (h-BN)

Bulk Hexagonal boron nitride (*h*-BN) has a layered crystal structure similar to that of graphite, with equal numbers of boron and nitrogen atoms replacing the carbon atoms in the hexagonal structure. Within each layer, the boron and nitrogen atoms are bonded by highly covalent bonds, while these layers are held together by the van der Waals force to form the bulk crystal. A single-layer *h*-BN nanosheet is therefore commonly known as the "white graphene". It has a very small lattice mismatch of about 1.7%, which is commonly regarded as a prerequisite for the growth of defect free epitaxial heterostructures. *h*-BN has a large optical phonon mode and belongs to the wide band gap class of insulators. Besides its exotic opto-electrical properties it is mechanically robust (Young's modulus is approximately 270 Nm^{-1}), thermal stability (at room temperature, the thermal conductivity of *h*-BN is up to 400 $\mathrm{Wm}^{-1}\mathrm{K}^{-1}$, which is higher than the majority of metals and ceramic materials) and chemical inertness [48]. It is thus extensively studied for application in field effect transistors (FETs), tunneling devices, deep UV emitters and detectors, photoelectric devices, and nanofillers. Single and multilayer *h*-BN demonstrate a lower lattice thermal conductivity as compared to the corresponding number of layers in graphene and is therefore intriguing to study its length and temperature dependence lattice thermal conductivity.

1.4.3.3 Doped graphene and $C_{2x}(BN)_{1-x}$

A practical method to control the semiconducting properties of graphene is by doping [14]. Experimental and theoretical studies on graphene doping show the possibility of making p-type and n-type semiconducting graphene by substituting C atoms with B and N atoms, respectively. Since the binding energies of B-B and N-N bonds are weaker than that of C-N and C-B bonds, boron or nitrogen are relatively easily doped into the lattice graphene. Also the atomic masses of these dopants are closest to carbon, thus making them acceptable for carbon lattices to adjust to, whilst at the same time significantly altering the electronic properties of the host material because of the electron-rich and electron-deficient nature of N and B atoms. Mukherjee *et al.* [80] have shown that doping graphene with nitrogen, the Dirac point in the bandstructure of the doped material relocates below the Fermi energy and creating a band gap at the high symmetric K-point. However, when the graphene is doped with boron, the Dirac point moves above the Fermi energy and a gap appears at the high symmetric K point. Moreover, co-doping both boron and nitrogen , the energy band gap is appears between the conduction and valence band, the Fermi level, having the characteristic as a narrow gap semiconductor. Strong charge transfer interactions with graphene are due to atoms having electron withdrawing or donating functional groups. These types of doping occur through the adsorbed dopant to graphene and *vice versa*. The relative position of the density of states of the highest occupied molecular orbital (HOMO) and the lowest unoccupied molecular orbital (LUMO) of the dopant, and the Fermi level of graphene determines if the charge transfer will occur.

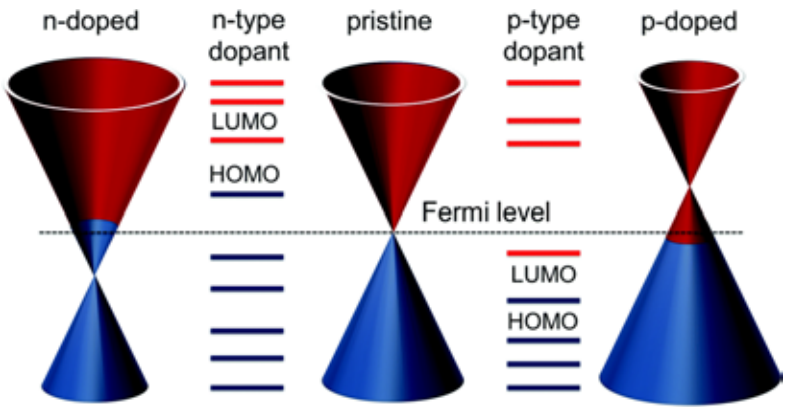

Figure 1.9: Schematic diagrams demonstrating the correspondence between the position of the HOMO-LUMO levels of dopants relative to the Fermi level of graphene pertaining n- and p-type doping. Figure adapted from references [11]

When the HOMO of the dopant is above the Fermi level of graphene, charge is transferred from the dopant to the graphene layer which results in n-type

doping. However, charge transfer takes place from graphene to the dopant resulting to p-type doping when the LUMO for the dopant is below the Fermi level of graphene. n-type (p-type) doping makes the Dirac point shift below (above) the Fermi level (See Fig. 1.9). The extent of charge transferred per molecule, besides the accurate separation of the HOMO/LUMO levels of the dopant with respect to the Dirac point, relies on the distance and orientation of the adsorbate with respect to the graphene plane.

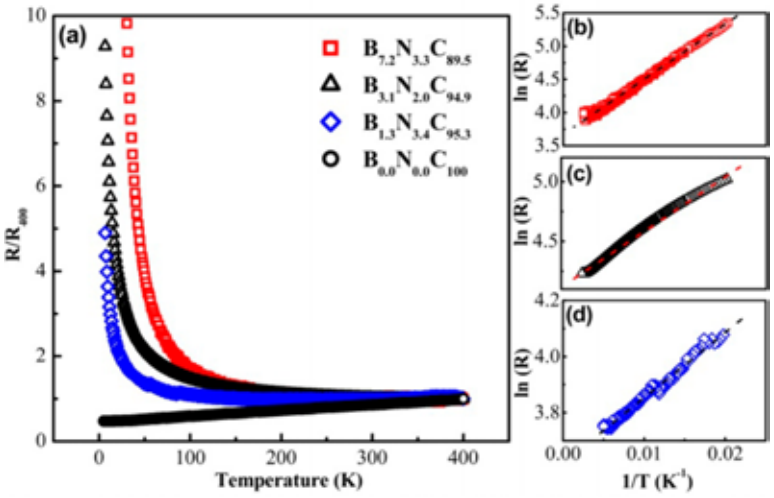

Figure 1.10: (a)Scaled resistance versus temperature for undoped and boron nitrogen doped graphene. The resistance is seen to increase with increasing temperature which shows a metallic behavior. The boron nitrogen doped samples show semiconducting behavior. (b-d) The logarithmic of resistivity versus the inverse of temperature in the temperature range 50-400K for various boron and nitrogen concentrations. Figure adapted from reference [12].

The response to physical properties of materials due to impurities have captivated material scientists for decades. Thus the capability to produce structural defects into 2D layered materials such as graphene through doping, such as boron and nitrogen, has unlocked many possibilities to understand the aftermath of disorder at the atomic level. The possibility to regulate the electronic properties of single layers CBN simply by varying its constituent concentration of B and N will bring about a boost in obtaining materials with tunable electronic properties which will be suitable from solid state devices.

Hexagonal Boron Nitride (*h*-BN) is insulating having a band-gap of nearly 5-eV and a lattice constant which is very close to that of Graphene. Therefore it can be easily synthesized in the form of monolayer flakes [81, 82], making it possible to provide a wide range of band-gap materials depending on the degree of mixing [83]. A great deal of effort has been made to synthesize hexagonal CBN (*h*-CBN) monolayer and multilayer nanomaterials with varying concentration of C/BN [84, 14, 48, 85] since such materials are of great importance in optoelectronic devices. Synthesis of laterally grown in-plane heterostructures of Graphene and

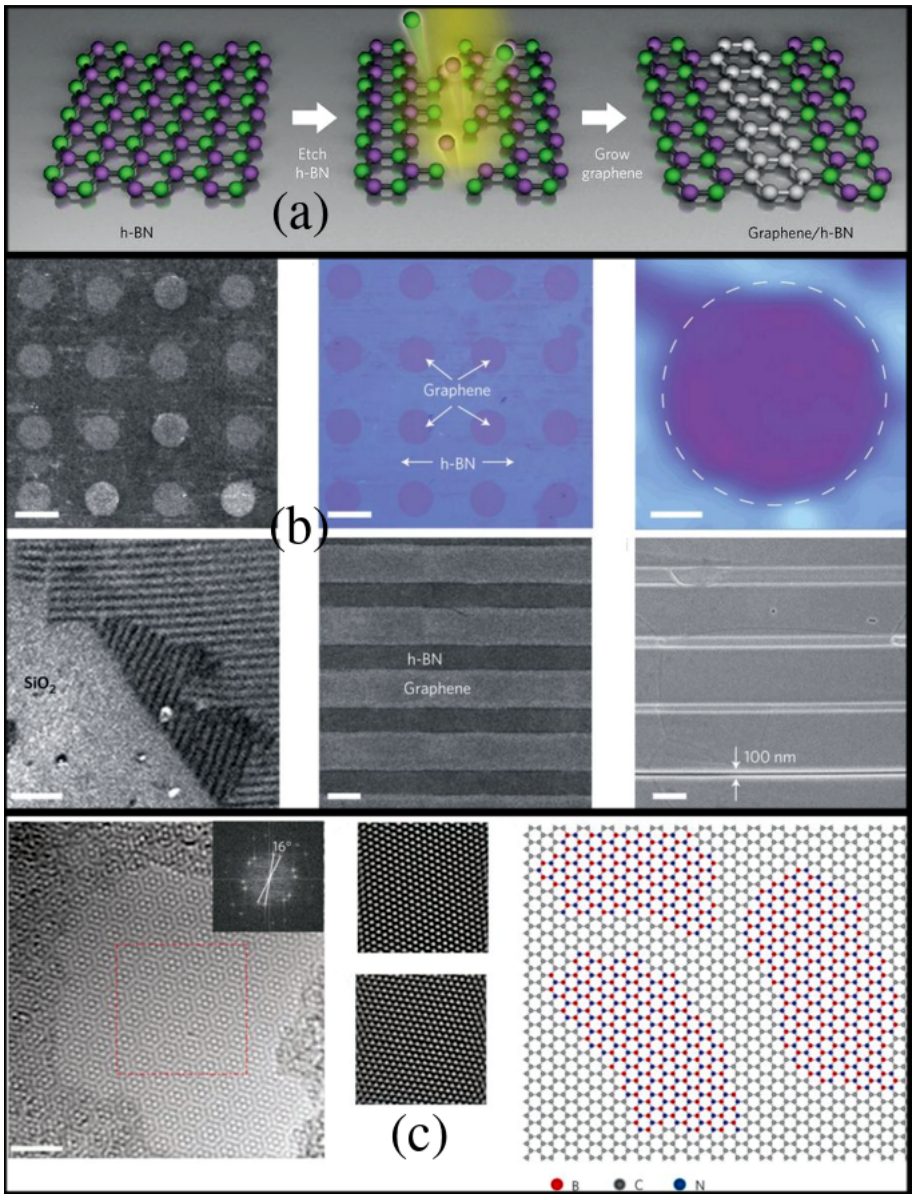

Figure 1.11: (a)Schematic description of the fabrication for in-plane graphene/*h*-BN heterostructures. (b)Scanning electron microscopic images, optical images and Raman mapping of various boron nitride patterns on graphene. (c)Atomic High-resolution transmission electron microscopy (HRTEM) images of *h*-BNC film. Figures adapted from References [13, 14]

h-BN, in which these two materials are seamlessly integrated lithographically with varying domain sizes have been experimentally reported by Liu *et. al.* [13].

Their method can make periodic arrangements of domains having sizes ranging from tens of nanometres to millimetres. (See Fig. 1.11). The derived atomic graphene/*h*-BN layers can be exfoliated from the growth substrate and relocated to various platforms such as flexible substrates. Using Chemical Vapour Deposition (CVD) techniques, Panchakarla *et. al.* [84] and Ci *et. al.* [14], initially synthesized *h*-CBN by carefully controlling the concentration of C or

BN. Samples of all *h*-CBN exhibited semiconducting behavior having band-gap between few meV to nearly an eV, a fact verified by first-principles calculations [12]. Various groups have studied the formation of band-gaps in graphene when doped by boron and nitrogen [86, 87, 88, 89, 90, 91]. Synthesis of these astounding laterally grown hybrid $C_{2x}(BN)_{1-x}$ two-dimensional heterostructures with different shapes such as circular dots, stripes patterns *etc.* of varying widths and sizes (See Fig. 1.11) has made the possibility of device applications of such materials a reality. Using different experimental conditions by other various groups [92, 93, 94] have also synthesised similar hybrid *h*-CBN heterostructures. Muchharla [12] *et. al.* measured the temperature dependent resistivity to demonstrate the effect of inserting boron and nitrogen to the electronic properties of the graphene lattice for three CBN having different concentrations. They plotted the logarithmic resistivity versus temperature inverse, which correlates to the thermally activated transport mechanism in the given temperature range, resulting in a linear behavior (See Fig. 1.10).

1.4.3.4 Graphene and h-BN heterostructures

Enormous class of 2D van der Waals layered materials have been investigated ever since graphene was made available by the scotch tape technique. What makes 2D van der Waals (vdW) materials more interesting is that the well-established physics and chemistry of the 3D bulk materials are frequently unimportant, resulting in fascinating characteristics in 2D vdW systems. By the ways of simple exfoliation methods, vast quantum mechanical devices have been achieved for fundamental physics research and technological application by assembling heterostructure of these materials in the vertical directions. Essentially, the interactions between adjacent layers of the 2D layer materials are described by the vdW forces due to the saturated chemical bonds on the their surface. Therefore, vdW interactions allow, without direct chemical bonding, the synthesis of highly disparate materials without the constraints of crystal lattice matching [95]. Multilayers are defined by stacking single layer of a material on top of each other. Since single and multi layer hexagonal boron nitride (*h*-BN) have a similar lattice constant, unit cell mass and Van der Waals type bonding to that of single and multi layer graphene, one can stack

h-BN along graphene, making *h*-BN a perfect substrate for graphene electronics. These heterostructures are atomically stable and have properties which are unique to the number of layers. For example, as mentioned previously, bilayer graphene can be used as a tunable band gap semiconductor. 2D G/*h*-BN heterobarriers have been proposed and investigated and hence graphene and *h*-BN layered architectures are potential candidates for device applications with novel transport properties. The comprehensive collection of 2D layer materials with preferable material properties gives rise to promising possibilities of heterogeneous synthesis at the atomic limit, developing innovative hybrid structures that demonstrate fundamental physics and allow distinct functionality.

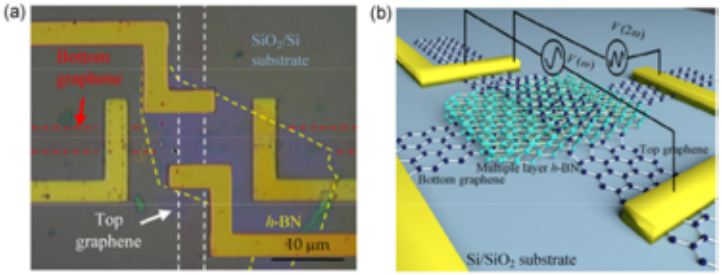

Figure 1.12: Schematic figure of the optical image and measurement setup of graphene/*h*-BN/graphene heterostructure device. Figure adapted from reference [15].

2D nanomaterial offer possibilities in exhibiting improved thermoelectric figure-of-merit when constructed in the form of compound semiconductors, semiconductor multilayers, and superstructures and hence been a subject of interest in recent years [96, 97, 98]. Appealing range of capabilities that extend beyond lateral graphene devices are shown in the electron transport in the cross-plane direction of layered material heterostructures. For *ex.*, graphene based heterjunction devices such as graphene/silicon and graphene/gallium arsenide diodes have shown improved behavior and gate-tunable photovoltaic responses [15]. Hybrid atomic layers with fascinating electronic applications can be deviced, if accurate two-dimensional domains of graphene and *h*-BN can be smoothly joined together [85]. Combining heterostructure devices with graphene with other 2D material like *h*-BN or MoS_2 have shown intriguing electron tunnelling transport, light absorption and negative differential conductance. Atomically layered graphene and *h*-BN systems are promising candidates for solid state device applications. Graphene transistors have been suggested and inspected from a theoretical point of view [99] which were initially motivated by the experimental success of graphene-boron-nitride lateral hecterostructures [100]. Vertical heterobarrier graphene based transistors, based on simulation

studies, have also been proposed by Sciambi *et al.* and Mehr *et al.* [101, 102]. Zhong [103]*et al.* have addressed theoretically the quantum transport in trilayers G/*h*-BN/G and *h*-BN/G/*h*-BN and predicted a metal-like conduction in the low-field regime. Using non-equilibrium Green's function method for different thickness of *h*-BN and graphene domains, thermoelectric transport in G/*h*-BN nanoribbons have been considered [104]. Using molecular dynamic simulation, thermal transport was investigated by Kinaci *et al.* [105]. A prototype field-effect tunnelling transistor with atomically thin boron nitride behaving as a vertical transport barrier was reported by Britnell *et al.* [106]. Aside from electron transport, in graphene based heterojunction devices, the heat dissipation is found to be influenced by vertical heat transfer [107, 108]. Recently the thermoelectric transport measurement across the G/*h*-BN/G heterostructure with different number of layers of *h*-BN layers [15]. Chen *et al.* [15] observed a Seebeck coefficient of -99.3 μV/K and power factor of 1.51×10^{-15}W/K^2 for the G/*h*-BN/G heterostructure device based on the thermoelectric voltage and temperature gradient. However graphene is gapless and hence it is not easy to modulate the electron current, which is an essential feature in electronics. When graphene is doped with boron *i.e.* hole doping, the Dirac point in the graphene band structure moves above the Fermi level and a gap appears, while for electron doping *i.e.* graphene doped with nitrogen, the point moves below the Fermi level. For the doped graphene to be a semiconductor, the Fermi level must lie between the conduction and valence band. This can be achieved by co-doping graphene with both B and N.

Chapter 2

Theoretical Framework

2.1 Density functional theory [1]

2.1.1 Introduction

Problems which do not have an analytical solution, numerical methods using computers are of vital importance. Computers have thus become an essential part in the world of physical chemistry, condensed matter physics, material science, molecular physics and solid state physics. The field of computational physics attends to the determination of energies, charge density distributions and electronic structure, principally with the ground state, of many-body systems. The aim is to get the vision of the molecular processes as seen in experiments as well as to predict them.

Hartree and Fock were the first to deal with the complicated non analytical many-body Schrödinger equation. They derived a wave-function based, self-consistent equations allowing an iterative calculation of energies. A major hurdle using the Hartree-Fock method is the high cost of computation time. It emerges from the dependency of the many-body wave function of the 3N spatial variables.

Lowering the computational cost of molecular and atomic calculations can be achieved by using a less complex base variable. The ground work for such

[1] This theory has been implemented in Chapter 3, 4,5 and 6

an approach was provided by Hohenberg and Kohn in 1964. They proved that a variable only depending on three spatial, the electron density, contains all the information about the ground state properties of the many-body system. This marked the beginning of density of functional theory (DFT).

Density functional theory (DFT) is a powerful, quantum mechanical modelling method for computing the quantum states of atoms, molecules and solids. DFT rests on two mathematical theorems proved by Hohenberg-Kohn (H-K). The first H-K theorem shows that for a many electron system, the ground state energy from Schrödinger equation is a unique functional of the electron density which depends only on 3 spatial coordinates. The second H-K theorem proves that the true ground state electron density minimizes the energy functional corresponding to the solution of the Schrödinger equation. In 1998 Kohn won the Nobel prize "for his Development of the density-functional theory". [109, 110] Kohn and Sham, in 1965, derived iteratively solvable, self-consistent equations which allowed the use of the only theoretical concept then applied by Hohenberg and Kohn in actual computer simulations [111]. Since the electron density is a function of only three spatial coordinates compared to the multi-electron wave function, the computation times of DFT based calculations are significantly lower.

Electronic structure calculations using the density functional theory became popular in condensed matter physics and material science in the 1990s. Today, it is by far the most universally used method to obtain electronic structure calculations. By having the basic structural information, one can determine the properties of a condensed matter system without any flexible parameter and hence it is referred to as first-principles or *ab initio* method. Other than conventional experimental methods, density functional theory serves as an alternative to examine condensed matter systems. Density functional theory is therefore a powerful tool for theorists as well as experimentalists to interpret the characteristic properties of materials and make distinct prediction of experimentally observable developments in real materials and to design new solid state devices and materials.

In the Kohn-Sham method, the original interacting system with the true potential is mapped onto a fabricated non-interacting system where the electrons

are influenced by an effective Kohn-Sham single-particle potential. Therefore, the Kohn-Sham approach is to substitute the initial many-body problem by an auxiliary independent system. Generally numerical codes are based on the Kohn-Sham approach to the primitive density functional theory. In the effective Khon-Sham single particle potential, the many body effects are approximated by the exchange-correlation functional. Extensively used exchange-correlation fucntionals are the local density approximation (LDA) and generalized gradient approximation (GGA). LDA originates from exchange-correlation functional of a homogeneous electron gas by a point by point mapping, *i.e.*, the LDA depends entirely on the value of the electronic density at each point in space. While GGA is a generalization of LDA by being inclusive of contributions from electron density gradient. The area of electronic structure calculations is quickly developing in basic theory, new algorithms, and computational methods and power.

2.1.2 Many-Body System and Born-Oppenheimer Approximation

The many-body Hamiltonian (H_{tot}) of a condensed matter system consisting of nuclei and electrons can be expressed as,

$$\begin{aligned} H_{tot} &= -\sum_{I} \frac{\hbar^2}{2M_I} \nabla^2_{\mathbf{R}_I} - \sum_{I} \frac{\hbar^2}{2m_e} \nabla^2_{\mathbf{r}_i} + \frac{1}{2} \sum_{\substack{I,J \\ I \neq J}} \frac{Z_I Z_J e^2}{|\mathbf{R}_I - \mathbf{R}_J|} \\ &+ \frac{1}{2} \sum_{\substack{i,j \\ i \neq j}} \frac{e^2}{|\mathbf{r}_i - \mathbf{r}_j|} - \sum_{I,i} \frac{Z_I e^2}{|\mathbf{R}_I - \mathbf{r}_i|}. \end{aligned} \tag{2.1}$$

The dummy variable i and j corresponds to the electrons and I and J to the nuclei. $\mathbf{R}_I$ and M_I are the positions and masses of the nuclei. Similarly, $\mathbf{r}_i$ and m_e are the positions and masses for the electrons. Z_I is the atomic number of nucleus I. The first and second term are the kinetic energies of the nuclei and electron, respectively. The third term, fourth and fifth term are the potential energies of the nucleus-nucleus, electron-electron and electron-nucleus interaction, respectively. The time-independent Schrödinger equation is expressed as,

$$H_{tot} \Psi(\mathbf{R}_I, \mathbf{r}_i) = E \Psi(\mathbf{R}_I, \mathbf{r}_i) \tag{2.2}$$

Here, $\Psi(\mathbf{R}_I, \mathbf{r}_i)$ is the total wavefunction of the system. Everything about the system, in principle, can be known by solving the Schrödinger equation Eq. 2.2. It is, however, a nearly impossible task to solve Eq. 2.2 in practice. The nuclei being much heavier than the electrons, the nuclei moves extremely slower ($\sim$ two order of magitude slower, since the mass of a proton is $\sim$ 1836 times the mass of an electron) than the electrons. Therefore, one can now separate the movement of nuclei and electron. This is the Born Oppenheimer (BO) approximation [112] where the electronic and nuclear motions in an atom, molecule or solid is treated independently, *i.e.* the total wavefunction is factorized into an electron wavefunction and a nuclear wave function. Assuming the nuclei to be stationary, the total wave function can now be, expressed as,

$$\Psi(\mathbf{R}_I, \mathbf{r}_i) = \Theta(\mathbf{R}_I)\phi(\mathbf{R}_I, \mathbf{r}_i) \tag{2.3}$$

$\Theta(\mathbf{R}_I)$ describes the wavefunction component of the nuclei and $\phi(\mathbf{R}_I, \mathbf{r}_i)$ that of the electron. The electron wavefunction depends parametrically on the position of the nuclei and satisfies the Schrödinger equation,

$$H_e\phi(\mathbf{R}_I, \mathbf{r}_i) = V(\mathbf{R}_I, \mathbf{r}_i)(\mathbf{R}_I, \mathbf{r}_i) \tag{2.4}$$

which represents a stationary eigenvalue problem for any given set of R_I. Here H_e, the electron Hamiltonian, is given by,

$$\begin{aligned} H_e &= -\sum_I \frac{\hbar^2}{2m_e}\nabla^2_{\mathbf{r}_i} + \frac{1}{2}\sum_{\substack{I,J \\ I\neq J}} \frac{Z_I Z_J e^2}{|\mathbf{R}_I - \mathbf{R}_J|} \\ &+ \frac{1}{2}\sum_{\substack{i,j \\ i\neq j}} \frac{e^2}{|\mathbf{r}_i - \mathbf{r}_j|} - \sum_{I,i} \frac{Z_I e^2}{|\mathbf{R}_I - \mathbf{r}_i|}. \end{aligned} \tag{2.5}$$

The eigenvalues $V(\mathbf{R}_I)$ determined from Eq. 2.4 are used as the operators of potential energy in the equation determining the nuclear motion,

$$\left[-\sum_I \frac{\hbar^2}{2M_I}\nabla^2_{\mathbf{R}_I} + V(\mathbf{R}_I) \right] \Theta(\mathbf{R}_I) = E^{'}\Theta(\mathbf{R}_I). \tag{2.6}$$

Where $E^{'}$ are the eigenvalues of the nuclei Hamiltonian. The BO approximation also called the adiabatic approximation, implies that the electrons are moving

in a external potential formed by fixed nuclei. This is the origin of any DFT calculation. Bohn and Huang extended the BO approximation [113] considering non-adiabatic effects in the electronic Hamiltonian.

2.1.3 The electron density - A new variable

The electron density ($n(r)$) is a scalar quantity depending on three spatial variables and is the measure of the probability of occupying an infinitesimal element of space at any given point. The electron density for N electron is obtained from the normalized N-electron wavefunction. The wavefunctions are in itself a function of 3N spatial variables. Conversely, the density also decides the wavefunction (along with a phase factor) which provides the academic foundation of the density functional theory. Mathematically, the basic variable of density functional theory is the electron density and for N electrons can be expressed as [109],

$$n(\mathbf{r}) = N \int d\mathbf{r}_2 \cdots \int d\mathbf{r}_N |\Psi(\mathbf{r}, \mathbf{r}_2 \cdots \mathbf{r}_N)|^2 \tag{2.7}$$

The factor of N in Eq. 2.7 originates from the fact that electrons are indistinguishable. Therefore Eq. 2.7 is the probability that any of the N electrons can be found in the infinitesimal vicinity volume of space, $d\mathbf{r}$. The electron density is an experimentally observable quantity which can be measured using X-ray diffraction [114]. One must make sure that that the electron density contains all necessary information about the system before using the electron density as the new base variable. The electron density must contain information about the number of electrons N along with the information contained in the external potential charcterized by V. The total number of electron is given by the integration of the electron density over the spatial coordinates.

$$N = \int d\mathbf{r} n(\mathbf{r}) \tag{2.8}$$

What we now need to prove is that the electron density describes the external potential uniquely. The proof relies on two theorems called the Hohenber-Kohn theorems.

2.1.4 The Hohenberg-Kohn Theorems

Hohenberg and Kohn proved that DFT is an exact theory and a low computational cost method of solving the quantum mechanical many-body problem [115]. DFT is applicable not only to condensed matter systems but to any system of interacting particles in an external potential $V_{ext}(\mathbf{r})$. DFT is based on the two following theorems.

Hohenberg-Kohn theorem I

The ground state electron density $n(\boldsymbol{r})$ of a system of interacting particles in an external potential $V_{ext}(\boldsymbol{r})$ uniquely determines the external potential $V_{ext}(\boldsymbol{r})$, except for a constant.

Except for a constant shift in energy, the ground state electron density decides the full Hamiltonian. All the states, in principle, including ground and excited states of the many-body wavefunctions can be calculated, *i.e.*, **the ground state energy density determines uniquely all properties of the system completely.**

Proof of Hohenberg-Kohn theorem I:

Here we consider the ground state of the system to be non-degenerate. Let us assume that there are two different external potential V_{ext} and $V_{ext}^{'}$ that differ more by than a constant however leading to the same electron density n(**r**). We use the proof based on the minimum energy principle. The two external potential would imply two different Hamiltonians, $\hat{H}$ and $\hat{H}^{'}$ leading to two different ground state wavefunctions, Ψ and $\Psi^{'}$ but with the same electron density. The Schrödinger equation then becomes, $\hat{H}\Psi = E_0\Psi$ and $\hat{H}^{'}\Psi^{'} = E_0^{'}\Psi^{'}$. Since $\Psi^{'}$ is not the ground state of $\hat{H}$ and Ψ is not the ground state of $\hat{H}^{'}$, it follows from there that,

$$\begin{aligned} E_0 &< \left\langle \Psi^{'} \middle| \hat{H}^{'} \middle| \Psi^{'} \right\rangle \\ &< \left\langle \Psi^{'} \middle| \hat{H}^{'} \middle| \Psi^{'} \right\rangle + \left\langle \Psi^{'} \middle| \hat{H} - \hat{H}^{'} \middle| \Psi^{'} \right\rangle \\ &< E_0^{'} + \int n(\mathbf{r})[V_{ext} - V_{ext}^{'}]d\mathbf{r} \end{aligned} \tag{2.9}$$

and

$$\begin{aligned} E_0^{'} &< \langle\Psi|\,\hat{H}^{'}\,|\Psi\rangle \\ &< \langle\Psi|\,\hat{H}\,|\Psi\rangle + \langle\Psi|\,\hat{H}^{'} - \hat{H}\,|\Psi\rangle \\ &< E_0 + \int n(\mathbf{r})[V_{ext}^{'} - V_{ext}]d\mathbf{r} \end{aligned} \tag{2.10}$$

Adding Eq. 2.9 and Eq. 2.10 leads to the contradiction that,

$$E_0 + E_0^{'} < E_0 + E_0^{'}. \tag{2.11}$$

This implies that there cannot be two different external potentials $V_{ext}(\mathbf{r})$ which can give rise to the same electron density $n(\mathbf{r})$, *i.e.*, the ground state electron density determines the external potential $V_{ext}(\mathbf{r})$ barring a constant. Even though the exact form of the electron density is not know, there is a one-to-one corresponding between the electron density $n(\mathbf{r})$ and the external potential $V_{ext}(\mathbf{r})$.

Hohenberg-Kohn theorem II

There exists a universal functional F[n($\mathbf{r}$*)] of the density, independent of the external potential* V_{ext}*(*$\mathbf{r}$*), such that the global minimum value of the energy functional E[n(*$\mathbf{r}$*) =* $\int n(\mathbf{r})V_{ext}(\mathbf{r})d(\mathbf{r}) + F[n(\mathbf{r})]$*] is the exact ground state energy of the system and the exact ground state density n(*$\mathbf{r}$*) minimizes this functional. Thus the exact ground state energy and density are fully determined by the functional E(*$\mathbf{r}$*).*

Proof of Hohenberg-Kohn theorem II**:**

Let $T[n(\mathbf{r})]$ and $E_{int}[n(\mathbf{r})]$ be the kinetic and the interaction energy of the particle. The universal functional can now be described as,

$$F[n(\mathbf{r})] = T[n(\mathbf{r})] + E_{int}[n(\mathbf{r})] \tag{2.12}$$

For any given wavefunction, $\Psi^{'}$, the energy function $E[\Psi^{'}]$ is expressed as,

$$E[\Psi^{'}] = \left\langle \Psi^{'} \middle| \hat{T} + \hat{V}_{int} + \hat{V}_{ext} \middle| \Psi^{'} \right\rangle. \tag{2.13}$$

According to the variational principle, with the constraint that the total number of particles is conserved, $E[\Psi^{'}]$ has its global minimum value only when $\Psi^{'}$ is the ground state wavefunction Ψ_0. Using the HK theorem I, $\Psi^{'}$ has to correspond

to the electron density $n^{'}(\mathbf{r})$ and external potential $V_{ext}^{'}(\mathbf{r})$, then $E[\Psi^{'}]$ is as functional of $n^{'}(\mathbf{r})$. In accordance with variational principle

$$\begin{aligned} E[\Psi^{'}] &= \left\langle \Psi^{'} \middle| \hat{T} + \hat{V}_{int} + \hat{V}_{ext} \middle| \Psi^{'} \right\rangle \\ &= E[n^{'}(\mathbf{r})] \\ &= \int n^{'}(\mathbf{r}) V_{ext}^{'}(\mathbf{r}) d\mathbf{r} + F[n^{'}(\mathbf{r})] \\ &> E[\Psi_0] \\ &= \int n(\mathbf{r}) V_{ext}(\mathbf{r}) d\mathbf{r} + F[n(\mathbf{r})] \\ &= E[n_0(\mathbf{r})] \end{aligned} \tag{2.14}$$

Therefore the energy functional $E[n(\mathbf{r})] = \int n(\mathbf{r}) V_{ext}(\mathbf{r}) d\mathbf{r} + F[n(\mathbf{r})]$ calculated for the correct electron density $n(\mathbf{r})$ is certainly lower than the value of this functional for any other electron density $n(\mathbf{r})$. Minimizing the total energy functional of the system with respect to variations in the electronic density would definitely guarantee the exact ground state electronic density and energy.

The HK theorems can be generalized to spin density functional theory having spin degrees of freedom [116]. DFT can also be generalized to account for temperature [117] and time dependence known as the time-dependent density functional theory [118]. HK theorems inserts the electron density as the basic variable. However, since the universal functional is unknown , it is still impossible to calculate any property of a system. Kohn and Sham [111] overcame this difficulty in 1965 which is well known as the Kohn-Sham formalism.

2.1.5 The Kohn-Sham formalism

Making DFT calculations possible even with a single personal computer by putting the HK theorems into practice is credited to the Kohn-Sham formalism. Electronic structure calculation based on DFT are hence the most popular tool.

The KS formalism is to substitute the original many-body system by an auxiliary independent-particle system while assuming both the systems have exactly the same ground state electron density. It maps the original interacting system with the actual potential onto an imaginary non-interacting system in which the electron's dynamics are governed by an effective Kohn-Sham single

particle potential $V_{KS}(\mathbf{r})$. The Hamiltonian in atomic units ($\hbar = m_e = e = \frac{4\pi}{\epsilon_0} = 1$) of the auxiliary independent-particle system is expressed as,

$$\hat{H}_{KS} = -\frac{1}{2}\nabla^2 + V_{KS}(\mathbf{r}) \tag{2.15}$$

With N independent electrons the ground state energy of the system is calculated by solving the N one-electron Schrödinger equations,

$$\left[\frac{1}{2}\nabla^2 + V_{KS}(\mathbf{r})\right]\psi_i(\mathbf{r}) = \varepsilon_i\psi_i(\mathbf{r}) \tag{2.16}$$

Each of the N orbitals $\psi_i(\mathbf{r})$ have one electron with the lowest eigenvalues ε_i. The electron density of the auxiliary system is derived from,

$$n(\mathbf{r}) = \sum_{i=1}^{N} |\psi_i(\mathbf{r})|^2 \tag{2.17}$$

which is dealt with the conservation condition similar to that of Eq. 2.8. The auxiliary non-interacting independent-particle kinetic energy $T_s[n(\mathbf{r})]$ is expressed as,

$$T_s[n(\mathbf{r})] = -\frac{1}{2}\sum_{i=1}^{N}\int \psi_i^*(\mathbf{r})\nabla^2\psi(\mathbf{r})d\mathbf{r} \tag{2.18}$$

and the universal functional $F[n(\mathbf{r})]$ is rewritten as,

$$F[n(\mathbf{r})] = T_s[n(\mathbf{r})] + E_H[n(\mathbf{r})] + E_{XC}[n(\mathbf{r})] \tag{2.19}$$

Here, $E_H[n(\mathbf{r})]$ is the Hartree energy of the electrons and is expressed as,

$$E_H[n(\mathbf{r})] = \frac{1}{2}\int\int \frac{n(\mathbf{r})n(\mathbf{r}')}{|\mathbf{r}-\mathbf{r}'|}d\mathbf{r}d\mathbf{r}'. \tag{2.20}$$

$E_{XC}[n(\mathbf{r})]$ is the exchange-correlation energy which is defined as the difference between the total exact energy and the sum of the kinetic and exchange energies. The ground state energy of the many-body system is obtained by minimizing the energy functional,

$$E[n(\mathbf{r})] = F[n(\mathbf{r})] + \int n(\mathbf{r})V_{ext}(\mathbf{r})d\mathbf{r} \tag{2.21}$$

governed by the condition that number of electrons N is conserved,

$$\delta\Bigg\{F[n(\mathbf{r})] + \int n(\mathbf{r})V_{ext}d\mathbf{r} - \mu\Bigg(\int n(\mathbf{r})d\mathbf{r} - N\Bigg)\Bigg\} = 0. \tag{2.22}$$

where μ is the Lagrange multiplier associated with the requirement of constant particle number. The chemical potential, μ, which is essentially the Lagrange multiplier associated with the requirement of constant particle number is given by,

$$\begin{aligned} \mu &= \frac{\delta F[n(\mathbf{r})]}{\delta n(\mathbf{r})} + V_{ext}(\mathbf{r}) \\ &= \frac{\delta T_S[n(\mathbf{r})]}{\delta n(\mathbf{r})} + V_{KS}(\mathbf{r}) \end{aligned} \tag{2.23}$$

The KS one-particle potential is expressed as,

$$\begin{aligned} V_{KS}(\mathbf{r}) &= V_{ext}(\mathbf{r}) + V_H(\mathbf{r}) + V_{XC}(\mathbf{r}) \\ &= V_{ext}(\mathbf{r}) + \frac{\delta E_H[n(\mathbf{r})]}{\delta n(\mathbf{r})} + \frac{\delta E_{XC}[n(\mathbf{r})]}{\delta n(\mathbf{r})} \end{aligned} \tag{2.24}$$

Where the second and third term are the Hartree and XC potentials.

Equations 2.16, 2.17 and 2.24 together represent the KS equations. The KS equations must be solved self-consistently since $V_{KS}(\mathbf{r})$ depends on the electron density through the exchange-correlation potential. To calculate the electron density, N equations in Eq. 2.16 are to be solved in the KS theory. The advantage of the KS method is that while the size of a system increases, the problem in itself does not get more difficult only the number of single particle equations increase.

Though in principle the theory is exact, the unknown exchange correlation energy functionals make the KS theory approximate in practice. An accurate, mathematical definition of $E_{XC}[n(\mathbf{r})]$ is given by,

$$E_{XC}[n(\mathbf{r})] = T[n(\mathbf{r})] - T_S[n(\mathbf{r})] + E_{int}[n(\mathbf{r})] - E_H[n(\mathbf{r})] \tag{2.25}$$

Here, $T[n(\mathbf{r})]$ and $E_{int}[n(\mathbf{r})]$ are the exact kinetic and electron-electron interaction energies of the interacting system, respectively. To have a decent description of a practical condensed matter system, an accurate energy functional, $E_{XC}[n(\mathbf{r})]$, or potential, $V_{XC}(\mathbf{r})$, are essential. In this thesis, the two most

extensively used approximation for the XC potential are the local density approximation and the generalized-gradient approximation.

It must be noted that the KS energy eigenvalues in Eq. 2.16 are not for the initial interacting many-body system and therefore have no physical meaning. The KS energy eigenvalues cannot be understood as the one-electron excitation energies of the many-body interacting system since the sum of the eigenvalues of the occupied states in Eq. 2.16 are not equal to the energies which are added or removed from the interacting many-body system, *i.e.*, $E_{tot} \neq \sum_i^{occ.} \varepsilon_i$. The eigenvalues in the Hartree-Fock theory represents the energy necessary to add or remove an electron from a given orbital, also known as Koopmans' theorem [119]. The eigenvalues of the KS equations have been shown empirically to give reasonable descriptions of the bandstructure. They have a physical (or at least a mathematical) interpretation, often termed as the Janak theorem [120]. The eigenvalue of the initial many-body system is the derivate of the total energy with respect to the occupation of a state, *i.e.*,

$$\begin{aligned} \varepsilon_i &= \frac{dE_{tot}}{dn_i} \\ &= \int \frac{dE_{tot}}{dn(\mathbf{r})} \frac{dn(\mathbf{r})}{dn_i} d\mathbf{r} \end{aligned} \tag{2.26}$$

Janak's theorem can only be applied to the addition or removal of an electron from the highest occupied orbital. This is in sharp contrast to Koopmans' theorem for the Hartree-Fock approach in which electron can be extracted from or added to any of the orbitals of the system.

2.1.6 Exchange-Correlation functionals

2.1.6.1 LDA: Local Density Approximation

The KS formalism maps successfully the initial interacting many-body system onto a set of independent single-particle equations making the problem much easier. Without the exact form of XC energy functional $E_{XC}[n(\mathbf{r})]$, the KS equations cannot be solved. One would assume that the exact correlation energy functional $E_{XC}[n(\mathbf{r})]$ would be very complicated. However, there have been simple but extremely successful approximations made which not only save computational

time but also predict various properties of many systems reasonably well. This has led to a wide use of DFT calculations for electronic structure calculations. The local density approximation is one of these approximations and is one of the most extensively used exchange correlation function. In LDA, the XC energy per electron is treated as that for a homogeneous electron gas (HEG) having the same electron density at some point $\mathbf{r}$. The total energy exchange-correlation functional $E_{XC}[n(\mathbf{r})]$ can be expressed as,

$$\begin{aligned} E_{XC}^{LDA}[n(\mathbf{r})] &= \int n(\mathbf{r})\epsilon_{XC}^{hom}[n(\mathbf{r})]d\mathbf{r} \\ &= \int n(\mathbf{r})\left[\epsilon_{X}^{hom}[n(\mathbf{r})] + \epsilon_{C}^{hom}[n(\mathbf{r})]\right]d\mathbf{r} \\ &= E_{X}^{LDA}[n(\mathbf{r})] + E_{C}^{LDA}[n(\mathbf{r})] \end{aligned} \tag{2.27}$$

Here the homogeneous exchange correlation electron density $\epsilon_{XC}^{hom}[n(\mathbf{r})]$ is a just a function of the density. It is decomposed into the exchange energy electron density $\epsilon_{X}^{hom}[n(\mathbf{r})]$ and the correlation energy electron density $\epsilon_{C}^{hom}[n(\mathbf{r})]$. Therefore the XC energy functional now gets decomposed into the exchange energy functional $E_{X}^{LDA}[n(\mathbf{r})]$ and the correlation energy functional $E_{C}^{LDA}[n(\mathbf{r})]$ linearly. The exchange energy functional $E_{X}^{LDA}[n(\mathbf{r})]$ uses the expression for a HEG since the analytical form is well known [121]. Thus $E_{X}^{LDA}[n(\mathbf{r})]$ is expressed as,

$$\begin{aligned} E_{X}^{LDA}[n(\mathbf{r})] &= \int n(\mathbf{r})\epsilon_{X}^{hom}[n(\mathbf{r})]d\mathbf{r} \\ &= -\frac{3}{4}\left(\frac{3}{\pi}\right)^{\frac{1}{3}} n(\mathbf{r})^{\frac{1}{3}} \end{aligned} \tag{2.28}$$

where, $\epsilon_{X}^{hom}(n) = -\frac{3}{4}\left(\frac{3}{\pi}\right)^{\frac{1}{3}} n(\mathbf{r})^{\frac{1}{3}}$, is the exchange energy electron density of the HEG first introduced by Dirac [121]. It is only in the low and high electron density limits that the analytic expressions for the correlation energy of the HEG are known. For the low electron energy density limit, the expression is given in the form,

$$\epsilon_C = \frac{1}{2}\left(\frac{g_0}{r_s} + \frac{g_1}{r_s^{\frac{3}{2}}} + \cdots\right) \tag{2.29}$$

Here the r_s is the Wigner-Seitz radius and is related to electron density in form expressed as,

$$\frac{4}{3}\pi r_s^3 = \frac{1}{n} \tag{2.30}$$

For example, Wigner solved the problem exactly in the row limit regime, the Wigner crystal, assuming the correlation energy would go to a constant in the high r_s limit and suggested a smooth interpolation inbetween the two extreme limits to have the form,

$$\epsilon_C = -\frac{0.44}{r_s + 7.8} \tag{2.31}$$

At the high density limit, the form of the correlation energy electron density of the HEG in expressed as,

$$\epsilon_C = A\ln(r_s) + B + rs(C\ln(r_s) + D) + \cdots \tag{2.32}$$

For example, Gellman and Breuckner following a diagrammatic method, summing an infinite series of Feynman diagrams, calculated the high r_s limit exactly shown to be,

$$\epsilon_C = 0.311\ln(r_s) - 0.048 + r_s(A\ln(r_s) + C) + \cdots \tag{2.33}$$

In this approach, the low r_s is retained and an interpolation is made between the two limits similar to Wigner's treatment. To accurately obtain intermediate electron density values, one would require quantum Monte Carlo (QMC) simulations for the energy of the HEG. These have been calculated for many intermediate electron density values [122]. While reproducing the exactly known limiting behavior, most local density approximations to the correlation energy density interpolate these QMC simulations. Built on these analytic forms for ϵ_C, various local density approximations were proposed by Vosko-Wilk-Nusair [123], Perdew-Zunger [124], Cole-Perdew [125], Perdew-Wang [126]. In LDA, the exchange correlation potential, $V_{XC}(\mathbf{r})$, is expressed as,

$$\begin{aligned} V_{XC}^{LDA} &= \frac{\delta E_{XC}^{LDA}}{\delta n(\mathbf{r})} \\ &= \epsilon(n(\mathbf{r})) + n(\mathbf{r})\frac{\delta \epsilon_{XC}(n(\mathbf{r}))}{\delta n(\mathbf{r})} \end{aligned} \tag{2.34}$$

The total energy of the system withing the LDA is expressed as,

$$\begin{aligned}
E_{tot}[n(\mathbf{r})] &= T_s[n(\mathbf{r})] + E_H[n(\mathbf{r})] + E_{XC}[n(\mathbf{r})] + \int n(\mathbf{r}) V_{ext}(\mathbf{r}) d\mathbf{r} \\
&= \sum_i^{occ} \langle \psi_i(\mathbf{r}) | -\frac{1}{2}\nabla^2 | \psi_i(\mathbf{r}) \rangle + E_H[n(\mathbf{r})] + E_{XC}[n(\mathbf{r})] + \int n(\mathbf{r}) V_{ext}(\mathbf{r}) d\mathbf{r} \\
&= \sum_i^{occ} \langle \psi_i(\mathbf{r}) | -\frac{1}{2}\nabla^2 + V_H + V_{XC} + V_{ext} | \psi_i(\mathbf{r}) \rangle \\
&- \sum_i^{occ} \langle \psi_i(\mathbf{r}) | V_H(\mathbf{r}) | \psi_i(\mathbf{r}) \rangle - \sum_i^{occ} \langle \psi_i(\mathbf{r}) | V_{XC}(\mathbf{r}) | \psi_i(\mathbf{r}) \rangle \\
&- \sum_i^{occ} \langle \psi_i(\mathbf{r}) | V_{ext}(\mathbf{r}) | \psi_i(\mathbf{r}) \rangle + E_H[n(\mathbf{r})] + E_{XC}[n(\mathbf{r})] + \int n(\mathbf{r}) V_{ext}(\mathbf{r}) d\mathbf{r} \\
&= \sum_i^{occ} \varepsilon_i - \frac{1}{2}\int \frac{n(\mathbf{r}) n(\mathbf{r'})}{|\mathbf{r} - \mathbf{r}'|} d\mathbf{r} d\mathbf{r}' + \int n(\mathbf{r})(\epsilon_{XC}(\mathbf{r}) - V_{XC}(\mathbf{r})) d\mathbf{r} \\
&= \sum_i^{occ} \varepsilon_i - \frac{1}{2}\int \frac{n(\mathbf{r}) n(\mathbf{r'})}{|\mathbf{r} - \mathbf{r}'|} d\mathbf{r} d\mathbf{r}' + \int n(\mathbf{r})^2 \frac{\delta \epsilon_{XC}(n(\mathbf{r}))}{\delta n(\mathbf{r})} d\mathbf{r} \qquad (2.35)
\end{aligned}$$

In the LDA, the modifications to the exchange-correlation energy as a result of the inhomogeneities in the electronic density are avoided. The LDA addresses the sum rule to the exchange-correlation hole correctly, *i.e.*, there is a total electronic charge of one electron eliminated from the surrounding of the electron at $\mathbf{r}$. It is therefore still remarkably successful and rewarding since it works well even with systems where the electron density vary promptly. However, it underestimates the atomic ground state energy as well as ionization energies while overestimating binding energies. The energy band gaps of few semiconductors are not represented correctly. The disadvantages have led to approximation of the XC energy functionals beyond the LDA through the addition of gradient corrections to integrate longer range gradient effects, known as the GGA.

2.1.6.2 GGA: Generalized Gradient Approximation

The exchange-correlation energy of inhomogeneous charge density can be greatly dissimilar from the HEG result. LDA disregards the inhomogeneities of the actual charge electron density. An initial attempt was the gradient-expansion approximation in which one tries to methodically calculate gradient corrections

having the form $|\nabla n(\mathbf{r})|$, $|\nabla n(\mathbf{r})|^2$, $|\nabla^2 n(\mathbf{r})|$, $\cdot$, *etc.*, to the LDA. The incorporation of lower-order gradient corrections never improve the LDA and sometimes even worsen it [127] while higher-order corrections are exceedingly difficult to calculate. Instead of using power-series-like gradient expansions, it was observed that one could apply general functions of $n(\mathbf{r})$ and $\nabla n(\mathbf{r})$. This gives rise to different generalized-gradient approximations (GGA) which incorporate density gradient corrections of the electron density which should result in better results as that compared to GGA in cases where the inhomogeneous electron charge density are distinct from the HEG. These functionals have the general form,

$$E_{XC}^{GGA}[n(\mathbf{r})] = \int f^{GGA}(n(\mathbf{r}), \nabla n(\mathbf{r}))d\mathbf{r}, \tag{2.36}$$

As a result of their dependence on ∇n(**r**), GGAs are often called "semi-local" functionals. Notably for covalent bonds and weakly bonded systems, GGAs are preferable over the LDA for calculations of physical properties such as geometries, ground state energies of solids and molecules. Due to the amount of various choices of f^{GGA}, plenty of GGA functionals have been developed. Depending on the system at hand a broad variety of results can be collected. Assuring the the compatibility with the known sum rules, the functional expression of f^{GGA} is derived as a correction to the LDA exchange and correlation energies. The GGA exchange energy is expressed as,

$$E_X^{GGA}[n(\mathbf{r})] = \int n(\mathbf{r})\epsilon_X^{hom} n(\mathbf{r}) F_X^{GGA}(s)d\mathbf{r}. \tag{2.37}$$

The exchange enhancement factor, $F_X^{GGA}(s)$, informs how much exchange energy is enhanced over its LDA value for a given electron density. Where s is the dimensionless reduced gradient and is expressed as,

$$s = \frac{|n(\mathbf{r})|}{2(3\pi^2)^{\frac{1}{3}} n(\mathbf{r})^{\frac{4}{3}}}. \tag{2.38}$$

This choice of $F_X^{GGA}(s)$ makes one GGA different from another. Two broadly used GGA exchange functionals are the Perdew-Burke-Ernzehof (PBE)[128] and Becke88 [129] functionals. To demonstrate what $F_X^{GGA}(s)$ is, we express

the forms of the enhancement factor for two popular GGA exchange functionals,

$$\begin{aligned} F_X^{PBE}(s) &= 1 + \kappa - \frac{\kappa}{1 + \frac{\mu s^2}{\kappa}} \\ F_X^{B88}(s) &= 1 + \frac{\beta x(s)^2}{C[1 + 6\beta x(s)\sinh^{-1}(x(s))]} \\ x(s) &= 2(6\pi^2)^{\frac{1}{3}} s \end{aligned} \tag{2.39}$$

The non-empirical parameters, κ and μ are obtained from physical constraints in the case of PBE. However, for the parameters in the B88 case, C and β are obtained from empirical fitting. It can be easily seen that when the energy density gradient is zero, we return to the LDA exchange since $F_X^{GGA}(s) = 1$. It is easy to see that for small s, *i.e.*, slowly varying densities, the LDA and GGA would yield similar results while for densities which vary rapidly, *i.e.*, the functionals differ. The other popular gradient correlation functionals for GGA are PW91 [130], Lee-Yang-Parr (LYP)[131] and Perdew86 (P86)[132]

2.1.7 Solving the Kohn Sham equations

The Kohn-Sham equations cater to obtaining the exact electronic density and energy of the grounds state of a many-body condensed matter system by using the independent particle method. Since the effective KS potential, V_{KS}, and the electron density, $n(\mathbf{r})$, are closely related, the KS equations ought to be solved consistently. As seen in Fig. 2.1, the process is numerically done through some self-consistent iterations. The approach starts with an initial electron density (usually a superposition of atomic electron density), then the effective KS potential, V_{KS}, is calculated and the KS equation is solved with single-particle eigenvalues and wavefunctions. From the wavefunctions, a new electron density is obtained. The self-consistent conditions are checked either by the change in ground state energy or the electron density

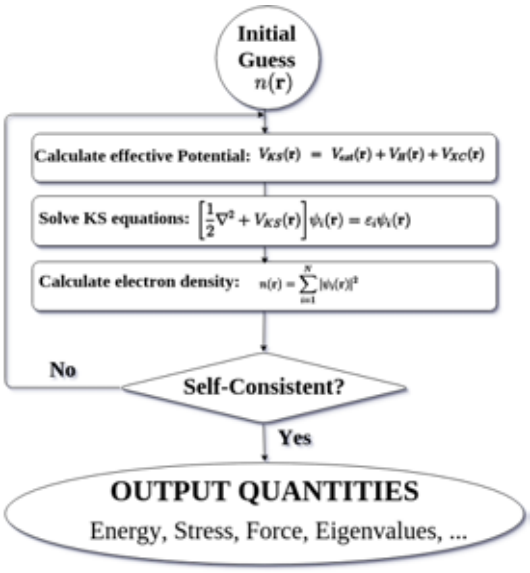

Figure 2.1: Flowchart of the self-consistent iterative method for solving the KS equations.

or if the force on each atoms has a value smaller than a given criteria. Once self-consistency is attained, physical quantities, *viz*, total energy, forces, stress, eigenvalues, electron density of states, bandstructure, *etc.* can be determined.

2.1.7.1 Basis Sets

Basis sets are essential to solve the electronic Schrödinger equation. All electronic structure codes and methods depend on the expansion of the unknown wavefunction in terms of a set of basis function. In principle, any type of basis function can be implemented. The most common basis sets are for example are plane-wave, Gaussian, polynomial, spline, Slater type orbitals, numeric atomic orbitals, *etc*. One should take care while selecting the basis functions. The following are two issues which should be taken into consideration - (i) The wavefunction and the electronic density should be accurately described by the basis function with as low a computational time as possible. (ii) The characteristics of the basis functions should represent the physics of the problem. For example, in molecular or atomic systems, the basis functions must vanish as the distance between the nucleus and the electron becomes large. For a crystal or solid or any condensed matter system, basis functions should have the periodicity of the crystal lattice. Therefore atom centered orbitals like Gaussian basis functions are popular for atomic and molecular systems while the plane wave basis functions are favored for electronic structure calculations of condensed matter systems.

2.1.7.2 Plane waves method

In this thesis, all our calculations were performed on solids and hence we discuss the approach based only on the plane wave basis functions with pseudopotentials. In present day DFT calculations the combination of plane wave basis sets and pseudopotentials are the main methods implemented for periodic systems. It is because of Bloch's theorem that plane wave basis sets have become the obvious choice for the treatment of periodic systems. Assume a periodic potential $U(\mathbf{r})$, such that $U(\mathbf{r}+\mathbf{R}) = U(\mathbf{r})$ where $\mathbf{R}$ is the Bravais lattice vector. Bloch's theorem states that the eigenfunctions of the one-electron Hamiltonian $H = -\frac{1}{2}\nabla^2 + U(\mathbf{r})$ can be expressed as a product of a plane wave, $(e^{i\mathbf{k}\cdot\mathbf{r}})$, and a

function, $\phi_{n,k}(\mathbf{r})$, having the same periodicity as that of the potential U($\mathbf{r}$),

$$\psi_{n,k}(\mathbf{r}) = e^{i\mathbf{k}\cdot\mathbf{r}}\phi_{n,k}(\mathbf{r}) \tag{2.40}$$

with the condition that $\phi_{n,k}(\mathbf{r}+\mathbf{R}) = \phi_{n,k}(\mathbf{r})$. The index n is a quantum number termed as the 'band index' and k represents a series of plane-waves inside the primitive unit cell. Bloch theorem permits the expansion of the electronic wave function in terms of discrete set of plane waves. Due to the periodicity, the solid will have an infinite number of electrons and therefore the spacing of the $\mathbf{k}$ points will vanish and the wave vector can be treated as a continuous variable. While only a finite number of electronic states are occupied for each $\mathbf{k}$ point, the infinite number of electrons in the solid are dealt with by an infinite number of $\mathbf{k}$ points. Physical properties such as the electronic potential, electronic density and ground state energy are attributed to the occupied states at each $\mathbf{k}$ point. Effective methods have been constructed to select finite sets of $\mathbf{k}$ points to obtain the mentioned physical properties. The most popular approach and the one used in this thesis is the method proposed by Monkhorst and Pack [133]. The Monkhorst and Pack method generates a uniform $\mathbf{k}$-point mesh along the three lattice vectors in reciprocal space. It is important to test the convergence of the results by the size of the $\mathbf{k}$ mesh used in calculations since the measure of error in the total energy or difference in the energy because of the inadequate number of $\mathbf{k}-$points sampling can be reduced by increasing the $\mathbf{k}$ point mesh. Expanding the periodic function $\phi_{n,k}(\mathbf{r})$ with plane waves having wave vectors that are the reciprocal lattice vectors ($\mathbf{G}$) of the periodic crystal,

$$\phi_{n,k} = \sum_{\mathbf{G}} C_{n,\mathbf{G}} e^{i\mathbf{G}\cdot\mathbf{r}} \tag{2.41}$$

Resulting in the electronic wave function to be expressed as,

$$\psi_{n,k} = \sum_{\mathbf{G}} C_{n,\mathbf{k}+\mathbf{G}} e^{i(\mathbf{k}+\mathbf{G})\cdot\mathbf{r}} \tag{2.42}$$

Solving the one electron Schödinger-like Kohn-Sham equation having an effective periodic potential, the KS wave function can be expanded using a plane wave basis set as shown in Eq. 2.42. The resultant KS equation can then be revised as,

$$\sum_{\mathbf{G}'} \left[\frac{1}{2}|\mathbf{k}+\mathbf{G}'|^2\delta_{\mathbf{G},\mathbf{G}'} + V_{eff}(\mathbf{G}-\mathbf{G}')\right] C_{n,\mathbf{k}+\mathbf{G}'} = \epsilon_n C_{n,\mathbf{k}+\mathbf{G}} \tag{2.43}$$

The Kronecker δ indicates that the kinetic energy is diagonal. Here ϵ_n represent the electronic energies. Eq. 2.43 is basically the Schödinger-like equations of a periodic crystal having a plane wave basis set. Since the sum is over $\mathbf{G}^{'}$, it would require an infinite number of plane waves to solve Eq. 2.43. The criteria to truncate the basis set to include only plane waves having kinetic energies lowere than a particular cutoff, E_{cut} is given by,

$$\frac{1}{2}|\mathbf{k}+\mathbf{G}|^2 \leq E_{cut}. \tag{2.44}$$

Implementing a finite basis causes an additional inaccuracy which can be minimized by increasing the number of plane waves, *i.e.*, increasing the numerical value of E_{cut} Therefore, one would have to run a convergence test to find a numerical value for E_{cut} to compute accurately the properties of interests.

2.1.7.3 Pseudopotentials

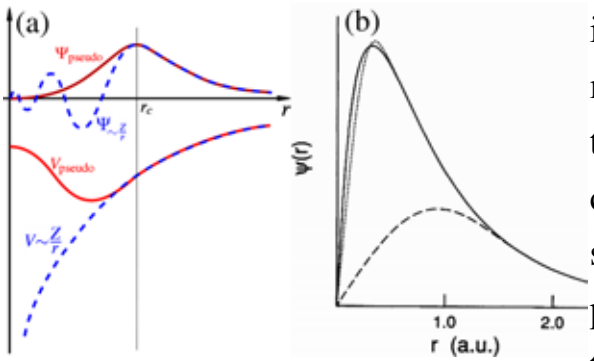

Figure 2.2: (a)Graphic interpretation of the all-electron ionic potential and wave function, shown in dashed line along with their pseudopotial and wave function shown in solid lines. (b) The radial wave function, shown in solid line for the Oxygen $2p$ orbital along with the pseudo wave function using norm conserving rule [16] and the ultrasoft Vanderbilt pseudo wave function [17]. Figure adapted from Ref. [17].

It is well accepted that most all physically interesting properties of solids are determined by the valence electrons rather than the core electrons. At the same time the core electrons need a large amount of basis function for their description within the plan-wave basis set. The core electrons take up most of the computational time. To resolve this dilemma, one uses the pseudopotential approximation, *i.e.*, the strong ionic potential is substituted with a pseudopotential. The pseudopotentials are based on the following two formalisms. (i) The pseudopotential has to be weaker than the strong ionic potential so as to get rid of the plane waves required to characterize the core electrons. (ii)To eliminate the swift oscillations of the valence electron wave functions near the core region. The two mentioned formalisms are illustrated in Fig. 2.2. It can be observed that pseudopotential is weaker than the all-electron potential. It can also be seen that the pseudo wave function has

no radial node within the core region. The most crucial requirement with the scheme is that outside the core region, the pseudopotential and pseudo wave functions become analogous with what corresponds to the all-electron ones. The most commonly used form of a pseudopotential is expressed as,

$$V_{ps} = \sum_{lm} |Y_{lm}\rangle \, V_l(r) \, \langle Y_{lm}| \tag{2.45}$$

An important class of pseudopotentials are the norm-conserving pseudopotentials. It necessitates that the all-electron and pseudo-wave function agree beyond some chosen radius (r_c). The name is derived from the fact the integrated density with r_c for the all-electron wave function and pseudo wavefunction are equivalent, hence 'norm conservation'. Troullier and Martins [134], Kerker [135], Hamann,Schlüter and Chiang [16], Vanderbilt [136], Goedecker-Teter-Hutter [137] have introduced some of the most popular norm-conserving pseudopotentials.

It sometimes happen that the pseudopotential wave functions generated are not smoother than the all-electron one due to the "norm-conserving" criteria. For example, as depicted in the Fig 2.2(b) for Oxygen, there is hardly any achievement for the norm-conserving pseudopotential as compared with its all-electron counterpart. To overcome this difficulty, Vanderbilt [17], made the rather unconventional modification to disobey the norm conservation rule, *i.e.*, to relax the criteria that the pseudo-wave function inside the core region should have the same charge or integrated density as the all-electron wave function. This shortfall of the charge is compensated by additional localized atom-centered charges. These additional charges are characterized by the charge difference between the all-electron and pseudo potential wave function. In this way, r_c can be chosen to be larger and the pseudo wave function can be made much softer as compared to the all-electron wave function, as depicted in Fig. 2.2(b). Therefore this type of pseudopotential derives it name, ultrasoft pseudopotential. They enable much lower plane wave cut-offs used in practical calculations. The merging of DFT, plane-wave basis set and pseudopotential is an effective technique in electronic structure calculations of condensed matter many body systems and is what we have used in all of our DFT calculations.

2.2 Density Functional Perturbation Theory.[2]

2.2.1 Introduction

DFT has provided a satisfactory technique to obtain the ground state properties of electronic systems for the many body system, whether in solids, nanostructures, or molecules. Many physical properties such as polarisabilities, phonons, Raman intensities and infra-red absorption cross-sections depend upon a system response to some form of perturbation. Density functional perturbation theory (DFPT) is a powerful theoretical technique that allows calculation of such properties within the DFT framework, thereby facilitating an understanding of the microscopic quantum mechanical mechanisms behind such processes, as well as providing a rigorous testing ground for theoretical developments. System responses to external perturbations may be calculated using DFT with the addition of some perturbing potential. The DFPT method was formulated at the end of 1980s and has been successful in predicting and confirming experimentally observable quantities. Initial advancement of DFPT was developed by Baroni, Giannozzi and Testa in Trieste [138]. The most significant numerical codes which implement DFPT are QUANTUM ESPRESSO [139], ABINIT [140], VASP [141], OCTOPUS [142] and CASTEP [143].

2.2.2 Response Function

The second, third or higher order derivatives of the total energy with respect to perturbations are termed as the responses functions. Many appealing response functions are the result of the application of an extrinsic perturbation to the system under consideration. Usual perturbations are atomic displacements, homogeneous external or magnetic fields, strain, *etc.*. The physical characteristics associated to the total, *i.e.*, contribution from electronic as well as ionic, energy can be classified as, 1^{st}-, 2^{nd}- and 3^{rd} order. Examples of physical properties pertaining to the 1^{st} order are forces, stress, dipole moment, *etc.*, pertaining to the 2^{nd} order are phonon dynamical matrix, elastic constants, dielectric susceptibility, Born effective charges, piezoelectricity, internal strain, *etc.*, and pertaining to

[2]This theory has been implemented in Chapter 3 and 4

the 3^{rd} order are non-linear dielectric susceptibility, phonon-phonon interaction, Grüneisen parameters, anharmonic elastic constants, *etc.* Thermal expansion and entropy are additional physical characteristics that are attained by integrating the total energy over phonon degrees of freedom. Using direct approaches such as finite differences, molecular dynamics spectral investigation or perturbative techniques, the total energy derivatives can be calculated. The direct approach involves shortcomings, arising from size effects, ergodicity restriction, complication in decoupling the responses to perturbation of different wavelengths. However, the pertubative technique used in DFT recognises not only periodic perturbations but also perturbations corresponding to non-zero, commensurate or incommensurate wavevectors [144]. The perturbative technique can be combined with the usual DFT framework since the calculations involving the 1^{st} order corrections to wavefunction incorporated in the perturbation theory can be accomplished *via* the variational method. These algorithms are analogous to those used in the unperturbed computations, *i.e.*, the ground state DFT calculations.

2.2.3 Mathematical groundwork

By minimizing the functional of the electronic density, the ground-state DFT energy can be calculated,

$$E_{el}[n(\lambda)] = \sum_{i=1}^{N_e} \langle \psi_i(\lambda)| \, T + V_{ext}(\lambda) \, |\psi_i(\lambda)\rangle + E_{H_{xc}}[n(\lambda)] \tag{2.46}$$

with the orthonormal constraint for the Kohn-Sham orbitals,

$$\langle \psi_i(\lambda) | \psi_j(\lambda) \rangle = \delta_{ij} \tag{2.47}$$

Where T is the kinetic energy operator, V_{ext} is the external potential including the nuclear potential, $E_{H_{xc}}$ is the combined Hartree and exchange-correlation energy functional and λ is the Lagrange multiplier. The summation in Eq. 2.46 runs over all occupied states. The electronic density can now be minimized utilizing the Lagrange multiplier approach,

$$n(\mathbf{r}, \lambda) = \sum_{i=1}^{N_e} \psi_i^*(\mathbf{r}, \lambda)\psi_i(\mathbf{r}, \lambda) = n^0(\mathbf{r}) + \lambda n^1(\mathbf{r}) + \lambda^2 n^2(\mathbf{r}) + \cdots \tag{2.48}$$

where λ is the Lagrange multiplier. The Euler-Langrange equations can be shaped in the form of a Schrödinger equation, with the Hamiltonian expressed as,

$$H = T + V_{ext}(\lambda) + V_{H_{XC}}(\lambda) \tag{2.49}$$

Here,

$$V_{H_{XC}}(\mathbf{r}, \lambda) = \frac{\delta E_{H_{XC}}[n(\lambda)]}{\delta n(\mathbf{r})} \tag{2.50}$$

As in standard perturbation theory, it is assumed that the unperturbed system ($\lambda = 0$) is exactly solvable and the information of the perturbing potential is certain at higher orders. The intention of density functional theory is to calculate the derivatives relative to the different perturbations of the DFT electronic energy. Detail derivation of the DFPT equations can be found in Reference [138]. The remaining electrostatic repulsion between nuclei has to be added to the electronic contribution to represent the Born-Oppenheimer energy. Generally, the nuclei-nuclei interaction energy is obtained by considering the nuclei as classical point charges. This does not demonstrate computational problems and we therefore concentrate only the contributions from electrons. Using perturbation theory, the first order correction to the electronic energy is calculated from the 0^{th} order wavefunctions and the perturbing potential at the 1^{st} order,

$$\begin{aligned} E_{el}^{(1)} &= \sum_{i=1}^{N_e} \left\langle \psi_i^{(0)} \right| H^{(1)} \left| \psi_i^{(0)} \right\rangle \\ &= \sum_{i=1}^{N_e} \left\langle \psi_i^{(0)} \right| T + V_{ext}^{(1)} \left| \psi_i^{(0)} \right\rangle + \frac{dE_{H_{XC}}[n^{(0)}]}{d\lambda}|_{\lambda=0}. \end{aligned} \tag{2.51}$$

The above equation (Eq. 2.51) is the Hellmann-Feynman theorem for DFT. At first order the constraint is given by,

$$\left\langle \psi_i^{(0)} \middle| \psi_i^{(1)} \right\rangle + \left\langle \psi_i^{(1)} \middle| \psi_i^{(0)} \right\rangle = 0 \tag{2.52}$$

By solving the Sternheimer equation [145, 146], the first order evolved wave-functions are calculated either by iterative techniques or by a self-consistent approach similar to that of the self-consistent solution of the unperturbed system in which the Kohn-Sham equation is replaced by,

$$(H^{(0)} - \epsilon_i^{(0)}) \left|\psi_i(1)\right\rangle = -(H^{(1)} - \epsilon_i^{(1)}) \left|\psi_i(0)\right\rangle . \tag{2.53}$$

Here, $\epsilon^{(0)}$ and $\epsilon^{(1)}$ are the 0^{th} and $1^{(st)}$ order eigenvalues. Sternheimer yields a system of N_e linearly coupled equations which is relatively easier than standard DFT, where the $E_{XC}[n]$ has a non linear dependence. Solution of $\psi_i^{(1)}$ of Eq. 2.53 is calculated implementing the *sum over states* expression,

$$\left|\psi_i^{(1)}\right\rangle = \sum_j \left|\psi_j^{(0)}\right\rangle \frac{\left\langle\psi_j^{(0)}\right| H^{(1)} \left|\psi_i^{(0)}\right\rangle}{\epsilon_i^{(0)} - \epsilon_j^{(0)}} \tag{2.54}$$

Other than the particular eigenstate under consideration, the sum runs over the entire states, both occupied as well as unoccupied states, of the system. The above evolved wavefunction deals on with the information of eigenvalues and eigenvectors of the unperturbed Hamiltonian and the perturbing potential at the 1^{st} order. The extent to which DFPT is valid is governed by the condition that the external perturbation is small, *i.e.*, $\lambda \left|\psi_i^{(1)}\right\rangle \ll \left|\psi_j^{(0)}\right\rangle$. Eq. 2.54 then implies that $\left|\lambda \left\langle\psi_j^{(0)}\right| H^{(1)} \left|\psi_i^{(0)}\right\rangle\right| \ll |\epsilon_i^{(0)} - \epsilon_j^{(0)}|$, meaning that the external perturbation must be small relative to the electronic excitations. The first order modified density can be calculated from the 1^{st} order change in wavefunction $\psi_i^{(1)}$ expressed as,

$$n^{(1)}(\mathbf{r}) = \sum_{i=1}^{N_e} \left[\psi_i^{*(1)}(\mathbf{r})\psi_I^{(0)(\mathbf{r})} + \psi_i^{*(0)}(\mathbf{r})\psi_I^{(1)(\mathbf{r})}\right] \tag{2.55}$$

and the calculation of the first-order change in the Hamiltonian is then expressed as,

$$\begin{aligned} H^{(1)} &= T^{(1)} + V_{ext}^{(1)} + V_{H_{XC}}^{(1)} \\ &= T^{(1)} + V_{ext}^{(1)} + \int \left.\frac{\delta^2 E_{H_{XC}}}{\delta n(\mathbf{r})\delta n(\mathbf{r}')}\right|_{n^{(0)}} n^{(1)}(\mathbf{r}')d\mathbf{r}' \end{aligned} \tag{2.56}$$

From a non-variational expression derived from perturbation theory, the 2^{nd} order derivative of the electronic energy is then expressed as,

$$E_{el}^{(2)} = \sum_{i=1}^{N_e} \left\langle\psi_i^{(0)}\right| H^{(2)} \left|\psi_i^{(0)}\right\rangle + \left\langle\psi_i^{(0)}\right| H^{(1)} \left|\psi_i^{(1)}\right\rangle \tag{2.57}$$

With the constraints $\left\langle \psi_i^{(0)} \middle| \psi_i^{(0)} \right\rangle = 0$ for all of the occupied states i, j, a more precise variational expression can be calculated by minimizing,

$$\begin{aligned} E_{el}^{(2)}(\psi_i^{(0)}), (\psi_i^{(1)})] = \sum_{i=1}^{N_e} \Bigg[& \left\langle \psi_i^{(0)} \right| (T + V_{ext})^{(2)} \left| \psi_i^{(0)} \right\rangle \\ + & \left\langle \psi_i^{(1)} \right| (H - \epsilon_i)^{(0)} \left| \psi_i^{(1)} \right\rangle + \left\langle \psi_i^{(0)} \right| (T + V_{ext})^{(1)} \left| \psi_i^{(1)} \right\rangle \\ + & \left\langle \psi_i^{(1)} \right| (T + V_{ext})^{(1)} \left| \psi_i^{(0)} \right\rangle + \frac{1}{2} \int \int \frac{\delta^2 E_{H_{XC}}[n^{(0)}]}{\delta n(\mathbf{r}) \delta n(\mathbf{r}')} n^{(1)}(\mathbf{r}) n^{(1)}(\mathbf{r}') d\mathbf{r} d\mathbf{r}' \\ + & \int \frac{d}{d\lambda} \frac{\delta^2 E_{H_{XC}}[n^{(0)}]}{\delta n(\mathbf{r})} \Bigg|_{\lambda=0} n^{(1)}(\mathbf{r}) d\mathbf{r} + \frac{1}{2} \frac{d^2 E_{H_{XC}}[n^{(0)}]}{d\lambda^2} \Bigg|_{\lambda=0} \Bigg], \end{aligned} \tag{2.58}$$

relative to $(\psi_i^{(1)})$. The 2^{nd} order derivatives of the total energy are entirely driven by the 1^{st} order derivatives of the wavefunctions which is evident from Eq. 2.57 and 2.58. In both methods, the standard perturbation theory and DFPT, it can be demonstrated that the 3^{rd} order correction to the energies are acquired by having the knowledge of the modification of the wavefunctions up to the 1^{st} order. These results are an aftermath of a more formally known theorem known as "$2n + 1$" theorem of quantum mechanics. The "$2n + 1$" theorem, which follows from variational principle and implemented in DFT [147], states that the information of the derivatives of the wavefunctions at order n allows the computations of the derivatives of the energy up to order "$2n + 1$". The practical significance of the "$2n + 1$" theorem is that it permits one to approach the 3^{rd} order derivatives, which deals with Grüneisen parameters, Raman scattering cross sections, phonon line widths, *etc.*, of the total energy having the same computational cost as that of harmonic properties. Another important property of the theorem is that once particular first-order wavefunctions are established, the non variational expressions extracted from Eq.2.57 can be used to acquire various other mixed perturbations, with no additional computational costs.

2.2.4 Phonon dispersion

The quantum mechanical description of bulk or two-dimensional materials are generally executed using the adiabatic approximation known as the Born-Oppenheimer (BO) approximation. If we recall section 2.1.2, the BO approxima-

tion depends on the mass of the nuclei being much greater relative to electrons, which follows that the motion of the nuclei is smaller that the motions of the electrons. This makes it possible to decouple the nuclear, *i.e.*, vibrational, and the electron degrees of freedom in the Hamiltonian and execute the calculations of the total energy of the system in two distinct steps. The kinetic energy of the nuclei is considered to be a constant and the calculation dealing with it are taken away from the total Hamiltonian. The following BO Hamiltonian, H_{BO} then depends parametrically on the positions of the nuclei, τ, and the dynamics of the interacting electrons are characterised by electrostatic field of the the nuclei at their fixed positions,

$$\begin{aligned} H_{BO}(\tau) &= -\frac{1}{2}\sum_{i}\frac{\partial^2}{\partial \mathbf{r}_i^2} + \frac{1}{2}\sum_{i\neq j}\frac{1}{|\mathbf{r_i}-\mathbf{r_j}|} \\ &- \sum_{i,\kappa}\frac{Z_\kappa}{|\mathbf{r_i}-\tau_\kappa|} + \frac{1}{2}\sum_{\kappa\neq\mu}\frac{Z_\kappa Z_\mu}{|\tau_\kappa-\tau_\mu|} \end{aligned} \tag{2.59}$$

Here, the electronic coordinates are denoted as $\mathbf{r}$ with labels i, j. Similarly the labels τ, μ correspond to the nuclei having a nuclear charge of Z. One can use DFT methods to achieve the ground state BO energy of the system, E_{BO}. The kinetic energy of the nuclei is then added, producing a Schrödinger equation for the nuclear motion governing the dynamics of the lattice of the system,

$$\Big(-\frac{1}{2}\sum_{\kappa}\frac{1}{M_\kappa}\frac{\partial^2}{\partial\tau_\kappa^2} + E_{BO}(\tau)\Big)\Psi(\tau) = E\Psi(\tau) \tag{2.60}$$

Here, M_κ are the atomic masses and E is the total energy of the system. Assuming that the system under consideration is periodic and therefore be described by the periodic repetition of a unit cell. Relative to the chosen origin, let vector $\mathbf{R}$ describe the position of a periodic image of the unit cell, where the labels κ and β correspond to the nucleus within the unit cell and the Cartesian directions, respectively. The nuclei are not rigid, *i.e.*, they are not fixed to their classical zero-temperature initial positions but carry out small displacements $u_{\mathbf{R}\kappa\beta}$ in the vicinity about their equilibrium positions, $\tau_{\mathbf{R}\kappa\beta}$. Expanding the BO energy of the system in Taylor series as a function of nuclear displacements,

$$E_{BO} = E_{BO}^0 + \frac{1}{2}\sum_{\mathbf{R}\kappa\beta}\sum_{\mathbf{R}'\kappa'\beta'}\frac{\partial^2 E_{BO}}{\partial\tau_{\mathbf{R}\kappa\beta}\tau_{\mathbf{R}'\kappa'\beta'}}u_{\mathbf{R}\kappa\beta}u_{\mathbf{R}'\kappa'\beta'} + \cdots \tag{2.61}$$

Here, E^0_{BO} is the minimum BO energy when there are no displacements, a quantity that can be obtained using DFT. The linear contribution in the series, Eq. 2.61, vanishes because the 1^{st} order term describes the forces on each nucleus. The forces at equilibrium, when E_{BO} reaches a minimum, $F_{\mathbf{R}\kappa\beta} = \frac{\partial E_{BO}}{\partial \tau_{\mathbf{R}\kappa\beta}} = 0$. Since the 2^{nd} derivative of energy is termed *'harmonic'*, truncating the Taylor series at the 2^{nd} order is known as the *'harmonic approximation'*.

According to the principle of virtual work, when a nucleus is disturbed from its equilibrium position a force emerges to get the atom to its initial position. In the harmonic approximation Eq. 2.61, the force on the nucleus demonstrates a linear dependence on the displacement of the nucleus under investigation,

$$\begin{aligned} F(\mathbf{R}^{'}\kappa^{'}\beta^{'}) &= \frac{\partial E_{BO}}{\partial u_{\mathbf{R}\kappa\beta}} = -\sum_{\mathbf{R}^{'}\kappa^{'}\beta^{'}} \frac{\partial^2 E_{BO}}{\partial \tau_{\mathbf{R}\kappa\beta}\partial \tau_{\mathbf{R}^{'}\kappa^{'}\beta^{'}}} u_{\mathbf{R}^{'}\kappa^{'}\beta^{'}} \\ &= -\sum_{\mathbf{R}^{'}\kappa^{'}\beta^{'}} \Phi^{(2)}(\mathbf{R}\kappa\beta;\mathbf{R}^{'}\kappa^{'}\beta^{'}) u_{\mathbf{R}^{'}\kappa^{'}\beta^{'}} \end{aligned} \tag{2.62}$$

Eq. 2.62 describes the force on the nucleus under consideration at κ due to the displacement of another nucleus at $\kappa^{'}$ and describes the matrix of the *interatomic force constants*(IFCs). The lattice dynamics is determined by classical mechanics where the solution, in the harmonic approximation, is a superposition of the normal modes of vibration of the crystal. The normal modes are written as Bloch states when periodicity of the crystal is taken into account, *i.e.*, the product of a lattice-periodic function and plane wave,

$$U_{\mathbf{R}m\mathbf{q}}(\kappa\beta) = e^{\mathbf{iq}\cdot\mathbf{R}} U_{\mathbf{R}m\mathbf{q}}, \tag{2.63}$$

where $\mathbf{q}$, which characterizes the normal modes of vibration, is the wavevector in the first Brillouin zone. The harmonic approach also indicates a phase dependency on time, e^{-} to be inserted in Eq.2.63. The nuclear displacements $U_{\mathbf{R}m\mathbf{q}}(\kappa\beta)$, in quantum mechanics, are quantized and are termed as phonons. These phonon eigen-displacements with their frequencies $\omega_{m\mathbf{q}}$ are calculated by solving the generalized eigenvalue equation for periodic Bloch state,

$$\sum_{\kappa^{'}\beta^{'}} \Phi^{(2)}(\kappa\beta;\kappa^{'}\beta^{'};q) U_{m\mathbf{q}}(\kappa^{'}\beta^{'}) = M_{\kappa}\omega^2_{m\mathbf{q}} U_{m\mathbf{q}}(\kappa\beta) \tag{2.64}$$

Here, $\Phi^{(2)}(\kappa\beta;\kappa^{'}\beta^{'};q)$ is the Fourier transform of the IFC matrix

$$\Phi^{(2)}(\kappa\beta;\kappa^{'}\beta^{'};q) = \sum_{\mathbf{R}^{'}} \Phi^{(2)}(0\kappa\beta;\mathbf{R}^{'}\kappa^{'}\beta^{'})e^{\mathbf{iq}\cdot\mathbf{R}^{'}} \tag{2.65}$$

with the eigen-displacement normalization constraint,

$$\sum_{\kappa\beta} M_{\kappa}[U_{m\mathbf{q}}(\kappa\beta)]^{*}U_{m\mathbf{q}}(\kappa\beta) = 1. \tag{2.66}$$

The dimension of the dynamical matrix for a system under consideration with N atoms in the unit cell is $3N \times 3N$. The eigen-displacements are vectors having length $3N$ which characterize the displacements of the N nuclei along the 3 Cartesian directions. As in the case in electrons, the following phonon band dispersion is not unbounded from above and contains exactly $3N$ bands. The IFCs are able to be calculated precisely and efficiently using DFPT since the IFC and dynamical matrices are 2^{nd}-order derivates of the BO energy relative to the atomic displacements.

2.3 Boltzmann Transport Theory.[3]

2.3.1 Introduction

The statistical description of a thermodynamic system which is not in the state of equilibrium is characterised by the Boltzmann equation or Boltzmann transport equation (BTE) introduced by Ludwig Boltzmann [148]. The dynamics of an energetic particle in a crystal is generally described by the Boltzmann transport equation. The equation is derived by not examining individual positions and momentum but instead by investigating a probability for the position and momentum for a typical particle, *i.e.*, the probability that the particle occupies a differential domain in space, $d^3\mathbf{r}$, centred at some position $\mathbf{r}$ having a momentum $\mathbf{p}$ occupying a differential domain in momentum space $d^3\mathbf{p}$. The BTE is used to govern how physical quantities change such as heat energy and momentum. Variation of other properties such as electrical conductivity, mobility, Seebeck coefficient, Power factor *etc.* can be obtained by treating the charge carriers in the material as an electron gas.

[3]This theory has been implemented in Chapter 3, 4, 5 and 6

The lattice thermal conductivity, κ_L, can also be derived from the phonon Boltzmann transport equation. κ_L for materials (mainly semiconductors) and has been studied for many years employing different theoretical methods. However, the ultimate aim is to obtain a predictive theory for κ_L. As the fundamental studies and manufacture of nano-scale based devices develop, a microscopic understanding of phonon transport is necessary. A rapidly progressing field is that of thermoelectric. A dimensionless parameter known as figure of merit, $ZT = \frac{S^2\sigma T}{\kappa}$, is a measure of efficiency of a thermoelectric material. Here, σ, S, T and κ is the electrical conductivity, Seebeck coefficient, temperature and total (contributions both due to electrons and phonons) thermal conductivity. The temperature dependence of each of parameters that constitute the figure of merit can be calculated using the BTE.

The capability of DFT as a rigorous approach in calculating electronic properties of materials, where the electron exchange and correlation effects are relatively weaker, is well established. As mentioned in the previous sections, the linear response of the electron density to lattice distortions is accessible through DFPT. Using the "$2n+1$" theorem, the DFPT method can be employed to derive the harmonic as well as the third order anharmonic interatomic force constants. In this section we describe a theoretical frame work by combining these *ab-initio* methods along with an iterative solution of the BTE equation without any form of adjustable parameters.

2.3.2 Boltzmann equations to obtain electron transport coefficients

The Boltzmann transport equation states that there is no net change in the distribution function, $f(\mathbf{r}, \mathbf{k}, t)$, which governs the probability of discovering an electron at position $\mathbf{r}$, with crystal momentum $\mathbf{k}$ and at time t at steady state. Due to the distinct three processes of diffusion, the effect of forces and fields, and collisions, the sum of the changes in $f(\mathbf{r}, \mathbf{k}, t)$ would result to zero,

$$\left.\frac{\partial(\mathbf{r}, \mathbf{k}, t)}{\partial t}\right|_{diffusion} + \left.\frac{\partial(\mathbf{r}, \mathbf{k}, t)}{\partial t}\right|_{fields} + \left.\frac{\partial(\mathbf{r}, \mathbf{k}, t)}{\partial t}\right|_{collisions} \tag{2.67}$$

A standard procedure is to rewrite the differential form for the diffusion process as,

$$\left.\frac{\partial(\mathbf{r},\mathbf{k},t)}{\partial t}\right|_{diffusion} = -\mathbf{v}(\mathbf{k})\cdot\frac{\partial(\mathbf{r},\mathbf{k},t)}{\partial \mathbf{r}} \tag{2.68}$$

which demonstrates the continuity equation without forces, fields and collisions in real space. The differential form for the forces and fields are correspondingly written as,

$$\left.\frac{\partial(\mathbf{r},\mathbf{k},t)}{\partial t}\right|_{fields} = -\frac{\partial \mathbf{k}}{\partial t}\cdot\frac{\partial(\mathbf{r},\mathbf{k},t)}{\partial \mathbf{k}} \tag{2.69}$$

to acquire the Boltzmann equation,

$$\frac{\partial(\mathbf{r},\mathbf{k},t)}{\partial t} + \mathbf{v}(\mathbf{k})\cdot\frac{\partial(\mathbf{r},\mathbf{k},t)}{\partial \mathbf{r}} + \frac{\partial \mathbf{k}}{\partial t}\cdot\frac{\partial(\mathbf{r},\mathbf{k},t)}{\partial \mathbf{k}} = \left.\frac{\partial(\mathbf{r},\mathbf{k},t)}{\partial t}\right|_{collisions} \tag{2.70}$$

The left hand side of equation 2.70 involves derivatives of all the variables of the distribution function while the right hand side are the collision terms. The first explicit time dependent term in 2.70 is essential for the solution of ac driving forces or for impulse perturbation. The Boltzmann's equation is generally solved adopting two approximations, (i) The perturbation caused because of the fields and forces is to be assumed small so that the distribution function can be linearized, $f(\mathbf{r},\mathbf{k}) = f_0(E) + f_1(\mathbf{r},\mathbf{k})$. $f_0(E)$, which depends only on the energy E, is the equilibrium distribution function, the Fermi function. $f_1(\mathbf{r},\mathbf{k})$ is the perturbation term contributing to the deviation from equilibrium. (ii) For the system to turn back to equilibrium uniformly, the collision term in the Boltzmann equation is expressed in the relaxation time approximation,

$$\left.\frac{\partial f}{\partial t}\right|_{collision} = -\frac{(f-f_0)}{\tau} = -\frac{f_1}{\tau} \tag{2.71}$$

τ expresses the relaxation time and formally is a function of the crystal momentum, $i.e.$, $\tau = \tau(\mathbf{k})$. The time correlated with the rate of return to the equilibrium distribution when the external fields, forces or thermal gradients are turned off is the physical interpretation of the relaxation time approximation. When the fields are turned off, the solution to Eq. 2.71 yields,

$$\frac{\partial f}{\partial t} = -\frac{f-f_0}{\tau} \tag{2.72}$$

having the solution,

$$f(t) = f_0 + [f(0) - f_0]e^{-\frac{t}{\tau}} \tag{2.73}$$

$f(0)$ is the distribution function at time $t = 0$ whereas, as stated previously, f_0 is the equilibrium distribution. It can be easily seen that the solution to Eq. 2.71 results in a Poisson distribution, which signifies that the collisions relax the distribution function exponentially to f_0 having a time constant τ. With these approximations, the Boltzmann equation can now be solved to obtain the distribution function and consecutively the number and current density can be calculated. Since the current density $j(\mathbf{r}, t)$ is expressed as,

$$j(\mathbf{r}, t) = \frac{e}{4\pi^3} \int v(\mathbf{k}) f(\mathbf{r}, \mathbf{k}, t) d^3\mathbf{k} \tag{2.74}$$

where the crystal momentum $\hbar\mathbf{k}$ acts as the momentum $\mathbf{p}$ in determining a volume in phase space. Every domain of the size of Planck's constant in phase space can contain only one spin up and one spin down electron. The carrier density is therefore clearly expressed by the integration of the distribution function over k-space,

$$n(\mathbf{r}, t) = \frac{1}{4\pi^3} \int f(\mathbf{r}, \mathbf{k}, t) d^3\mathbf{k} \tag{2.75}$$

where $d^3\mathbf{k}$ is a domain of 3D wavevector space. The velocity of a carrier with crystal momentum $\hbar\mathbf{k}$ is associated with the energy dispersion $E(\mathbf{k})$ and is given by,

$$\mathbf{v}(\mathbf{k}) = \frac{1}{\hbar} \frac{\partial E(\mathbf{k})}{\partial \mathbf{k}} \tag{2.76}$$

The Fermi distribution function, which describes the equilibrium state, is,

$$f_0(E) = \frac{1}{1 + e^{\frac{E - E_F}{k_B T}}} \tag{2.77}$$

where E_F is the Fermi energy and k_B is the Boltzmann constant.

2.3.2.1 Electrical transport parameters

Consider an applied electric field $\mathbf{E}$ along the $x-$direction, with no magnetic fields and no thermal gradients. The electrical conductivity tensor σ is computed

explicitly from the equation,

$$\mathbf{j} = \sigma \cdot \mathbf{E} \tag{2.78}$$

using $\mathbf{j}$ from eq. 2.74, $\mathbf{v}$ from Eq. 2.76 and the distribution function $f(\mathbf{r}, \mathbf{k}, t)$ from the Boltzmann equation 2.70.

The first term in Eq. 2.70 vanishes because the dc field $\mathbf{E}$ applied has no time dependence. Since we have assumed that there are no thermal gradients, the second term in Eq. 2.70 also vanishes,

$$\mathbf{v} \cdot \frac{\partial(\mathbf{r}, \mathbf{k}, t)}{\partial \mathbf{r}} \simeq \frac{\partial f_0}{\partial \mathbf{r}} = \frac{\partial f_0}{\partial T}\frac{\partial T}{\partial \mathbf{r}} = 0 \tag{2.79}$$

The third term in Eq. 2.70 can now be expressed as,

$$\dot{\mathbf{k}} \cdot \frac{\partial f(\mathbf{r}, \mathbf{k}, t)}{\partial \mathbf{k}} = \sum_{\alpha} \dot{\mathbf{k}}_{\alpha} \frac{\partial(\mathbf{r}, \mathbf{k}, t)}{\partial k_{\alpha}} \tag{2.80}$$

The summation α runs over each of the vector components. The equation of motion yield, $\hbar\dot{\mathbf{k}} = e\mathbf{E}$ along with

$$\frac{\partial f(\mathbf{r}, \mathbf{k}, t)}{\partial \mathbf{k}} = \frac{\partial(f_0 + f_1)}{\partial \mathbf{k}} = \frac{\partial f_0}{\partial E}\frac{\partial E}{\partial \mathbf{k}} + \frac{\partial f_1}{\partial \mathbf{k}} \tag{2.81}$$

The last term in the above equation vanishes because we assume a linearized Boltzmann equation and thus only the leading term, $\frac{\partial f_0}{\partial}\hbar\mathbf{v}(\mathbf{k})$ is retained. In the case of an applied dc electric field having no thermal gradients, the linearized Boltzmann equation is given by,

$$\dot{\mathbf{k}} \cdot \frac{\partial f(r, k, t)}{\partial \mathbf{k}} = \frac{\phi}{\tau}\frac{\partial f_0}{\partial E} = -\frac{f_1}{\tau}. \tag{2.82}$$

Since, f_1 here is defined as $f_1 = -\phi\left(\frac{\partial f_0}{\partial E}\right)$, it explicitly demonstrates the $\left(\frac{\partial f_0}{\partial E}\right)$ dependence. We now we substitute the equation of motions, $\hbar\dot{\mathbf{k}} = e\mathbf{E}$ and Eq. 2.81 in Eq. 2.82,

$$\left[\frac{e\mathbf{E}}{\hbar}\left(\frac{\partial f_0}{\partial E}\right)\right] \cdot [\hbar\mathbf{v}(\mathbf{k})] = \frac{\phi(\mathbf{k})}{\tau}\left(\frac{\partial f_0}{\partial E}\right) \tag{2.83}$$

such that, $\phi(\mathbf{k}) = e\tau\mathbf{E} \cdot \mathbf{v}(\mathbf{k})$. We correlate $\phi(\mathbf{k})$ with $f_1(\mathbf{k})$ by,

$$f_1(\mathbf{k}) = -\phi(\mathbf{k})\frac{\partial f_0(E)}{\partial E} = -e\tau\mathbf{E} \cdot \mathbf{v}(\mathbf{k})\frac{\partial f_0}{\partial E} \tag{2.84}$$

The current density is then obtain from the distribution function $f(\mathbf{k})$ by computing the average value of $\langle ne\mathbf{v} \rangle$ over all momentum space,

$$\mathbf{j} = \frac{1}{4\pi^3} \int e\mathbf{v}(\mathbf{k}) f(\mathbf{k}) d^3\mathbf{k} = \frac{1}{4\pi^3} \int e\mathbf{v}(\mathbf{k}) f_1(\mathbf{k}) d^3\mathbf{k} \tag{2.85}$$

since $\frac{1}{4\pi^3} \int e\mathbf{v}(\mathbf{k}) f_0(\mathbf{k}) d^3\mathbf{k} = 0$, no net current flows in the absence of a static electric field which is the equilibrium condition. Substituting Eq.2.82 into Eq. 2.74 yields,

$$\mathbf{j} = -\frac{e^2\mathbf{E}}{4\pi^3} \int \tau \mathbf{v} \cdot \mathbf{v} \frac{\partial f_0}{\partial E} d^3\mathbf{k} \tag{2.86}$$

A comparison between the Eq.2.86 and Eq. 2.78 yields,

$$\sigma = -\frac{e^2}{4\pi^3} \int \tau \mathbf{v} \cdot \mathbf{v} \frac{\partial f_0}{\partial E} d^3\mathbf{k} \tag{2.87}$$

where σ is the conductivity tensor which is a symmetric second rank. More explicitly, the components of the conductivity (Eq. 2.87) can be expressed as,

$$\frac{\sigma_{\alpha\beta}(T,\mu)}{\tau} = \frac{1}{V} \int e^2 v_\alpha(i,\mathbf{k})\, v_\beta(i,\mathbf{k}) [\frac{-\partial f_0(T,\epsilon)}{\partial E}] d\epsilon \tag{2.88}$$

Where V is the volume of the unit cell. The temperature dependence is derived from the $\frac{\partial f_0}{\partial E}$ term and the evaluation of the integral depends on the E($\mathbf{k}$) and $\mathbf{v}$ relations. Analogous to the density of states, the energy projected conductivity tensors can be expressed by,

$$\sigma_{\alpha\beta}(E) = \frac{1}{N} \sum_{i,k} \sigma_{\alpha\beta}(\mathbf{k}, i) \frac{\delta(E - E_{i,\mathbf{k}})}{dE} \tag{2.89}$$

where N is the number of $\mathbf{k}$ sampling points.

The Seebeck tensor is defined by

$$S_{i,j} = E_i (\nabla_j T)^{-1} = (\sigma^{-1})_{\alpha i} v_{\alpha j} \tag{2.90}$$

where the velocity tensor is derived from the conductivity tensor,

$$v_{\alpha\beta}(T,\mu) = \frac{1}{eT\mu} \int \sigma_{\alpha\beta}(E)(E-\mu) \Big[- \frac{\partial f_\mu(T,E)}{\partial E} dE \Big] \tag{2.91}$$

The Seebeck coefficient is then calculated using,

$$S_{\alpha\beta}(T,\mu) = \frac{1}{eT}\frac{\int v_\alpha(i,\mathbf{k})v_\beta(i,\mathbf{k})(\epsilon-\mu)[\frac{-\partial f_\mu(T,\epsilon)}{\partial\epsilon}]d\epsilon}{\int v_\alpha(i,\mathbf{k})v_\beta(i,\mathbf{k})[\frac{-\partial f_\mu(T,\epsilon)}{\partial\epsilon}]d\epsilon} \tag{2.92}$$

where, μ is the chemical potential. In semi-metallic materials where the transport occurs only near the Fermi level, one can use the Sommerfeld expansion of 2.92 to obtain,

$$S = -\frac{\pi^2 k_B^2 T}{3e}\frac{d}{dE}\left[ln\,\sigma(E)\right]\Big|_{E=E_F} \tag{2.93}$$

Eq. 2.93 is known as the Mott formula [149]. The derivation can be found in Appendix B

2.3.3 Solving Boltzmann equations for lattice transport coefficient

For the spatially non-uniform phonon distribution, the Boltzmann equation is expressed as,

$$\left(\frac{\partial N}{\partial t}\Big|_{drift}\right) + \left(\frac{\partial N}{\partial t}\Big|_{scattering}\right) = 0 \tag{2.94}$$

here, N is the number of phonons in each mode. Generally, one performs the differentiation in the relaxation time approximation expressing the scattering term as $\left(\frac{\partial N}{\partial t}\Big|_{scattering}\right) = -\frac{n}{\tau}$, which leads to [150],

$$n = -\tau(\mathbf{v}\nabla T)\frac{\partial N_0}{\partial T}. \tag{2.95}$$

The Bose-Einstein distribution function is defined here as $N_0 = \frac{1}{e^{\frac{\hbar\omega}{k_B T}-1}}$ and n is the non-equilibrium part of the phonon distribution function, $N = N_0 + n$. ∇T and $\mathbf{v}$ is the temperature gradient and phonon group velocity, respectively. The heat flux for a 2D material is obtained from the expression [150],

$$\mathbf{Q} = \sum_{s,\mathbf{q}} \mathbf{v}(s,\mathbf{q})\hbar\omega(\mathbf{q})n[\mathbf{q},\omega(\mathbf{q})] \tag{2.96}$$

where $n(\omega, \mathbf{q})$ is the number of phonons in the heat flux and $\mathbf{v}\hbar\omega$ is the energy carried by a phonon. Substituting Eq. 2.95 in Eq. 2.96, the heat flux can be expressed as,

$$\mathbf{Q} = -\sum_{\beta}(\nabla T)_{\beta}\sum_{s,\mathbf{q}}\tau v_{\beta}(s,\mathbf{q})\frac{\partial N_0}{\partial T}\mathbf{v}(s,\mathbf{q})\hbar\omega(\mathbf{q}). \tag{2.97}$$

The macroscopic definition of the lattice thermal conductivity is derived from,

$$\mathbf{Q}_{\alpha} = -\kappa_{\alpha\beta}(\nabla T)_{\beta}\, hL_xL_y \tag{2.98}$$

where $\kappa_{\alpha\beta}$ is the lattice thermal conductivity tensor, L_x is the sample width, L_y is the sample length and h is the sample height. Comparing Eq. 2.97 and Eq. 2.98, we obtain the following expression for the lattice thermal conductivity tensor,

$$\kappa_{\alpha\beta} = \frac{1}{hL_xL_y}\sum_{s,\mathbf{q}}\tau(s,\mathbf{q})v_{\alpha}(s,\mathbf{q})v_{\beta}(s,\mathbf{q})\frac{\partial N_0(\omega)}{\partial T}\hbar\omega(\mathbf{q}). \tag{2.99}$$

2.3.3.1 Real space super cell approach

In this method the third order anharmonic IFCs are calculated from a set of displaced supercell configurations depending on the size of the system, their symmetry group and the number of nearest neighbour interactions. The third order anharmonic IFCs are constructed from a set of third-order derivatives of energy, calculated from these configurations using the plane wave method [139]. The phonon lifetimes are calculated from the phonon BTE which are limited by phonon-phonon, isotropic impurity and boundary scattering [151]. The three-phonon scattering rates are incorporated in this method, as implemented in the the ShengBTE code [152]. Elaborate details on the work-flow of the three-phonon scattering rates can be found in reference [152]. The thermal conductivity matrix $\kappa_L^{\alpha\beta}$ is given as,

$$\kappa_L^{\alpha\beta} = \frac{1}{k_BT^2\Omega N}\sum_{s} f_0(f_0+1)(\hbar\omega_s)^2v_s^{\alpha}\tau_s^0(v_s^{\beta}+\Delta_s^{\beta}). \tag{2.100}$$

$\kappa_L^{\alpha\beta}$ is then diagonalized to obtain the scalar lattice thermal conductivity κ_L in a preferred direction in the xy plane. In Eq. 2.100 Ω is the volume of the unit cell, N denotes the number of q-points in the Brillouin zone sampling. $f_0 =$

$1/(e^{\hbar\omega_s/k_BT}-1)$ is the Bose-Einstein distribution function, τ_s^0 is the relaxation time for the mode s with phonon frequency ω_s, v_s is the phonon group velocity, and Δ_s denotes the measure of how much associated heat current deviates from the relaxation time approximation. Mathematically, Δ_s and τ_λ^0 is expressed as [152],

$$\begin{aligned}\Delta_\lambda &= \frac{1}{N}\sum_{i=+,-}\sum_{\lambda'\lambda''}\Gamma^i_{\lambda\lambda'\lambda''}(\xi_{\lambda\lambda''}F_{\lambda''}-\xi_{\lambda\lambda'}F_{\lambda'}) \\ &+ \frac{1}{N}\sum_{\lambda'}\Gamma_{\lambda\lambda'}\xi_{\lambda\lambda'}F_{\lambda'} \qquad (2.101)\\ \frac{1}{\tau_\lambda^0} &= \frac{1}{N}(\sum_{\lambda'\lambda''}^{+}\Gamma^+_{\lambda\lambda'\lambda''}+\frac{1}{2}\sum_{\lambda'\lambda''}^{-}\Gamma^-_{\lambda\lambda'\lambda''}+\sum_{\lambda'}\Gamma_{\lambda\lambda'}) \qquad (2.102)\end{aligned}$$

here $\lambda(\lambda^{'},\lambda^{''})$ represents the phonon branch index $s(s^{'},s^{''})$ and wave vector $q(q^{'},q^{''})$ while $\xi_{\lambda\lambda'}$ and F_λ is short-hand for $\frac{\omega_{\lambda'}}{\omega_\lambda}$ and $\tau_s^0(v_s^\beta+\Delta_s^\beta)$ respectively. The three-phonon scattering rates denoted by $\Gamma^i_{\lambda\lambda'\lambda''}(i=+,-)$ and the scattering probabilities due to isotopic disorder denoted by $\Gamma_{\lambda\lambda'}$ have the following expressions,

$$\begin{aligned}\Gamma^\pm_{\lambda\lambda'\lambda''} &= \frac{\hbar\pi}{4\omega_\lambda\omega_{\lambda'}\omega_{\lambda'}}\begin{bmatrix} f_0(\omega_{\lambda'})-f_0(\omega_{\lambda''}) \\ f_0(\omega_{\lambda'})+f_0(\omega_{\lambda''}+1)\end{bmatrix} \\ &\times \left|V_{\lambda\lambda'\lambda''}\right|^2\delta(\omega_\lambda\pm\omega_{\lambda'}+\omega_{\lambda''}) \qquad (2.103)\\ \Gamma_{\lambda\lambda'} &= \frac{\pi\omega^2}{2}\sum_i f_s(i)\left[1-\frac{M_s(i)}{\overline{M}(i)}\right]^2 \\ &\times \left|e^*_\lambda\cdot e_\lambda\right|^2\delta(\omega_\lambda-\omega_{\lambda'}). \qquad (2.104)\end{aligned}$$

Where $V^\pm$ is the scattering matrix element and is expressed in terms of the anharmonic IFCs (Φ), eigen functions (e) and mass (M) of an atom as

$$V_{\lambda\lambda'\lambda''}=\sum_{i,j,k}\sum_{\alpha\beta\gamma}\frac{\Phi^{\alpha\beta\gamma}_{ijk}e^\alpha_\lambda e^\beta_{\lambda'}e^\gamma_{\lambda''}}{\sqrt{M_iM_jM_k}}. \qquad (2.105)$$

In the above expression, i,j,k run over the atomic indices and α,β,γ are the Cartesian coordinates. $\overline{M}=\sum_s f_s(i)M_s(i)$ is the average of masses ($M_s(i)$) of isotopes s of the atoms i having a relative frequency f_s. $\Gamma^{+(-)}$ represents the absorption (emission) processes. A phonon which is a result of the absorption process is a combined energy of two incident phonons, *i.e.* $\omega_\lambda+\omega_{\lambda'}=\omega_{\lambda''}$.

Similarly, the emission process depicts the energy of an incident phonon being separated among two phonons, $\omega_\lambda = \omega_{\lambda'} + \omega_{\lambda''}$. Therefore in eq.2.103 it is easy to see that the Dirac delta function, $\delta(\omega_\lambda \pm \omega_{\lambda'} + \omega_{\lambda''})$, imposes the conservation of energy in the absorption and emission processes.

It should be noted that the relaxation times is calculated in the ShengBTE code using an iterative approach by solving the phononBTE starting with the zeroth-order approximation, $\Delta_\lambda = 0$, also known as the RTA solution. These iterations continue till two successive values of κ_L differ by 10^{-5} $\mathrm{Wm^{-1}K^{-1}}$. The interatomic third-order force constants (IFCs) are calculated using a real space supercell approach.

Length dependent thermal conductivity is then calculated by taking into account only phonons with a mean free path (MFP) below a certain threshold value. This is done by calculating the cumulative lattice thermal conductivity with respect to the allowed MFP. Furthermore, advanced experimental techniques have recently been proposed to measure the cumulative κ_L as a function of phonon mean free path [153, 154, 155].

In order to compare our calculations with experimental measurements, we fit the cumulative length dependent thermal conductivity in the form [152],

$$\kappa_L(L) = \frac{\kappa_{L_{max}}}{1 + \frac{L_0}{L}}. \tag{2.106}$$

where L_0 is a fitting parameter. κ_L corresponding to a given length is calculated over a temperature range using Eq. 2.106 and the thermodynamic limit of the thermal conductivity ($\kappa_{L_{max}}$) is the value of κ_L as $L \to \infty$.

2.3.3.2 Callaway-Klemens approach (Analytical and numerical solutions)

In the Callaway-Klemens's [156, 157] approach which has been modified by Nika *el al* [158], the expression for thermal conductivity along x and y directions for two-dimensional layered materials, with relaxation time approximation (RTA)

to BTE and isotropic approximation to phonon dispersion is given by,

$$\begin{aligned}\kappa &= \frac{1}{4\pi k_B T^2 N\delta} \\ &\times \sum_s \int_{q_{min}}^{q_{max}} [\hbar\omega_s(q)]^2 v_s^2(q)\tau_{U,s}(q)\frac{e^{\frac{\hbar\omega_s(q)}{k_B T}}}{[e^{\frac{\hbar\omega_s(q)}{k_B T}}-1]^2} q dq, \end{aligned} \tag{2.107}$$

where k_B is the Boltzmann constant, $\hbar$ is the reduced Planck constant, T is the absolute temperature, N is the number of layers, δ is the distance between two consecutive layers, $\omega_s(q)$ and $v_s(q)$ are the phonon frequency and velocity corresponding to the branch s at phonon wave vector q. The wave vector corresponding to the Debye frequency and low cut-off frequency are denoted by q_{max} and q_{min}, respectively. The method to calculate the low cut-off frequency will be discussed shortly. $\tau_{U,s}$ is the three-phonon Umklapp scattering corresponding to branch s at the wave vector q expressed as,

$$\tau_{U,s} = \frac{M v_s^2(q)\omega_{D,s}}{\gamma_s^2(q) k_B T \omega_s(q)^2}. \tag{2.108}$$

Here, M is total mass of the atoms in the unit cell, $\gamma_s(q)$ is the mode and wave vector dependent Grüneisen parameter.

The validity of the form of relaxation time in the Umklapp scattering in eq. 2.108 for a 2D and 3D material was originally proposed by Klemens *et. al.*[159], where phonons were treated by a two-dimensional Debye model. This sets up a mode for the thermal conductivity in terms of a 2D phonon gas. On the basis of the phonon frequency dependence of the specific heat and mean free path, the form of $\tau_{U,s}$ in eq. 2.108 is valid for both 2D and 3D. Moreover, the calculations by Shen *et. al.* [160] use the same form to describe the relaxation time of the Umklapp process for graphene and their results, when $\tau_{U,s}$ is multiplied by a factor of 3, are consistent with the paper of Lindsay *et. al.* [151] which solves the phonon BTE beyond the RTA. Since eq. 2.108 cannot determine whether the U-processes are forbidden or not, the factor of 3 is added due to the symmetries seen in graphene which is explained in detail later.

Grüneissen parameter ($\gamma_s(q)$) and the Debye frequency ($\omega_{D,s}$) corresponding

to the branch s is calculated by solving,

$$\frac{A}{2\pi}\int_0^{\omega_{D,s}} q\left|\frac{dq}{d\omega}\right| d\omega = 1, \tag{2.109}$$

where A is the area of the unit cell.

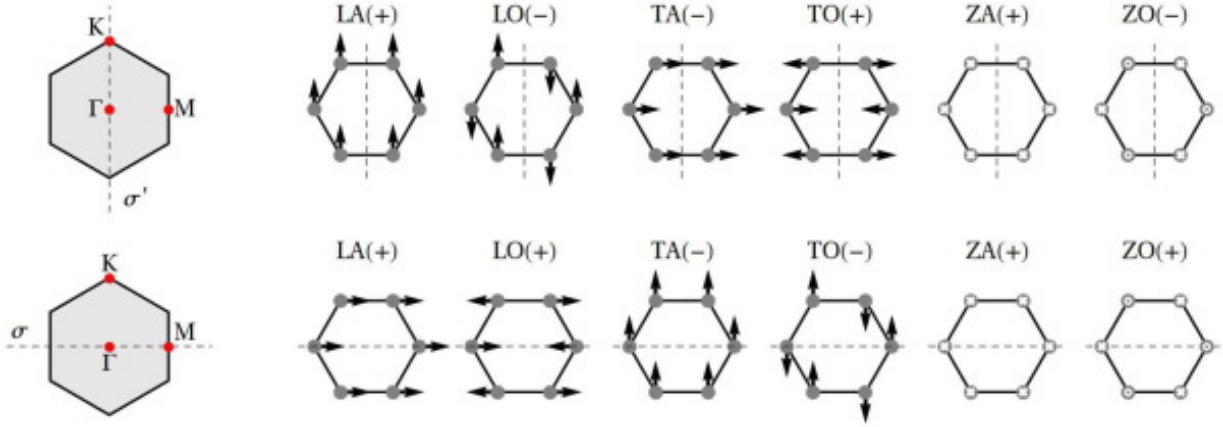

Figure 2.3: The acoustic (A) and optical (O) phonon modes defined along their polarization relative to the Γ K direction (top) and Γ M(bottom) directions for a two-dimensional hexagonal system such as graphene and boron nitride. The modes are associated with the in-plane longitudinal (L) and transverse (T) atomic displacements as well as the out-of-plane (Z) atomic displacements. Figure adapted from Reference [18].

The acoustic branches for in-plane modes for MLG, BLG, SLBN, BLBN, 5LBN and Bulk-*h*BN are linear whereas the out-of-plane acoustic mode have a quadratic behavior and hence for a simplified analytical solution we express the phonon frequencies as,

$$\omega_s(q) = v_s q \Rightarrow [s = \mathrm{LA}, \mathrm{TA}] \tag{2.110}$$

$$= \alpha q^2 \Rightarrow [s = \mathrm{ZA}] \tag{2.111}$$

Substituting these values in Eq. 2.109, we find the Debye frequency is given by

$$\omega_{D,s} = 2v_s\sqrt{\frac{\pi}{A}} \Rightarrow [s = \mathrm{LA}, \mathrm{TA}] \tag{2.112}$$

$$= \frac{4\pi\alpha}{A} \Rightarrow [s = \mathrm{ZA}] \tag{2.113}$$

The in-plane and out-of-plane phonon modes related to the atomic displacements are shown in Fig. 2.3.

The mode dependent anharmonic (Grüneissen) parameters were calculated by applying a biaxial strain of $\pm$ 0.5% to each of the structures.

$$\begin{aligned}\gamma_s(q) &= \frac{-a_0}{2\,\omega_s(q)}\frac{\delta\omega_s(q)}{\delta a} \\ &\approx \frac{-a_0}{2\,\omega_s(q)}\left[\frac{w_+ - w_-}{da}\right]\end{aligned} \tag{2.114}$$

Fig. 2.4 shows that the Grüneisen parameter for the in-plane modes have a slight deviation from its average value along the Γ to K direction. Therefore assuming a constant value for γ_s (s=LA,TA), Nika *et al* [158] have derived the following analytical solution for κ associated with a particular mode s.

$$\kappa_s = \frac{M\omega_{D,s}v_s^2}{4\pi T(N\delta)\gamma_s^2}\left[\ln(e^x-1) + \frac{x}{1-e^x} - x\right]\Bigg|_{\frac{\hbar\omega_{min,s}}{k_BT}}^{\frac{\hbar\omega_{D,s}}{k_BT}} \tag{2.115}$$

Since there is no ZO$'$ branch in SLBN, the low bound cut-off frequency cannot be introduced in analogy to that of bulk graphite. One can however avoid the logarithmic divergence by restricting the phonon mean free path on the boundaries of the sheets [150]. This is accomplished by selecting the mode dependent low cut-off frequency ($\omega_{s,min}$) from the condition that the mean free path cannot be greater in size than physical length L of the sheet, *i.e,*

$$\omega_{s,min} = \frac{v_s}{\gamma_s}\sqrt{\frac{Mv_s\omega_{D,s}}{k_BTL}} \tag{2.116}$$

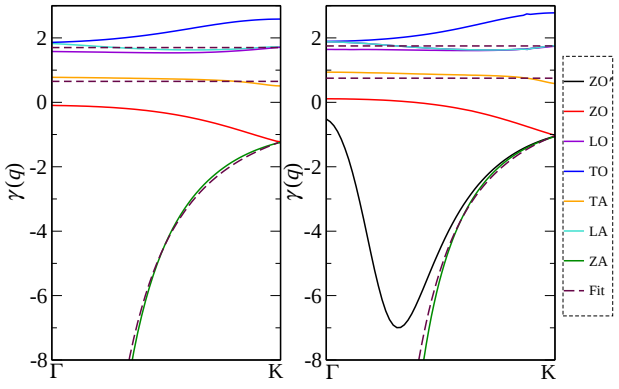

Figure 2.4: The calculated Grüneisen (γ) parameters of all the modes along the Γ to K direction of the 2D Brillouin zone of the hexagonal unit cell for MLG(left) and BLG(right). The maroon dashed lines are the best constant and inverse squared wave dependent fits to the in-plane (LA,TA) and out-of-plane (ZA) γ parameters, respectively.

In the spirit of in-plane thermal conductivity study we extend our calculations to find an analytical form to the flexural phonons modes since the contribution from these branches are vital to the total thermal conductivity. Unlike for the case of in-plane modes, the Grüneisen parameters for the acoustic out-of-plane ZA modes have a strong q-dependence. From Fig. 2.4 it can be seen that the expression

$$\gamma_{ZA} = \frac{\beta}{q^2}, \tag{2.117}$$

is a very good fit to the actual wave vector dependent Grüneisen parameters. This inverse square wave dependence behavior can be understood by studying the phonon dispersion under positive and negative strain. Consider the phonon dispersion of the ZA mode under a biaxial strain. The phonon dispersion for the ZA mode just shifts by a small constant. For example, in the case of *h*-BN, P. Anees *et al.* [161] have plotted the phonon dispersion under positive and negative strain. Therefore the phonon dispersion with biaxial strain would become $\omega_{\pm} = \alpha q^2 \pm \delta a$. Where δa is a small constant. Substituting these values in Eq. 2.114, we get, $\gamma \propto \frac{-2\delta a}{\alpha} \propto \frac{-1}{q^2}$.

Substituting eq. 2.117 and eq. 2.111 into eq. 3.12 and making a transformation, $x = \frac{\hbar\omega}{k_B T}$, the analytical form for κ_{ZA} is given by

$$\begin{aligned} \kappa_{ZA} &= \frac{2M\omega_D k_B^3 T^2}{\pi N \delta \beta^2 \hbar^3 \alpha} \int_0^{\frac{\hbar\omega_D}{k_B T}} x^4 \frac{e^x}{[e^x - 1]^2} dx \\ &= \frac{2M\omega_D k_B^3 T^2}{\pi N \delta \beta^2 \hbar^2 \alpha} \, G\Big(\frac{\hbar\omega_D}{k_B T}\Big), \end{aligned} \tag{2.118}$$

where the function $G(z)$ is expressed as

$$\begin{aligned} G(z) &= \frac{-4\pi^4}{15} + \frac{e^z z^4}{1 - e^z} + 4z^3 \ln(1 - e^z) \\ &+ 12z[z\mathrm{Li}_2(e^z) - 2\mathrm{Li}_3(e^z)] + 24\mathrm{Li}_4(e^z). \end{aligned} \tag{2.119}$$

Here, the polylogarithm function is defined as, $\mathrm{Li}_n(z) = \sum_{i=1}^{\infty} \frac{z^i}{i^n}$.

The total phonon relaxation time τ_{tot} comprises of the contributions from, (i) the phonon-phonon Umklapp scattering, (ii) the boundary scattering, and (iii) scattering due to point defects. The phonon-phonon Umklapp scattering rate (τ_U) for a given mode s is given by Eq. 2.108 [157, 156, 158].

The rough boundary scattering rate are shown to be given by [158],

$$\tau_{B,s}(q) = \frac{d}{v_s\big(\omega_s(q)\big)} \frac{1 + p}{1 - p}, \tag{2.120}$$

where, d is the width of the sample. The specularity parameter (p) depends on the roughness of the edges. For example an ideal smooth sample would have a

specularity parameter $p = 1$. The scattering rate due to point defects is written as[158],

$$\tau_{P,s}(q) = \frac{4v_s\big(\omega_s(q)\big)}{S_0\Gamma_0 q_s\big(\omega_s(q)\big)}\frac{1}{\omega(q)_s^2}, \tag{2.121}$$

where, Γ_0 is a dimensionless parameter to determine the strength of the point-defect scattering, given by $\Gamma_0 = \sum_i f_i(1 - \frac{M_i}{\overline{M}})$, where $\overline{M} = \sum_i M_i f_i$ is the average atomic mass, f_i is the fractional concentration of the impurity atoms with mass M_i. The cross-sectional area per atom of the lattice is denoted by S_0. Each of the mentioned scattering rates can be combined to calculate the total phonon relaxation time which is given by the Matthiessen's rule [162, 163],

$$\frac{1}{\tau_{tot,s}(q)} = \frac{1}{\tau_{U,s}(q)} + \frac{1}{\tau_{B,s}(q)} + \frac{1}{\tau_{P,s}(q)}. \tag{2.122}$$

We now extend our calculations with point defects and specularity parameters for values of p less than 1. With these approximations, Eq. 3.12 for the LA,TA and ZA mode can be easily shown to be,

$$\kappa_{L_{LA,TA}} = \frac{1}{C_0}\int_{\omega_{min}}^{\omega_D} \hbar^2\omega^3\tau_{tot}\frac{e^{\frac{\hbar\omega}{k_BT}}}{[e^{\frac{\hbar\omega}{k_BT}}-1]^2}d\omega, \tag{2.123}$$

$$\kappa_{L_{ZA}} = \frac{2}{C_0}\int_{\omega_{min}}^{\omega_D} \hbar^2\omega^3\tau_{tot}\frac{e^{\frac{\hbar\omega}{k_BT}}}{[e^{\frac{\hbar\omega}{k_BT}}-1]^2}d\omega, \tag{2.124}$$

where C_0 is given by $C_0 = 4\pi k_B T^2(N\delta)$ and the separate relaxation times for the in-plane and out-of-plane modes with these approximation become,

$$\tau_{U,s}(\omega) = \frac{C_1}{\omega^2} \;;\; C_1 = \frac{Mv^2\omega_{D_s}}{\gamma^2 k_B T} \Rightarrow [s = \text{LA, TA}] \tag{2.125}$$

$$= C_2\omega \;;\; C_2 = \frac{4M\omega_{D_s}}{\beta^2\alpha k_B T} \Rightarrow [s = \text{ZA}] \tag{2.126}$$

$$\tau_{B,s}(\omega) = C_3 \;;\; C_3 = \frac{d}{v}\frac{1+p}{1-p} \Rightarrow [s = \text{LA, TA}] \tag{2.127}$$

$$= \frac{C_4}{\sqrt{\omega}} \;;\; C_4 = \frac{d}{2\sqrt{\alpha}} \Rightarrow [s = \text{ZA}] \tag{2.128}$$

$$\tau_{P,s}(\omega) = \frac{C_5}{\omega^3} \;;\; C_5 = \frac{4v^2}{S_0\Gamma_0} \Rightarrow [s = \text{LA, TA}] \tag{2.129}$$

$$= \frac{C_6}{\omega^2} \;;\; C_6 = \frac{8\alpha}{S_0\Gamma_0} \Rightarrow [s = \text{ZA}] \tag{2.130}$$

2.4 Molecular Dynamics[4]

2.4.1 Introduction

Molecular dynamics (MD) is a computer simulation technique for understanding the physical movements of a many body system such as atoms and molecules, widely used in material science and physical chemistry. The atoms in MD simulations generally follow the classical equations of motions, *i.e.*, $m_i \frac{d^2\mathbf{r_i}}{dt^2} = \mathbf{F_i}$, where m_i is the mass of the ith atom at position $\mathbf{r_i}$ and $\mathbf{F_i}$ is force acting on it. The goal of MD simulations are to solve these equations from the initial position, velocity of the atoms, and the forces of the interactions between them numerically and to derive important information from the atomic trajectories. There are two types of MD simulations, the *ab-initio* MD [164] and classical MD [165, 166]. In the *ab-initio* MD technique, the force is computed on the nuclei from electronic structure calculations such as density functional theory (DFT) calculations. However, this technique is only practical for relatively smaller systems because of its challenging computation load. In the second method, which is used in this thesis, the classical MD, the forces operating on the atoms are extracted from empirical inter-atomic potentials (EIPs), $\mathbf{F_i} = -\nabla_{\mathbf{r_i}} V(\mathbf{r_1}, \mathbf{r_2}, \cdots, \mathbf{r_N})$, where N is the total number of atoms. The computation challenge is greatly decreased in this technique because the electrons are not accounted in the calculations therefore making it possible to perform large-scale simulations. The simulation cells used in all our molecular dynamic studies are shown in Fig. 5.2.

2.4.2 Tersoff potential

The Tersoff potential is a three-body functional involving explicitly the angular contribution of the force. The essential assumptions are that the dynamics are treated classically, the atoms are spherical and chemically inert. The interatomic potential energy described in this method is similar to the Taylor expansion of

[4]This theory has been implemented in Chapter 5

the potential as a function of the atomic positions,

$$E = \sum_i V_1(\mathbf{r_i}) + \sum_{i<j} V_2(\mathbf{r_i}, \mathbf{r_j}) + \sum_{i<j<k} V_3(\mathbf{r_i}, \mathbf{r_j}, \mathbf{r_k}) + \cdots \tag{2.131}$$

where V_1, V_2, V_3 are the one, two and three body potentials. Considering just the interatomic forces would result in the vanishing of the first term since it is associated with an external force. The pair potential term (V_2) alone is convenient for closed packed structures but would not be appropriate for strongly covalent systems. The detailed form of the pair potential term varies from a *Lennard-Jonnes* type, $\frac{1}{r^n}$ interaction to a *Morse* type, $e^{-\alpha r}$ interaction or a merge between them. Therefore a cut-off function must be introduced to confine the extent of the potential which would in turn reduce the computational load. The implementations of the $N-$body potential were discarded by J. Tersoff [167] and suggested an approach coupling efficiently two body and higher multi atom correlations into the method. J. Tersoff defined a pair potential in which the strength depended on its environment, *i.e.*, an atom having many neighbors formed relatively weaker bonds with respect to atoms with few neighbors. The Tersoff potential were initially calibrated for silicon [167] and carbon [168]. The Tersoff potential is expressed as,

$$E = \sum_i E_i = \frac{1}{2} \sum_{i \neq j} V_{ij} \tag{2.132}$$

where V_{ij} has the following form,

$$V_{ij} = f_C(r_{ij})[f_R(r_{ij}) + b_{ij} f_A(r_{ij})] \tag{2.133}$$

Here the potential energy consists of a site energy E_i and a bonding energy V_{ij}. The distance between atoms i and j are written as r_{ij}. The attractive and repulsive pair potential terms are denoted as f_A and f_R, respectively, expressed as,

$$f_R(r) = Ae^{-\lambda_1 r} \tag{2.134}$$

and

$$f_A(r) = -Be^{-\lambda_2 r} \tag{2.135}$$

The smooth cut-off function has the expression,

$$f_C = \begin{cases} 1, & r < R - D \\ \frac{1}{2} - \frac{1}{2}\sin\left[\frac{\pi}{2}\frac{r-R}{D}\right], & R - D < r < R + D \\ 0, & r > R + D \end{cases} \tag{2.136}$$

Parameters R and D are not systematically optimized but are selected so as to only involve the first neighbor shell for a selected structure. The cut-off function, f_C, has values that decrease from 1 to 0 in the range $R - D < r < R + D$. An essential characteristic of this potential is the existence of the b_{ij} term. It is this term that makes the strength of the potential depended on its environment. The form of the term b_{ij} is expressed as,

$$b_{ij} = \frac{1}{(1 + \beta^n \zeta_{ij}^n)^{\frac{1}{2n}}} \tag{2.137}$$

where ζ_{ij} is written as,

$$\zeta_{ij} = \sum_{k \neq i,j} f_C(r_{ij}) g(\theta_{ijk}) e^{[\lambda_3^3 (r_{ij} - r_{ik})^3]} \tag{2.138}$$

The term ζ describes the effective coordination number of an atom i, *i.e.*, the number of nearest neighbors which takes into account the relative distance between two neighbors, $r_{ij} - r_{ik}$ and the bond angle, θ. and $g(\theta)$ is written as,

$$g(\theta) = 1 + \frac{c^2}{d^2} - \frac{c^2}{\left[d^2 + \left(h - \cos(\theta)^2\right)\right]} \tag{2.139}$$

The sharpness of an angle is dictated by the parameter d while c describes the strength of the angular effect. The function $g(\theta)$ has its minimum value at $h = \cos(\theta)$. These potential parameters are generally chosen by fitting theoretical and experimental data obtained from practical configurations such as cohesive energy, lattice constants, bulk modulus, *etc.*

2.4.3 Equilibrium Molecular Dynamic simulations

There is no net macroscopic flow of energy or matter in the equilibrium molecular dynamics (EMD). In this approach the lattice thermal conductivity is obtained

from the Green-Kubo formula derived from the linear response theory [169, 170],

$$\kappa_{\alpha\beta} = \frac{1}{k_B V T^2} \int_0^\infty \langle \mathbf{J}_\alpha(t) \mathbf{J}_\beta(0) \rangle \, dt \tag{2.140}$$

The Cartesian directions are denoted by α and β. k_B, V, J are the Botlzmann constant, volume and heat current, respectively. The integral is recognised as the heat current autocorrelation function (HCAF). The heat current vector is defined as,

$$\mathbf{J(t)} = \frac{d}{dt} \sum_i \mathbf{r_i}(t) E_i(t) = \sum_i \mathbf{v_i} E_i + \sum_i \mathbf{r_i} \frac{d}{dt} E_i, \tag{2.141}$$

The time-dependent atomic position and site energy are denoted by $\mathbf{r_i}$ and E_i, respectively. The $\sum_i \mathbf{v_i} E_i$ term is identified with the convection heat transfer which generally occurs in fluids. The conduction is described by $\sum_i \mathbf{r_i} \frac{d}{dt} E_i$ term which is dominant in solids [170]. For EIPs consisting of either two or three body term and if only the conduction term is considered, the heat current then can be written as [170],

$$\mathbf{J(t)} = \frac{\mathbf{1}}{\mathbf{2}} \sum_{\mathbf{i,j}} \mathbf{r_{ij}} (\mathbf{F_{ij}} \cdot \mathbf{v_i}) + \frac{\mathbf{1}}{\mathbf{6}} \sum_{\mathbf{i,j}} (\mathbf{r_{ij}} + \mathbf{r_{ik}}) (\mathbf{F_{ijk}} \cdot \mathbf{v_i}), \tag{2.142}$$

The relative position of atom i with j is denoted by $\mathbf{r_{ij}}$. The force which acts on atom i derived from the two body potential involving atom i and atom j is denoted by $\mathbf{F_{ij}}$. Similarly, the force which acts on atom i derived from the three-body potential involving atoms i, atom j and atom k is denoted by $\mathbf{F_{ijk}}$. Generally, a huge supercell is chosen as the simulation cell having periodic boundary condition in all three directions. Similar to that done in DFT, fow low dimensional materials, one has to create a large vacuum layer in the appropriate direction to avoid interaction between the periodic atoms (See Fig. 5.2(b)) which in turn mimics the free surface.

Before describing how MD simulations are run, one must define the nomenclature for the different ensembles. (i) In the microcanonical ensemble (NVE) the system is isolated from its N particle (N), Volume (V) and energy (E). The ensemble therefore relates to an adiabatic process having no heat exchange. (ii) Often referred to as constant temperature MD, the canonical ensemble (NVT) conserves the number of particles (N), volume (V) and temperature (T). The

energy of Exothermic and Endothermic processes are exchanged with a thermostat in NVT. (iii) For the isothermal-isobaric (NPT) ensemble, the total number of particles (N), pressure (P) and temperature (T) are conserved. Therefore in addition to a thermostat, a barostat would be required in the NPT ensemble. The MD simulations are initially run in the NPT ensemble. When the system reaches thermal equilibrium and the strain is released, the MD simulation is followed by the run in NVT and NVE ensembles. The heat current is then obtained from the NVE ensemble and the thermal conductivity is calculated using Eq. 2.140. In comparison to the non-equilibrium molecular dynamic (NEMD) simulation, EMD simulations are a better choice for the intrinsic simulation because there is only a weak size truncation effect along the thermal transport direction. However, this weak size effect can be minimized by increasing the number of atoms in the simulation cell.

2.5 Regular solution model and Monte Carlo simulations[5]

2.5.1 Regular solution model

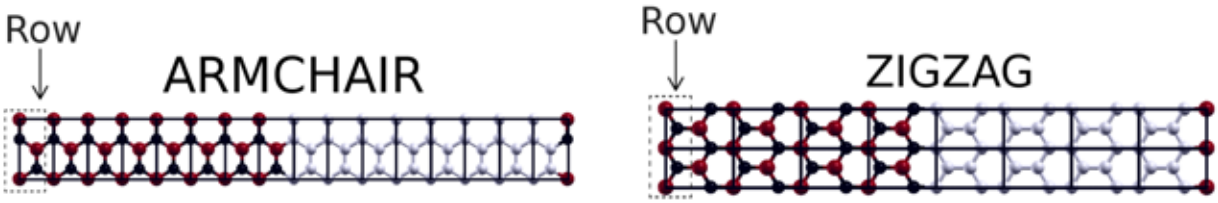

Figure 2.5: The arm-chair (left panel) and zig-zag interface created between h-BN and graphene within the supercell. The 16×1 armchair and 8×2 zigzag supercells generated by the orthorhombic unit cells are shown by the solid black lines. The row used for replacing C atoms by BN atoms in two cases have been marked by the black dotted boxes. The carbon, B and N atoms are shown as white (light gray), red (dark gray) and black colored balls.

A solution whose entropy of mixing is equal to that of an ideal solution having the same composition, however, is not ideal since the enthalpy of mixing is non-zero. Such a solution is termed as the regular solution. The entropy of mixing is the same that of an ideal solution having the same composition because

[5]This theory has been implemented in Chapter 6

the random mixing is without strong specific interactions,

$$S = -k_B \sum x \ln x, \tag{2.143}$$

where the sum runs over all the configurations. In this thesis, we study the phase stability of $C_{2x}(BN)_{1-x}$ treating the carbon dimers and boron-nitride as two-different components. For a two-component system, the entropy of mixing can therefore be written as,

$$S = -2k_B[x \ln x + (1-x)\ln(1-x)] \tag{2.144}$$

where k_B is the Boltzmann constant, x is the concentration of carbon and therefore the concentration of the BN dimers is given by $1-x$. The factor of two in Eq. 2.144 arises due to the mixed occupancy of the two sub-lattices. The concentration and temperature dependent free energy, $F(T,x)$ is expressed as,

$$F(T,x) = \Delta E(x) - TS. \tag{2.145}$$

where $\Delta E(x)$ is the concentration dependent cohesive energy or mixing energy because it is related to the energies of the alloy related to the energies of pristine graphene and boron nitride. The tendency to phase separate is dictated by the positive value of the mixing energy while the negative values of ΔE indicate the tendency to form a homogeneous solid solution. For each concentration x, the mixing energy per formula unit (f.u.) of the system using DFT, is expressed as,

$$\begin{aligned} \Delta E &= E\{(C_2)_x(BN)_{1-x}, a(x)\} \\ &- [xE(C, a_C) + (1-x)E(h\mathrm{BN}, a_{h\mathrm{BN}})], \end{aligned} \tag{2.146}$$

where where $E\{(C_2)_x(BN)_{1-x}, a(x)\}$ is the total energy per formula unit of $(C_2)_x(BN)_{1-x}$ at the equilibrium in-plane lattice constant $a(x)$; $E(C, a_C)$ and $E(h\mathrm{BN}, a_{h\mathrm{BN}})$ are the total energies per formula unit of pristine graphene and *h*-BN at the equilibrium in-plane lattice constants a_C and $a_{h\mathrm{BN}}$, respectively. The critical temperature within the regular solution model can be calculated from the condition, $\frac{d^2F}{dx^2} = 0$ at x when $\frac{dF}{dx} = 0$,

$$\left.\frac{d^2F}{dx^2} = 0\right|_{x(\frac{dF}{dx}=0)} \tag{2.147}$$

2.5.2 Monte Carlo simulation

2.5.2.1 Infinite Sheets

DFT calculations involve large computer time even for a modestly small number of atoms and can be almost impossible for calculations involving a large number of atoms. MC simulations are ideal to deal such situations. It is also a convenient method to know what kind of interfaces are formed if the system is allowed to evolve without any constraint. We therefore employed Monte Carlo simulations to study the segregation of BN domains on graphene and calculate it's solid solution phase from the spinodal line. The Monte Carlo Simulations, within the framework of Metropolis [171] algorithm, are based on the following Hamiltonian, defined on a bond basis with bond energies extracted out from DFT calculations.

$$H = \frac{1}{2}\sum_{i=1}^{N}\sum_{j=1}^{3} E_b(\alpha_i, \beta_j) \tag{2.148}$$

where, N is the total number of atoms in the simulation cell, $E_b(\alpha_i, \beta_j)$ is the bond energy between α_i and β_j. α_i is the atom at position i, β_j is the nearest neighbor atom. α and β can be either C, B or N. The factor of 2 in the denominator accounts for double counting. In order to estimate $E_b(\alpha_i, \beta_j)$ for different kinds of bonds, which can be CC, BN, CB or CN, we first considered an isolated pair of CC, BN, CB or CN atoms in which the C atoms are passivated with hydrogen atoms. We calculated the energy of this H-bonded pair of atoms, which is denoted as E_{sp_3}. We then calculated the energy of the hexagonal infinite sheets built up by same pair of atoms, which would be a graphene or BN sheet if the pair of atoms is CC or BN. For rest of the combinations, these are artificial computer-generated sheets. Energy of this infinite sheet is denoted as E_{inf}. Considering the case of graphene, and the fact that energy of the infinite sheet in the unit cell is given by the energy of two isolated C atoms (C_{iso}) and the bond energy of C-C, $E_b(CC)$, we have,

$$E_{inf} = 2C_{iso} + nE_b(\mathrm{CC}) \tag{2.149}$$

where n is the number of bonds on each carbon atom. Similarly the energy of hydrogen passivated C-C pair can be also expressed as a sum of energy of

isolated atoms and bond energies. Thus,

$$E_{sp_2} = 2C_{iso} + E_b(\mathrm{CC}) + 4H_{iso} + 4E_b(\mathrm{CH}) \tag{2.150}$$

taking into account of the fact that there are 6 hydrogen atoms required to passivate the two carbon atoms completely. From the above two equations, one can arrive at a definition of CC bond energy as,

$$E_b(\mathrm{CC}) = \frac{E_{inf} - (E_{sp_2} - 4H_{iso} - 4E_b(\mathrm{CH}))}{n-1} \tag{2.151}$$

The bond energies of other pairs can be defined similarly.

2.5.2.2 Nanoribbons

Having computed the bond energies in a DFT derived way which are the input to the MC simulation for the infinite sheet of $(\mathrm{C}_2)_x(\mathrm{BN})_{1-x}$, we proceed to calculate the same for cases when the systems are nanoribbons. As can be anticipated, the bond energies of the pair of atoms positioned near the edge of the ribbon will be different from that inside the ribbon. This effect may also extend to atoms adjacent to the edge. Thus to compute the position-dependent bond energies, we proceed as follows. We passivate the edges of the nanoribbon with hydrogen atoms. For zig-zag (arm-chair) edged ribbon there are 2 (4) such H atoms in the unit cell. We built up the nanoribbons of increasing width by adding rows of atoms along the lateral dimension of the ribbon. At each stage, two rows were added which amounts to one unit cell (u.c.). Considering the graphene nanoribbon with smallest width which consists of two rows of atoms, the energy of the H-passivated system is given by

$$E_{2row} = 4C_{iso} + 7E_{b1}(\mathrm{CC}) + 2H_{iso} + 2E_b(\mathrm{CH}) \tag{2.152}$$

where $E_{b1}(\mathrm{CC})$ is the CC bond energies of the carbon atoms belonging to the smallest possible nanoribbon. From knowledge of DFT energies for E_{2row}, C_{iso}, H_{iso}, $E_b(\mathrm{CH})$, the bond energy $E_{b1}(\mathrm{CC})$ is estimated. Adding two additional rows of carbon atoms lead to the energy given by,

$$E_{4row} = 8C_{iso} + 8E_{b1}(\mathrm{CC}) + 7E_{b2}(\mathrm{CC}) + 2H_{iso} + 2E_b(\mathrm{CH}) \tag{2.153}$$

Inputting the estimate of $E_{b1}(\mathrm{CC}$ obtained from previous calculation of E_{2row} gives the estimate of $E_{b2}(\mathrm{CC})$ which is the CC bond energies of the carbon atoms immediately adjacent to rows belonging to the edges. This process is continued to extract the row-dependent bond energies in the nanoribbon geometry. The bond energies for each of the dimers in an infinite sheet and nanoribbons are tabulated in Table 6.3.

Chapter 3

Thermoelectric transport properties of monolayer (MLG) and bilayer graphene (BLG)[1]

3.1 Introduction

The experimental works carried out by various groups such as Kim $et\ al$ [8], Geim $et\ al$[172], Ong $et\ al$ [173], Nam $et\ al$ [174] and Wang $et\ al$ [60] on gate-dependent electron transport properties of MLG and BLG have motivated us to carry out computational studies based on first-principles calculations of MLG-doped hexagonal boron nitride (h-BN) and pure BLG under the influence of an electric field, since there is a direct correspondence between gate voltage and chemical potential. It is observed that S is strongly dependent on the amount of doping in the case of MLG. A marked increase of S is observed when an electric field is applied perpendicularly to the plane of the bilayer graphene sheets.

A further motivation to study the effects of impurity scattering on graphene sheets was provided by a recent paper by Ghahari $et\ al$ [175], which reported

[1]Based on publications by **R D'Souza**, S Mukherjee, Physical Review B **95**, 085435 (2017) & *Enhancement of thermoelectric figure-of-merit of Graphene upon BN-doping and sample length reduction (Manuscript submitted),* ***R D'Souza****, S Mukherjee.*

an enhanced Seebeck coefficient in graphene due to scattering. We have used a tight-binding model for graphene with impurities and solved the Boltzmann transport equations for electrons to study the effect of impurities on electrical conductance. Our study used a large k mesh to capture correctly the enhancement of the Seebeck coefficient and a constant decrease in electrical conductivity due to doping and decrease in mobility by an order of magnitude as observed experimentally [175, 70, 7].

Further, we have reexamined the lattice thermal conductivity in MLG and BLG using the lattice Boltzmann transport method [152] employing the phonon bandstructure calculated from first-principles DFT [139]. Our calculated phonon dispersion agrees with previous results [176, 158, 177, 178, 179], whereas the lattice thermal conductivity shows quantitative agreement with recent experimental data [23].

Allen [180] has shown that the Callaway method underestimates the suppression of the normal processes and has proposed an improved method [180] which has been compared with the earlier iterative method for various materials [181]. However, this has been done only for three dimensional materials. There have also been studies on the length dependence thermal conductivity of single layer graphene using either a Monte Carlo simulation with a quadratic and linear fit to the acoustic phonon modes [182] or the improved Callaway model [183, 184].

In all of these calculations, none of the relaxation times were calculated beyond the relaxation time approximation (RTA) using an iterative method. All length dependence calculations were done at room temperature. Moreover, those calculations do not take the symmetry of the sample into account.

Studies using density functional perturbation theory (DFPT) to calculate the thermal conductivity by solving the BTE exactly have been reported for graphene [185], bilayer graphene [186], and, B and N doped graphene [187]. For example, Fugallo *et al.*[186] have solved the BTE exactly for MLG and BLG using phonon-phonon scattering rates derived from DFPT. Their calculations concentrate on the collective phonon excitations in comparison to the single phonon excitations. Our calculations, on the other hand, deal with solving the BTE beyond the RTA for each acoustic mode at various lengths and temperatures. The temperature dependent behavior of each acoustic mode using the iterative

method has been demonstrated by Lindsay *et. al* [185] only for MLG.

Earlier theoretical calculations on mode dependent lattice thermal conductivity for BLG have used the Tersoff potential [188] and hence a first-principle calculation showing the length, temperature dependence of the lattice thermal conductivity is of great importance. Concentration dependent lattice thermal conductivity for B and N doped graphene calculations suggest a decrease in lattice thermal conductivity [187], a feature similar to what is seen in our calculations. Reproducing these previously reported results for graphene justifies our predictions for the temperature dependent lattice thermal conductivity for BLG. Merging the lattice thermal conductivity calculations, which are in good agreement with previous theoretical and experimental data, with the calculations of the electrical transport parameters ensure that our calculated figure of merit is accurate for MLG, BLG, and BN doped MLG.

Here we provide an analytical solution using the Callaway-Klemens method using a quadratic fit to the out-of-plane ZA and linear fit to the in-plane LA and TA acoustic phonon dispersion, respectively, and show that the results are in perfect agreement with experiments for MLG at room temperature only. The Callaway-Klemen method overestimates κ_L at lower temperatures for MLG and overestimates κ_L at all temperatures and lengths for BLG when compared to experimental measurements. This motivated the present study on the thermal conductivity by calculating the scattering rates for each acoustic mode beyond the RTA using the first-principles iterative ShengBTE [152] method for MLG and BLG at various lengths as well as temperatures and compare our results with various experimental data. Moreover, using the scattering rates from the ShengBTE method, we also calculate the length dependent κ_L for doped MLG treating BN dimers as point defects.

Using the above accurate calculations of κ_L and our earlier calculated data [22] on S and σ for these materials, we calculate the thermoelectric figure-of-merit (ZT) of MLG and BLG and study the effect of sample length and BN-doping on ZT.

This chapter illustrates that all essential thermoelectric parameters of MLG and BLG, both for electrical and lattice thermal transport, can be accurately calculated using first-principles electronic and phonon band structure together

with the Boltzmann transport theory. Our results are in excellent agreement with available experimental data.

We demonstrate that the iterative ShengBTE method gives accurate results of κ_L and its dependence on sample length for both MLG and BLG without any fitting parameters in quantitative agreement with experimental data. We have also found κ_L to decrease ($\sim 70\%$) for MLG upon BN-doping. This leads to nearly ten fold increase in the thermoelectric figure-of-merit (ZT) upon BN-doping and decrease in sample length.

3.2 Computational details

Density functional theory based electronic structure calculation

All electronic structure calculations were carried out using the density functional theory (DFT) based plane-wave method, described in Section 2.1, as implemented in the Quantum Espresso code [139]. A hexagonal unit cell has been used in all these calculations. For the exchange-correlation potential, we use the generalized gradient approximation (GGA) [128] and the core electrons were represented by the ultrasoft pseudopotential [17]. Monkhorst–Pack k-point grids [133] of $120 \times 120 \times 1$ and $70 \times 70 \times 4$ were implemented for monolayer and bilayer graphene in the self-consistent calculations with a 40Ry kinetic energy cutoff and a 160Ry charge density energy cutoff, respectively. The Kohn-Sham equations are solved self-consistently to achieve an accuracy of 10^{-9} Ry in the total energy. Plane-wave methods incorporate periodicity and hence in order to avoid interaction between sheets we have a vacuum spacing of 22Å along the z direction. The van der Waals interaction was included for multilayered systems.

Boltzmann transport theory for band electrons

The semiclassical Boltzmann transport theory (BTE), as described in section2.3.2, applied to band electrons, as implemented in the Boltztrap code [31], was used to calculate the transport properties. The BTE allows us to calculate the thermoelectric parameters along two orthogonal principal axes in the plane of the two-dimensional graphene layers. Thus the calculated thermoelectric parameters are taken as average over those along the principal directions. The energies and their corresponding k-points were taken from the electronic structure calculations

to deduce various transport parameters.

Transport properties from tight-binding method

In order to study the effect of dilute impurities in graphene on its electrical conductivity, we have used a tight-binding (TB) model of graphene using the method described in [189] (See Appendix A) for MLG and [9] for BLG. Thermo-electrical parameters are then calculated from the Boltzmann transport equations described above. The TB model allows us to calculate using a very large unit cell containing hundred atoms or more with k pont grids of $120 \times 120 \times 1$ for MLG and $70 \times 70 \times 4$ for BLG, not accessible by the DFT-based plane wave methods.

Lattice thermal conductivity from BTE

We have used the phonon Boltzmann transport method, as described in section 2.3.3 to solve the Boltzmann transport equations for phonons starting from a set of interatomic force constants (IFCs) obtained from the phonon dispersion obtained using *ab initio* calculations [139], as implemented in the ShengBTE code [152]. Lattice thermal conductivity calculations require the harmonic second-order interatomic force constants (IFCs) as well as the anharmonic third-order IFCs. The harmonic IFCs were calculated using density functional perturbation theory. To attain the anharmonic IFCs, we use a real-space supercell approach. The phonon Boltzmann transport calculates the converged set of phonon scattering rates and uses them to obtain the lattice thermal conductivity κ_L using the expression shown in 2.100.

Lattice thermal conductivity calculations for MLG and BLG using ShengBTE method, having two and four atoms in its unit cell, using third nearest neighbor interactions for a $4 \times 4 \times 2$ supercell, yields 72 and 156 displaced supercell configurations, respectively. From a set of third order derivatives of energy, calculated by implementing the plane-wave method on these displaced supercell configurations, the third-order anharmonics IFCs are constructed. The number of such configurations increase exponentially with increase in number of atoms in the unit cell.

3.3 Results and Discussion

3.3.1 Electron transport coefficients of MLG and BLG

3.3.1.1 Electrical conductivity and Seebeck coefficient of MLG

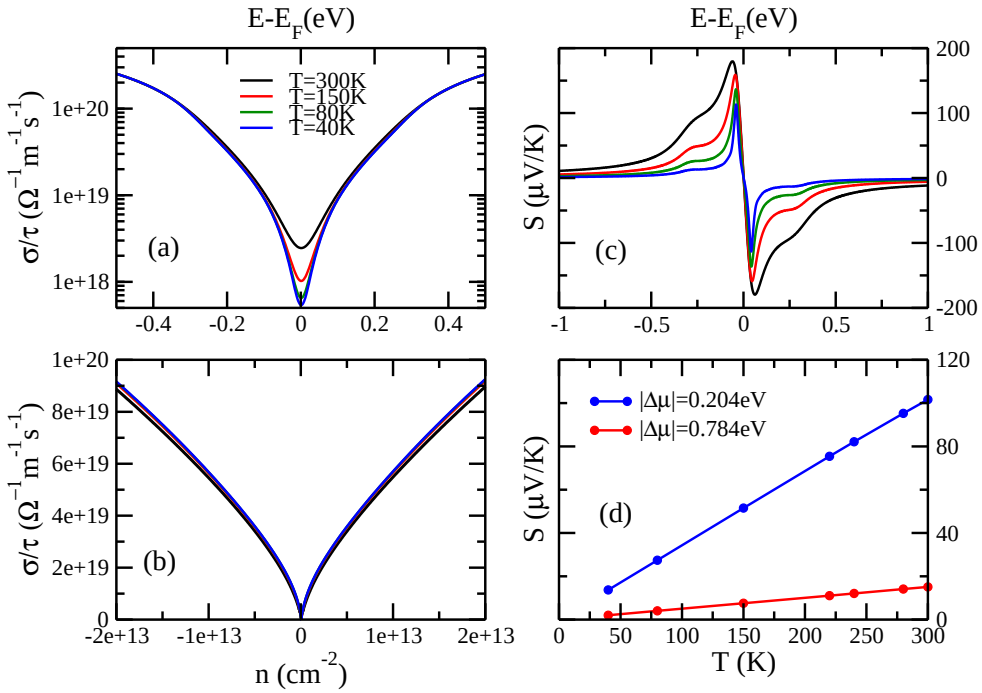

Figure 3.1: (a) Scaled electrical conductivity (σ/τ) as a function of energy at different temperatures, (b) σ/τ as a function of charge carriers n at different T, (c) Seebeck coefficient(S) as a function of energy at different T and (d) S as a function of T at two values of μ.

The calculated lattice constants for both MLG and BLG were 2.47 Å using GGA and 2.46 Å using LDA, respectively. The interlayer separation for BLG was found to be 3.32 Å.

As the precise numerical value of the electron relaxation time τ for graphene is not known and can only be estimated from experiments [7], we show in Figs. 3.1(a,b) the scaled electrical conductivity σ/τ, calculated from the Bolzmann transport theory (Eq. 2.88), as a function of energy and carrier concentration in the temperature range 40K$-$300K, respectively. It is observed that close to the Fermi energy ϵ_F, σ increases with increasing temperature but is almost independent of T away from Fermi energy. This behavior has been reported by Morozov *et al.* [6]. In Fig. 3.1(b) we observe σ of MLG to be proportional to $\sqrt{n}$ where n is the charge carrier density.

This $\sqrt{n}$ behavior can be explained using a tight-binding model with an energy expansion around the k point to get $\epsilon_F = \hbar v_F k_F$, where $\hbar$ is the reduced Planck constant, v_F is the Fermi velocity and k_F is the Fermi wavenumber. For a 2-dimensional sample,

$$n = \frac{k_F^2}{\pi} = \frac{\epsilon_F^2}{\pi(\hbar v_F)^2} \tag{3.1}$$

Therefore the MLG's density of states $D(\epsilon_F)$ is given by,

$$D(\epsilon_F) = \frac{dn}{d\epsilon} = \frac{2\sqrt{n}}{\hbar v_F \sqrt{\pi}} \tag{3.2}$$

Substituting this in the Einstein relation $\sigma \propto D(\epsilon_F)$, we obtain $\sigma \propto \sqrt{n}$. This behavior has been experimentally confirmed for pristine graphene [5].

The Seebeck coefficient was calculated using the Mott relation Eq. 2.93 numerically and is plotted in Fig. 3.1(c) as a function of energy. Our calculated form of S is in very good agreement with the experimental results reported by Zuev $et\ al$ [8]. Using a back-gated field effect transistor, the Fermi energy can be tuned by adjusting the gate voltage. Zuev $et\ al$ [8] have used this method for a mesoscopic graphene sample using the formula $S = -\frac{\pi^2 k_B^2 T}{3e}\frac{1}{\sigma}\frac{d\sigma}{dV_g}\frac{dV_g}{dE}|_{E=E_f}$. It can be easily seen that this is identical to Eq. 2.93. Therefore there is a direct correspondence between the gate voltage and the chemical potential. In Fig. 3.1(d) we plot S against T for two different values of chemical potential. The linear dependence of S on T, which has also been reported by experimental measurements by Zuev $et\ al.$ [8], suggests that the mechanism of thermoelectric transport is diffusive [190].

3.3.1.2 Resistivity and fit to the Bloch-Grüneisen form

In Fig. 3.2 we plot ρ as a function of T calculated from the Boltzmann transport equations for electron transport. The electron relaxation time τ of graphene depends on the degree of doping and carrier concentration as indicated by experimental measurements [7] and can vary in the range 10 fs to 1 ps. For simplicity we have assumed $\tau \sim 1\times10^{-14}$ s; however, our temperature dependent behaviour of ρ should not depend on the choice of τ. The behaviour of ρ at certain values of μ having the Bloch-Grüneisen form has been observed experimentally

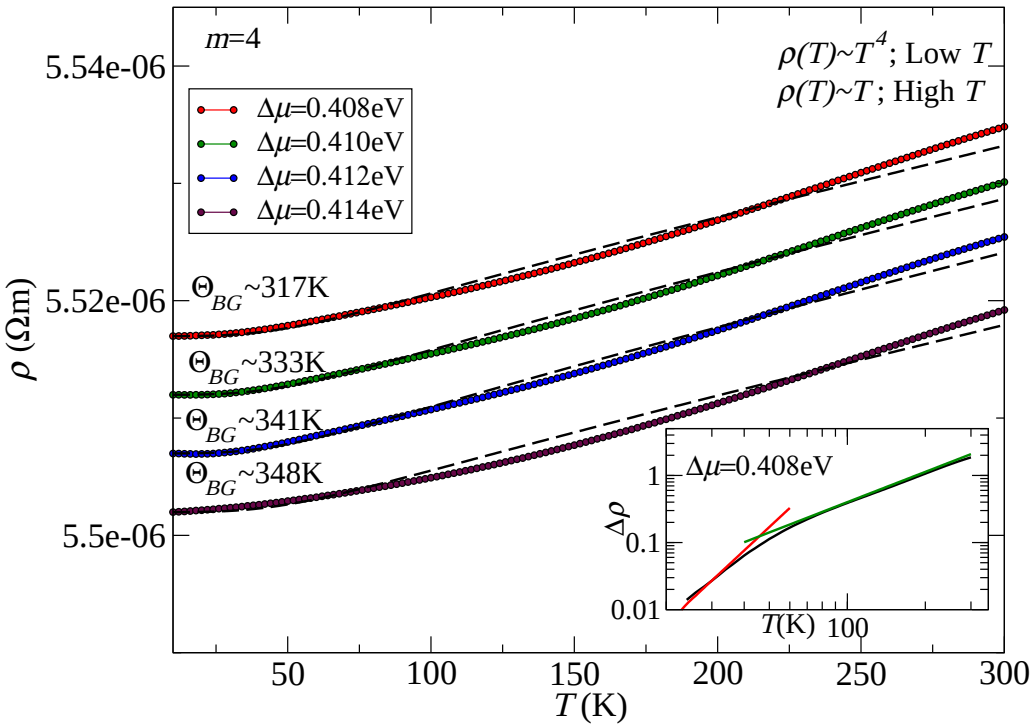

Figure 3.2: Calculated resistivity ρ as a function of T for MLG at different chemical potential. Dashed black lines are the best fit of the Bloch-Grüneisen formula. Points refer to our calculated values of ρ from the Boltzmann transport equations, assuming $\tau = 1 \times 10^{-14}$ s. Inset: $\Delta\rho$ plotted against T in logarithmic scale to highlight the T^4 and T features. The red and green lines are equations of $\propto T^4$ and $\propto T$. The curves referring to different $\Delta\mu$ are shifted slightly along the y axis for clarity.

[10, 5]. In order to understand the behaviour, we fit our calculated values of ρ to the Bloch-Grüneisen formula [191],

$$\rho(T) = \rho(0) + A\left(\frac{T}{\Theta_{BG}}\right)^m \int_0^{\frac{\Theta_{BG}}{T}} \frac{x^m}{(e^x - 1)(1 - e^{-x})} dx \tag{3.3}$$

with m and T as fitting parameters. Our best fit resulted in $m = 4$ and Θ_{BG} as shown in Fig. 3.2. This suggests that in the low-T regime, resistivity scales as T^4 and smoothly scales to a linear T behavior at higher T regimes. The T^4 behavior of resistivity reflects the two-dimensional nature of electrons in graphene. At high temperatures the quantization of lattice waves is irrelevant; therefore the scattering is proportional to the square of the amplitude of the fluctuations about their equilibrium position that is proportional to $\sqrt{T}$, which leads to the linear behavior of resistivity at higher temperatures. The reduction from the T^5 behavior of the resistivity for a typical bulk metal to the T^4 one, as seen in graphene, is due to reduced electron Fermi surface of graphene, smaller than the size of its phonon Brillouin zone. Therefore, only a small fraction of acoustic phonons will scatter off the electrons. An excellent illustration and

explanation of the high, low and Bloch-Grüneisen temperature regimes, by taking into account different sizes of the Fermi surface of graphene and a conventional metal at different temperatures, was given by Fuhrer [192].

As mentioned previously, Θ_{BG} is defined as $\Theta_{BG} = \frac{2v_{ph}k_F}{k_B}$, where v_{ph} is the phonon velocity. However when expressed as a function of carrier concentration, it can be easily shown [193] to have the form $\Theta_{BG} = A_0\sqrt{n}\,\mathrm{K}$, with carrier concentration measured in $10^{12}\mathrm{cm}^{-2}$. In our calculation, when fitted to the above form, we obtain A_0=45.5, which is close to the earlier estimated value of 54 [193].

In the inset of Fig. 3.2 we plot $\Delta\rho\ (= \rho(T) - \rho(0))$ against temperature. This parameter will now show us the increase in resistivity with respect to temperature and when plotted in logarithmic scale, we can see that the increase in resistivity in the lower regime has a $\sim T^4$ feature and $\sim T$ feature at higher temperatures. The red and green lines in the inset are $\propto T^4$ and $\propto T$ equations where the constant of proportionality was found by a best fit method. Θ_{BG} is in the same order of magnitude range as reported by [10]. We must note that this behavior of ρ is found only for a certain range of chemical potential. If we compare our Seebeck coefficient result to that of the experimental results by Zuev $et\ al$ [8] we find that as we vary our chemical potential from 1 eV to -1 eV, the same behaviour is found when they vary their gate voltage from 40V to -40V. This implies that a small change in the chemical potential is equivalent to a large change in gate voltage. This is the reason why we choose only a small range of chemical potentials to demonstrate the Bloch-Grüneisen behavior as observed experimentally. If one looks at the study by Kim $et\ al$ [5], the linear part of resistivity (higher T regime) increases quickly with an increase of gate voltage of only 1eV. As observed experimentally [10], we found that the slope of the ρ vs T curves in the linear-T regime increases with μ. The present study of the temperature dependent resistivity, which has been theoretically predicted [73] and experimental observed [10], is here done using the Boltzmann transport theory applied to band electrons.

3.3.2 Impurity scattering in graphene

Increasing the Seebeck (S) coefficient of low-dimensional materials such as graphene has always been a pursuit in thermoelectric applications. Enhancement of S by inelastic scattering has been reported recently by Ghahari $et\ al$ [175]. Experimental electrical conductivity studies of graphene doped with potassium as a function of charge carrier has been reported by Chen $et\ al$ [70]. From Mott's formula Eq. 2.93, it can be readily seen that a decrease in electrical conductivity will enhance the Seebeck coefficient. As pointed in the previous section doping of boron nitride decreases the electrical conductivity and hence increases S. The unit cells used in those calculations are relatively small to mimic the experimental behavior of doping since there is no long-range nature of charge-impurity scattering. In order to understand the behavior of electrical conductivity as reported by Chen $et\ al$ [70] one would require a long range nature of impurity scattering and hence a large simulation cell making first-principles (DFT) calculations extremely hard.

As only the π states are responsible for transport in MLG and BLG [194], a tight-binding band calculation would be more useful since it would allow incorporation of a very large unit cell to account for the long-range nature of the impurity scattering. In this section we report the calculation of electrical conductivity of graphene with impurities with the help of the tight-binding method.The tight-binding model has the potential of modeling several impurity properties and is described by Pedersen *et al.* [195] (See Appendix A).

In this model, we consider an infinite graphene sheet but with one or more atoms replaced by an impurity representing the graphitic impurities. Since we are interested only in the transport properties, our Hamiltonian states would consist only of the p_z π states. The Hamiltonian would then be written as

$$H = H_0 + H_{imp} \tag{3.4}$$

with H_0 defined as

$$H_0 = \sum_i \epsilon |i\rangle\langle i| - \sum_{i,j} t_{ij} |i\rangle\langle j| \tag{3.5}$$

where ϵ is the on-site energy of carbon, and t_{ij} is the hopping integral which is described by H_0 between the p_z π states on site i and j. The added H_{imp} is the

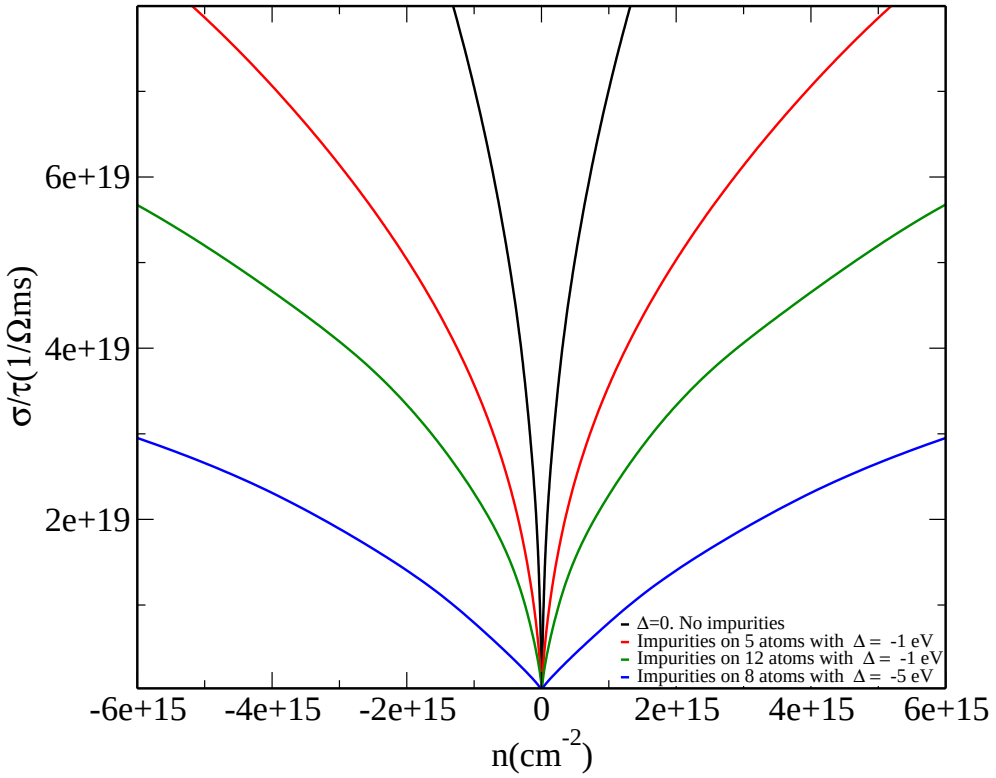

Figure 3.3: Plot of scaled electrical conductivity (σ/τ) of graphitic impurities with a supercell of 98 atoms and a K mesh of 150×150×1 with different values of Δ and different number of atoms replaced with an impurity.

impurity Hamiltonian. It depends on which site an atom has been replaced by an impurity and takes the form

$$H_{imp} = \Delta \sum_i |i\rangle\langle i| \tag{3.6}$$

where Δ is the increase or decrease of the on site energy on site i. It must be noted that the difference between H_{imp} and the first term of H_0 is that the summation in H_{imp} runs over those sites where an atom has been replaced by an impurity whereas in the first term of H_0 it runs over all available sites. From Fig. 3.3 it can be seen that the behavior of electrical conductivity when plotted against charge carrier is that which is observed experimentally [70] for doped systems. Larger values of Δ for the same number of atoms replaced by an impurity decreases the electrical conductivity and hence from Eq. 2.93 would increase the Seebeck coefficient. One can also see the behavior for electrical conductivity on pristine graphene ($\sigma \sim \sqrt{n}$) tending to the linear behaviour of electrical conductivity ($\sigma \sim n$) for graphene sheets with impurities, a fact that has be observed experimentally [5].

3.3.2.1 Mobility (μ_{FE}) of doped and undoped MLG

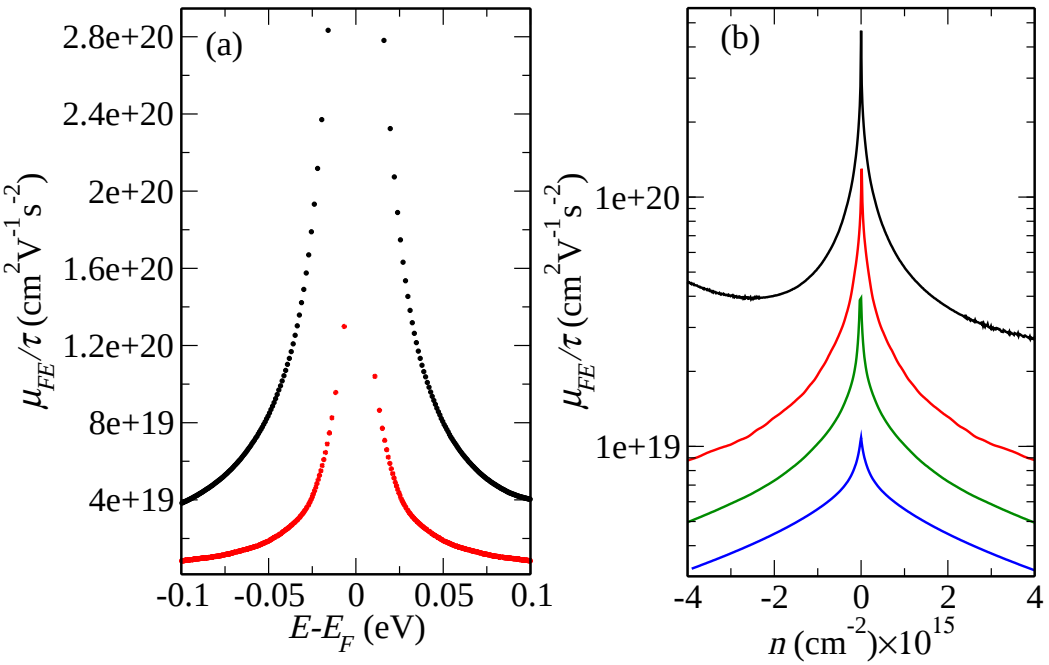

Figure 3.4: (a) Calculated scaled mobility (μ_{FE}/τ) as a function of energy, and (b) as a function of carrier concentration. The black curves are the results for pristine graphene using DFT and Boltzmann transport equations. The red, blue, and green curves refer to results using the tight-binding model. The red curves refer to the results for graphene with impurity, where the onsite energy of one atom in the unit cell is decreased by 1 eV, whereas the green and blue curves refer to those where the on-site energies of 2 and 4 atoms are decreased by 1 eV, respectively.

In Fig.3.4(a,b) we show the scaled mobility (μ_{FE}/τ) of MLG as function of energy and carrier concentration n, calculated from the Boltzmann transport equations, showing similar trends as to those seen in experiments by tuning the gate voltage and carrier concentration [172, 175], respectively. We have calculated μ_{FE} using,

$$\mu_{FE} = \frac{1}{e}\frac{d\sigma}{dn} \tag{3.7}$$

It is easy to understand the behavior of μ_{EF} since the derivative of electrical conductivity with respect to n should be proportional to $\frac{1}{\sqrt{n}}$. This behavior has been reported by Ponomarenko *et al.* [172]. The method used to introduce impurities is discussed in detail in the previous section. Experimental data [7, 70] for graphene samples with increasing doping concentrations have been shown to reduce its mobility by an order of magnitude. This effect can be seen in Fig. 3.4(b), where variation of μ_{FE}/τ is shown as a function of carrier concentration n plotted in logarithmic scale. Our results on mobility show similar behavior to that observed experimentally [172, 175].

Expressing mobility in units of $\tilde{n} = \frac{n}{10^{10}}$ cm^{-2} and $\tilde{\sigma} = \frac{\sigma}{h/e^2}$ kΩ^{-1}, and assuming the electron relaxation time $\tau \sim 1 \times 10^{-14}$s, our calculations result in a value of $\mu_{FE} \approx 1.6 \times 10^4 \frac{\tilde{\sigma}}{\tilde{n}}$ [cm^2/Vs] which is close to the earlier estimate of $\mu_{FE} \approx 2.42 \times 10^4 \frac{\tilde{\sigma}}{\tilde{n}}$ [cm^2/Vs] [193].

3.3.3 Enchancement of Seebeck coefficient

3.3.3.1 Enchancement of Seebeck coefficient in MLG upon doping with BN dimers

As mentioned previously, the performance of a thermoelectric material is measured by a dimensionless parameter, the figure of merit($ZT = \frac{S^2\sigma}{\kappa}$). Hence a technique to increase the Seebeck coefficient and simultaneously decrease the thermal conductivity is highly desired. Very recent studies [196, 197] have shown that doping of and impurities in graphene sheets will decrease the thermal conductivity. Pop $et\ al.$ [198] have mentioned that any surplus residue from sample fabrication or any form of disorder will reduce the thermal conductivity further. There have been many experimental [86, 87, 88, 89, 90, 91] and theoretical [30, 199, 200] reports to show the formation of a band gap by doping graphene with boron nitride. Similarly there are reports to show the formation of band gaps in bilayer graphene [201, 202, 203] when under the influence of an electric field. We have successfully used the Boltzmann transport equation for electron transport to calculate the thermoelectric parameter of $C_{2x}(BN)_{1-x}$ [200] and graphene/h-BN/graphene heterostructures [204]. Therefore in this section, using the Boltzmann transport equations, we study the behavior of these transport parameters focusing mainly on enhancing the Seebeck coefficient.

In Fig. 3.5 we show the calculated electrical conductivity (σ) and the Seebeck coefficient (S) for MLG upon doping by BN. To study the behaviour of doped graphene, we have substituted one and two dimers of boron and nitrogen in our graphene unit cell as shown in Fig. 3.5. Since boron is an acceptor and nitrogen is a donor, the total number of charge carriers remains unchanged, leading to a gap at the Fermi energy [80, 200]. This band gap transforms the metal to a semiconductor, thereby decreasing the electrical conductivity as shown in Fig. 3.5 (a) and (c). The inverse dependence of the electrical conductivity term in Eq.

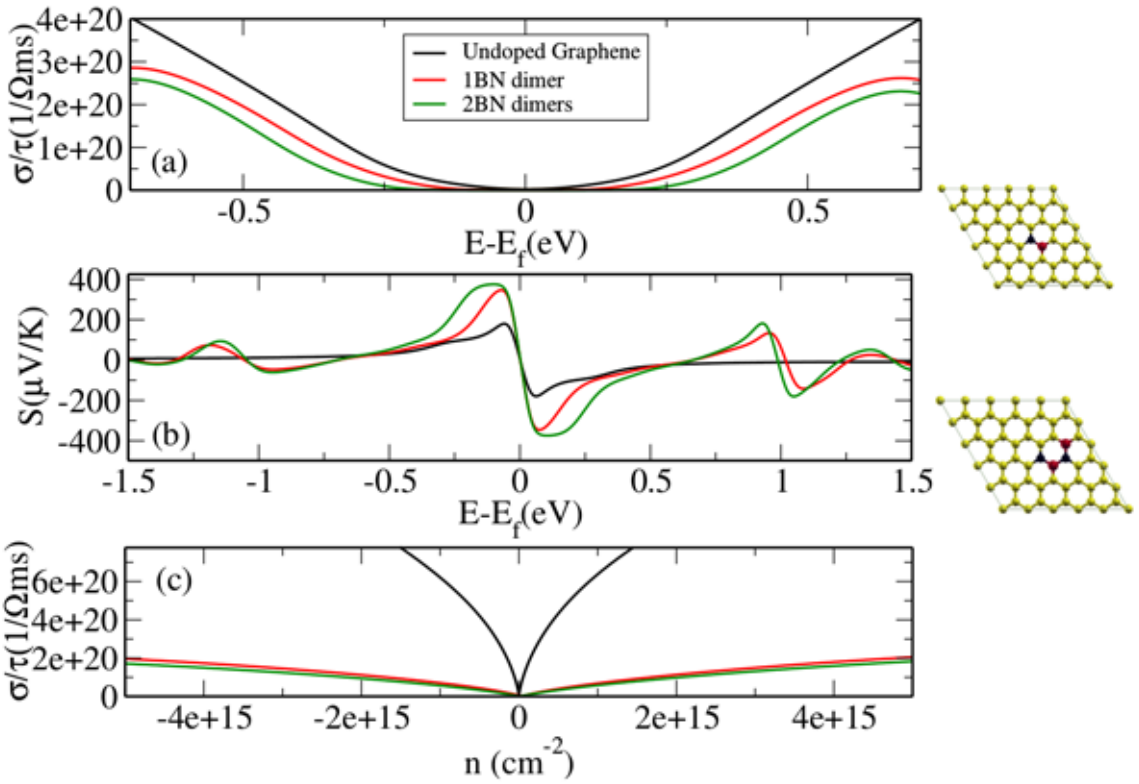

Figure 3.5: (a) σ/τ plotted as a function of energy. (b) Seebeck coefficient plotted as a function of energy. (c) σ/τ plotted as a function of n. The graphene supercell containing one and two BN dimer are shown on the right.

2.93 increases the Seebeck coefficient. This is evident in Fig. 3.5(b). We can therefore predict that doping graphene with boron and nitrogen will increase the Seebeck coefficient.

3.3.3.2 Enhancement of Seebeck coefficient in presence of an electric field

Since a band gap decreases the electrical conductivity thus increasing the Seebeck coefficient, we apply an electric field perpendicularly to the monolayer graphene sheets. BLG in an electric field has been shown to have a band gap [201]. We have thus considered the effect of an electric field for three different values of external potential (U), i.e., U=0.2, 0.3, 0.5 eV. The averaged Coulomb potential plotted as a function of its perpendicular length (z), is shown in Fig. 3.6(a). In Fig. 3.6(b) we plot the Seebeck coefficient of BLG under the influence of an electric field, showing that an increase in the external potential results in an increase in S.

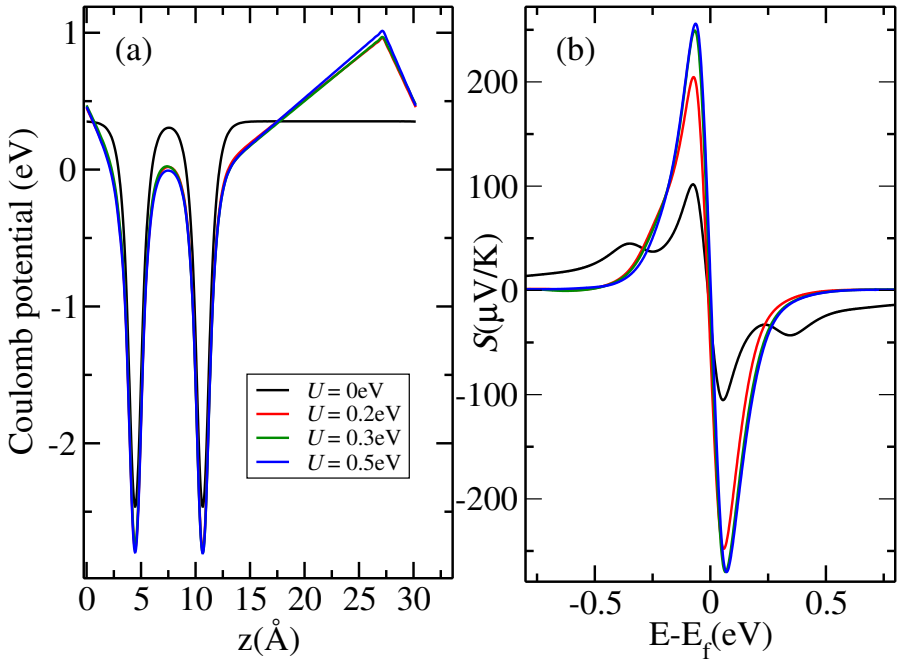

Figure 3.6: (a) Average Coulomb potential plotted as a function of z for different electric fields U, (b) S plotted as a function of energy. Differently colored curves refer to different U as in (a).

Experimentally the effect of electric field on S for BLG has been studied by Wang *et al.* [60], showing enhancement of S with increasing electric field as our calculations indicate.

3.3.4 Lattice thermal conductivity of MLG and BLG

3.3.4.1 Phonon dispersion

In Fig. 3.7 we show our calculated phonon band structure along the high-symmetric points in the irreducible hexagonal Brillouin zone (BZ) for the monolayer and bilayer graphene. Accurate calculation of phonon dispersion of MLG and BLG is necessary to understand the thermal conduction in these materials. Based on the harmonic second-order IFCs, we calculate the phonon dispersion of MLG and BLG along high-symmetric q points obtained within the linear response framework by employing density functional perturbation theory (DFPT) [138], as implemented in the Quantum Espresso code [139] described earlier.

The out-of-plane (ZA), in-plane longitudinal (LA), and in-plane transverse (TA) modes, which arise from the Γ point of the BZ of MLG, correspond to the acoustic mode while the remaining branches correspond to the optical modes (ZO, LO and TO) [205]. The TA and LA modes show linear q dependence

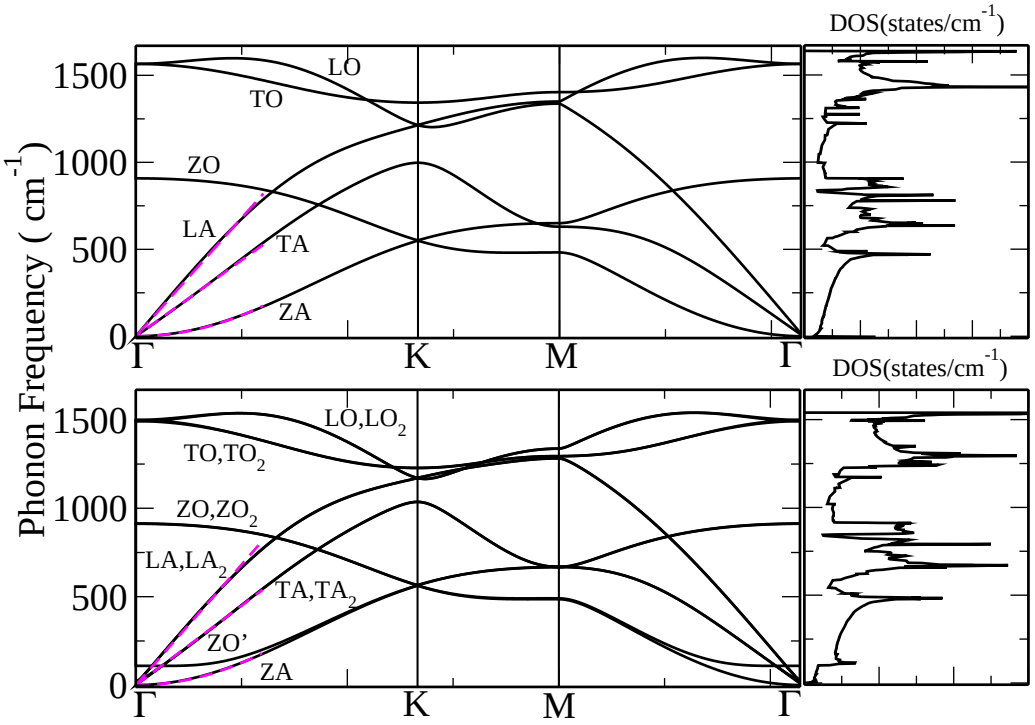

Figure 3.7: Calculated phonon dispersion and phonon density of states of MLG (above) and BLG (below) along the high symmetry points of the 2D hexagonal Brillouin zone. The magenta dashed lines are the best linear and quadratic fit to the in-plane and out-of-plane wave dependent fit to the phonon dispersion.

at low q, as is usually seen for acoustic modes. The out-of-plane ZA mode shows a quadratic (q^2) dependence, which is a distinctive feature of layered crystals as observed experimentally [206, 207]. An explanation of this quadratic dependence could be due to the two-dimensional out-of-plane phonon mode and threefold rotational symmetry for BLG (sixfold for MLG) [189]. The LO and TO modes are degenerate at Γ having a frequency of 1580 cm^{-1}. Our calculated value of the degenerate frequency is in good agreement with the result using inelastic x-ray scattering measurements by Maultzsch $et\ al.$ [179] having a value of 1587 cm^{-1}. High-voltage transport measurements by Yao $et\ al$ [178] estimated that for graphite the frequency of zone-boundary phonons should be around 1300 cm^{-1}. Our calculations show that at K, the BZ corner, the phonon energy of the in-plane transverse optical (TO) mode has a frequency of 1370 cm^{-1} for MLG and 1287 cm^{-1} for BLG. This suggests that our calculations agree well with the experiment. The phonon dispersion of BLG is very similar to that of MLG except for a characteristic feature of an additional low-frequency optical mode with energy nearly about 108 cm^{-1} at Γ. This layer breathing mode arises due to the interlayer movements. The phonon dispersions shown in Fig.

3.7, calculated using harmonic IFCs, are consistent with both experimental and previous theoretical studies [176, 158, 177, 178, 179].

3.3.4.2 Grüneisen parameter (γ)

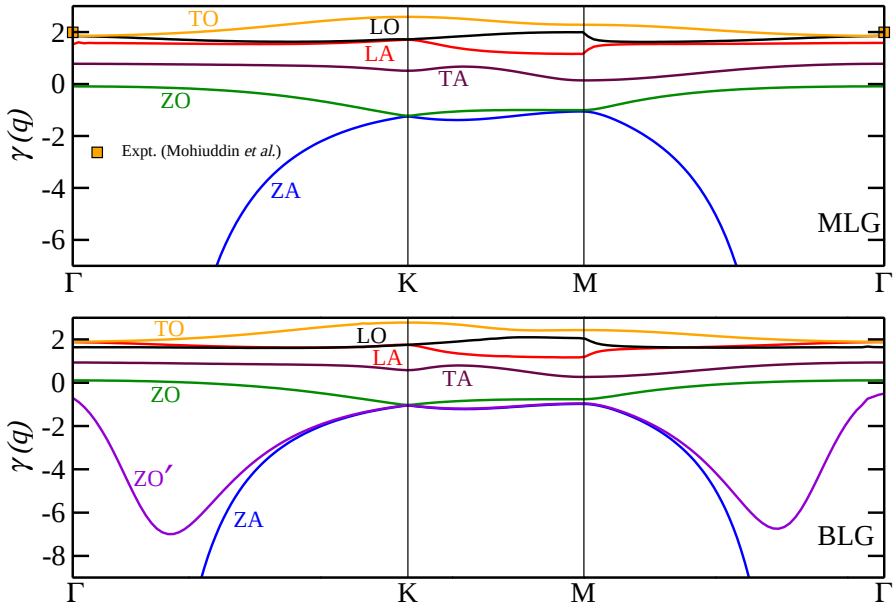

Figure 3.8: Mode-dependent Grüneisen parameters for MLG (top) and BLG (below) along the high-symmetric q points in the first Brillouin zone, calculated from the first-principles phonon dispersion. The experimental data for MLG corresponding to TO phonons at the Γ point are taken from Mohiuddin *et al* [19].

To carry out a precise calculation of the lattice thermal conductivity, effects from the harmonic and anharmonic lattice displacements should be taken into account to include contributions of higher order phonon-phonon scattering processes [208]. Since the Grüniesen parameter (γ) provides useful information on the phonon relaxation time and the anharmonic interactions between lattice waves and the degree of phonon scattering, we have therefore calculated the mode-dependent Grüneisen parameter (γ) for MLG and BLG. We employ the method as developed previously [177, 209, 206] to calculate the degree of phonon scattering. It is carried out by dilating the lattice applying a biaxial strain of $\pm 0.5\%$. In Fig. 3.8 we show the calculated mode-dependent Grüneisen parameter along the high-symmetric q points. γ is defined in Eq. 2.114, where a_0 is the relaxed lattice constant without strain, ω is the phonon frequency, ω_+ and ω_- are the phonon frequencies under positive and negative biaxial strain, respectively, and da is the difference in the lattice constant when the system is under positive and negative biaxial strain.

MLG and BLG both have negative values for γ along the high-symmetric q points for the out-of-plane acoustic (ZA) and optical (ZO and ZO') modes while γ has only positive values for the in-plane longitudinal and transverse modes. Negative (positive) γ implies an increase (decrease) in phonon frequency when the lattice constant is increased. The slight difference in the Grüneisen parameters in MLG and BLG is, in the case of BLG near the long-wavelength limit (Γ point), γ_{ZO} corresponding to the out-of-plane optical mode changing sign unlike in MLG. This suggests that near the long-wavelength limit the atom vibrations perpendicular to the plane of the sheet between the two layers lose their coherence hence decreasing the phonon frequencies of ω_{ZO} when under a biaxial strain. Since the TO mode in graphene is Raman active at the Γ point, the Grüneisen parameter can be measured experimentally using Raman spectroscopy. Mohiuddin *et al* [19] have measured $\gamma_{E_{2g}}$ to be 1.99, which is in excellent agreement with our calculated value of $\gamma_{TO} = 1.85$ ($\gamma_{TO} = 1.89$) for MLG (BLG). In Table 3.1 we show the phonon frequencies and the Grüneisen parameters of MLG and BLG at high-symmetric q points Γ, K, and M for different vibrational modes.

Table 3.1: Calculated phonon frequency ω (in cm^{-1}) and the Grüneisen parameter γ of MLG and BLG at the high-symmetric q points in the hexagonal BZ for different vibrational modes.

System	q		ZA	TA	LA	ZO	TO	LO	ZO'
MLG		ω	0	0	0	907	1580	1580	-
		γ	-100	0.779	1.848	-0.086	1.850	1.605	-
	Γ								
BLG		ω	0	0	0	915	1540	1544	108
		γ	-50	0.936	1.640	0.110	1.892	1.878	-0.498
MLG		ω	545	1000	1230	545	1370	1230	-
		γ	-1.245	0.510	1.713	-1.245	2.584	1.713	-
	K								
BLG		ω	554	1046	1205	557	1287	1206	554
		γ	-1.06	0.581	1.753	-1.025	2.779	1.749	-1.049
MLG		ω	578	631	1350	645	1430	1372	-
		γ	-1.057	0.139	1.953	-1.004	2.281	1.184	-
	M								
BLG		ω	478	672	1327	660	1348	1363	485
		γ	-0.982	0.267	2.040	-0.762	2.432	1.195	-0.956

3.3.4.3 Lattice thermal conductivity using the Callaway-Klemens method

We first obtain the analytical solution of κ_L for an ideal sheet of MLG and BLG and then calculate κ_L numerically for them with defects and specularity parameter (p) with values other than one.

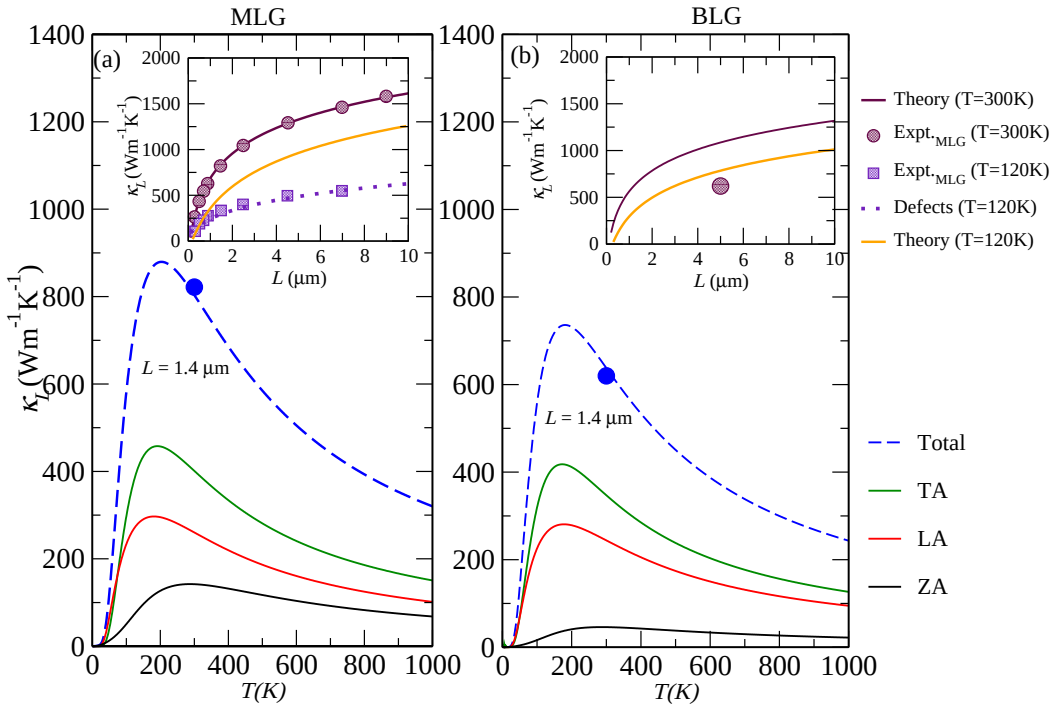

Figure 3.9: Temperature dependence of κ_L using the analytical solutions of the Callaway-Klemens method for each of the acoustic modes at a constant length for (a) MLG and (b) BLG. Inset: Length dependence of κ_L at constant temperatures, T=120K and T=300K. The maroon dotted lines are the length dependence with point defects with parameters used to fit the experimental data [20, 21].

Fig. 3.9 shows the acoustic mode dependent κ_L as a function of temperature for (a) MLG and (b) BLG at a constant length of 1.4 μm. The insets in Fig. 3.9 (a) and (b) are the length dependent κ_L at temperatures 120K and 300K. Length is defined as the direction along which the heat propagates. The fitting parameters, discussed in the previous section, used in this study are shown in table 4.2. The length dependent analytical form for κ_L for MLG at RT is in excellent agreement with a recent experiment [21]. However, our results of κ_L overestimate the experimental data at T=120K. One explanation for this could be that in the lower temperature range (0-100 K), κ_L increases rapidly and hence a small change in the temperature in this range would result into a large change in the lattice thermal conductivity, making comparison with experimental data difficult. Another possible reason could be that we have considered a sample

Table 3.2: Parameters used in the analytical solutions of the Callaway-Klemens method.

System	v_{LA} (m/s)	v_{TA} (m/s)	γ_{LA}	γ_{TA}	$\alpha \times 10^{-7}$ (m^2/s)	$\beta \times 10^{-20}$ (1/m^2)
MLG	18021.5	12968.4	1.70	0.65	5.64	-7.7
BLG	18014.3	12624.9	1.75	0.72	5.89	-7.47

with an ideal sheet without any form of defects or impurity. We find that, using a large specularity parameter of $p = 0.9$ and an extremely small value of Γ_0=0.001 of Eq. 2.121, our length dependent calculations with point defects for MLG agree with experimental measurements at T=120K.

The major difference between the thermal conductivity of MLG and BLG is due the out-of-plane ZA phonon mode. MLG has a total of twelve process involving the flexural phonons (ZA). Seol *et. al.* [210] obtained a selection rule for the three-phonon scattering rates stating that only an even number of ZA phonons is attributed to each process. The four allowed processes involving flexural phonon-modes have been listed by Shen *et. al.* [160]. Therefore, the scattering rate given by Eq. 2.108 needs to be multiplied by three for the case of MLG. Our calculations suggest that the LA and TA modes contribute maximum to the total κ_L.

3.3.4.4 Lattice thermal conductivity using the Iterative method

Figs. 3.10(a) and 3.10(b) show, in logarithmic scale, the length dependence of the contribution from each of the acoustic modes (LA,TA,ZA) to the total lattice thermal conductivity (κ_L) at temperature 300K and 120K, respectively for MLG and BLG, calculated using the iterative ShengBTE method [152]. The iterative method clearly shows that the out-of-plane acoustic ZA mode contributes the most to the total lattice thermal conductivity. At room temperature (RT) and at the thermodynamic limit, the contribution for MLG (BLG) are 79% (70%), 19% (26%) and 2% (4%) from the ZA, TA and LA modes, respectively.

We find that for BLG, ther is a $\sim$ 9% drop in κ_L as compared to that for MLG due to the ZA mode. The major difference between the phonon dispersions between MLG and BLG is the additional out-of-plane optical mode ZO$'$. Due to this additional low-frequency mode, more phase space states are now available

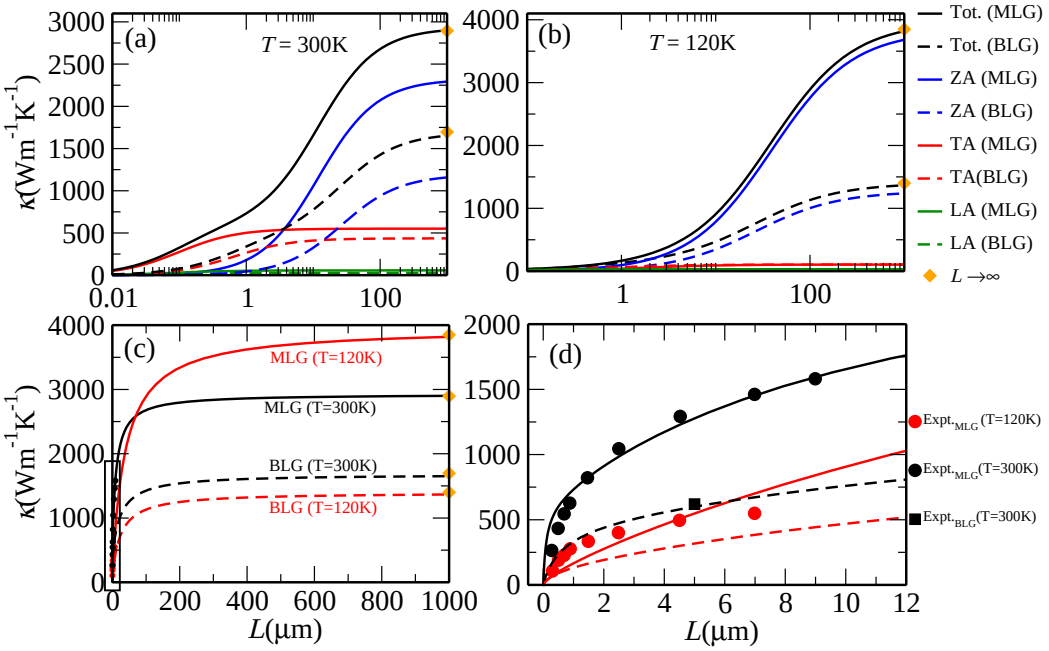

Figure 3.10: The calculated mode-dependent (κ_L) and total κ_L plotted as a function of sample-length L in logarithmic scale(a,b) and linear scale (c,d) at two temperatures, $T = 120$K and $T = 300$K. Solid(dashed) curves refer to calculation on MLG(BLG). The orange diamond points are the values of κ_L [22] at the thermodynamic limit ($L \to \infty$). (d) Zoomed box in (c) comparing our calculations with available experimental data [20, 21].

for phonon scattering and is one of the reason for the decrease in κ_L in BLG. As evident from Fig. 3.10(b), we find at small sample lengths and at lower temperatures, the mode dependent contributions to κ_L are identical for both MLG and BLG indicating that the phonon transport is ballistic and independent to the number of layers.

In Fig. 3.10(c), we plot the total κ_L as a function of sample length. Since most of the lattice thermal conductivity measurements were carried out at small sample lengths, in order to compare our calculations to experimental data, we show in Fig. 3.10(d) the zoomed data in the thin rectangular box of Fig. 3.10(c) where experimental measurements are available for the given sample length range.

The orange diamond points shown in Figs. 3.10(a), 3.10(b) and 3.10(c) are values of κ_L at the thermodynamic limit, reported previously [22], at the corresponding temperatures. The thermodynamic value of κ_L for MLG at 120K is higher than that its value at RT while reverse is case for BLG. This suggests that the temperature dependence of $\kappa_L(T)$ has a peak closer to T =120K for MLG, whereas this peak shifts to a higher value for BLG. Lindsay *el. al.* [185] have shown that the mode dependence of κ_L for MLG depends only slightly on

strain. The length dependent calculations of κ_L using first principles calculation based on DFPT [185] at RT, referring to each of the acoustic modes, for the unstrained MLG are in very good agreement with our calculations shown in Fig. 3.10(a). Our length dependent κ_L calculations are in excellent agreement with earlier theoretical calculations [186] shown in Fig. 3.10(d).

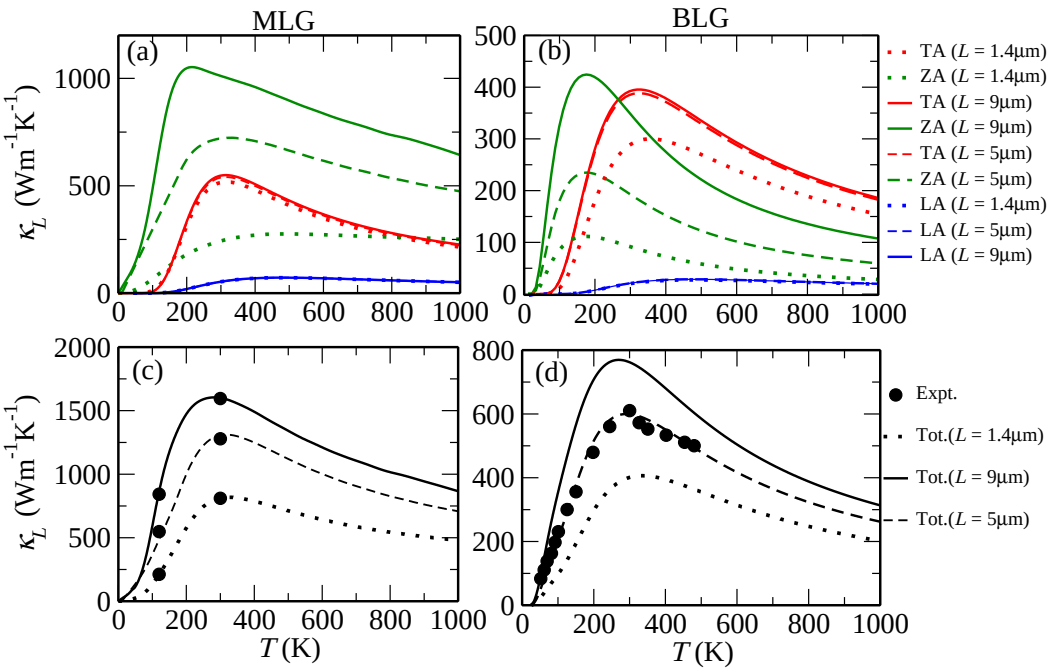

Figure 3.11: The calculated mode-dependent contributions to κ_L at three different sample lengths (a,b), and total κ_L (c,d) as a function of temperature. Black circular dots are available experimental data [20, 21].

Fig. 3.11 shows the temperature dependence of each of the acoustic modes and the total lattice thermal conductivity at three constant lengths, L=1.4 μm, 5 μm and 9 μm, calculated using the ShengBTE method [152], along with the available experimental data. The ZA out-of-plane mode is shown to be the most sensitive to length as compared to the in-plane, LA and TA modes. This suggests that the ZA phonons travel ballistically in the sheets while the TA and LA modes travel diffusively. Measurements of graphene [210] on a SiO_2 substrate show a reduction in κ_L which has been explained with a scattering model where the contributions from the out-of-plane are the most dominant, in line with our calculations.

Experimental results at the thermodynamic limit ($L \rightarrow \infty$) of κ_L at room temperature for graphite show a value of $\sim$ 2000 Wm^{-1}K^{-1} [186]. Our calculated thermodynamic limit of κ_L for BLG is $\sim$ 1700 Wm^{-1}K^{-1}. This proximity of κ_L between BLG and graphite implies that the interlayer interactions are short

ranged.

In Figs. 3.11(a) and 3.11(b), it can be seen that at low temperatures, the ZA mode is always larger than the in-plane acoustic modes (LA,TA). This behavior can be understood by considering the phonon density of states (PDOS) which is proportional the number of phonon-modes per frequency interval [185]. Using the definition of the 2D density of states, $D_s(\omega) \propto \frac{q}{2\pi}\frac{dq}{d\omega}$, one can measure the contributions from each phonon modes to the total thermal conductivity. Denoting D_o and D_i as the PDOS for the out-of-plane and in-plane modes, it can be easily shown that, assuming a quadratic ($\omega_i = \alpha q^2$) and linear ($\omega_i = v_i q$) fit to the out-of-plane and in-plane phonon modes, respectively, $\frac{D_o}{D_i} = \frac{v_i^2}{2\alpha\omega_i}$. Where, v_i, ω_i (i=LA,TA), are the fitting parameters to the phonon velocity and phonon frequency shown in Table 4.2 and is plotted in Fig. 3.7. Substituting the values from Table 4.2, it is evident that at the long wavelength limit ($q \to 1$), $\frac{D_o}{D_i} \gg 1$.

3.3.4.5 Lattice thermal conductivity of MLG and BLG at the thermodynamic limit

In the ShengBTE method [152], the third-order anharmonic interatomic force constants (IFCs) were also taken into account apart from the usual second-order harmonic IFCs which produced the phonon dispersion, in the calculations of thermal conductivity (κ_L). The third-order anharmonic IFCs were calculated using a finite-difference supercell approach with a set of displaced supercell configurations depending on the size of the system. We have used a $4 \times 4 \times 1$ supercell for both MLG and BLG, which generated 72 and 156 configurations for MLG and BLG, respectively. The three-phonon scattering amplitudes are then computed from a set of third-order derivatives of energy, calculated from these configurations using the Quantum Espresso code [139].

In Fig. 3.12 we show our calculated lattice thermal conductivity (κ_L) of MLG and BLG using Eq. 2.100 as implemented in the ShengBTE code [152]. In the inset we compare our results to experimental data of Li *et al* [23] available in the temperature range 300K to 700K. Our results are in very good agreement with experimental measurements. Graphene at room temperature (RT) has one of the highest know κ_L.

The experimental results of κ_L for MLG [211, 212, 213, 214, 215, 216] have

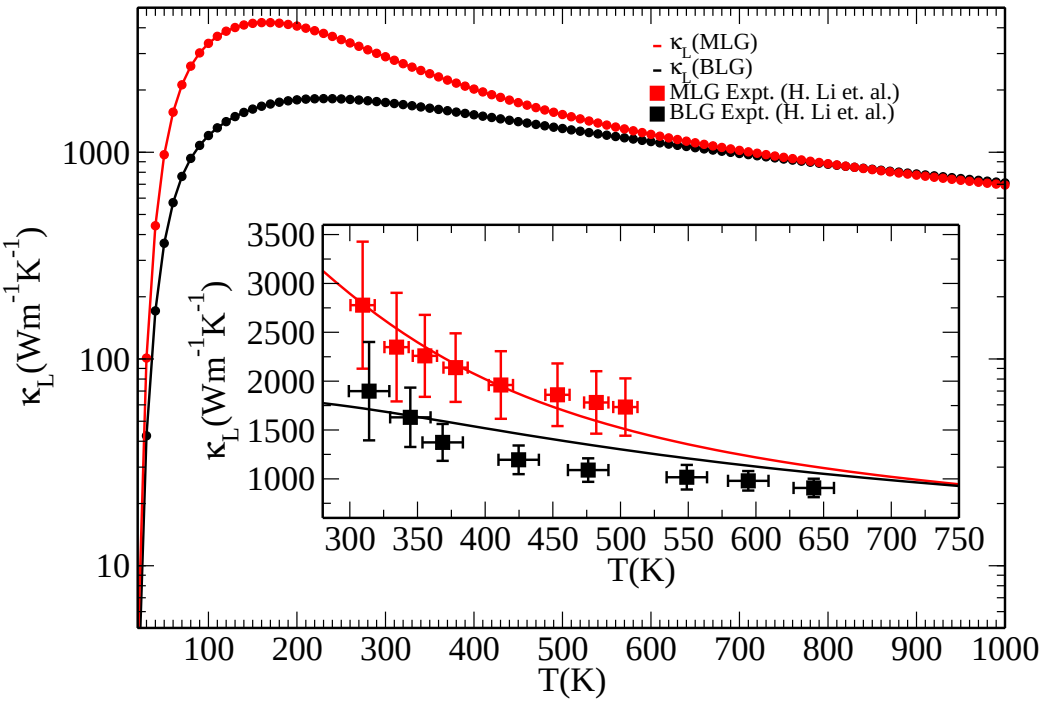

Figure 3.12: Calculated lattice thermal conductivity (κ_L) in log scale of monolayer (red) and bilayer (black) graphene in the temperature range 20 K to 1000 K. Inset: κ_L of MLG and BLG in linear scale in the temperature range 300 K to 700 K, compared with experimental results [23] shown with red and black square points, respectively.

shown that for freely suspended samples κ_L lies between 2000-5000 $Wm^{-1}K^{-1}$. This wide variation in experimental estimate of κ_L is presumably due to any disorder or residue from fabrication leading to an increase in the phonon scattering. We have, therefore, taken the most recent data by Li *et al.* [23] to compare with our calculations. Our calculated κ_L at RT of MLG and BLG were found to be 2870 $Wm^{-1}K^{-1}$ and 1730 $Wm^{-1}K^{-1}$, respectively, which is within the range seen experimentally, and are in good agreement with the previous literature [158, 23, 198, 211, 212, 51]. Our calculations also show that at higher temperatures, κ_L does not change significantly by addition of another layer which is consistent with the report by Koh *et al.* [217], suggesting that κ_L between graphene and its environment has a much larger influence than that of individual graphene sheets. We find that κ_L increases initially from 20 K to 170 K for MLG and to 230 K for BLG, before decreasing. For MLG, if we compare our results to the experimental data by Chen *et al* [211], we find that the maximum values of κ_L seen experimentally occuring at a temperature between 150 K and 200 K are in agreement to our calculations. Therefore, calculations involving both harmonic and anharmonic IFCs, solving the BTE for phonons as done in the

ShengBTE method, provides an accurate method for the calculation of the lattice thermal conductivity.

3.3.5 Figure of Merit of undoped MLG and BLG

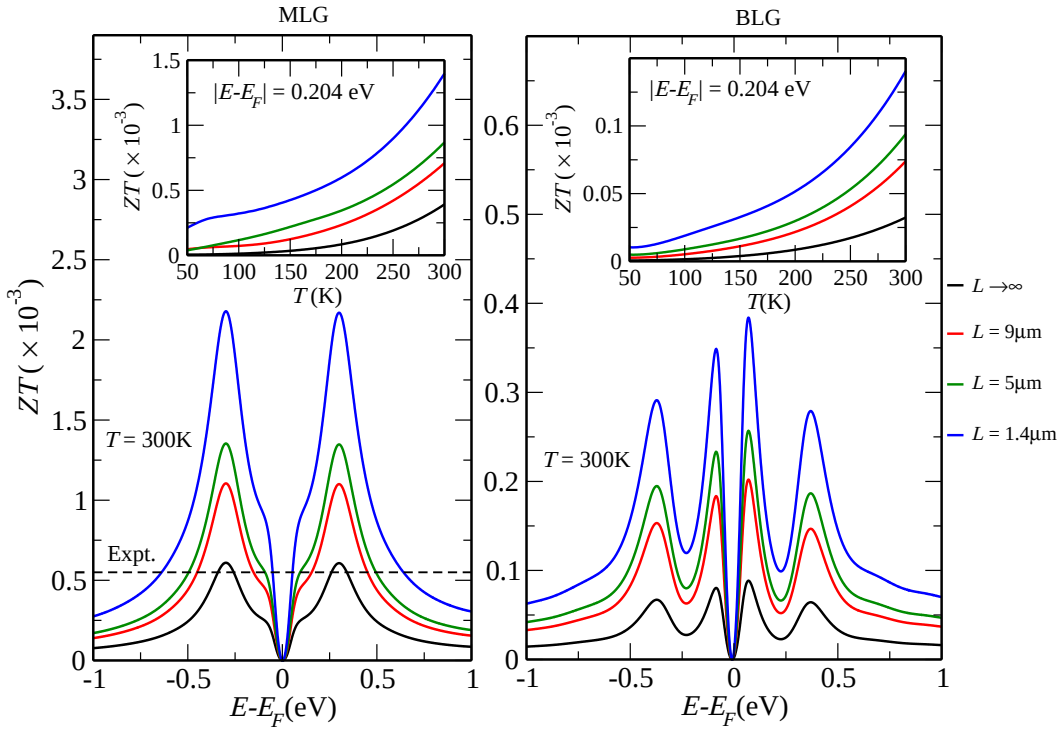

Figure 3.13: The calculated Figure of merit (ZT) for undoped MLG (left) and BLG (right) at three different lengths, L=1.4μm, L=5μm and L=9μm together with its thermodynamic limit ($L \to \infty$). The black dashed line refers to the experimental data [24]. Inset: Calculated ZT as a function of temperature for fixed chemical potential.

Fig. 3.13 shows the figure of merit (ZT) of undoped MLG and BLG at three different lengths together with thermodynamic limit ($L \to \infty$). The $L \to \infty$ results at RT, $ZT_{max} = 0.60 \times 10^{-3}$, are in very good agreement with a recent experimental measurements [24], ZT=0.55 $\times 10^{-3}$ (shown as black dashed line). The electrical Boltzmann transport equations using the RTA yields an electrical relaxation time (τ_e) scaled electrical conductivity ($\frac{\sigma}{\tau_e}$). Berger *et. al.* [218, 219] have experimentally measured the resistivity to be $\rho = 1$ $\mu\Omega$cm which results in an electrical conductivity $\approx 7.1 \times 10^7 \frac{1}{\Omega \mathrm{m}}$. Adopting a Drude model, Tan *et. al.* [7] have estimated τ_e as a function of charge density having values in the range 10fs-100ps. Using the lower bound for the relaxation time we obtain σ, as calculated by us recently [22], in the same range as seen experimentally [218]. Therefore, we use τ_e = 10 fs in all our calculations for the estimate of the figure of merit for MLG.

In the inset of Fig. 3.13 we see that the for a fixed chemical potential, in the temperature range 50-300K, ZT is larger for smaller sample lengths. Our calculated ZT for both, MLG and BLG, are symmetric along the chemical potential. Due to the linear and parabolic electronic bandstructure of MLG and BLG, respectively; MLG has one peak while BLG has two in their ZT as a function of chemical potential. Both, MLG and BLG are semi-metals and hence transport would occur only near the Fermi energy because for electrons away from the Fermi energy, there are no available states within a small energy window. At the Fermi energy, the ZT is zero because the electronic density of states corresponding to chemical potential at the Fermi energy is zero.

3.3.6 Decrement of κ_L and Enhancement of ZT in BN-doped MLG

Defects are commonly considered to be destructive to the properties of a material used in solid states devices. Nonetheless, defects can occasionally be useful in supplying dopants to control their carrier concentration depending on the carriers either being n-type or p-type. [220]. Systems such as graphene have defects introduced in them for technological applications. Point defects arise within the planes of graphene mostly in the form of impurity atoms and lattice vacancies. Foreign impurities such as boron and nitrogen are common p-type and n-type dopants for graphene.

Micro-Raman spectroscopy is a method to characterize in-plane defects in graphene-like systems. The disorder-induced band, also known as the D-band, is a characteristic Raman feature in graphene-like systems. The D-band has no intensity in the absence of any defects and any given impurity that breaks the translation symmetry of the lattice introduces a D-band intensity in the Raman spectrum. Along with the D-band, the G-band in Raman spectrum also gives information in understanding defects in graphene-like materials predominantly when the impurity atoms dopes the material to change the bonding strength of the foreign species in the host carbon atom. Therefore, the ratio of the intensity of the D band to the G-band ($\frac{I_D}{I_G}$)in the Raman spectrum plays an vital role in understanding the defects due to impurity scattering in graphene-like systems.

Study of the disorder due to defects in graphene caused by low energy Ar^+ ion bombardment was done by Lucchese *et al.*[221] using Raman scattering. This was carried out by varying the densities of the defects induced with different doses in the ion bombardment. The results of the experiment were modelled by inferring that a single impact of an ion on the graphene sheet would modify the sheet on two length scales [222]. The model is known as *the local activation model*. The two length scales are referred to as r_A and r_S which are the radii of two circular areas measured from the impact point as shown in Fig. 3.14. The shorter radius, r_S, is the structural disorder from the impact point and is know as the structurally-disordered region or the S-region. At distance for radii greater r_S but smaller than r_A causes a mixing of Bloch states near the K point and hence enhances the intensity in the D-band in the Raman spectrum. This region is termed as the activated or A-region beyond which the lattice structure is preserved and absent from any defect or impurity [222].

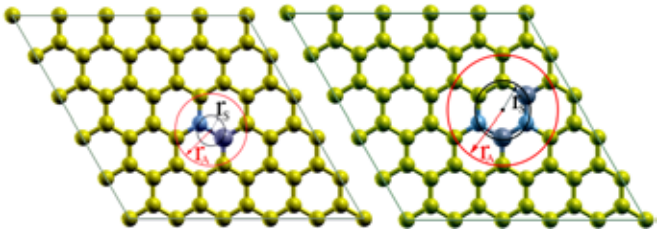

Figure 3.14: Unit cell containing 50 atoms with one BN-dimer (left) and two BN-dimers (right) embedded in graphene used in our calculation. The red and black arrow correspond to the radius of the activated region (r_A) and the structurally defective (r_S) region, respectively.

The local activation model for the $\frac{I_D}{I_G}$ ratio is a function of the average distance between two defects, L_D and is expressed as [222, 220, 24],

$$\begin{aligned}\frac{I_D}{I_G} &= C_A \frac{r_A^2 - r_S^2}{r_A^2 - 2r_S^2}\left[e^{\frac{-\pi r_S^2}{L_D^2}} - e^{\frac{-\pi(r_A^2 - r_S^2)}{L_D^2}}\right] \\ &+ C_S\left[1 - e^{\frac{-\pi r_S^2}{L_D^2}}\right] \end{aligned} \tag{3.8}$$

where C_A and C_S are adjustable dimensionless parameters. For graphene-like materials the value of C_A and C_S are found to be 4.2 and 0.87 respectively [222, 220, 24] and are the values used in our calculations. The remaining parameters used in our paper are as follows: The average length between the defects is the same as the length of the unit cell, $L_D = 12.33$Å. The radii used for

the A-region and S-region for one BN-dimer are $r_A = 1.85$Å and $r_S = 0.722$Å, respectively. Similarly, the radii used for the A-region and S-region for two BN-dimers are $r_A = 2.69$Å and $r_S = 1.44$Å respectively (See Fig.3.14). The resulting $\frac{I_D}{I_G}$ ratio of one and two BN-dimers are calculated to be 0.253 and 0.451, respectively. The method to calculate the lattice thermal conductivity of BN-doped graphene will be discussed shortly and the results are plotted in the inset of Fig. 3.15 as a function of the $\frac{I_D}{I_G}$ ratio.

We have used our previous results [22] on electrical transport of BN-doped MLG obatined using first-principles DFT based electronic band structure and Boltzmann transport equations for the band electrons for obtaining σ and S, which are then used to evaluate ZT.

For calculating κ_L for BN-doped MLG, we have used the iterative ShengBTE method taking BN dimer as point defects in graphene sheets. Calculation of the thermal conductivity of doped MLG was performed by extracting the phonon frequency (ω) dependent phonon relaxation time from the iterative method for MLG, adding the ω-dependent point defects (Eqs. 2.129,2.130) with calculated parameters, and solving Eqs. 2.123 and 2.124 with the new calculated phonon relaxation time derived from the Matthiessen's rule (Eq. 2.122). The required parameters for one and two BN-doping were calculated to be $\Gamma_0^{\mathrm{BN}} = 7.48 \times 10^{-4}, \Gamma_0^{\mathrm{2BN}} = 1.48 \times 10^{-3}$, which enter in Eqs. 2.129,2.130.

Polanco *et al.* [187] have calculated the scattering rates due to point defects by various atoms including boron and nitrogen in graphene. The point defect formula used in their paper is very similar to the Eqs. 2.129 and 2.130, with a linear fit (for the LA,TA modes) and a quadratic fit (for the ZA mode) to the phonon dispersion, as done by Lindsay *et. al.* [185].

In Fig. 3.15 we show the figure of Merit for MLG doped with one and two BN dimers at three different sample lengths, L=1.4μm, L=5μm and L=9μm along with its thermodynamic limit. The two fold increase in S, thereby increasing ZT, for MLG upon doping [22] is attributed to the occurance of a small band gap. Further increase in ZT for smaller sample-lengths is attributable to decrease in κ_L as shown in earlier sections.

Our calculations predict that ZT is almost symmetric around the Fermi energy showing an increase with gate voltage for both n(p)-type doping. As one

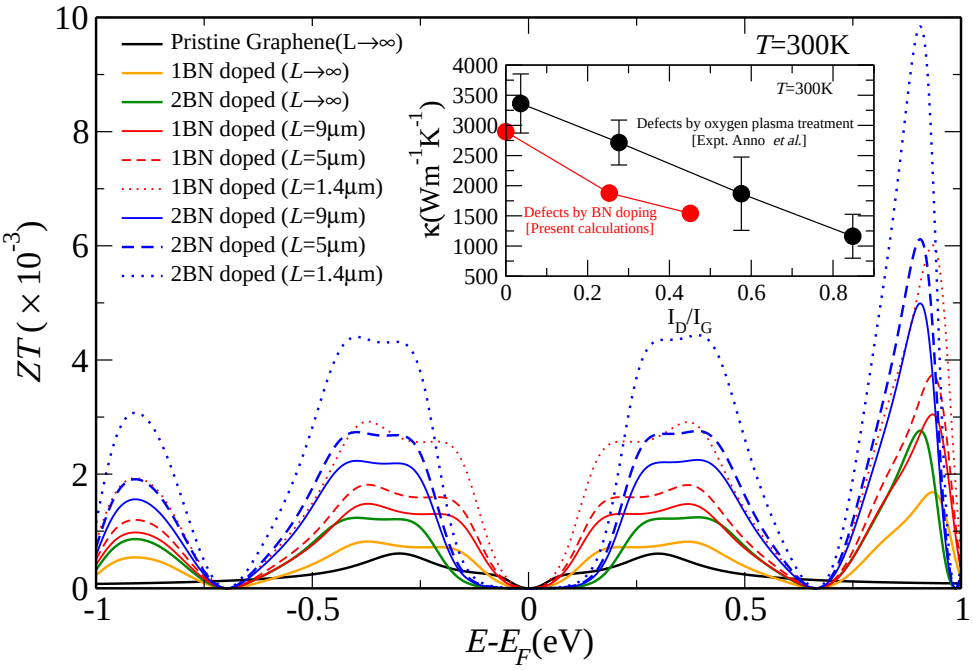

Figure 3.15: The calculated Figure of merit (ZT) of one and two BN dimers doped Graphene at three different lengths, L=1.4μm, L=5μm and L=9μm along with its thermodynamic limit. Inset: The lattice thermal conductivity plotted as a function of the ratio of intensity of the D and G band. The black circular points refer to the experimental data of Anno *et al.*[24]. The red circular points refer to the present calculations.

goes to higher values of energy (or gate voltage), there are additional peaks in ZT separated by minima at around 0.7eV above and below the Fermi energy. The higher values of ZT found at various energy range may lead to increased thermoelectric performance of doped graphene based devices.

Graphene is semi-metallic and gapless which leads to extremely small thermoelectric power factor ($S^2\,\sigma$). However, a band gap is created at the Fermi level when graphene is doped simultaneously with boron and nitrogen [223], which leads to enhancement in its thermoelectric power factor. Elaborate work have been carried out by various groups [200, 224, 30] on band gap engineering of boron-nitride doped graphene by varying their constituent concentration. Therefore, graphene doped with two BN dimers have negligible ZT around the Fermi level for a larger chemical potential range as compared to MLG doped with one BN dimer which in turn has negligible ZT for a larger chemical potential range as compared to pristine MLG. This is the product of two BN dimers doped MLG having band gaps greater than one BN dimer doped MLG and that pristine MLG has a no band gap. In order to have a better understanding of all the peak seen when ZT is plotted versus the chemical potential, we do a model calculation in the next section.

3.3.6.1 Model calculation of σ and S of BN-doped Graphene

The behavior of the ZT can be apprehended by studying the Seebeck coefficient. For semiconductors with small energy band gaps, the Seebeck coefficient, at a constant temperature, can be shown to be $S \propto \frac{d}{dE}[\ln \sigma(E)\big|_{E_F}]$ [22, 149]. Where, σ is the electrical conductivity. The electrical conductivity as a function of wave vector $\sigma(k)$ was derived from the wave vector dependent velocity ($v(k) = \frac{d\epsilon}{dk}$), $\sigma(k) \propto v(k)^2$. ϵ is the energy dispersion derived from the electronic bandstructure. The energy dependent electrical conductivity and velocity are then calculated using, $\sigma(\epsilon) = \sum_{i,k} \sigma(k) \frac{\delta(\epsilon - \epsilon_{i,k})}{d\epsilon}$ and $v(\epsilon) = \sum_{i,k} v(k) \frac{\delta(\epsilon - \epsilon_{i,k})}{d\epsilon}$, respectively. The dummy variable $'i'$ corresponds to the band index. In our model calculation, i runs from $i = 1$ to $i = 4$, two bands below and above the Fermi energy. This sections aims to understand the behavior of ZT and hence all of the constants in our calculations are set to 1.

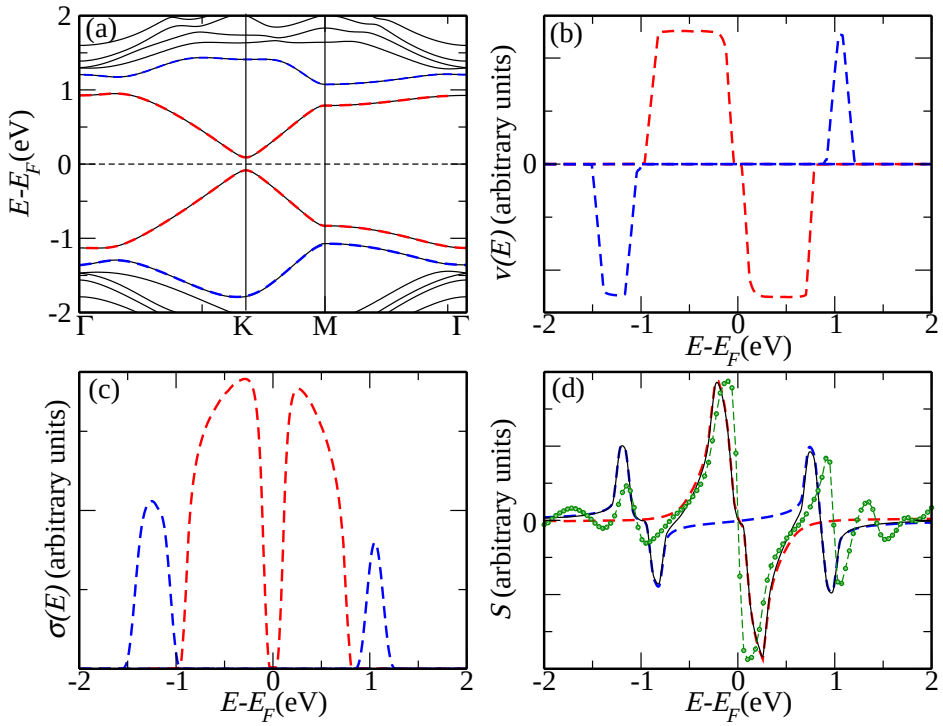

Figure 3.16: (a) Bandstructure of one BN-doped graphene, (b) group velocity of electrons belonging to the two closest bands to the Fermi energy, shown in red and blue, (c) electrical conductivity of these electron system, (d) their Seebeck coefficient. The blue and red curves in (b,c,d) refer to the bands of the same colour as in (a). The green circles in (d) are the first-principles calculations of S taking contributions from all bands [22].

Fig. 3.16 (a) shows the the bandstructure of one BN dimer doped graphene. The red curves are the two bands closest to the Fermi energy and the blue curves are the next closest. The energy dependent velocity, electrical conductivity and

Seebeck coefficient are plotted in Fig. 3.16 (b,c,d) respectively. The colour conventions for these curves correspond to the colour of the bands in Fig.3.16 (a). It is evident from our calculations that the zeros in the Figure of Merit are due to the vanishing electron velocities and hence electrical conductivities. Our results using this model calculation show that the features at $|E - E_F| \sim 1$ eV, which are absent in pristine graphene, are due to the bands which are second to the closest bands to the Fermi energy. The form of the Seebeck coefficient shown in Fig. 3.16 (d) is in decent agreement to the form calculated using the Boltzmann equations implemented in the BOLTZTRAP code, shown in green circles[22, 31].

3.4 Summary

In this chapter we have discussed various transport properties such as electrical conductivity, resistivity, the Seebeck coefficient, mobility and lattice thermal conductivity of MLG and BLG graphene using first-principles DFT calculations and Boltzmann transport equations. We were able to capture many essential features seen in MLG and BLG, for example the $\sqrt{n}$ behavior of electrical conductivity and its temperature dependence, the increase of the Seebeck coefficient with temperature, and a linear dependence of the Seebeck coefficient on temperature for a constant chemical potential, as observed in experiments. For a particular range of chemical potentials we obtained the Bloch-Grüneisen behavior of resistivity in MLG, where the resistivity increased linearly at higher temperatures whereas it showed a $\sim T^4$ behavior at lower temperatures, as observed experimentally. We have also observed an order of magnitude decrease in mobility when the energy on impurity sites is decreased, a fact that has been verified experimentally. The Seebeck coefficient was found to increase almost twofold upon doping by boron nitride. Our results for graphene with impurities show a systematic decrease in electrical conductivity (and hence mobility) when we decrease the on-site terms of particular atoms in the sheet. We also observe that for a high concentration of impurities, the electrical conductivity was found to change from $\propto \sqrt{n}$ behavior to $\propto n$ behavior.

Our calculated phonon dispersion and Grüneisen parameters with harmonic

and anharmonic IFCs, for both MLG and BLG show good agreement with available experimental data and previously published calculations. We finally show the result of the lattice thermal conductivity, calculated using phonon Boltzmann transport theory and first-principles phonon bandstructure including both harmonic and anharmonic interactions, showing excellent agreement with recent experimental data [23] available in the temperature range 300-700 K. Further experimental measurements are needed to verify the occurrence of a peak in κ_L near $T \sim$150-200 K for both MLG and BLG.

Making a linear and quadratic fit to the in-plane and out-of-plane acoustic phonon dispersion along with constant in-plane and an out-of-plane inverse square wave vector dependent Grüneisen parameters, we find an analytical solution to the mode, length and temperature dependent lattice thermal conductivity for the Callaway-Klemens method. The Callaway-Klemens method suggests that the out-of-plane ZA modes contribute the least to the total lattice thermal conductivity due to the large negative Grüneisen parameters and vanishing velocities at the long wavelength limit and that the major contribution to κ_L are due to the in-plane modes, LA and TA, due to their large velocities and small Grüneisen parameters. The lattice thermal conductivity was also calculated beyond the RTA using an iterative method implemented in the ShengBTE code. The iterative method suggests that, in direct contrast to the Callaway-Klemens method, that the ZA modes contribute the most to the total κ_L while the in-plane modes contribute the least.

The Callaway-Klemens and iterative method both yield excellent agreement to total κ_L for MLG at room temperature. However they yield different mode contributions. This raises the question as to which mode contributes the most to κ_L. In order to solve this discrepancy, we calculate the mode, length, and temperature dependent κ_L of BLG since the selective rule is broken in the ZA modes for BLG. We find that the Callaway-Klemens method overestimates the thermal conductivity and additional point defects parameters are required to make the theory fit with the experiments. However, using the iterative method, we observe that all our calculations are in excellent agreement with many available experiments without the use of any fitting parameters. We therefore conclude that the thermal conductivity has its major contribution from the ZA mode and

is also the most sensitive to the sample length. We also conclude that the mode dependent relaxation time calculated from the Callaway-Klemens method are not accurate and one must go beyond the RTA to solve the relaxation times especially for 2D materials like MLG and BLG.

Along with the electrical transport parameters like electrical conductivity, Seebeck coefficient and hence power factor calculated by us earlier, we have calculated the figure of merit of MLG and BLG. The lattice thermal conductivity used in our calculations were only taken from the iterative method. Our calculation for pristine graphene at the thermodynamic limit are in excellent agreement with available experimental data. We also find an enhancement of the figure of merit when the sample lengths are in order of μm as compared to that of the thermodynamic limit. Moreover, we show that when pristine graphene is doped with one or two boron nitride dimers, the figure of merit is found to be enhanced over a wide range in chemical potential. We have therefore found a new route to enhance the figure of merit of graphene and hence improve graphene based devices over a wide range in gate voltage.

Chapter 4

First-principles calculations of lattice thermal conductivity of multi-layered hexagonal boron nitride and comparison to experiments[1]

4.1 Introduction

We investigate numerically the sample length and temperature dependence of the thermal conductivity (κ_L) of single and multilayer h-BN by solving the phonon BTE beyond the relaxation time approximation (RTA) using the force constant derived from a real space super cell method, and also by solving the phonon BTE in the RTA using the Callaway-Klemens approach. A long standing puzzle has been to answer which acoustic phonon mode dominates the total lattice thermal conductivity for such 2D materials [225]. There have been arguments on whether the out-of-plane ZA vibrational mode contributions to κ_L are the most dominant or the least in comparison to the other acoustic modes. Owing to the selection rules restricting the phase space for phonon-phonon scattering in ideal graphene [226, 227, 210] and boron nitride [151], the ZA mode seem to be the most dominant. In a rather sharp contrast, references [158, 150] suggest

[1]Based on a publication by **R D'Souza**, S Mukherjee, Physical Review B **96**, 205422 (2017)

that since in the long wavelength limit ($q \to 0$), the phonon dispersion of the ZA modes seem to be flat thus making the phonon velocities small, and also the fact that the Grüneisen parameters are large, would make the ZA contributions to κ_L the least in comparison to other acoustic modes. Here, using the Callaway-Klemens approach, we examine this discrepancy from analytical solutions to the phonon BTE for each of the acoustic modes using a closed form for the scattering rate for the three-phonon processes derived by Roufosse *et. al.* [228] and an exact numerical solution for the phonon BTE beyond the relaxation time approximation (RTA) in which the phonon lifetimes are formed in terms of a set of coupled equations and solved iteratively. We also examined the sample length (L) dependence of κ_L and found this to be very sensitive to L, which may justify the application of multilayered h-BN in thermoelectric devices by manipulating κ_L.

4.2 Computational details

Density functional theory

First-principles DFT and DFPT calculations, as described in section 2.1 and 2.2, were carried out on a hexagonal supercell for the monolayer, bilayer and bulk boron nitride, whereas an orthorhombic supercell was used for five layers h-BN sample, using the plane wave pseudopotential method as implemented in the QUANTUM ESPRESSO code [139]. We have used 2 atoms in the unit cell for SLBN, 20 atoms for five layered BN and 4 atoms in both bilayer and bulk boron nitride. To prevent interactions between the layers, a vacuum spacing of 20 Åwas introduced along the perpendicular direction to the layers (z-axis) mimicking an infinite BN sheet in the xy plane. For MLBN and bulk-hBN, the Van der Waals interaction as prescribed by Grimme [229], was used between the layers. For the electronic structure calculations, Monkhorst-Pack grids of $16 \times 16 \times 1$ and $16 \times 16 \times 4$ were chosen for SLBN and MLBN, resepectively, for the k-point sampling. Self-consistent calculations with a 40 Ry kinetic energy cut-off and a 160 Ry charge density energy cutoff were used to solve the Kohn-Sham equations with an accuracy of 10^{-9} Ry for the total energy. We used ultrasoft pseudopotential to describe the atomic cores with exchange-correlation potential

kernel in the local density approximation [230]. The electronic structure and total enrgy calculations were used to obtain the groundstate geometry before persuing the phonon calculations.

Density functional perturbation theory

For the phonon bandstructure calculations, the q-grid used in the calculations were $6 \times 6 \times 1$ for SLBN, $6 \times 6 \times 2$ for BLBN and bulk h-BN and $4 \times 4 \times 2$ for 5-layer BN, respectively. The density functional perturbation theory (DFPT) [138], as implemented in the plane wave method [139], was used to calculate the phonon dispersion and phonon density of states (DOS) along the high-symmetric q-points.

Calculation of the lattice thermal conductivity

The calculation of lattice thermal conductivity κ_L involves evaluation of second-order harmonic interatomic force constants (IFCs) as well as the third-order anharmonic IFCs. We have used first a real space supercell method which evaluates the third-order IFCs in a real space grid using DFT [152], whereas the second-order IFCs are obtained from the DFPT method [139, 138]. Secondly, using the Callaway-Klemens method [156, 157], the relaxation times were obtained from the Grüeisen parameters. Finally, the length, thickness and temperature dependence of κ_L were studied.

Real space super cell approach

In the real space super cell iterative approach, the third order anharmonic IFCs are calculated from a set of displaced supercell configurations depending on the size of the system, their symmetry group and the number of nearest neighbour interactions. A $4 \times 4 \times 2$ supercell including upto third nearest neighbour interactions were used to calculate the anharmonic IFCs for all the structures, generating 128 configurations for single and bulk BN, 156 for bilayer BN (BLBN) and 828 for five-layered BN (5LBN). The third order anharmonic IFCs are constructed from a set of third-order derivatives of energy, calculated from these configurations using the plane wave method [139]. The phonon lifetimes are calculated from the phonon BTE which are limited by phonon-phonon, isotropic impurity and boundary scattering [151]. The three-phonon scattering rates are incorporated in this method, as implemented in the the ShengBTE code [152]. Elaborate details on the work-flow of the three-phonon scattering rates can be found in reference

[152] while Lindsay [151] specifically discuses this for bulk h-BN.

4.3 Results and discussion

4.3.1 Phonon dispersion and density of states

Accurate calculations of the harmonic second order IFCs are necessary for a precise description and understanding of the thermal conductivity. Deviations due to numerical artifacts from the expected behavior of acoustic modes can lead to incorrect results especially for 2D marterials [231]. The full structural relaxation of SLBN, BLBN, 5LBN and Bulk-*h*BN yield a lattice constant (a_0) of 2.49 Å. The interlayer spacing (c) for MLBN is found to be 3.33 Å. The experimentally measured a_0 is 2.50 Å [232] and the ratio of interlayer spacing and the lattice constant ($\frac{a_0}{c}$) is 1.332 [232] which is in excellent agreement with our calculated value of 1.337.

The calculated phonon dispersion and phonon density of states are shown in Fig. 4.1 for (a) SLBN, (b) BLBN, (c) 5LBN and (d) Bulk-*h*BN along the high symmetric q-points in the irreducible hexagonal and orthogonal Brillouin zone (BZ) together with some available experimental data for Bulk-*h*BN [25]. As usually seen for acoustic modes, the in-plane longitudinal (LA) and transverse (TA) modes show a linear q dependence at the long-wavelength limit while the out-of-plane (ZA) mode shows a quadratic (q^2) dependence. This quadratic dependence, which is a typical feature of layered crystals, is due the rotational symmetries of the out-of-plane phonon modes.

For SLBN, there are six modes for each wave vector, three acoustic (LA,TA,ZA) and three optical (LO,TO,ZO). At the Γ point the optical LO and TO modes are degenerate. For BLBN, if the two SLBN layers are far apart, effects due to their interlayer coupling can be neglected and the phonon dispersion will be exactly as what is seen in SLBN. However, when these two SLBN come closer, due to the interlayer coupling, the two-fold degeneracy is removed giving rise to in-plane and out-of-plane phase modes. The LA and TA modes are not perturbed much implying that the main effect of the interlayer interactions is due to the ZA modes. This is because the transverse motion of atoms in both the layers

associated with these modes interact strongly with each other. The same reasons hold on why 5LBN has one zero and four raised frequencies at the Γ point. In Bulk-*h*BN, there are four atoms per unit cell and the two atoms in each layer are now inequivalent therefore doubling each of the acoustic and optical modes. The acoustic modes at the zone boundaries fold back to the zone centre as two rigid layer modes [233], *viz*, an optically Raman inactive and an Raman active mode. The Raman active LA_2 and TA_2 modes are doubly degenerate at the Γ point having a finite value mentioned in Table 4.1. The layered breathing modes for MLBN are denoted by $ZO^{'}$ for BLBN and Bulk-*h*BN and $ZO^{'}_{i}$ $(i = 1, 2, 3, 4)$ for 5LBN.

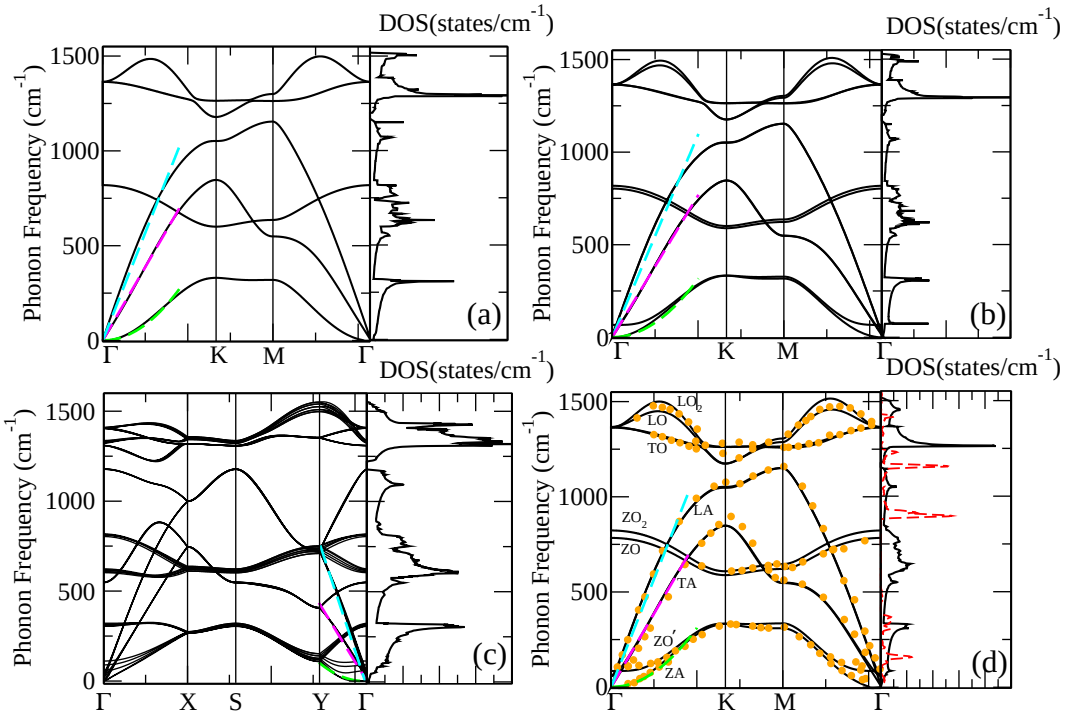

Figure 4.1: The calculated phonon dispersion (left) and phonon density of states (right) of (a) SLBN, (b) BLBN, (c) 5LBN and (d) Bulk-*h*BN along with experimental data (orange circles) [25]. The phonon dispersion were calculated along the high-symmetry points of the 2D Brillouin zone ($q_z = 0$) corresponding to the hexagonal cell for SLBN, BLBN, and Bulk-*h*BN and orthorhombic cell for 5LBN. We also plot in (d) the two-phonon DOS shown for Bulk-*h*BN in red dashed line. The cyan, magenta and green curves in (a,b,c,d) are the best linear and quadratic fit to the phonon dispersion referring to LA, TA and ZA modes, respectively.

The symmetries of SLBN, BLBN, 5LBN and Bulk-*h*BN structures at Γ can be described using the character table shown in table 4.1. Using a standard group theoretical technique (see Appendix C.1), it can be shown that for Bulk-*h*BN and BLBN that the 12 phonon modes are decomposed into the following irreducible representations: $2(A_{2u} + B_{1g} + E_{2g} + E_{1u})$ and $2(A_{2u} + E_g + A_{1g} + E_u)$. Similarly for SLBN, the irreducible representation is $A_{2u} + B_{1g} + E_{2g} + E_{1u}$ for the six

Mode	Expt. (& Prev. calculated[a]) ω (cm^{-1})	Bulk-*h*BN (Sym.)	BLBN (Sym.)	SLBN (Sym.)
LA_2 & TA_2	51.62[b] (52.43)	58.55 (E_{2g})	25.73 (E_g)	-
ZO′	Silent (120.98)	85.01 (B_{1g})	66.54 (A_{1g})	-
ZO	783.16[c] (746.87)	784.05 (A_{2u})	803.01 (A_{2u})	819.37 (A_{2u})
ZO_2	Silent (809.78)	823.17 (B_{1g})	818.25 (A_{1g})	-
LO	1366.30[b], 1370.33[c], 1363.88[d] (1379.20)	1363.80 (E_{2g})	1364.45 (E_g)	1363.88 (E_{2g})
TO	1367.10[c] (1378.4)	1366.95 (E_{1u})	1365.66 (E_u)	1363.88 (E_{1u})
	LA & TA (cm^{-1}) (Point Group Symmetry)	LO (cm^{-1}) (P.G. Symmetry)	TO (cm^{-1}) (P.G. Symmetry)	ZO (cm^{-1}) (P.G. Symmetry)
5LBN	14.60 (E'')	1409.46 (E')	1405.23 (E')	817.59 (A')
	31.10 (E')	1408.91 (E'')	1404.94 (E'')	814.58 (A'')
	38.95 (E'')	1408.71 (E')	1404.81 (E')	812.58 (A')
	47.43 (E')	1408.36 (E'')	1404.49 (E'')	810.27 (A'')
		1405.57 (E'')	1404.40 (E')	803.27 (A')

Table 4.1: Experimentally measured Raman and Infrared phonon frequencies for bulk-*h*BN and those obtained from present calculations for all the systems studied are shown at the Γ point in the BZ. Previously calculated values for bulk-*h*BN are also shown together with the experimental data for comparison.

[a] From *ab initio* dispersion calculations, Ref. [25].
[b] Experimental Raman data, Ref. [234].
[c] Experimental Raman and Infrared data, Ref. [235].
[d] Experimental Raman data, Ref. [236].

phonon modes and 5LBN has an irreducible presentation given by 4($A_1^{'}$ + $E^{''}$) + 6($A_2^{''}$ + $E^{'}$). Transitions corresponding to the basis x, y, z (xy, yz, z^2, etc.) are Infrared (Raman) active. Those that are neither Infrared or Raman are the silent modes. Due to the momentum conservation requirement ($q = 0$), the first-order Raman scattering process is limited to the phonons at the center of the Brillouin zone. We therefore compare our calculated frequencies at the Γ point corresponding to A_{2u}, E_{1u}, $A_2^{''}$, $E^{'}$, and E_u to the infrared experimental data and E_{2g}, $E^{''}$, A_{1g}, E_g, and $A_1^{''}$ to the Raman experimental data as shown in table 4.1.

Raman spectroscopy is the most adaptable tool that offers a direct probe for multi-layered samples [233]. Table 4.1 shows the transitions corresponding to the Infrared ($E^{'}$ and $A^{''}$) and Raman ($E^{''}$ and $A^{'}$) active modes in the case of 5LBN. Further experiments for layered boron nitride would be required to verify the correctness of calculations. However, LDA with VdW interaction have shown to accurately describe the phonon dispersions for layered graphene when the geometry (*i.e.* interlayer distance) is represented correctly even though the local or semi-local exchange correlation functionals may not represent the interactions correctly [233].

Another experimental technique to analyse the modes of a system is the second-order Raman spectroscopy in which the peaks are seen over the entire

frequency range. Most of these peaks are in agreement with the phonon density of states when the frequency is scaled by a factor of 2 [25, 232]. We have hence plotted, to the right of our phonon dispersion, the frequency scaled DOS. However, as pointed out by Serrano *et al.*, peaks which are absent in the DOS can be seen in the second-order spectroscopy because the DOS does not take both overtones, *i.e.* summation of modes having the same frequencies, into account. The two phonon density of states (DOS_{2ph}) are also essential for the understanding of phonon anharmonic decay [237]. Experiments on the second-order Raman spectrum of h-BN has been performed by Reich *et al* [236]. We show in Fig. 4.1(d) the two-phonon DOS [238],

$$\mathrm{DOS}_{2ph}(\omega) = \sum_{i,j} \delta(\omega - \omega_i - \omega_j) + \delta(\omega - \omega_i + \omega_j), \tag{4.1}$$

for Bulk-*h*BN using our calculated harmonic interactions. The peaks seen experimentally [236] at 1639.4 cm^{-1}, 1809.907 cm^{-1} and 2289.8068 cm^{-1} are absent in the DOS. However, these large spectral features are now observed at 1680.4 cm^{-1}, 1821.2 cm^{-1} and 2306.7 cm^{-1}, due to two phonon DOS (DOS_{2ph}).

4.3.2 Grüneisen parameter

Besides providing important information on the phonon relaxation time, the Grüneisen parameter (γ) also provides information on the degree of phonon scattering and anharmonic interactions between lattice waves. Therefore, an accurate calculation of the lattice thermal conductivity (κ_L) would require a precise calculation of γ since anharmonic lattice displacements play a vital role in calculations of κ_L. Fig. 4.2 displays the mode dependent γ for SLBN, BLBN, 5LBN and Bulk-*h*BN along the high symmetric q points. The anharmonic lattice displacements are carried out by dilating the unit cell by applying a biaxial strain of $\pm$ 0.5 % and is expressed as shown in Eq. 2.114. We find that the acoustic modes correspond to the lowest Grüneisen parameters which is in-line with experimentally measured γ [239]. As in the case of graphene, the out-of-plane acoustic transverse mode has the largest negative γ parameters.

Positive (negative) Grüneisen parameters suggest a decrease (increase) in phonon frequencies as the lattice constant increases. Near the long-wavelength

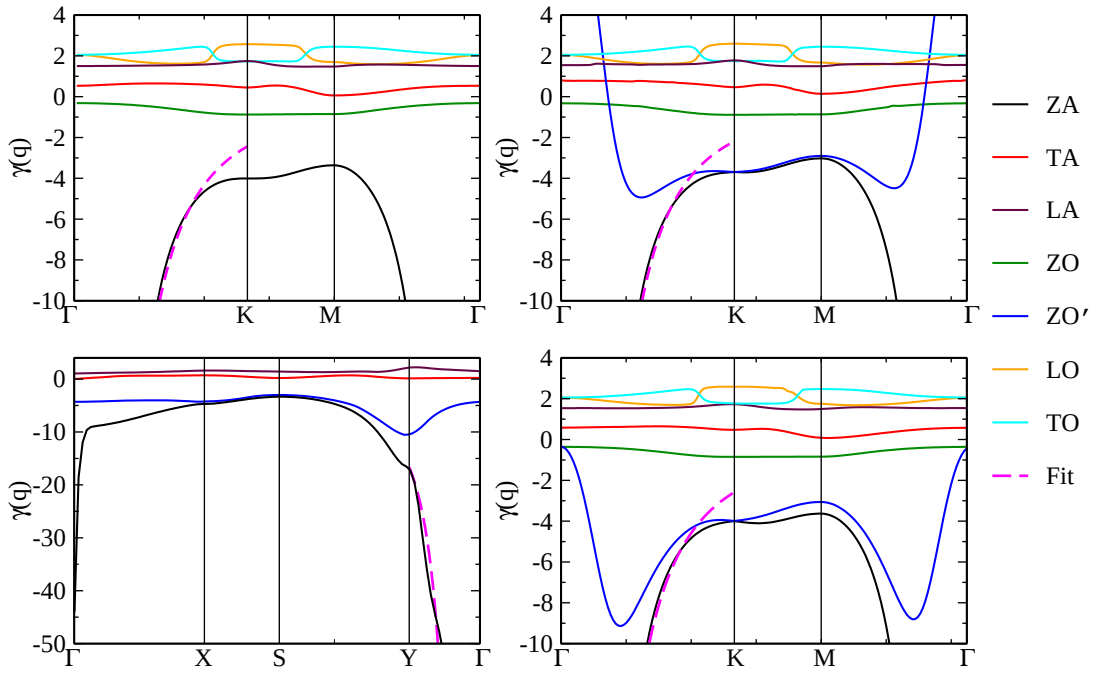

Figure 4.2: Grüenisen parameters of each mode for (a) SLBN, (b) BLBN, (c) 5LBN and (d) Bulk-*h*BN. The colour representation of each mode and fit are shown on the right. The magenta curves are the best fit to the ZA mode along the direction in the BZ chosen to calculate the lattice thermal conductivity.

limit, $\gamma_{ZO'}$ for 5LBN is positive but becomes negative as we move along the Γ to Y direction in the BZ. $\gamma_{ZO'}$, associating with the layer breathing mode suggests that due to the additional layers the atom vibrations along the perpendicular direction between them lose their coherence and hence decreases the phonon frequencies when the system is under a biaxial strain.

As described in table C.1, E_{2g}, E'', A_{1g}, E_g, and A_1'' are Raman active and hence in principle their Grüneisen parameter can be calculated experimentally using Raman spectroscopy. There exist experimental data for bulk *h*-BN but to the best of our knowledge there does not exist experimental data for single or MLBN. We therefore compare our results to that of bulk-*h* BN.

The lowest Grüneisen parameters along the Γ-K-M directions for the TO and LO modes were found to be 1.72 and 1.59, respectively. Our calculations for these modes are only $\sim 1.1\%$ and $\sim 1.3\%$ larger than the experiment values of Sanjurjo *et al.* [239] who have obtained the Grüneisen parameters by measuring the pressure dependence of Raman lines. The slight deviance from the experimental measured value could be because the measured values are for Zinc-blende-BN and not hexagonal BN.

4.3.3 Analytical and Numerical solutions to the Callaway-Klemens's Approach

In order to compare the results obtained from the real space super cell approach (ShengBTE), we now study the mode, temperature and length dependence of single and MLBN calculated using the Callaway-Klemens's approach as described earlier. We first obtain analytical solutions for each acoustic mode of the Phonon BTE by making some reasonable approximations to understand the basic behavior of temperature and length dependence of κ_L. In order to compare with the experimental results, we resort to exact numerical computation.

We have carried out all the length dependent calculations at a constant temperature for MLBN at RT. The corresponding length dependent curves for MLBN are plotted in Fig. 4.3 (e). The parameters used in our study are shown in Table 4.2. Equations 2.110 and 2.111 are plotted in Fig. 4.1 and Equation 2.117

Table 4.2: Relevant parameters used in the calculations for the analytical solutions of the lattice thermal conductivity.

System	υ_{LA} (m/s)	υ_{TA} (m/s)	γ_{LA}	γ_{TA}	$\alpha \times 10^{-7}$ (m^2/s)	$\beta \times 10^{-20}$ (1/m^2)
SLBN	17020.1	11599.8	1.546	0.452	3.99	-6.827
BLBN	16379.4	11474.9	1.585	0.5673	3.75	-6.086
5LBN	21095	11420.6	1.48	0.424	4.2	-6.348
Bulk-*h*BN	16379.4	11474.9	1.57	0.59	3.72	-7.18

is plotted in Fig. 4.2 to compare the analytical fit to the actual phonon dispersion and Grüenisen parameters.

The individual contributions of each of the acoustic modes LA, TA, ZA and the sum of these, *i.e.* κ_L, for single and multilayered *h*-BN are shown in Fig. 4.3 (a,b,c,d). The variation of κ_L values for BLBN and Bulk-*h*BN are quite similar but are lower for 5LBN. This is in good agreement with experiments [26, 27, 28]. In all cases it is observed that amongst the acoustic modes the TA contribution is the largest, ZA to be the least whereas LA contribution is somewhere in between. It has been quite controversial as to which acoustic mode contributes the most to the total lattice thermal conductivity. For example, while some reports [240, 151, 188, 210, 226] show that the contributions from ZA to be the most dominant, there are many other reports [160, 241, 177, 242, 158, 225, 243, 244]

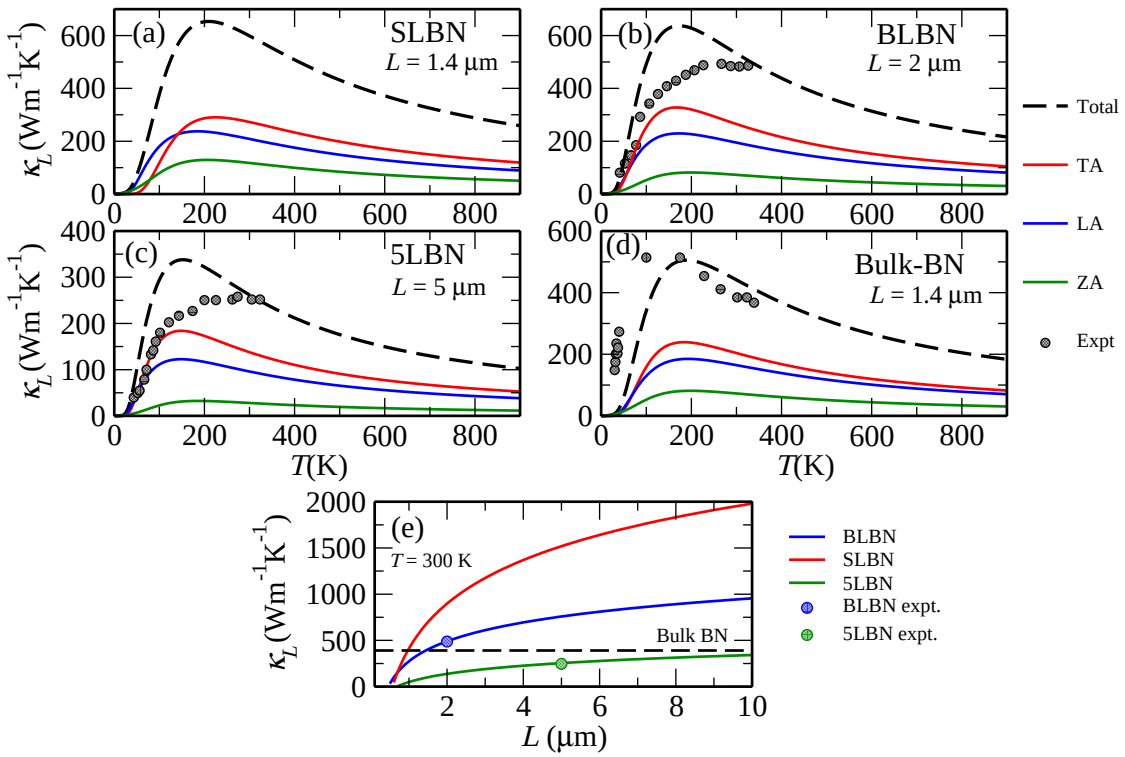

Figure 4.3: Acoustic modes and temperature dependence of lattice thermal conductivity for (a) SLBN (b) BLBN (c) 5LBN and (d) Bulk-*h*BN at a constant length. The theoretical calculations are carried out by using Eq. 2.115 for the LA and TA modes while Eq. 2.118 was used for the ZA mode. The parameters used in our calculations are shown in Table 4.2. The colour representation for each mode are shown on the right. The black dots are the experimental measurements [26, 27, 28]. Length dependence is worked out by varying L in Eq. 2.116

that show exactly the opposite. Our analytical results concur with the latter, *i.e.* the contribution from the ZA mode is the least.

The thermal conductivity for two-dimensional layered materials given by Eq. 3.12 is derived assuming both phonon energy dispersions and phonon scattering rates are weakly dependent on the direction of the Brillouin zone [158]. The calculation of κ_L should be independent of the direction chosen resulting in an isotropic in-plane scalar κ_L. Calculation of κ_L should therefore be independent of direction chosen. We move along the Γ to K direction for systems in which a hexagonal unit cell is used and along Γ to Y in the case of an orthorhombic unit cell. SLBN has the highest calculated κ_L, 5LBN has the least while κ_L lies in between BLBN and Bulk-*h*BN. From Fig. 4.4 it can be easily seen that for temperatures below 100K, the contribution to the total κ_L is mainly due to the flexural ZA modes.

As in the case of graphene, SLBN can have a total of 12 processes involving the flexural phonons. However, Seol *el al* [210] obtained a selection rule for the three-phonon scattering. This rule states that only an even number of ZA

phonons is allowed to be involved in each process. Shen *et al* [160] have listed four flexural allowed processes. Hence, the scattering rate of the Umklapp phonon-phonon process for the acoustic flexural branch is multiplied by a factor of $\frac{4}{12}$ and the relaxation time for the ZA mode becomes 3 times of that of Eq. 2.108. Therefore besides having a larger velocity and a smaller averaged Grüneisen parameters compared to the other systems, the major contribution for an increased κ_L is due to the symmetry of the ZA mode.

Phonon dispersions and Grüneisen parameters for BLBN and Bulk-*h*BN are very similar which explains why their calculated κ_L have the same magnitude. In the case of 5LBN, there are additional five low frequency modes (also termed as layer-breading modes), which arise due to the interlayer moment. Due to this change in phonon dispersion, more phase-space states become available for phonon scattering and therefore decreases κ_L [52]. Numerical calculations

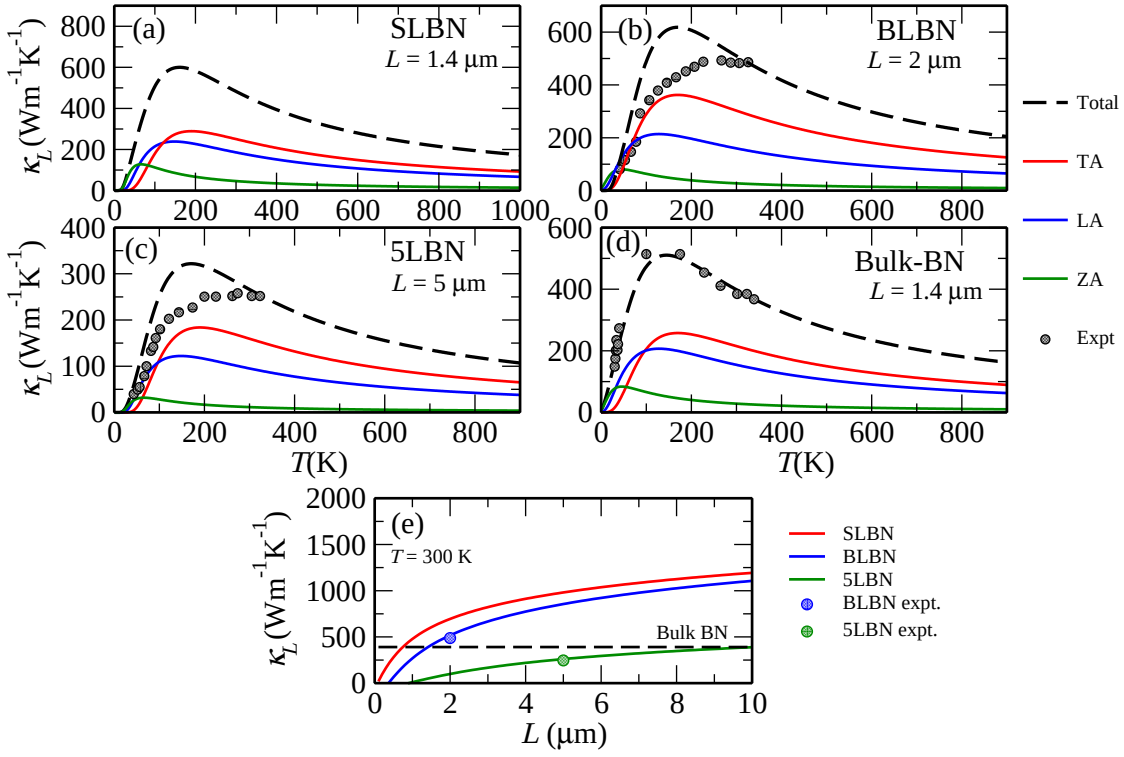

Figure 4.4: Acoustic modes and temperature dependence of lattice thermal conductivity for (a) SLBN (b) BLBN (c) 5LBN and (d) Bulk-*h*BN at a constant length. The theoretical calculations are carried out by solving Eq. 3.12 numerically for each of the modes. The colour representation for each mode are shown on the right. The black dots are the experimental measurements [26, 27, 28]. Length dependence is worked out by varying L in Eq. 2.116.

are carried out using the exact form of the phonon dispersion and Grüneisen parameters as displayed in Fig. 4.1 and Fig. 4.2 rather than the analytical form of the acoustic modes and averaged Grüneisen parameters. We numerically

solve Eq. 3.12 for each of the modes at a constant sample length varying temperature as well as at a constant temperature varying lengths between 0.1 to 10 μm. These results are compared with experimental data [26, 27, 28] and shown in Fig. 4.4. Numerically calculated values of κ_L are in better agreement with the experimental data as compared to the analytical form. We find the contribution from the ZA modes to dominate at lower temperatures but rapidly decreases as the temperature increases making the flexural modes contribute the least at relatively higher temperatures. This is in line with previous theoretical calculations [242].

4.3.4 Thermal conductivity calculated using real space supercell approach

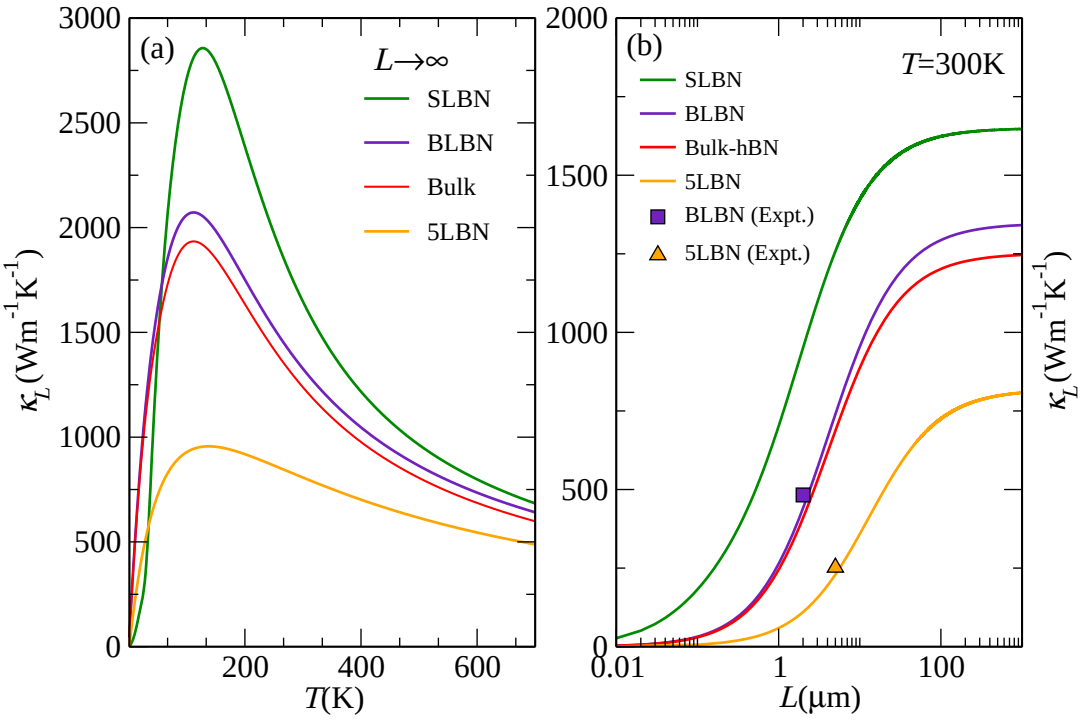

Figure 4.5: Calculated thermal conductivity of single and multilayer BN shown as a function of (a) temperature and (b) length, using the real space approach. In (a) the curves refer to the thermodynamic limit ($L \to \infty$). In (b) the sample length is in logarithmic scale. The square and triangle data points refer to experimental measurements for BLBN [28] and 5LBN [27], respectively.

In Fig. 3.9 (a) and (b) we show the variation of thermal conductivity as a function of temperature (T) and sample length, respectively. The sample length is measured along the direction of the heat flow. The theoretical computation was carried out using the interatomic force constants obtained from the real

space approach and an iterative method in calculating the relaxation times as implemented in the ShengBTE code [152]. To have a broad understanding of the thermal conductivity, we study different types of possible unit cells, *i.e.*, MLBN considered here have even, odd and infinite number of layers since each unit cell has a different character table. Calculations were done using orthogonal cell for 5LBN and hexagonal cells for SLBN, BLBN and bulk-*h*BN. The study was carried out over a wide range of sample lengths between 0.01 μm and 1000 μm with 0.1μm grid. The temperature of each sample was varied between 10 K to 1000 K with a grid of 10 K. On plotting the thermodynamic limit ($L \to \infty$) for each of the system we find that κ_L is practically independent of length for lengths greater than 100 μm.

Our recent results of κ_L in the thermodynamic limit ($L \to \infty$) for monolayer and bilayer graphene [22] are in excellent agreement with the recent experimental work of Li *et. al* [23], whereas the thermodynamic limit for MLBN is much larger than some recent experimental measurements [27, 28]. Sample lengths used by Li *et. al.* were of the order of millimetres for the measurement of single and bilayer graphene while Jo *et. al.* and Wang *et. al.* have used sample lengths of 5 μm and 2 μm for 5LBN and BLBN, respectively. As mentioned earlier, κ_L does not vary much for lengths larger than 100 μm but is extremely sensitive when the lengths are between 1 and 100 μm. Not surprising therefore, our thermodynamic limit of κ_L are in good agreement for graphene but not for MLBN.

In order to compare our calculations to that of experiments, we calculate the cumulative lattice thermal conductivity at lengths corresponding to the sample lengths used in the experiments. The cumulative κ_L was calculated in the temperature range 10-1000 K. Fig. 3.9 (b) shows the cumulative thermal conductivity at room temperature (RT).

The curves in Fig. 4.6, are the calculated values of κ_L at constant lengths which are compared with the experimental observations [28, 26, 27]. For the lengths used in the experiments the magnitudes of κ_L for bulk-*h*BN and bi-layer lie in between SLBN and 5LBN with SLBN (5LBN) being the highest(lowest). The maxima of κ_L of $\sim$ 500 Wm^{-1}K^{-1} for Bulk-*h*BN is found in the temperature range 250-300 K and tends to saturate to a value $\sim$ 450 Wm^{-1}K^{-1}. Experimen-

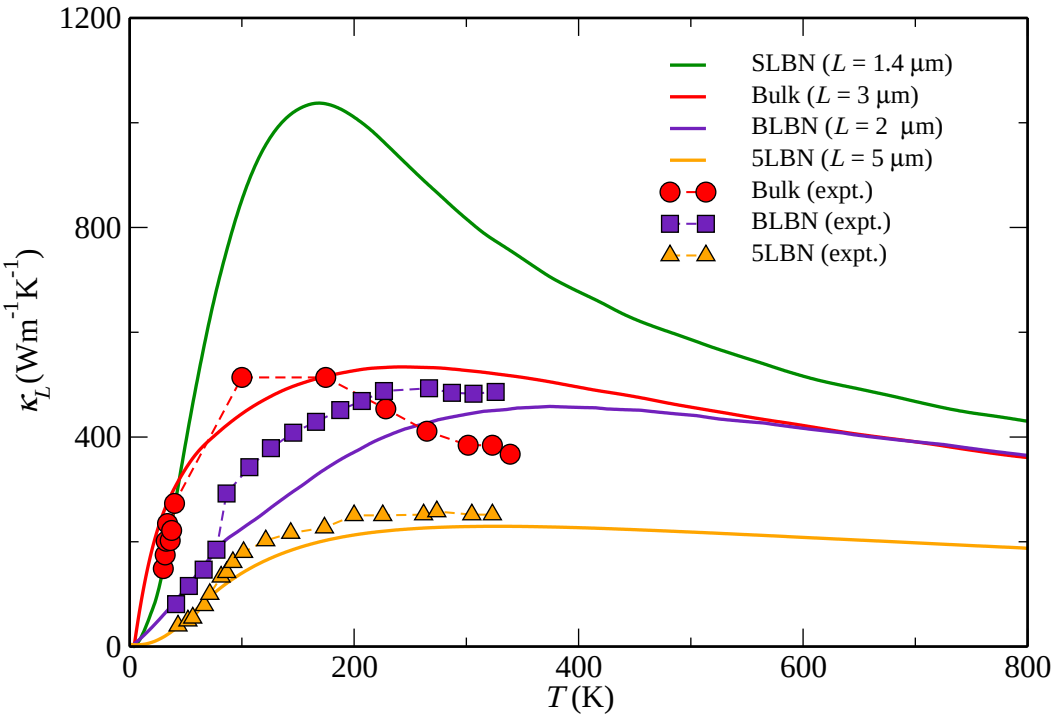

Figure 4.6: Calculated thermal conductivity of single and multilayer BN shown as a function of temperature at a constant length, using the real space approach. The square, circle, triangle data points refer to experimental measurements for BLBN [28], Bulk *h*-BN [26] and 5LBN [27], respectively.

tally [26] the maxima is found between 150-200 K and tends to saturate to a value $\sim$ 400 Wm^{-1}K^{-1}. Lindsay *et. al.* [151] varies the sample length and finds an excellent fit with the experimental data for $L = 1.4\mu$m. It must be noted that the sample length is not mentioned in the experimental reference [26] for Bulk-*h*BN. As the length of the sample increases, the maxima of $\kappa_L(T)$ shifts towards the left, *i.e.* the maxima is found at a lower temperature. Therefore for BLBN and 5LBN, where the lengths used in the experiments are larger than 1.4 μm, the maxima would be at lower temperatures, in total disagreement with the experiments [28, 27]. Our calculations for BLBN and 5LBN are in excellent agreement with experiments for the same lengths. Even though our calculated values diverge from the experimental measurements by Sichel *et. al.* [26] at higher temperatures, we believe that the behavior of κ_L as calculated by us for bulk-*h*BN is correct. However, further experiments should throw more light on these discrepancies. It is our conjecture that κ_L of Bulk-*h*BN should be similar to that of BLBN since the phonon dispersions in the two cases are very similar.

In Fig. 4.7 we show the acoustic mode dependent contributions to the total thermal conductivity for SLBN and MLBN by solving the phonon BTE beyond

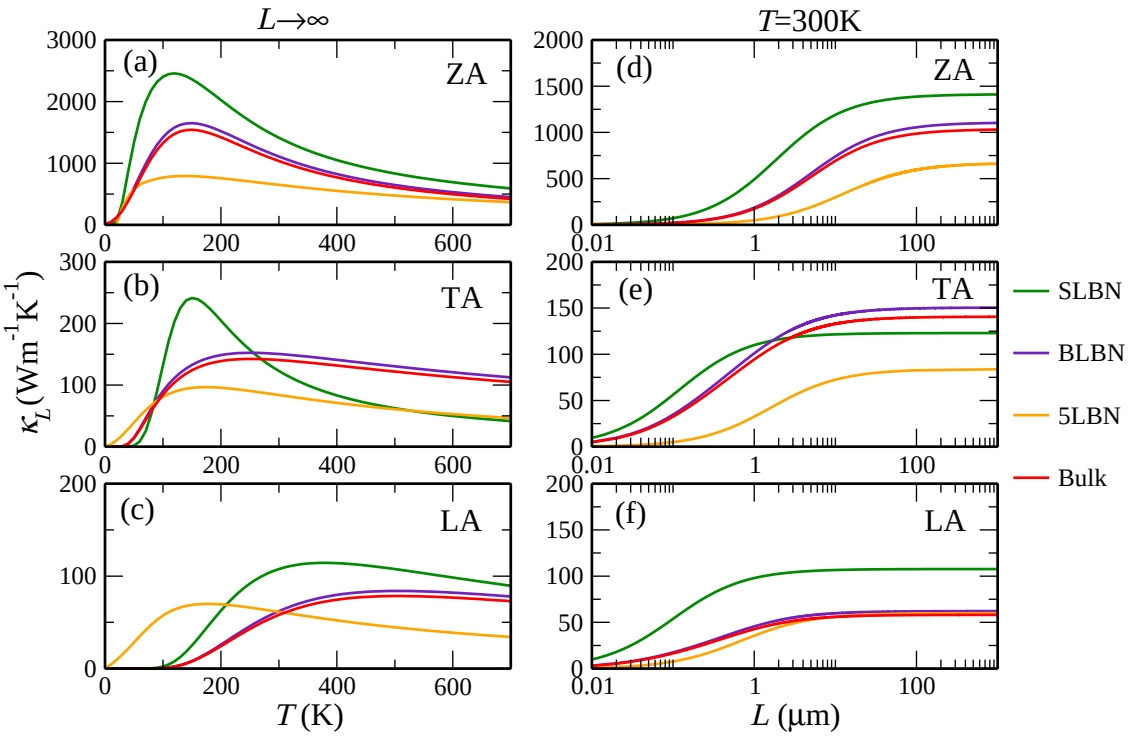

Figure 4.7: Contribution to the thermal conductivity of single and multilayer BN from the acoustic modes; (a) ZA, (b) TA and (c) LA, shown as a function of temperature in thethermodynamic limit ($L \to \infty$), and as a function sample length at $T = 300$K (d,e,f) using the real space approach.

the RTA. The out of plane mode is clearly seen to contribute the most to the lattice thermal conductivity for all the mentioned structures. For SLBN the contributions from the ZA, TA and LA modes to κ_L at room temperature are $\sim$ 86.1 %, 7.4 % and 6.5 %. A similar trend is observed in graphene [226]. Qualitatively one can understand why the ZA mode contributes the most to κ_L by calculating the number of modes per frequency for each of the acoustic mode. Now the number of modes per frequency is proportional to the 2D density of phonon modes, $D_s(\omega) \propto \frac{q}{2\pi}\frac{dq}{d\omega}$, and hence the ratio of $D_{ZA}(\omega)$ and $D_{TA(LA)}(\omega)$ would give a measure of the contribution of the respective phonon modes. Assuming a quadratic fit to the ZA dispersion, $\omega_{ZA} = \alpha q_{ZA}^2$, and a linear fit to the in-plane TA and LA phonon dispersion, $\omega_{TA(LA)} = v_{TA(LA)} q_{TA(LA)}$, the ratio of the density of phonon modes is $\frac{D_{ZA}}{D_{TA(LA)}} = \frac{v_{LA(TA)}^2}{2\alpha\omega_{LA(TA)}}$. Here α and $v_{LA(TA)}$ are fitting parameters to the phonon dispersions shown in Fig. 4.1 and their values are shown in table 4.2. Substituting these values, it is evident that $\frac{D_{ZA}}{D_{TA(LA)}} \gg 1$ at the long wavelength limit suggesting that the major contributions to the lattice thermal conductivity are due to the out of plane modes. Representing the ZA contribution of the thermal conductivity of MLBN at room temperature

with respect to SLBN, we observe that $\kappa_{ZA}^{SLBN} = 1.28\kappa_{ZA}^{BLBN} = 2.17\kappa_{ZA}^{5LBN}$, suggesting that the significant decrease of κ_L from SLBN to MLBN is because of the additional raised frequencies of the ZA layered breathing modes.

Kong *et. al.* [177] reported that the lattice thermal conductivity of single layer graphene and bilayer are similar, $\kappa_L^{graphene} \approx \kappa_L^{bilayer}$, while Lindsay *et. al* [188] reported $\kappa_L^{graphene} \approx 1.37\kappa_L^{bilayer}$. The difference in their methodologies is that the latter has taken graphene symmetry into account, which is discussed in detail by Seol *et.al.* [210] and Lindsay *et.al.* [188]. Besides the contribution due to the layer breathing out of plane modes, a decrease in κ_L is also due to the violation of the selection rule [210, 188] which is incorporated in the formalism in the super-cell real space approach. In Fig. 4.7 (d,e,f), we show the mode dependent κ_L at room temperature as a function of sample length. At any given length, the maximum difference in κ_L contributed from LA and TA modes for all the mentioned structure is ~ 47 and 65 $\mathrm{Wm^{-1}K^{-1}}$ respectively while that from the ZA mode is ~ 750 $\mathrm{Wm^{-1}K^{-1}}$, an order of magnitude larger, implying that the contribution from the in-plane thermal conductivity is almost independent of the number of layers. This characteristic has been seen using a Tersoff potential in the case of single and multilayered graphene and boron nitride [188, 245]. This rapid decrease in κ_L by increasing the number of layers, which is mainly due to the ZA mode, suggests that the interlayer interactions are short ranged, *i.e.*, the BN layers only interact with neighbouring BN layers [188]. In all of the structures, the contribution to κ_L from the ZA mode have a stronger L dependence as compared to the TA and LA modes, *i.e.*, the contributions from the in-plane modes saturate to their thermodynamic limit at a lower L value as compared to the contributions from the out-of-plane modes. This is due to the larger intrinsic scattering times allowing the ZA phonons to travel ballistically and the relatively smaller scattering time which reflects the diffusive transport of the TA and LA phonons [188]. Calculations based on the mode dependent contributions to κ_L as a function of mean free path and recent advanced experimental techniques [153, 154, 155] should motivate further studies in these directions.

The in-plane phonon contributions having a small L dependence in comparison to the contributions from the out of plane has been calculated for graphene recently using the Tersoff potential [185] and their calculated cumulative mode

dependent thermal conductivity behavior is in good agreement with our calculations for SLBN.

4.4 Summary

Phonon dispersions using a LDA pseudopotential with vdW interactions, density of states (DOS), the Grüneisen parameters and the lattice thermal conductivity have been calculated by the Callaway-Klemens and Real space super cell approach for SLBN, BLBN, 5LBN and Bulk-*h*BN. Additionally, in the case of Bulk*h*-BN, we calculate the two-phonon DOS. Irreducible representation using the character table at the Γ point in the BZ for each of the systems have been derived in order to compare the symmetry modes with those obtained from Raman and infrared spectroscopy experiments. Results from the investigations by EELS data, Raman, second-order Raman and Infrared spectroscopy are found to be in excellent agreement with the theoretical calculations based on the phonon dispersion, DOS and two-phonon DOS which rely on the harmonic second order inter atomic force constants.

Further, we have calculated the sample length and temperature dependence of lattice thermal conductivity by the real space super cell approach with the help of the second order IFCs calculated by DFPT. Lattice thermal conductivity at the thermodynamic limit for each system has a maximum between the 110-150 K. For sample sizes in the range 1-5 μm, κ_L does not have a maximum. However with increase in temperature it tends to saturate at a value which is an order smaller than the thermodynamic limit.

Our mode dependent calculations using the real space method suggests that the majority of the contributions to the thermal conductivity are due to the ZA phonons for all of the structures. The substantial decrease in κ_L from single to MLBN is because of the additional layer breathing modes but mainly due to the fact that the interlayer interactions breaks the SLBN selection rule resulting in suppressing the ZA phonons contributions to κ_L in MLBN. Contribution to κ_L from the in-plane modes are not sensitive to the number of layers and have a lower L dependence compared to the out of plane modes. This reduction in κ_L from SLBN to MLBN which is mainly due to the ZA phonons indicate that

the interlayer interactions are short ranged. The L dependence of the TA and LA contributions to κ_L saturate to their thermodynamic limit faster than that of the contribution from the ZA phonons implying that the ZA phonons travel ballistically along the sample while the TA phonons travel diffusively.

Grüneisen (γ) parameters were obtained from first principle calculation by applying a positive and negative biaxial strain. For the in-plane acoustic modes, we find that γ does not vary much from its mean value but the out-of-plane modes have a strong q-dependence. Our calculated γ values for Bulk-*h*BN at the Γ point is $\sim 1\%$ larger than those obtained from experiments which measures the pressure dependence of Raman lines. γ parameters for 5LBN suggest that due to the layer breathing modes, atoms along the perpendicular direction lose their coherence between each layer and decrease the phonon frequencies when under a biaxial strain.

In comparison to the real space super cell approach, lattice thermal conductivity has been calculated, both analytically and numerically, using Callaway-Klemens formalism. To obtain analytical solution of the phonon, we make a linear fit to the LA and TA modes, a quadratic fit to the ZA mode, and use an averaged value for its Grüneisen parameters for the γ parameters corresponding to the in-plane acoustic modes and an inverse square wave-vector dependence γ for the out-of-plane modes. Theoretical results for sample length and temperature dependence of κ_L are in good agreement with experimental observation. The phonon BTE is then solved analytically and numerically for SLBN, BLBN, 5LBN and Bulk-*h* BN to calculate κ_L for a constant length over a wide range of temperatures and *vice versa* again in good agreement with available experimental results.

Both the theoretical approaches, *i.e.* real space super cell and Callaway-Klemens, show the same magnitude for κ_L but the temperature dependence by the two methods are different. The lattice thermal conductivity for these materials are practically length independent for sample lengths greater than 100 μm which tends to their thermodynamic limit. Calculated values for κ_L for BLBN and 5LBN agree very well with experiments when calculated by the real space approach rather than by the Callaway-Klemens method. This may be because the experimental behavior of κ_L for both BLBN and 5LBN tend

to saturate at higher temperatures instead of having a maxima. However, the Callaway-Klemens method agrees better with available experimental data for Bulk-*h* BN. Further experiments could resolve this discrepancy.

Mode dependent numerical calculations using the Callaway-Klemens formalism suggest that ZA modes dominate only at very low temperatures and have the least contribution as the temperature is increased. This is in stark conflict with our calculations based on real space super cell approach. Since the velocities and Grüneisen parameters are extremely similar for single and bi layer boron nitride, one would expect κ_L for both the systems to be similar. However, in the case of graphene, we have a significant reduction in κ_L which is seen both experimentally [23] and theoretically [188, 22]. The larger κ_L in SLBN in comparison to BLBN using the Callaway-Klemens method was due to the symmetry put by hand and not a consequence of the theory. This implies that the closed form of the relaxation time used in Callaway-Klemens method is a poor approximation having little predictive value and one must solve the BTE beyond the RTA. Our calculations suggests that for an enhanced figure of merit, ZT, in such materials, the sample length must be in the μm range or smaller and should be stacked on top of each other.

Chapter 5

Thermoelectric transport properties of graphene/boron-nitride/graphene heterostructure nanomaterials[1]

5.1 Introduction

In this chapter we present a computational study of the thermoelectric properties of sandwiched heterostructures of Graphene and *h*-BN. We have used density functional theory (DFT) based electronic structure method and Boltzmann transport theory for the band electrons to calculate the electrical conductivity (σ) and Seebeck coefficient (S). A large-scale equilibrium molecular dynamics (MD) simulation using Green-Kubo formalism [246, 247] at constant temperatures was used to compute thermal conductivity (κ) of these heterostructures at various temperatures. Our calculations allow us to study electrical and thermal transport in the directions parallel and normal to the plane of G/*h*-BN/G and thus permit a direct comparison of our simulation results to the experimental data. Our calculations show that for certain configurations of the heterostructured nanomaterials the Power factor and Figure-of-merit (ZT) are close to recent measurements [15]. Moreover, our calculated κ for the multilayers and bulk

[1] Based on a publication by **R D'Souza**, S Mukherjee, Physica E **81**, 96 (2016)

h-BN shows a qualitative agreement with recent experimental results of Jo *et al.* [27]. Calculated κ along orthogonal directions in planar G/*h*-BN striped heterostructures also quantitatively agree with previous calculations [29].

5.2 Computational details

Density functional theory

All the electronic structure calculations were carried out using Density Func-

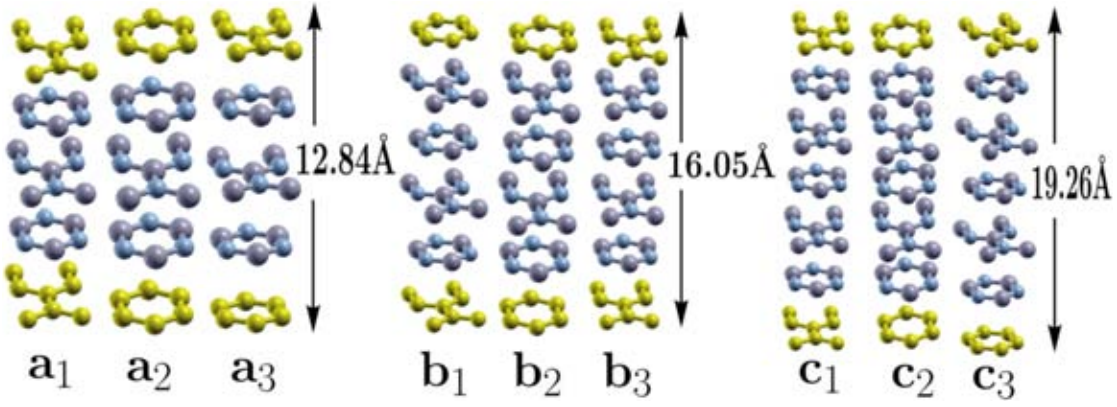

Figure 5.1: Supercells of G/*h*-BN/G heterostructures with three (left), four (middle) and five (right) *h*-BN layers showing three different types of arrangement of Graphene and *h*-BN layers. The numbers indicate thickness of the heterostructures in Å.

tional Theory (DFT) based plane-wave method, described in section 2.1, as implemented in the Quantum Espresso code [139], using an orthorhombic unit-cell. The generalized gradient approximation (GGA) [128] was used for the exchange-correlation potential and the ultrasoft pseudopotential [17] was used to describe the core electrons. Self-consistent calculations were performed using a converged Monkhorst–Pack k-point grid [133] of $48 \times 48 \times 2$ with a plane wave basis with kinetic energy cutoff of 40Ry and charge density energy cutoff of 160Ry, respectively. The periodically repeated unit cells are separated by a vacuum spacing of 22Å along the z-direction. This is reasonable since, the widths are typically 10^4 times larger than the height of the sample [27]. We have considered Van der Waals interaction [248, 229] between the layers. For one *h*-BN layer sandwiched between two graphene layers, we have minimized the total energy and pressure to get a lattice constant of 2.48Å and interlayer distance of 3.21Å. *h*-BN layers were added at a distance of 3.21Å above the previous layer. It should be noted that addition of layers does not change the pressure

of the unit cell. As it has been shown that the AB stacking is the most stable [249] the *h*-BN layers were fixed to the AB stacking while graphene sheets were changed as shown in Fig. (5.1).

Equilibrium molecular dynamics for the calculations of lattice thermal conductivity

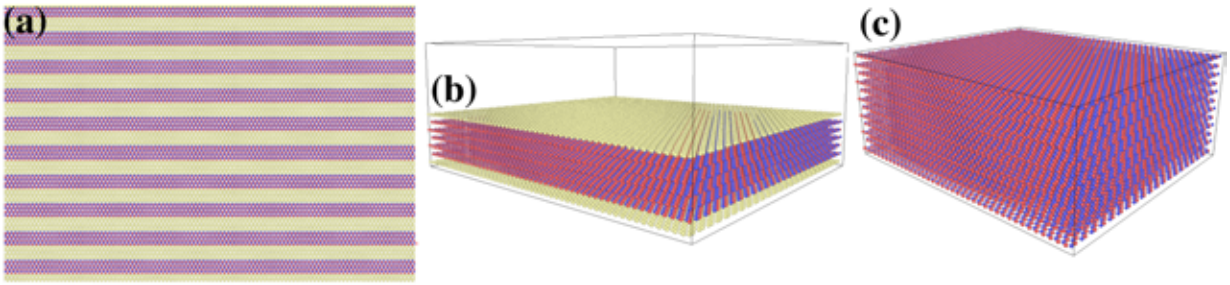

Figure 5.2: The simulation cells used in our molecular dynamics study for (a) graphene/ boron-nitride striped heterostructure (b) Graphene/boron-nitride/Graphene layered heterostructure and (c) Bulk-Boron nitride. The yellow balls refer to that of carbon. The blue and red balls refere to that of boron nitride.

The equilibrium molecular dynamics calculations as described in Section 2.4 were carried out using the LAMMPS code [250]. The total number of iterations in the calculations of thermal conductivity were 10^5 with a time step of 1 fs. The number of atoms in the simulation cells varied between 40000 to 60000 atoms. The simulation cells used in the calculation of the lattice thermal conductivity are shown in Fig. 5.2. Each of the simulations started with different random initial velocities. The error bars in all our MD calculations are estimated from five different sets of MD runs having these different random initial velocities.

5.3 Results

5.3.1 Electron transport coefficients of G/h-BN/G heterostructures

The relaxation time for G/*h*-BN/G heterostructures are not known but are typically in the order of 10^{-14}sec. Hence the numerical value used here is 1×10^{-14}sec. Calculations were performed for all topologies as shown in Fig 5.1 but the results are almost identical except for a small change in Fermi energy (E_F). We therefore report Seebeck coefficient, Power Factor and Figure of Merit for only a specific arrangement as shown in Fig.5.3 a3,b3,c3. Fig. 5.3 and 5.5

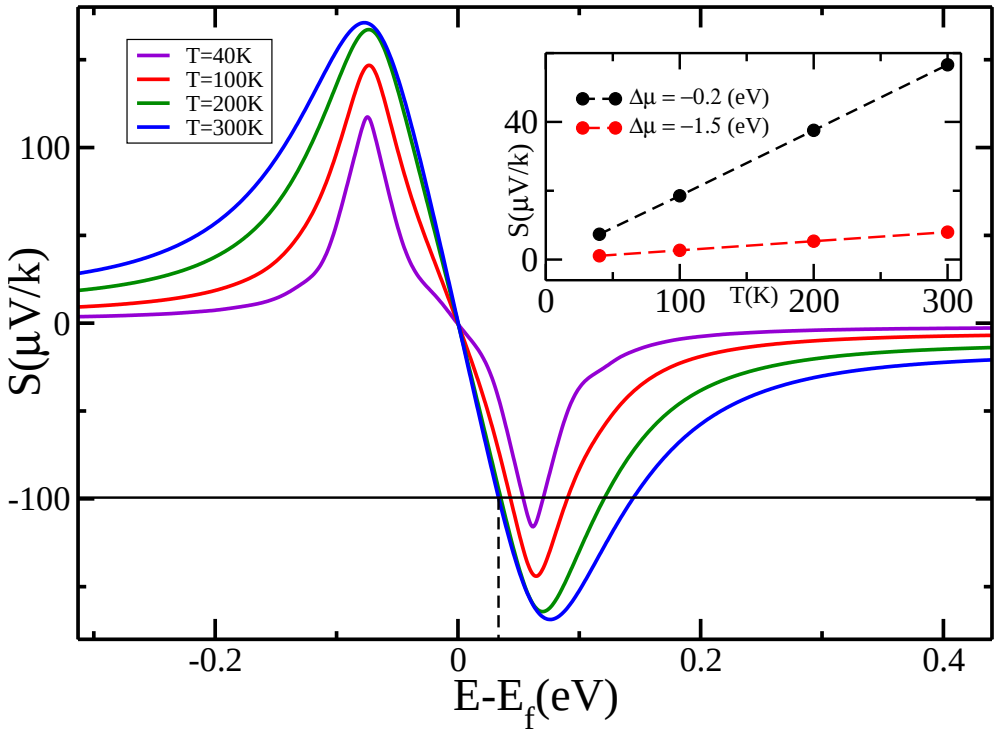

Figure 5.3: Calculated Seebeck coefficient of G/*h*-BN/G plotted against energy using the Mott's formula using equation 2.93 at various temperatures. The black horizontal line refers to the experimental value at T=300K [15]. The inset shows the Seebeck coefficient plotted against Temperature at a constant chemical potential.

refers to the Seebeck coefficient and power factor of G/*h*-BN/G heterostructure having 5 BN layers as shown in Fig.5.3 c3.

Though the band gap of G/*h*-BN/G heterostructure is formed due to *h*-BN, the Fermi level does not shift since the number of boron atoms is equal to the number of nitrogen atoms. Further, since boron is an acceptor whereas nitrogen is a donor, the total number of charge carriers n remains the same as that in graphene and hence the conductance at low temperatures, which is essentially proportional to $\sqrt{n}$ is essentially that of graphene [5]. We therefore expect that the form of S, which depends only on conductivity, to have a similar form as that of graphene. In Fig. 5.3 we see that, as expected, the form of S is that of graphene. However, at very low temperatures the Seebeck coefficient has a flat region around the Fermi energy which is due to the band gap.

In the 40K - 300K temperature (T) range it is seen that the conductivity decreases as T increases. Therefore S increases as T increases as seen in the inset of Fig 5.3, where we plot S as a function of T at constant chemical potential. The linear dependence of S on T suggests that the mechanism for thermoelectric generation is diffusive thermopower [190]. $S > 0$ for chemical potentials lower than the

Fermi energy, $S = 0$ at Fermi energy and $S < 0$ for values greater the Fermi energy.

The sign of S indicates the sign of the majority charge carriers. This is also observed experimentally when the gate voltage crosses the charge neutrality point (CNP). $S = 0$ at the CNP. We thus see a direct correspondence between chemical potential and gate voltage. Thus, the gate voltage can tune the chemical potential. As seen in Fig 5.3, the chemical potential changes sign at the Fermi level. The effect of chemical potential on S can thus be demonstrated by tuning the chemical potential (Fermi energy E_F).

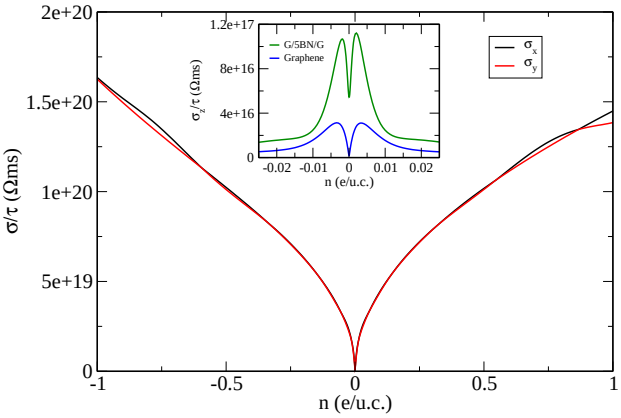

Figure 5.4: A plot of conductance (σ) calculated along x-, y- and z-directions (inset) against the charge carrier (n).

We would like to mention that we have calculated the the components of σ along the Cartesian axes, with z-axis being normal to the plane of the G/*h*-BN/G heterostructure, as seen in Fig. 5.4. Then using the Mott's formula 2.93, Seebeck coefficients were calculated along the principal directions Fig. 5.6. We have obtained a finite S_z near the Fermi energy which contributes to the total Seebeck coefficient which could be due to periodic boundary condition. We feel that the electrical conduction along the z-axis should include contributions also from the other two principal directions, as planar Graphene is used as the contact on both sides of multi-layer *h*-BN in the experiment [15].

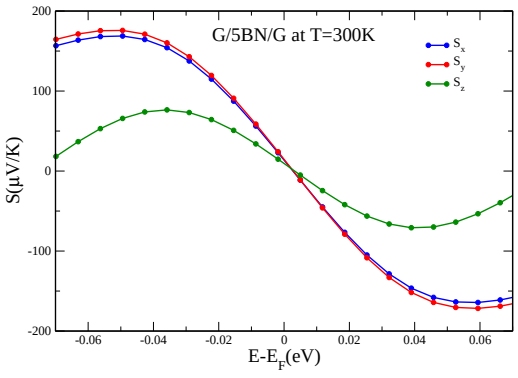

Figure 5.6: Calculated components of Seebeck coefficient of G/*h*-BN/G heterostructure with five *h*-BN layers along x-, y- and z-directions using the Mott's formula (Eq (7)). Note, the finite contribution of S_z near the Fermi energy.

Experimentally the Seebeck coefficient of G/*h*-BN/G was measured by applying a temperature gradient between the top and bottom Graphene layers using Raman spectroscopy [15]. For a temperature gradient $\Delta T = 39$ K at a constant thermoelectric voltage $\Delta V = 4$mV, they obtained $S = -99.3\mu$V/K. This method was employed by Chen *et al* [15] to measure the Seebeck coefficient of G/*h*-BN. To com-

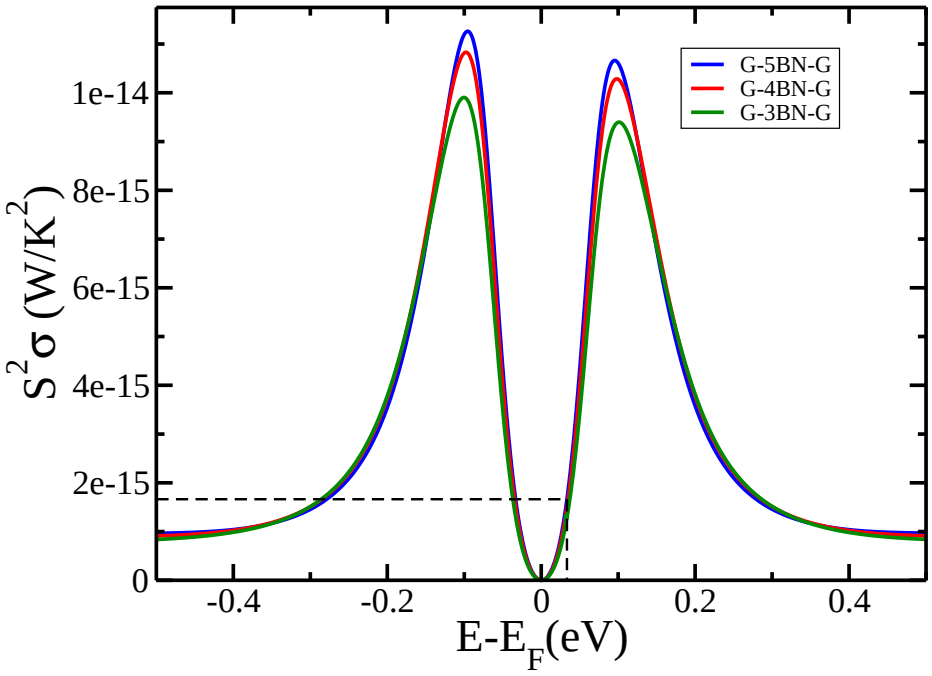

Figure 5.5: Calculated Powerfactor for different layers in G/*h*-BN/G. The black horizontal line refers to the powerfactor which corresponds to the chemical potential that yields the experimental Seebeck coefficient by Chen et al [15].

pare our calculations with that of Chen *et al.* [15] we fixed the chemical potential corresponding to the experimentally measured S as shown in Fig. 5.3. The power factor for the three different arrangements of G/*h*-BN/G heterostructures are shown in Fig. 5.5. The chemical potential which corresponds to that of the gate voltage of Chen et al [15] has been shown by the black dotted line.

5.3.2 Lattice thermal conductivity using equilibrium molecular dynamics

5.3.2.1 G/*h*-BN Planar striped heterostructure

In order to test the equilibrium MD method [250] for the calculation of thermal conductivity, we first calculated κ for two-dimensional striped heterostructures of Graphene and *h*-BN with both armchair and zigzag interfaces between Graphene and *h*-BN domains at $T = 300$K. Our simulation results for κ shown in Fig. 5.7, both parallel and perpendicular to the crystal edges as shown in the inset, compare quite well with the earlier calculations of Kinaci *et al.*[29] which are also plotted for comparison.

We have also compared the ratio κ/κ_0, κ_0 being thermal conductivity of

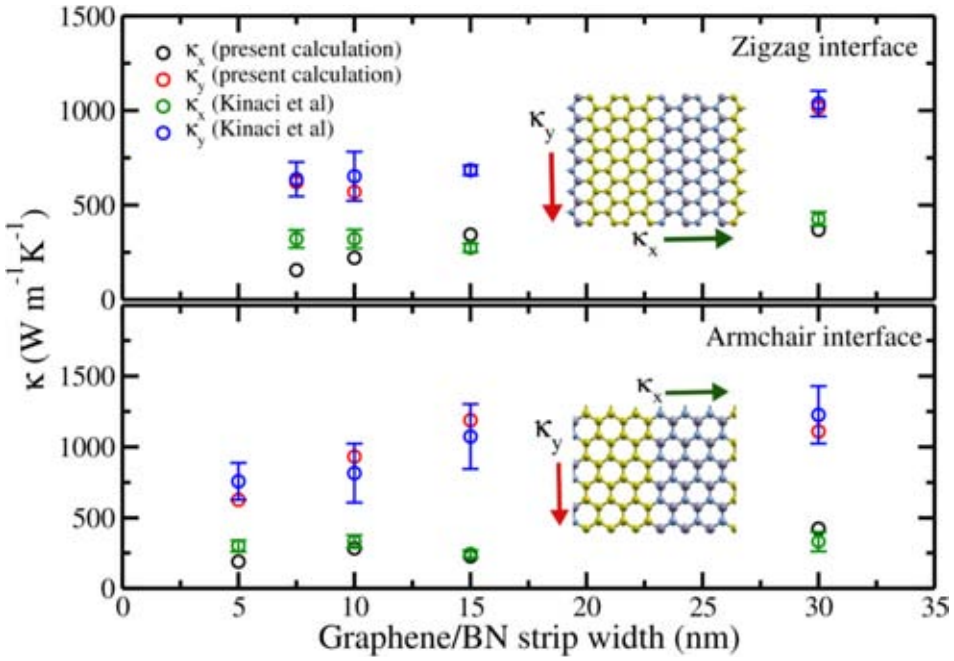

Figure 5.7: Calculated parallel and perpendicular components of thermal conductivity of *h*-BN/Graphene planar striped heterostructures with zigzag and armchair interfaces between G and *h*-BN domains plotted against the width of the domains. For comparison calculations by Kinaci et al. [29] are also shown. The inset shows the atomic arrangements in each interfaces.

pristine Graphene, and obtained this to be 0.3203 for the zigzag and 0.3273 for the armchair interfaces, respectively. These results are in excellent agreement with calculations performed using non-equilibrium Green's function method for Graphene and *h*-BN nanoribbons [104]. Therefore, the use of Tersoff potential based force field was found to be satisfactorily applicable for the thermal transport simulations in Graphene and *h*-BN based heterostructures. The calculated κ for G/*h*-BN/G heterostructures for different sample thickness are given in Fig 5.9 at different T.

5.3.2.2 Bulk and multilayers of h-BN

In Fig 5.8 we show the results of thermal conductivity as a function of the temperature in the range 25-400K, calculated from the equilibrium MD simulation at constant temperature (NVT thermostat)for pure *h*-BN 5-, 11-layers and bulk, and compared with the available experimental results of Jo et al [27]. In each of the calculations, the system was first thermalized to the desired temperature for each set of initial uniform distribution of velocities. κ was calculated for five different sets of initial velocities and the error bar was estimated from the standard deviation.

We found κ increases with T and tend to saturate at $T \sim 220$K for each samples of *h*-BN, with results for 11-layer tending towards the bulk value. Moreover, for each of the three samples of *h*-BN multilayered films, κ shows maxima in the temperature region of 200-250K. We observed an overall agreement of our MD simulation results with recent experimental measurements [27]. For 11-layer and bulk *h*-BN samples the agreement between the simulation and experimental data is better in temperature range 25-300K, whereas for the 5-layer sample the MD results seem to agree only in the temperature range 100-250K.

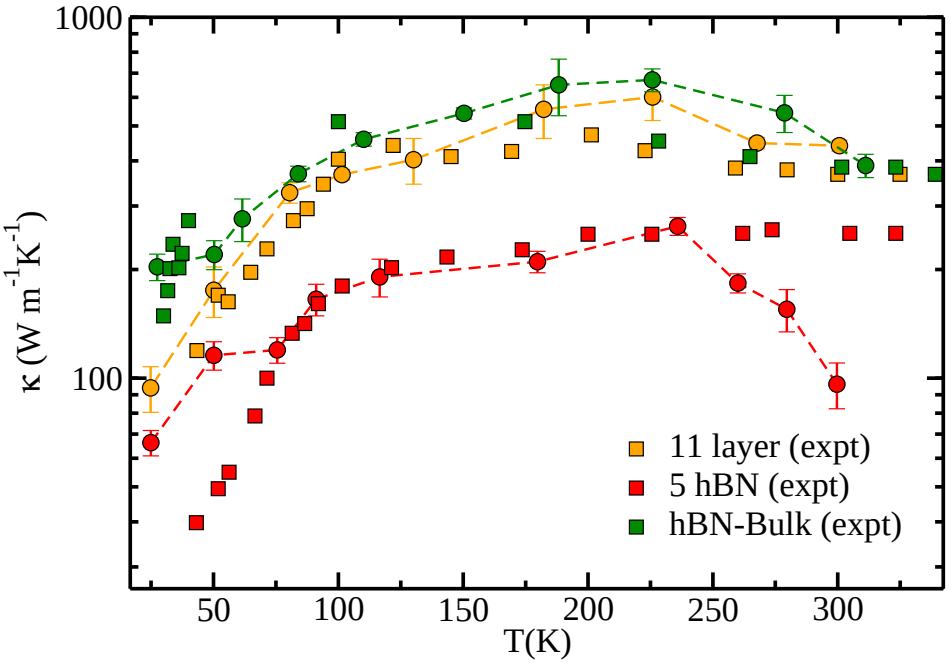

Figure 5.8: Calculated temperature dependence of the thermal conductivity of *h*-BN layers of different thickness. Experimental results [27] are shown as squares and present calculations as circles. The error-bars are calculated from five different sets of calculations using different seeds.

Recently, several calculations have been reported on thermal conductivity of single-layer *h*-BN [151, 251, 252]. Transport calculations by Lindsay et al [151] and Ouyang et al [252], which were calculated from the phonon spectrum using the phonon Boltzmann transport equation, indicate that κ shows a maxima around $T \sim 150$K and decreases with T. Mortazavi et al using MD simulations have reported κ monotonically decreasing with temperature, however all reported values are for temperatures greater than 200K. Our calculated κ for single-layer *h*-BN shows a monotonic decrease with T, not shown here. The numerical value of κ and its variation with T depends on the direct and Umklapp phonon-phonon scattering mechanism [151] and also on the lifetime of such processes. We plan

to investigate these effects using phonon Boltzmann transport theory from the phonon bandstructure later.

5.3.2.3 Thermal Conductance, Power Factor and Figure-of-merit of G/*h*-BN/G Heterostructures

The calculated thermal conductance (K), Power Factor (S^2G) and the Figure-of-merit (ZT) of G/*h*-BN/G Heterostructures with three-, four- and five-layers of *h*-BN at the fixed chemical potential are shown in Fig 5.9. The chemical potential was fixed to obtain the experimentally observed Seebeck coefficient of -99.3 μV/K as shown in Fig 5.3. Note, we have plotted the thermal conductance in Fig 5.9, obtained by multiplying the thermal conductivity (κ) with the height of the G/*h*-BN/G heterostructure as indicated in Fig 5.1. Similarly, for the Power Factor (S^2G), we have taken G as the electrical conductance, so that ZT becomes a dimensionless quantity. It can be seen from Fig 5.5 that as we increase the number of layers, the power factor increases whereas the thermal conductivity decreases with temperature. As a result the power factor increases with temperature. For G/*h*-BN/G heterostructures having 4- and 5-layers, our calculated values agree well with the experimental results as the temperature tends towards room temperature. The Power factor and Figure of Merit will have the same characteristics when plotted against energy at a given temperature, since κ is a function of only temperature.

We would like to emphasize that our calculations involve electrical transport not strictly along the vertical direction, because the Boltzmann transport theory yields smaller contributions to electrical conductivity along that direction compared to those along x- and y-directions. We have calculated the z-component of the Seebeck coefficient (S_z) (Fig.5.6) and found this to be finite and comparable to S_x and S_y close to the Fermi energy. However, this could be due to the periodic boundary we have implemented also along z- directionwith a vacuum of 22 between the sandwiched layers. The total Seebeck coefficient S shown in Fig 5.3, however, shows a quantitative agreement with the experimental data [15]. Thus, we conclude that in the thermoelectric measurements [15] the electrical transport may not be strictly along the z-direction as the upper and lower Graphene contacts with multilayer *h*-BN would allow transport channels

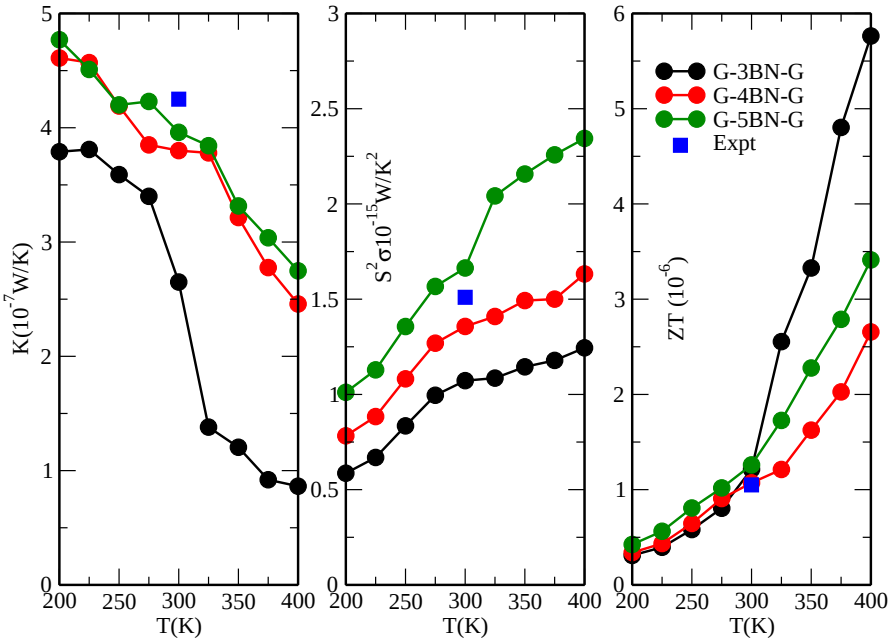

Figure 5.9: Calculated temperature dependence of Thermal Conductance (K), Power Factor (S^2G) and the Figure-of-merit (ZT) of h-BN layers of different thickness shown in the left, middle and right panels; respectively. The available experimental data [15] in each panel at 300K is also indicated.

involving components along x- and y-directions as well. A good quantitative agreement with experimental data also supports above conclusion.

5.4 Summary

We have shown that for three, four and five BN layers sandwiched between Graphene layers, the Boltzmann transport theory gives accurate results for the power factor and the Figure-of-merit, comparable to the experimental data. We have also shown that for sufficiently large number of atoms, MD simulations using the Tersoff type potential yields results in good agreement with experiments for thermal conductance of multilayer h-BN, laterally grown striped Graphene and h-BN two-dimensional heterostructures and sandwiched films of Graphene and multilayered h-BN, using the equilibrium Green-Kubo method. Our calculations may be extended to include phonon bandstructure based transport calculations and using non-equilibrium Green's function based methods.

Chapter 6

Thermodynamic, Electronic Structure and resistivity of Hybrid Hexagonal $C_{2x}(BN)_{1-x}$ Two-dimensional Nanomaterial[1]

6.1 Introduction

Electronic structure [86, 87, 88, 89, 90, 91, 253, 254] and phase stability calculations of $C_{2x}(BN)_{1-x}$ [255] have been reported earlier. In this chapter, we calculate the phase stability of *h*-BN from the free energy using a solution model. Moreover, applying the transport theory of band electrons on the DFT bandstructures we obtain the temperature dependent resistivity of $C_{2x}(BN)_{1-x}$ at different concentrations of C(or BN), which has not been addressed earlier. The interfaces between domains are either armchair or zigzag. We have studied both the interfaces using a $5 \times 5 \times 1$ hexagonal unit cell giving rise to a hexagonal Brillouin zone for each of the interfaces. Calculations using different unit cells for armchair and zigzag interfaces have been reported by Bernardi *et. al.* [30] and Kumar *et. al.* [199]. We then calculate the bandstructure, density of states,

[1]Based on publications by **R D'Souza**, S Mukherjee, Physica E, **69**, 138 (2015) &
R D'Souza, S Mukherjee, T Saha-Dasgupta, Journal of Alloys and Compounds **708**, 437 (2017)

charge density and formation energy of $C_{2x}(BN)_{1-x}$. The emergence of Dirac-cone like features are observed with increasing C concentration. Since *h*-BN has a band gap of nearly 5 eV whereas Graphene is gapless at the high symmetric K-point in the hexagonal Brillouin zone, one would expect the band gap to decrease with increasing C concentration, ultimately becoming zero for $x = 1$. A non-monotonic decreasae of the band gap was obtained for $C_{2x}(BN)_{1-x}$ with increasing x and the concentration dependence, for the two different interfaces, are different. The density of states and charge density suggest that the charge transfer effects play an important role in the formation of the band gap. Using a regular solution model, we studied the phase stability of $C_{2x}(BN)_{1-x}$ calculated from the formation energy and estimated the order-disorder transition temperature. The onsets of substitutional disorder were found to occur at temperatures $\sim$ 3850 K and 6090 K for the zigzag and armchair interfaces, respectively. Finally, using the Boltzmann transport theory applied to the band electrons, we calculate the electrical conductivity (σ) from the bandstructures of $C_{2x}(BN)_{1-x}$. Obtaining the temperature dependent resistivity $\rho(T)$ from $\sigma(T)$ we find, when $\rho(T)$ is plotted in the logarithmic scale versus the reciprocal of temperature $\frac{1}{T}$, a linear behaviour as expected for semiconductors as seen experimentally for $C_{2x}(BN)_{1-x}$ [14, 12].

6.2 Computational details

Density functional theory

The *ab-initio* DFT calculations were carried out using the Quantum espresso code [139] on a 5×5 *h*-CBN unit cell with armchair and zigzag interfaces. Plane wave calculations assume periodicity. To avoid interactions between the sheets, we use a vacuum spacing of 13Å. An ultrasoft pseudopotential [17] was used to describe the core electrons. For the exchange-correlation kernel [128] we used the generalized gradient approximation. A kinetic energy cut-off of 40Ry was used for the plane-wave basis set and of 160Ry for the charge density, and an accuracy of $10^{-}9$Ry was obtained in the self-consistent calculation of total energy. Minimizing the total energy with respect to the lattice constants by ensuring the stress on each atom is zero, the equilibrium lattice constants

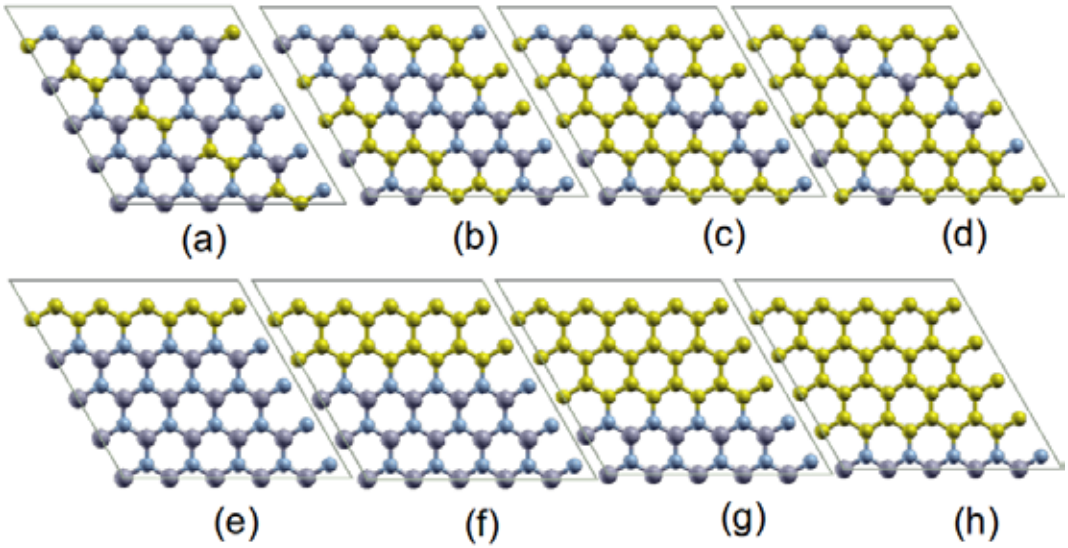

Figure 6.1: 5×5 unit-cell of $C_{2x}(BN)_{1-x}$ with armchair interface (a, b, c, d) and zigzag interface (e, f, g, h), between Graphene and *h*-BN domains, at x = 0.2, 0.4, 0.6 and 0.8; respectively. Carbon atoms are denoted by yellow, Boron by grey and Nitrogen by blue colored balls; respectively.

were obtained. A converged Monkhorst-Pack [133] having a $6 \times 6 \times 1$ k point grid was employed in the self-consistent (SCF) calculations. At each of the equilibrium lattice constants, for both armchair and zigzag interfaces, band structure calculations were performed with 150 k points along the Γ-K-M-Γ high symmetric pints in the irreducible hexagonal Brillouin zone.

6.3 Results and Discussion

6.3.1 Electronic structure and bandgap engineering of $C_{2x}(BN)_{1-x}$ having zigzag and armchair interfaces

Our computed values of the in-plane lattice constant (a_0) for graphene and *h*-BN were to be 2.466Å and 2.501Å, respectively, which compare well with those obtained from experiments. In Fig.6.2 we plot the bandstructure along with the corresponding density of states (DOS) of hexagonal $C_{2x}(BN)_{1-x}$ for $x = 0.2, 0.4, 0.6$ and 0.8, for zigzag and armchair interfaces between Graphene and *h*-BN domains. The total DOS include contribution from $2s$, $2p_x$, $2p_y$ and $2p_z$ of carbon, boron and nitrogen atoms in the unit cell. For each of the atoms, we also plot the partial density of states (PDOS) of the $2p_z$ orbital. The DOS and

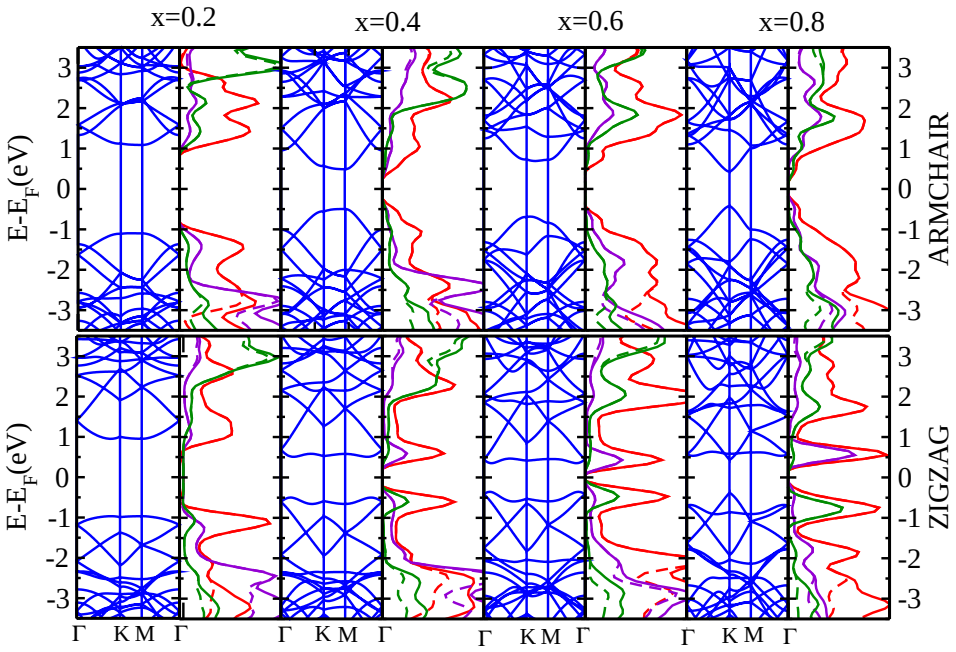

Figure 6.2: The calculated bandstructure and the density of states (DOS) of $C_{2x}(BN)_{1-x}$ at $x = 0.2, 0.4, 0.6$ and 0.8 for armchair (upper panel) and zigzag (lower panel) interfaces. The Fermi energy is at the centre of the band gap. The bands (blue) are shown in the high-symmetry directions Γ-K-M-Γ in the hexagonal Brillouin zone. The total DOS is shown as full-line for C (red), N (violet) and B (green); the corresponding projected density of states (PDOS) of $2p_z$ states for each atoms being shown as dashed-line with similar colors, respectively. The DOS and PDOS are in arbitrary units.

PDOS were calculated for all non-equivalent atoms in the unit cell. The Fermi energy was found to be in the middle of each of the energy gap between the conduction and valence bands. The electronic structure of graphene around the Fermi energy are dominated by the π and π^* orbitals of carbon. The conduction and valence bands of *h*-BN, above and below the energy gap are represented by the π^* orbital of boron and π orbital of Nitrogen [249]. The DOS plotted in Fig.6.2 show that the nature of the bands around the energy gap of hexagonal $C_{2x}(BN)_{1-x}$ are essentially due to the $2p_z$ states of C, B and N since the total DOS is dominated by the PDOS of $2p_z$ orbitals around 2.5eV above and below the band gap at each concentration. With increase in the concentration of Carbon, the bandstructure in Fig. 6.2 shows that the band gap of $C_{2x}(BN)_{1-x}$ decreases. The calculated band gap of undoped *h*-BN was 4.76eV, showing that the band gap of $C_{2x}(BN)_{1-x}$ decreases from 4.76eV as the carbon concentration is increased till it vanishes for pristine graphene ($x = 1$).

For the armchair and zigzag interface between graphene and boron nitride, the nature of the decrease of the band gap with increasing carbon concentration (x) was found to be different and non-monotonic as seen in Fig 6.3. The minimum

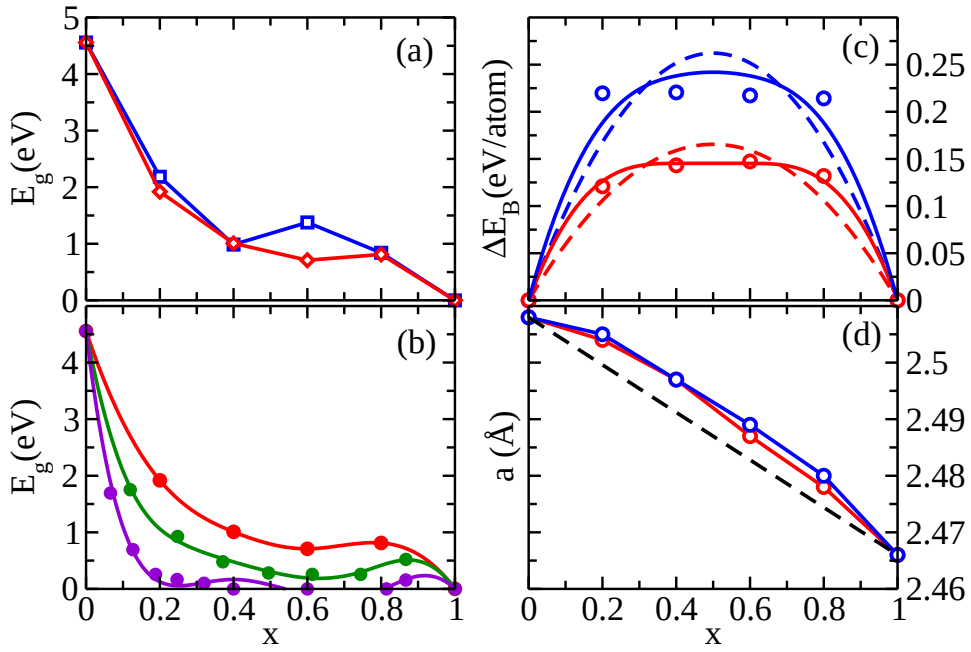

Figure 6.3: Various calculated physical properties of $C_{2x}(BN)_{1-x}$ shown as a function of x, both for armchair (blue) and zigzag (red) interfaces between Graphene and *h*-BN domains. (a) The minimum band gap. (b) Band gap for the zigzag interface fitted with Eq (1), shown for present calculation (red), that of 8×8 cell (green) and that of 16×16 cell (violet) of Bernardi *et al* [30]. (c) Formation energy ΔE_B for both type of interfaces. Calculated data are shown as open circles. Parabolic fit by functions $4\,\Delta H\,x(1-x)$ are shown as dashed lines. A fit by a function of the form $H_0 + H_1\,x(1-x) + H_2\,x^2(1-x)^2$ are shown by solid lines. (d) The equilibrium in-plane lattice constant a. The dashed line refers to Vegard's law.

band gap for the armchair interface appears near the high symmetric M-point of the hexagonal Brillouin zone at $x = 0.2$ and $x = 0.4$. For $x = 0.6$, the minima of the conduction band lies between the high symmetric K and M point having the characteristic of an indirect band gap for the armchair interface. This behavior changes at higher concentration of carbon. At $x = 0.8$, the Dirac cone-like feature appears at the K-point, as expected since the concentration is close to that of graphene, is seen in both interfaces, armchair and zigzag. $C_{2x}(BN)_{1-x}$ having an zigzag interfaces has the characteristic of an indirect gap material at concentrations $x = 0.2$, 0.4 and 0.6. However, at $x = 0.8$ the direct band gap has a value very similar to that seen in the armchair case. The spin up and spin down components of the DOS are the same unlike reported by [86, 87, 88, 89, 90, 91] since those calculation have been performed for nanoribbons. As we move into the nanoribbon, the spin polarization on each atom diminishes and therefore infinite sheets have no spin polarization on each atom. For both, armchair and zigzag interfaces between graphene and *h*-BN, the calculated band gap E_g, the formation energy ΔE_B, and the equilibrium lattice constant a_0 are shown in Fig.

6.3 for $C_{2x}(BN)_{1-x}$ as a function of x. For $x < 0.8$, the indirect band gap is slightly smaller than the direct band at the high symmetric K-point as seen in Fig. 6.3 (a). The Dirac cone-like feature starts evolving at $x \geq 0.8$ having a direct band gap at the K-point. This has been observed in earlier published calculations [30, 199] and is apprantely not observed in seminconductor alloys. To best describe the x dependence of E_g for $C_{2x}(BN)_{1-x}$, we have used a fifth-order polynomial.

$$E_g(x) = [E_g^{h\mathrm{BN}} + E_0\, x + E_1\, x^2]\,(1-x) + [E_2\, + E_3\, x]\, x^2(1-x)^2. \quad (6.1)$$

Where, $E_g^{h\mathrm{BN}}$ is the energy gap of undoped *h*-BN. E_0 is the optical bowing parameter, E_1, E_2, E_3 are the higher order corrections to the bowing parameter, obtained by the fitting procedure given in Table 6.1. We observe that the concentration dependence of the band gap results of Bernardi *et al* [30] performed for larger zigzag interface unit-cell, fit nicely with the form given in Eq. (6.1) shown in Fig 6.3(b).

6.3.1.1 Formation energy and phase stability

The formation energy ΔE_B plotted in Fig. 6.3(c) as a function of concentration x, was calculated using Eq. 2.146. From the calculated formation energy, we investigated the phase stability [256, 257] of $C_{2x}(BN)_{1-x}$ by fitting the calculated data with a parabola, expressing $\Delta E_B(x) = 4\,\Delta H\, x(1-x)$, where ΔH is the formation energy at $x = 0.5$. In the regular solution model, the entropy of mixing can be expressed as point probabilities or the concentration x as shown in Eq. 2.144. The Free energy F(T,x) is defined in Eq. 2.145. At low temperatures $F(T, x)$ shows a maximum at $x = 0.5$, with two minima symmetrically located around $x = 0.5$. As the temperature is increased these two minima converge to give rise to a single minimum at a critical temperature T_C when $x = 0.5$. The critical temperature was obtained from the equation for F(T,x) fulfilling the condition for instability, *i.e.*, $d^2F/dx^2 < 0$ and bounded by the spinodal line, given by [256],

$$k_B T \;=\; 8\,\Delta H\, x(1-x). \quad (6.2)$$

Thus, the critical temperature, $T_C = 2\,\Delta H/k_B$, was estimated to be 3850K for the zigzag and 6090K for the armchair interfaces, respectively. Therefore it is

expected $C_{2x}(BN)_{1-x}$ would be in the disordered phase above those temperatures. A lower bound of T_C can be obtained by estimating ΔH directly from interpolation of the calculated ΔE_B at $x = 0.5$, yielding the transition temperatures to be 3390K and 5060K for the zigzag and armchair interfaces, respectively.

We have also investigated the phase stability of $C_{2x}(BN)_{1-x}$ by using the fit $\Delta E_B(x) = H_0 + H_1\, x(1-x) + H_2\, x^2(1-x)^2$, which gives better than parabolic fit shown in Fig 6.3(c) as full lines. Inclusion of such higher order terms in $\Delta E_B(x)$ leads the transition from binodal to spinodal line to occur at temperatures lower than in the previous model. The free energy was calculated numerically and the T_C was found to be 4869K for the armchair and 3389K for the zigzag interface, respectively (See Fig.6.4). We would like to mention that above calculations for larger supercells are under investigation and will be reported later.

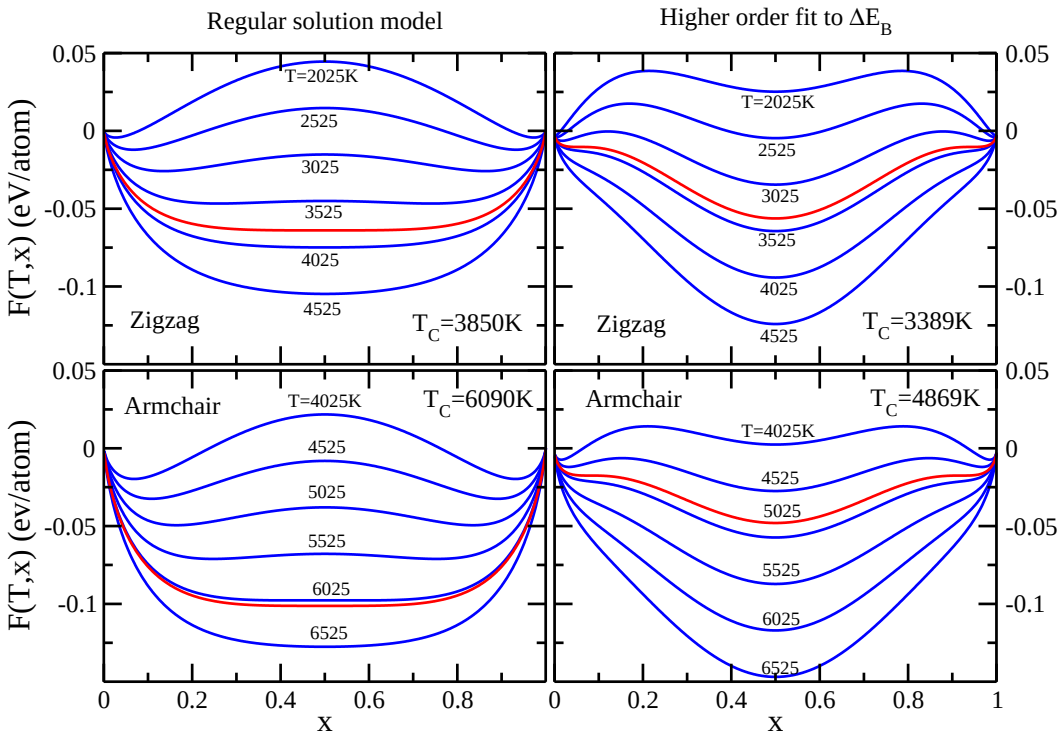

Figure 6.4: (color online). Calculated free energy as a function of concentration x in $C_{2x}(BN)_{1-x}$ at various temperatures for the armchair (lower panel) and zigzag (upper panel) interfaces. The red line, in each figure, indicates the spinodal line at the critical temperature T_C calculated numerically in each case. Figures in the left panel refer to the regular solution model, $\Delta E_B(x) = 4\,\Delta H\, x(1-x)$; and those in the right refer to the higher order fit, $\Delta E_B(x) = H_0 + H_1\, x(1-x) + H_2\, x^2(1-x)^2$, respectively.

The in-plane lattice constant of $C_{2x}(BN)_{1-x}$, $a(x)$ shows a deviation from Vegard's law [258] in Fig. 6.3(d), which has been fitted to,

$$a(x) \;=\; x\, a_{\rm C} + (1-x)\, a_{h\rm BN} + A\, x(1-x). \qquad (6.3)$$

Table 6.1: Numerical value of the parameters in Eqs. 6.2, 6.1 and 6.3. E_0, E_1, E_2, E_3 are in eV, ΔH in eV/atom and A in Å, respectively. The values of E_n without parenthesis refer to that of the band gap at K-point and those within parenthesis to the indirect band gap, respectively.

Interface	E_0	E_1	E_2	E_3	ΔH	A
Armchair	-5.0	-3.993	-48.698	116.768	0.262	0.028
	(0.1813)	(-10.823)	(-76.328)	(158.151)		
Zigzag	-16.554	18.333	11.053	-6.605	0.166	0.022
	(-17.952)	(25.333)	(23.568)	(-52.396)		

Here, A is the deviation parameter for the lattice constant a, obtained from fitting. The fitting parameters in Eqs. 6.2, 6.1 and 6.3 are given in Table 6.1.

6.3.1.2 Charge density and density of states of $C_{2x}(BN)_{1-x}$

Finally, in Fig. 6.5 we show the PDOS and the valence charge density on all in-equivalent atoms across the armchair (Figs. 6.5a and 6.5b) and the zigzag (Figs 6.5c and 6.5d) interfaces of $C_{2x}(BN)_{1-x}$ at $x = 0.6$. The calculated PDOS give a idea about the contributions coming from each in-equivalent C, B and N atoms towards the total DOS shown in Fig. 6.5. The calculated valence charge density (Figs 6.5b and 46.5) indicates that covalent sp-bonding nature is preserved in $C_{2x}(BN)_{1-x}$.

The band structure and the DOS of $C_{2x}(BN)_{1-x}$ are somewhat different for the zigzag interface than armchair interface. The bands immediately above and below the energy gap are more flat, as evidenced by a strong peaks in the DOS. It should be noted that unlike in the armchair interface, in zigzag interface the C atoms are terminated by either all B-atoms or by all N-atoms (Fig. 6.2). This leads to different type of excess charge at the inter-facial C-atoms. We have calculated this excess charge from the difference of the Löwdin charges between the similar atoms in $C_{2x}(BN)_{1-x}$ and that of undoped Graphene and *h*-BN (See Fig. 6.6).

We found, a C-atom terminated by a B (N) atom at the zigzag interface would have more negative (positive) charge than that in undoped Graphene; whereas on the zigzag interface on the other side of the same domain the excess charge on the interfacial C atom would be reversed. This leads to strong peaks in the DOS above or below E_F, which alternates as one goes onto atoms lying deeper in the domain. This effect is illustrated in Fig. 6.5c where we show the calculated

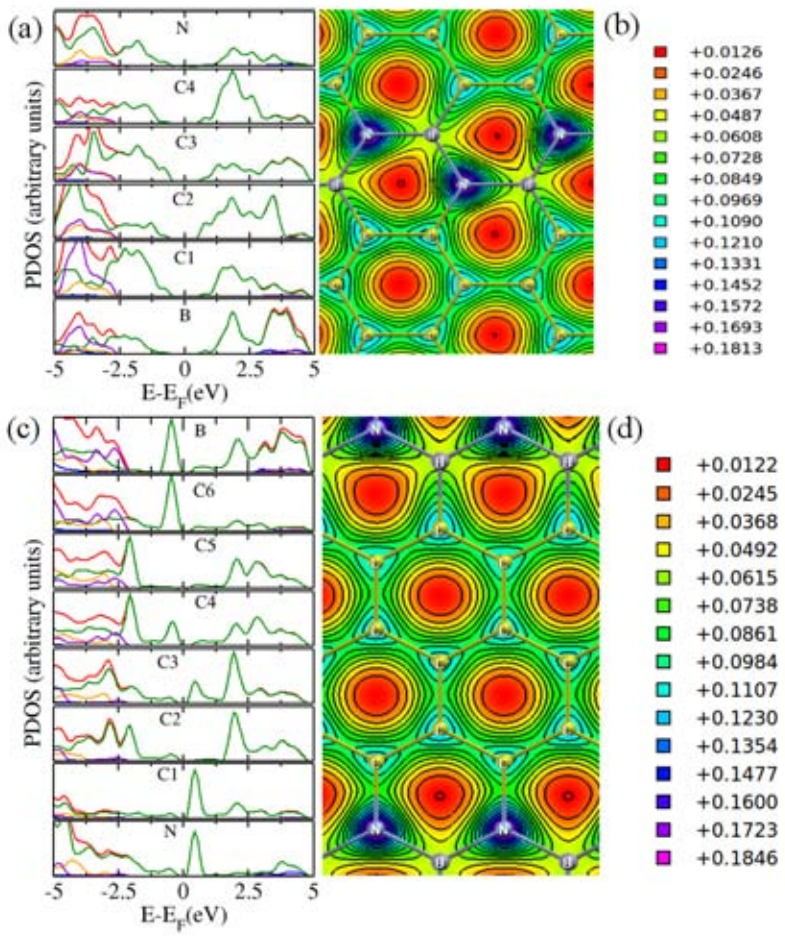

Figure 6.5: (a) : Calculated PDOS on the in-equivalent B, C and N atoms in the unit-cell. C1, C2, C3, C4 denote four C-atoms on the upper hexagon, terminated by B and N shown in (b). The PDOS referring to $2s$, $2p_{\rm total}, 2p_z, 2p_x$ and $2p_y$ orbitals are shown in blue, red, green, orange and violet, respectively. (b) : Calculated valence charge density shown across the armchair interface between Graphene and *h*-BN domains. The contours are in the units of e/Bohr^3. (c) : Calculated PDOS on the in-equivalent B, C and N atoms in the unit-cell. C1 ... C6 denote six C-atoms on the chain, terminated by N and B atoms on two opposite zigzag interfaces shown in (d). (d) : Calculated valence charge density shown across the zigzag interface between Graphene and *h*-BN domains. (a) and (b) refer to $C_{0.6}(BN)_{0.4}$ armchair interface, whereas (c) and (d) refer to the zigzag interface.

PDOS on C-atoms going from one end of the zigzag interface to the other end. Comparing the excess charges on the interfacial C atoms, for both armchair and zigzag interfaces, we found higher is this excess charge, larger is the band gap E_g.

Present calculations may be extended to include higher order corrections to the exchange-correlation energy using HSE [259] or GW [260] methods to check the validity of our results. However, the GGA exchange-correlation kernel used in present calculations yields the ground state physical properties of Graphene and *h*-BN, in good agreement with experimental results.

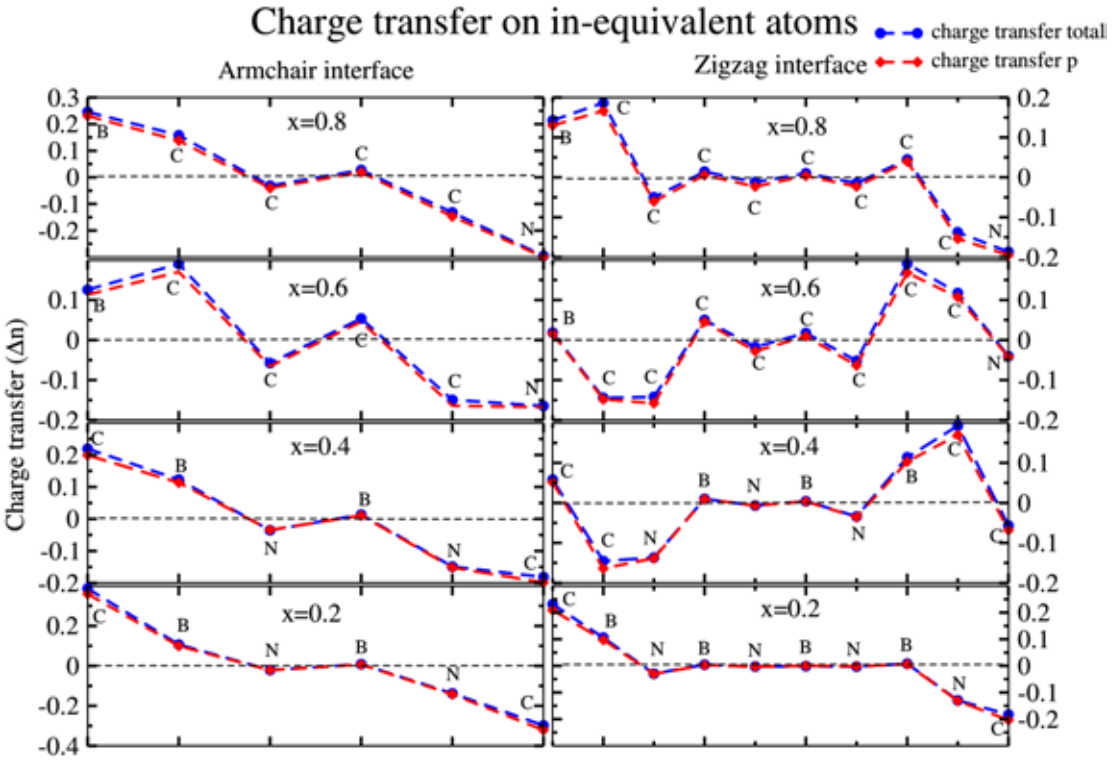

Figure 6.6: (color online). The charge transfer calculated from the calculated Löwdin charges on each inequivalent atoms in the $C_{2x}(BN)_{1-x}$ unit-cell for the armchair (left panel) and zigzag (right panel) interfaces between the Graphene and *h*-BN domains. For each concentration the charge transfer is shown on a set of C, B and N atoms, in a chain or hexagonal ring, which constitute the inequivalent atoms.

6.3.2 Resistivity of $C_{2x}(BN)_{1-x}$

Now we turn to our results of the resistivity $\rho(T)$ of $C_{2x}(BN)_{1-x}$ from the transport calculations. The resistivity of CBN nanomaterials was measured earlier [14, 13]. It was reported that $\ln(\rho)$ varies linearly with T^{-1} for different concentration of B and N, indicating that CBN is semiconducting. The band gap E_g of CBN was estimated from Eq. (6.4) [261]. In Fig. 6.7 we show the results of $\ln(\rho)$ against T^{-1}, assuming $\tau = 10^{-14}$s, for the zigzag interface of $C_{2x}(BN)_{1-x}$ at $x = 0, 0.2, 0.4, 0.6, 0.8, 1$, in the temperature range of 200K to 800K. The calculated data can be fitted very well to straight lines as shown in Fig 6.7 and the band gap E_g at each concentration was calculated from the slope of the lines using the relation,

$$\rho(T) = \rho_\infty \exp\left(\frac{E_g}{2k_B T}\right). \tag{6.4}$$

Here, ρ_∞ is a constant value of resistivity at temperatures tending toward infinity. As mentioned earlier the k-point mesh had to be enhanced to $150 \times 150 \times 1$ for pure Graphene ($x = 1$) to capture the Dirac-point correctly. Also, for the pure

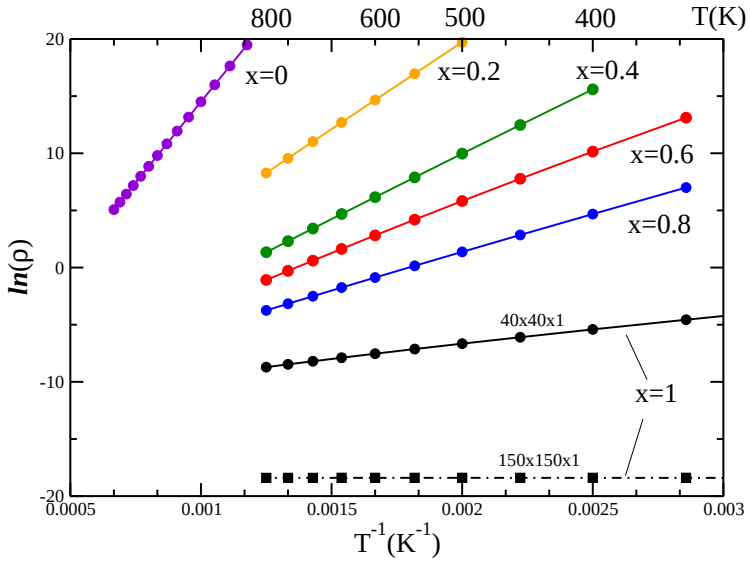

Figure 6.7: $\ln(\rho(T))$ plotted against T^{-1} for $C_{2x}(BN)_{1-x}$ at different concentrations calculated from the Boltzmann transport theory [31] at different concentration.

h-BN we had to calculate $\rho(T)$ at higher temperatures to obtain the measurable slope as shown in Fig. 6.7. In Table 6.2, the band gap E_g of $C_{2x}(BN)_{1-x}$ calculated from the transport theory and those calculated directly using DFT are compared. We find an overall good agreement. It should be mentioned that the numerical value of the relaxation time τ does not affect the the band gap estimation from the slope of Fig 6.7, since the constant ρ_∞ in Eq (6.4) will only shift the origin of the lines in Fig. 6.7 and not affect their slopes. Any discrepancy of the calculated E_g should thus come from inadequate k-point mesh. To our knowledge, this is apparently the first calculation of $\rho(T)$ for the semiconducting nanomaterial $C_{2x}(BN)_{1-x}$ from Boltzmann transport theory.

Table 6.2: Band gap calculated by Bandstructure and Boltzmann transport theory for $C_{2x}(BN)_{1-x}$ for zigzag interface at different concentrations.

x	Bandstructure (Quantum Espresso)	Using Eq. (7) and Fig. (4) (Boltztrap)
0	4.557	4.87
0.2	1.919	2.63
0.4	1.008	1.97
0.6	0.709	1.53
0.8	0.812	1.153

6.3.3 Thermodynamic stability of $C_{2x}(BN)_{1-x}$ and $C_{2x}(BN)_{1-x}$ nanoribbons

6.3.3.1 First-principles study of zig-zag and arm-chair interfaces between strips of h-BN and graphene

In order to study the phase stability of h-CBN, we first computed the cohesive energy(ΔE) of $(\mathrm{C}_2)_x(\mathrm{BN})_{1-x}$, which is also termed as mixing energy since it is related to the energies of the alloy related to the energies of pristine graphene and boron nitride. The negative value of ΔE indicates tendency to form homogeneous solid solution while positive value of ΔE indicates the tendency to phase separate. For each concentration x, we calculated the mixing energy per formula unit (f.u.) of the system using DFT, which is given by the following formula shown in Eq. 2.146, ΔE_B for different values of concentration, x is shown in left panel of Fig. 6.8, for the arm-chair and zig-zag interface. First of all, we find that mixing energy is positive in all cases, suggesting phase segregation between *h*-BN and graphene, in conformity with the literature [262, 263, 200]. Very interestingly we find that the mixing energy is substantially reduced in case of arm-chair interface compared to zig-zag interface. This reduction is most effective at x = 0.5, for which the reduction is about 30%. The difference in the mixing energy between the armchair and zizag interfaces arise because of unequal number of CN and CB bonds per unit length along the interface. We have estimated the number of such bonds to be $\frac{1}{a_0}$ for the zigzag interface while for armchair interface is $\frac{2}{\sqrt{3}} \cdot \frac{1}{a_0}$, where a_0 is the relaxed lattice constant of $(\mathrm{C}_2)_x(\mathrm{BN})_{1-x}$.

From the knowledge of mixing energy, the phase stability of $(\mathrm{C}_2)_x(\mathrm{BN})_{1-x}$ can be computed from a mean field approach, using the so-called regular solution model. The configuration entropy of mixing is defined as Eq. 2.143. Hence for $(\mathrm{C}_2)_x(\mathrm{BN})_{1-x}$ alloys, the entropy of mixing is given by Eq. 2.144 [262]. The free energy $F(T, x)$ is then given by Eq. 2.145. $\Delta E(x)$ is the mixing energy, as plotted in left panel of Fig 6.8. The critical temperature within the regular solution model can be obtained from the condition expressed in Eq. 2.147. Fitting the mixing energy to the analytical form, $\Delta E = \frac{1}{b}\mathrm{Sech}[a(x - \frac{1}{2})]$, it can be shown that the critical temperature will be given by $T_C = \frac{a^2}{8bk_B}$. Fitting

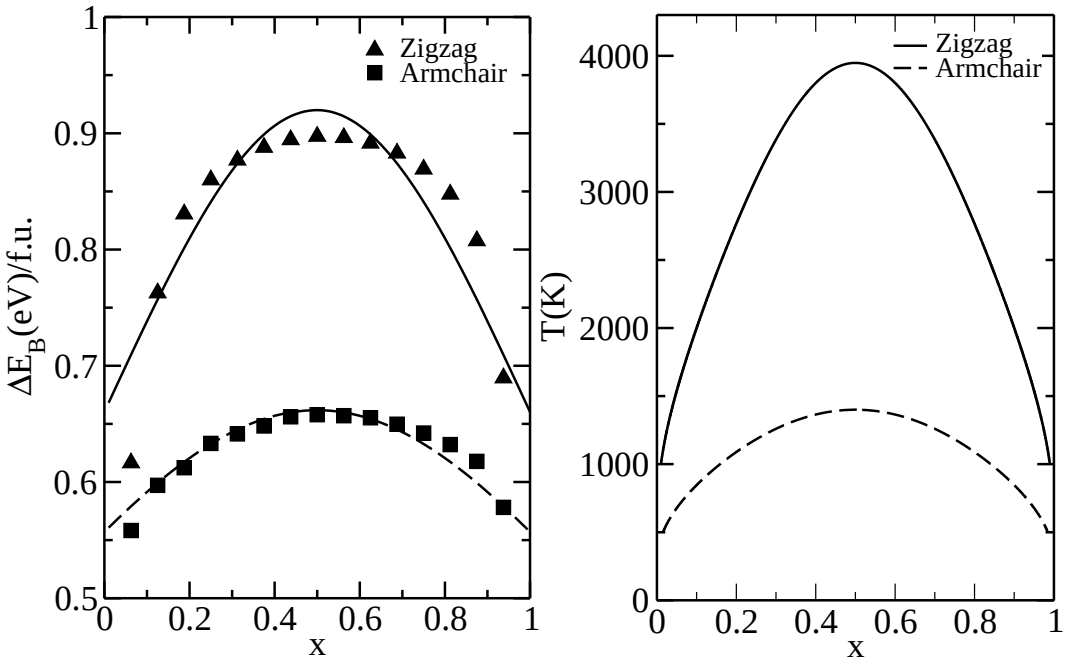

Figure 6.8: Left panel: The mixing energy of $(C_2)_x(BN)_{1-x}$ hybrid for the arm-chair and zig-zag interfaces, plotted as a function of the concentration, x. The lines are the fit of the calculated data points of the analytical form (see text). Right panel: Mean-field phase diagram of $(C_2)_x(BN)_{1-x}$ as a function of the composition range. For each composition, the phase below the line is the segregated phase, while the phase above is the solid solution phase.

parameters for x=0.5, for arm-chair and zig-zag interfaces were found to be $a = 1.208$, $b = 1.511$ and $a = 1.720$, $b = 1.087$ respectively, resulting in a critical temperature of 1400 K and 3948 K. Our computed value of critical temperature for zig-zag interface is in good agreement with the value obtained previously in literature using cluster expansion technique and Monte Carlo,[263] which did not take into account the specficity of the interface geometry. The plot of critical temperatures for the arm-chair and zig-zag interfaces for different values of concentration x is shown in the right panel of Fig 6.8. It follows the same trend as the mixing energy. Notably about a 65$\%$ suppression of the the critical temperature for segregation is obtained in the arm-chair geometry of the interface at x = 0.5, compared to that of the zig-zag geometry. We note that the computed temperatures for arm-chair interfaces are substantially smaller compared to melting point of $(C_2)_x(BN)_{1-x}$ hybrids, which can be approximately estimated from the melting points of h-BN and graphene, which are about 3300 K for h-BN and 4200 K for graphene. Thus if the $(C_2)_x(BN)_{1-x}$ hybrids can be prepared with selectively chosen arm-chair interfaces, it may be possible to arrive at a homogeneous solution of h-BN and graphene, for an

appreciable range of temperature.

6.3.3.2 Calculation of Spinodal line

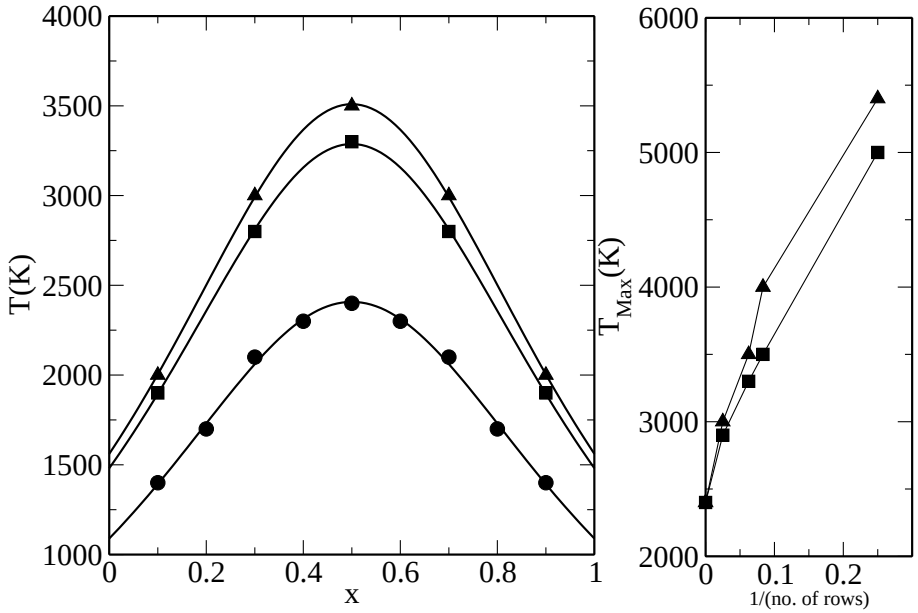

Figure 6.9: Left panel: Spinodal lines for the infinite (circles) sheet, arm-chair (square) as well as zig-zag (triangle) edged nanoribbon of $(C_2)_x(BN)_{1-x}$, calculated by MC simulation. Shown are the data for nanoribbons of width 8 u.c. The lines are guide to eye. Right panel: Calculated transition temperature at x = 0.5 plotted as a function of the inverse of the width of the nanoribbon, for the zig-zag (triangle) and arm-chair (square) edged nanoribbons. The width is measured in terms of number of row of atoms counted along the transverse dimension of the ribbon. Two rows of atoms constitute a unit cell. The data point at zero of the x-axis corresponds to the value obtained for the infinite sheet.

In order to calculate the spinodal line based on MC results, we first defined a suitable order parameter in the following manner. If the number of nitrogen nearest neighbors of boron is n_b, we define an order parameter on each boron to be $\eta_{p_b} = \frac{n_b}{3}$. Similarly, if the number of boron nearest neighbors of nitrogen is b_n , we define an order parameter on each nitrogen to be $\eta_{p_n} = \frac{b_n}{3}$. We then define an average order parameter $\langle\eta\rangle$ for the system as $\langle\eta\rangle = \frac{1}{N_B+N_N}\sum_{i\in B,N}\frac{\eta_{p_b}+\eta_{p_n}}{2}$, which is averaged over all the nitrogen (N_N) and boron (N_B) atoms in the simulation cell. We found that at low temperatures the value of the order parameter increases as the system evolves from an initial random configuration to a final configuration, while at higher temperatures the order parameter evolves close to that of the initial random configuration. After a critical temperature the system accepts any exchange of BN and C dimers keeping the order parameter the same as the random configuration. We defined this temperature as the critical temperature. We repeated this procedure for various concentrations

Table 6.3: Calculated Bond energies of h-CBN infinite sheet (middle column) and zig-zag nanoribbon (right column) for different pairs (left column), obtained from DFT calculations. Similar values are obtained for arm-chair nanoribbon

Type	$E_b(eV)$ Bulk	$E_b(eV)$ Outer most row of nanoribbon
CC	-0.919	-1.30
BN	-0.921	-1.45
CB	-0.654	-1.27
CN	-0.314	-0.85

thus obtaining the spinodal line. The points above the spinodal line refers to the disordered solid solution phase while those below refers to the segregated phase. The left panel of Fig. 6.9 shows the spinodal line for the infinite sheet of $(\mathrm{C}_2)_x(\mathrm{BN})_{1-x}$, and the nanoribbons of $(\mathrm{C}_2)_x(\mathrm{BN})_{1-x}$ having width of 8 u.c. with zig-zag and arm-chair edges. For the infinite sheet, results were obtained for about 20000 atoms in the periodic unit cell, and 2×10^5 MC steps were used to reach the equilibrium. For the nanoribbons, the number of atoms in the lateral direction with periodic boundary condition was chosen to be 10000. We find the critical temperature of phase segregation is substantially high in case of ribbons compared to the infinite sheet, which makes it comparable to the corresponding melting point. This observation that the critical temperature of ribbons being larger than that of infinite sheets is rationalized by the strengthening of bond strengths at edges compared to bulk values (See Table 6.3).

In case of infinite sheet, with interfaces of mixed character the calculated transition temperatures though less than that of the ribbon geometries are high enough, prohibiting mixed solution of h-BN and graphene under normal condition, unless the concentration is very low. In the right panel, we show the variation of the critical temperature at x = 0.5, as a function of the width of the nanoribbon for both zig-zag and arm-chair cases. We find the transition temperature for arm-chair is systematically less than that of the zig-zag nanoribbon with the difference being larger for ribbons of smaller widths. This is in line with our observation from mean-field study of infinite sheet that transition temperatures are suppressed in case of arm-chair interface compared to that of zig-zag interface.

6.3.3.3 MC snapshots

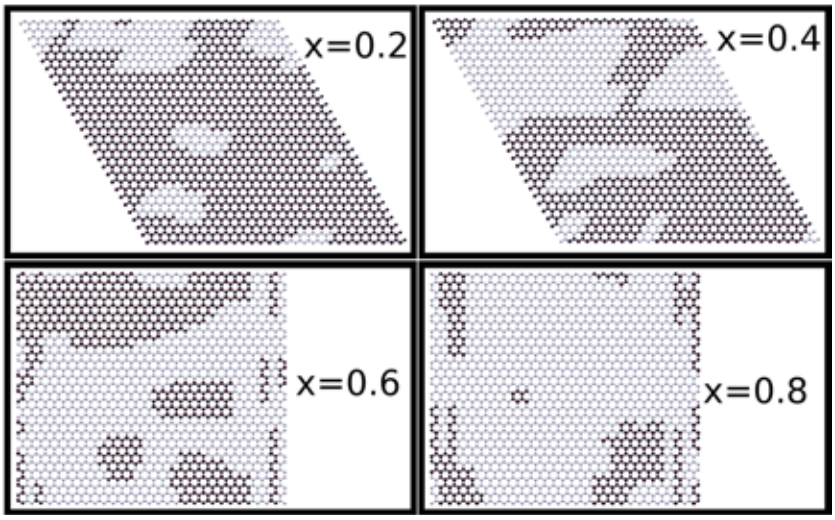

Figure 6.10: Snapshots of equilibrium configuration obtained in MC simulations at T = 300 K for $(C_2)_x(BN)_{1-x}$ infinite sheet using an hexagonal (above) and orthogonal (below) super-cell with x = 0.2, 0.4, 0.6 and 0.8. The color convention of the balls is same as in Fig 2.5.

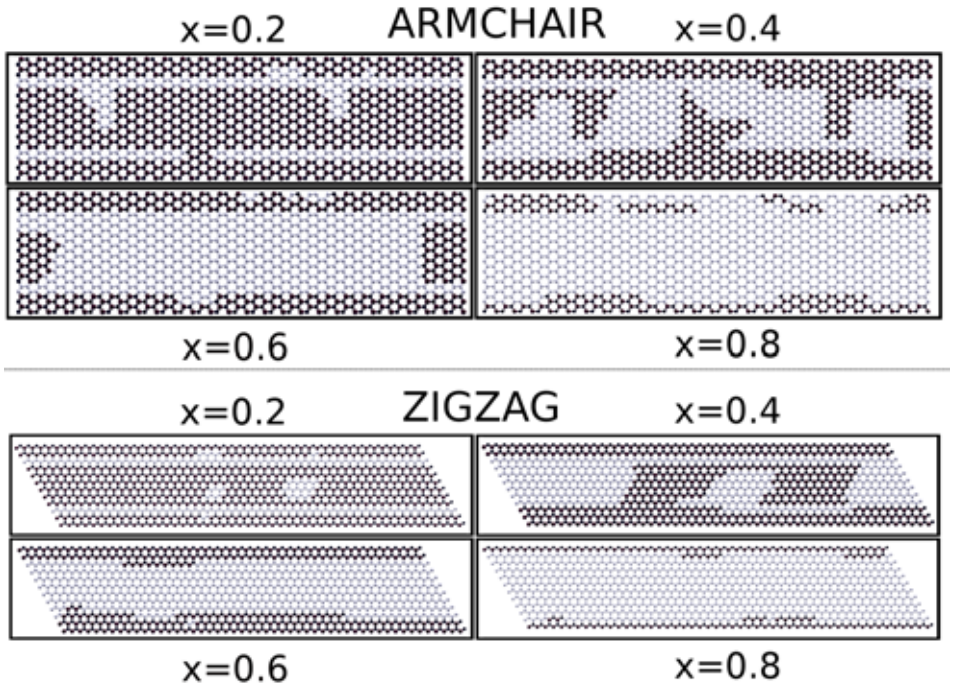

Figure 6.11: Snapshots of equilibrium configuration obtained in MC simulations at T = 300 K for an arm-chair and zig-zag edged $(C_2)_x(BN)_{1-x}$ nanoribbon with x = 0.2, 0.4, 0.6 and 0.8. The color convention of the balls is same as in Fig 2.5.

Considering the case of infinite $(C_2)_x(BN)_{1-x}$ sheet, the achieved equilibrium configurations at room temperature are shown in Fig 6.10, for x = 0.2, 0.4, 0.6 and 0.8. In all cases, we find that depending on the concentration, the final configuration consists of either nanopatches of C atoms embedded in matrix of

BN atoms or BN nanopatches, embedded in the matrix of carbon, suggesting the typical case of segregation. The edges formed between BN and C atoms turned out to be of mixed character with dominance of zig-zag boundaries over arm-chair. Thus, unless enforced through special growth condition, the $(C_2)_x(BN)_{1-x}$ sheet tends to segregate with creation of edges with mixed character, as observed in initial experiments.[14] We further find from the snapshots that in case of ribbon geometry the BN atoms tend to segregate at the edges forming extending phase segregated domains running along the lateral direction of the ribbon, with carbon atoms in general positioned towards the central part of the ribbon. Fig. 6.11 shows the achieved equilibrium configurations for a arm-chair and zig-zag edged nanoribbon at room temperature for x = 0.2, 0.4, 0.6 and 0.8.

6.3.4 Bandgap Engineering in $(C_2)_x(BN)_{1-x}$ including mixed interfaces

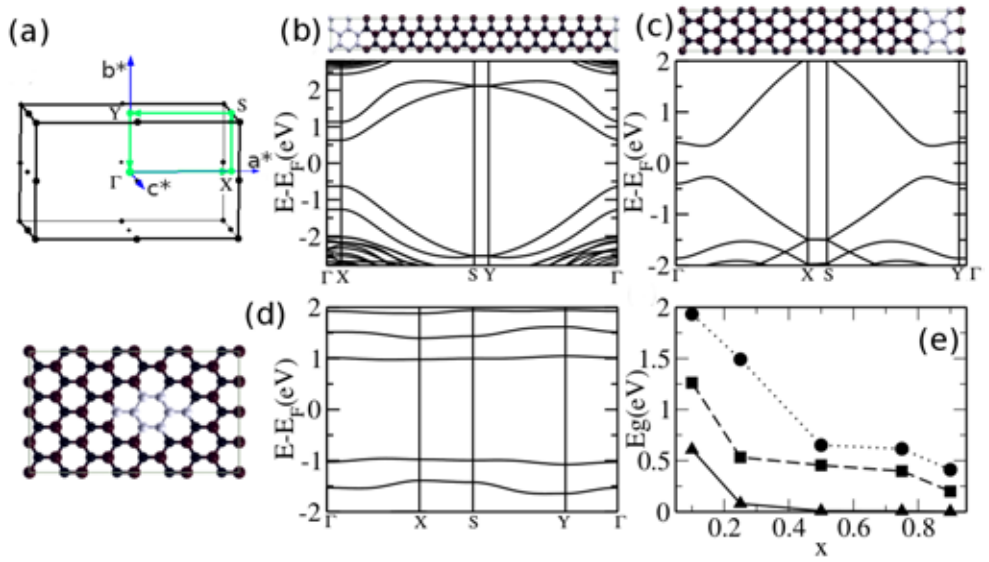

Figure 6.12: (a) Orthorhombic BZ with high symmetry points. (b,c,d): Band structure of $(C_2)_x(BN)_{1-x}$ with x = 0.1, plotted along the high-symmetry points of the BZ corresponding to the orthorhombic cell. (b,c) show the band structure for arm-chair and zig-zag interfaces, while (d) shows the band structure for the mixed interface. The corresponding interface geometries are shown by the side of band structure plots. The color convention of the balls in these figures is same as in Fig 2.5. (e): The band gap values plotted as a function of varying concentration, x. The circles, squares and triangles represent the data corresponding to mixed, arm-chair and zig-zag interfaces.

Finally, we investigate the influence of the interface geometry on the band gap engineering. In the study described so far, we have considered selectively created zig-zag type interface, or arm-chair type interface, and freely evolved interface generated in MC simulation which turned to be of mixed kind. Therefore a

systematic study of electronic structure of the composite structures possessing these different interfaces i.e. armchair, zigzag and patches (mixed combination of zigzag and armchair) is important and necessary. These results may throw light on the underlying physics of band-gap engineering in optoelectronic devices.

In the upper middle, upper right and lower middle panels of Fig 6.12, we show the band structure of $(\mathrm{C}_2)_x(\mathrm{BN})_{1-x}$ hybrids considering the zig-zag, arm-chair and patchy interfaces for x = 0.1. In lower right most panel we also show the variation of band gap as a function of varying concentration x for each of these interface geometries. From the three band structure plots it is evident that in all different cases of interface geometries the band-gaps are direct band-gaps and hence an electron can directly emit a photon without a change in momentum, giving such materials a high optical absorption. This aspect continues for other x values as well. A significant difference in the bandstructure of patchy interface compared to that of zigzag or armchair interfaces is that the bands are almost flat in case of patchy structure, while there is appreciable dispersion for the zig-zag or arm-chair interface, arising due to extended connectivity. This in turn implies the quenching of kinetic energy of electrons for the patchy interfaces amounting localization of the electrons at the states close to valence band maximum (VBM) and conduction band minimum (CBM). For the plot of the band gap, we further find that for a given concentration the band-gaps depend crucially on for the interface geometry. Since the band along YS (XS) direction in the arm-chair (zig-zag) interface is flat, we believe that the graphene nanoribbon geometry embedded in the CBN sheet mainly determines the entire low-energy band structure [264]. For a zig-zag interface, the closing of the band gap and a metallic behavior is obtained already for a concentration of x = 0.5, with significant suppression of band-gap at a concentration of x = 0.25. On the other hand, both for arm-chair and mixed interfaces, band gap is not closed even with large substitution of carbon atoms e.g. x = 0.9, giving rise to a large concentration window available for band gap tuning.

6.4 Summary

In this chapter, we have presented a detailed first-principles calculation of the band structure, DOS, the band gap and the formation energy of $C_{2x}(BN)_{1-x}$ at different concentrations. From the formation energy, we have also investigated the phase stability of the material using a regular solution model. Although we have used only the single-site probabilities for the entropy, which can be improved further by incorporating the pair or cluster probabilities, we have given an estimate of the transition temperature for the order-disorder transition in $C_{2x}(BN)_{1-x}$, apparently for the first time. We have calculated the resistivity of $C_{2x}(BN)_{1-x}$ using Boltzmann transport theory and have estimated the band gap of this semiconducting nanomaterial at different concentrations which agrees with earlier experimental observations. Our calculated DOS and PDOS should motivate further angle resolved photoemission spectroscopic (ARPES) measurements on this technologically important nanomaterial.

Further, we have studied theoretically the influence of various geometrical shapes of the interfaces formed between phase segregated graphene and h-BN on the properties of h-BN substituted graphene systems. For this purpose we employed a mean-field regular solution model as well as Monte Carlo simulations of first-principles derived models. Our calculations show a rather strong dependence of the interface geometry both on the phase stability and the band gap engineering, the latter being the original motivation for studying graphene-BN hybrid systems.

We find a significant suppression of the segregation temperature for the arm-chair shaped interfaces, giving rise to the possibility of achieving homogeneous solution of graphene-BN alloy phase if extended arm-chair interfaces can be created selectively. We further found achieving such homogeneous solution phase becomes progressively difficult upon reduction of dimensionality, in moving from infinite sheet to nanoribbons of $(C_2)_x(BN)_{1-x}$ of smaller and smaller widths.

Our study on band structure showed for band gap tuning, arm-chair or mixed interfaces are better candidates compared to zig-zag interface. For the later the gap is significantly reduced and closes completely beyond a substitution limit of 0.5. On the other hand, the band gap remains finite for the arm-chair or mixed

interfaces even for high level of substitution of BN with 0.9 of carbon atoms (the highest value studied in the present study). Our band gaps have been calculated using GGA exchange-correlation functional which is expected to underestimate the values of the band gap, but the calculated trend should be robust, as has been shown in the study employing both hybrid functional and GGA functional.[265]

Finally, our thorough and extensive study considering different possible interfaces in bulk as well as reduced dimensionality in $(\mathrm{C}_2)_x(\mathrm{BN})_{1-x}$ composite systems should provide an useful insight on the interfacial geometry effect on properties. Given the experimental possibility of control on phase stability of $(\mathrm{C}_2)_x(\mathrm{BN})_{1-x}$ composite systems using supported and patterned substrates,[266] it might be possible to selectively create interface of one type over other with desired properties. In this context, band structure and stability of various isomers of 2D infinite sheet of $(\mathrm{BN})_m(\mathrm{C}_2)_n$ composites have been studied from the view point of chemical concepts of conjugation and aromaticity,[265] which also pointed out that the relative widths and arrangement of graphene phases in embedded h-BN matrix in an infinite sheet will be crucial in realizing BN substituted graphene systems with desired band gap. Our alternative approach of study reconfirms that idea, and additionally shows the effect of reduced dimensionality which is detrimental to achieve homogeneously mixed state.

Chapter 7

Conclusion and Future outlook

7.1 Conclusion

In this thesis we have studied, using first-principles DFT methods without any adjustable parameters, several transport and thermodynamic properties of two-dimensional materials. Different theoretical frameworks are used to study properties such as electrical conductivity, resistivity, mobility, Seebeck coefficients, Figure of merit, Grüneisen parameters and lattice thermal conductivity. The theoretical frameworks include density functional theory, density functional perturbation theory, linearized Boltzmann transport theory for both electrons and phonons and molecular dynamics. The detailed descriptions for each of the theoretical frameworks are carried out in chapter 2. Most of the work in this thesis is concerned with solving the linearized Boltzmann equation for electrons and phonons to calculate transport parameters.

In Chapter 3, we examine important characteristics of monolayer and bilayer graphene. We find that the charge density dependent electrical conductivity shows a $\sqrt{n}$ behavior which is seen in experiments for annealed graphene. The other characteristic that we find which agrees well with experiments is that the Seebeck coefficient increases linearly with temperature for a constant chemical potential. Further for a small range in chemical potential, we have demonstrated the Bloch-Grünesien behavior of resistivity in graphene. Our results show

that at temperature higher than Bloch-Grünesien temperature, the resistivity increased linearly while at lower temperatures it displayed a $\sim T^4$ behavior, a characteristic of a two-dimensional electron gas. Mobility showed an order of magnitude decrease when doped with impurities and at high concentrations, the $\sqrt{n}$ behavior changed to $\sim n$ behavior. We have shown that doping graphene with a boron nitride dimer increases the Seebeck coefficient by two-folds and also decreases the lattice thermal conductivity thus proffering a new method to increase the figure of merit of graphene based devices. Moreover, we calculated the phonon dispersion, Grüneisen parameter and lattice thermal conductivity and found our results to be in excellent agreement with available experimental data. We calculated the lattice thermal conductivity using the Callaway-Klemens method in the relaxation time approximation and an iterative real space method beyond the relaxation time approximation. Our lattice thermal calculations suggest that for two-dimensional materials, one must go beyond the relaxation time approximation to accurately describe the length, temperature and mode dependent lattice thermal conductivity. A similar study was done for multilayer hexagonal boron nitride in Chapter 4.

In Chapter 5, we calculated the figure of merit of boron nitride sandwiched between graphene heterostructures. The electronic transport parameters was calculated using the linearised Boltzmann equations while the lattice thermal conductivity were calculated using equilibrium molecular dynamics. For a chemical potential corresponding to the experimental gate voltage, our results for four- and five- layered boron nitride sandwiched between graphene were in excellent agreement with the available experimental data. Our result for three layered boron nitride sandwiched between graphene sheets showed the highest figure of merit in comparison with the four and five layered boron nitride heterostructures.

In Chapter 6, the thermodynamic properties were calculated using the regular solution model (mean field approximation) and a Monte Carlo simulation for graphene doped with boron nitride having an armchair, zigzag and mixed interfaces between graphene and boron nitride. An appreciable repression of the segregation temperature was seen in armchair interfaces. These homogeneous solutions become even more difficult to achieve upon reducing their dimension-

ality. Our electronic band structure for each of these materials demonstrates that all band gaps are direct, implying such materials have high optical absorption. Since the band gaps vary due to their constituents' concentration as well as their interface geometry, boron nitride doped graphene (and carbon doped boron nitride) are extremely useful for band gap engineering. We have also shown in Chapter 6, the logarithmic resistivity of doped graphene having zigzag and armchair interfaces when plotted against the inverse of temperature was shown to be linear, demonstrating the semiconducting behavior of such materials.

7.2 Future Outlook

All transport calculations in this thesis have assumed that the electronic relaxation time is a constant and isotropic, *viz*, independent of direction. However in general, the relaxation time is a function of temperature and depends on the momentum of the electron and hence the direction of the Brillouin zone. Durczewski *et al.* [267] have devised a formalism to calculate the electron relaxation time and Zahedifar *et al.* [268] have used this model to calculate the figure of merit of half-Heusler semiconductors. Using similar techniques, we plan to investigate the electronic transport properties without treating the relaxation time as a constant and without the isotropic approximation. Also, our transport calculations are semi-classical and do not take contacts into account. We therefore plan to use a quantum transport technique, the non equilibrium green function formalism, as done by various groups, *viz*, Lu *et al.* [269] and Xu *et al.* [270] have calculated the thermal transport in grain boundaries of graphene, and graphene junctions and quantum dots, respectively, using the non-equilibrium Green's function method [271]. Though most of the results for the materials studied in this thesis are in good agreement with experiments, the figure of merit come out extremely small. We therefore plan to theoretically predict a material having a large figure of merit having realistic applications in solid state devices.

This thesis does not consider magnetic properties of two dimensional materials, which is an important property that needs to be explored. In this connection, we have already initiated work on layered Organic-Inorganic hybrid perovskites. Hybrid organic-inorganic materials are not simple physical mixtures

but, molecular or nano-composites with organic and inorganic components, with at least one of the component domains having a dimension ranging from a few angstroms to several nanometers. Since they mix at the microscopic scale these hybrid materials show characteristics which are in between that of two original phases or show new properties which are absent in either of their building blocks. Specifically, we have considered layered materials that have a general formula of $(RNH_3)_2A_mX_{3m+1}$, where R is an alkyl, A is a metal cation and X is a halide. The number of metal cation layers between the two sheets of organic chains is indicated by a variable, "m". Consider the two extreme values of m. For m=∞ the structure becomes a three-dimensional bonded perovskite crystal, while for $m = 1$ the structure becomes a quantum well[47]. The com-

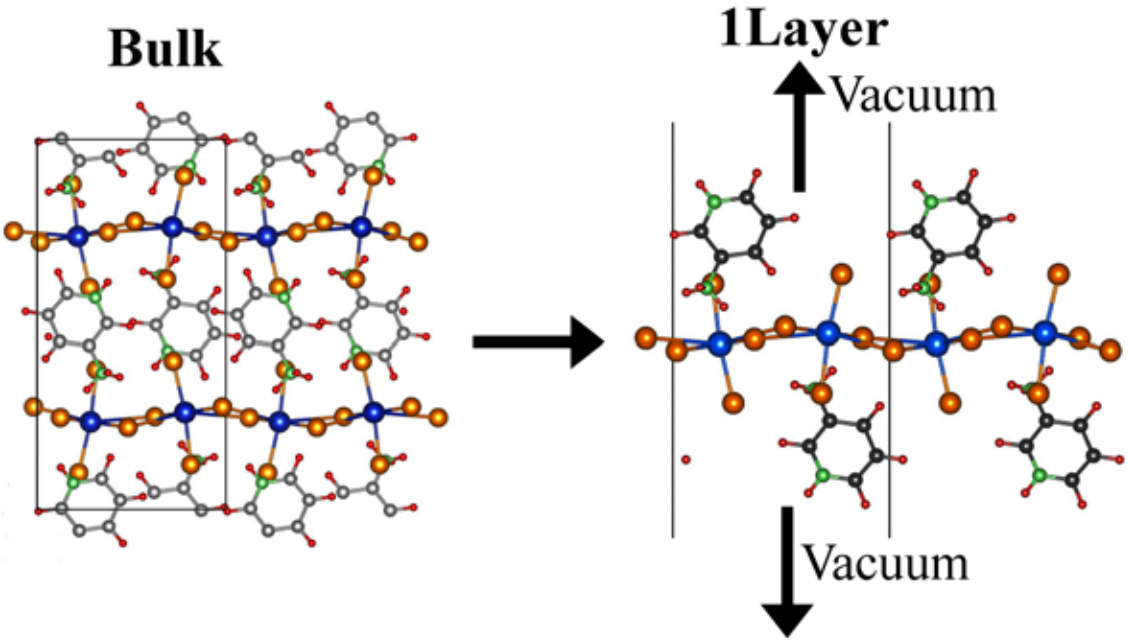

Figure 7.1: Unit cell of Bulk (left) and a single layer (right) of 3-ammoniumpryidinium (3AP) tetrabromocuprate ($CuBr_4$)

pounds, 3-ammoniumpryidinium (3AP) tetrabromocuprate ($CuBr_4$) and 3AP tertrachlorocuprate ($CuCl_4$) in this family of compounds are of special interest because these non centrosymmetric crystals whose crystal structure consists of the two copper halide layer perovskites might show some novel magnetic properties. These copper halide layer perovskites were first reported in 1988 [272]. However, predictions about their magnetic properties are limited as there exists inadequate data to make concrete correlations for the tetrahedrally distorted anions. These copper halide layer perovskite salts are expected to show

a ferromagnetic exchange inside the layer and antiferromagnetic exchange between the layers. Hence in order to explain the magnetic behaviour of 3APCuBr$_4$ and 3APCuCl$_4$ microscopic investigations of these materials are needed. Similar to the paper reported by Letian Dou $et.\ al.$ [47], these layered structures are held together by weak hydrogen bonds and hence can be crystallized into 2D layer perovskite structures which is expected to play a very important role in the development of low-dimensional magnetism. We are currently studying the electronic and magnetic properties of these materials by varying the number of their layers using DFT.

Appendix A

Tight Binding model of graphene (Referred in section 1.4 and 3.3.2)

In the tight binding approximation, the two Bloch functions are constructed from the atomic orbitals for the two inequivalent atoms, A and B. Considering only the nearest-neighbor interactions, the diagonal terms in the tight binding model for the π-band consists of only an integration over a single atom therefore $H_{AA} = H_{BB} = \epsilon_{2p}$. The off-diagonal matrix elements are calculated considering the three nearest-neighbor B atoms with respect to atom A. We denote the vectors as $\overrightarrow{R_1}, \overrightarrow{R_2}$ and $\overrightarrow{R_3}$ and their contribution to the off-diagonal matrix is given by,

$$H_{AB} = t(e^{i\mathbf{k}\cdot\mathbf{R_1}} + e^{i\mathbf{k}\cdot\mathbf{R_2}} + e^{i\mathbf{k}\cdot\mathbf{R_3}}) \tag{A.1}$$

With $\overrightarrow{R_1} = (1, 0)a, \overrightarrow{R_2} = (-\frac{1}{2}, \frac{\sqrt{3}}{2})a$ and $\overrightarrow{R_3} = (-\frac{1}{2}, \frac{-\sqrt{3}}{2})a$, Eq. A.1 becomes

$$H_{AB} = t(e^{iak_x} + 2e^{\frac{-iak_x}{2}} \cos\left(\frac{\sqrt{3}}{2}ak_y\right)) = f(\mathbf{k}) \tag{A.2}$$

The off-diagonal matrix becomes,

$$H = \begin{pmatrix} 0 & tf(\mathbf{k}) \\ f^*(\mathbf{k}) & 0 \end{pmatrix} \tag{A.3}$$

In order to understand the term Dirac cone, we recall the Dirac equation,

$$-i\hbar(\sigma_x\frac{\partial}{\partial x}+\sigma_y\frac{\partial}{\partial y}+\sigma_z m)=\begin{pmatrix} m & p_x-ip_y \\ p_x+ip_y & -m\end{pmatrix} \tag{A.4}$$

Where $\sigma_x=\begin{pmatrix}0&1\\1&0\end{pmatrix}$, $\sigma_y=\begin{pmatrix}0&-i\\i&0\end{pmatrix}$ and $\sigma_z=\begin{pmatrix}1&0\\0&-1\end{pmatrix}$ known as the Dirac matrices.

We now expand the off-diagonal elements around the K-point $(\frac{2\pi}{3a},\frac{2\pi}{3\sqrt{3}a})$, $K_x=\frac{2\pi}{3a}+q_x$ and $K_y=\frac{2\pi}{3\sqrt{3}a}+q_y$. Therefore,

$$\begin{aligned}\cos(ak_x) &= \cos\left((\frac{2\pi}{3a})+q_x\right)=\cos\left(\frac{2\pi}{3}\right)\cos(q_xa)-\sin\left(\frac{2\pi}{3}\right)\sin(q_xa)\\ &= -\frac{1}{2}(1-\frac{(q_xa)^2}{2})-\frac{\sqrt{3}}{2}q_xa\end{aligned} \tag{A.5}$$

and

$$\begin{aligned}\sin(ak_x) &= \sin\left((\frac{2\pi}{3a})+q_x\right)=\sin\left(\frac{2\pi}{3}\right)\cos(q_xa)+\cos\left(\frac{2\pi}{3}\right)\sin(q_xa)\\ &= \frac{\sqrt{3}}{2}(1-\frac{(q_xa)^2}{2})-\frac{\sqrt{1}}{2}q_xa\end{aligned} \tag{A.6}$$

Similarly,

$$\begin{aligned}\cos\left(\frac{k_xa}{2}\right)&=\frac{1}{2}(1-\frac{q_x^2a^2}{8})-\frac{\sqrt{3}}{2}q_xa\\ \sin\left(\frac{k_xa}{2}\right)&=\frac{\sqrt{3}}{2}(1-\frac{q_x^2a^2}{8})-\frac{1}{4}q_xa\\ \cos\left(\frac{k_ya}{2}\right)&=\frac{1}{2}(1-\frac{3q_ya}{2}-\frac{3q_y^2a^2}{8})\end{aligned} \tag{A.7}$$

Writing $f(\mathbf{k})$ in terms of trigonometric functions and substituting Eq. A.5 to Eq. A.7 in Eq. A.2 we get,

$$\begin{aligned}f(q_x,q_y)&=\frac{-3q_x}{4}q_xi-\frac{3\sqrt{3}}{4}q_x-\frac{3}{4}q_y+\frac{3\sqrt{3}}{4}q_yi\\ &\quad+\frac{3}{8}q_xq_yi+\frac{3\sqrt{3}}{8}q_xq_y+\mathcal{O}(q_x^2,q_y^2)\\ f(q_x,q_y)&\approx\frac{3q_xi}{2}(\frac{-1}{2}+i\frac{\sqrt{3}}{2})+\frac{3q_y}{2}(\frac{-1}{2}+i\frac{\sqrt{3}}{2})\\ f(q_x,q_y)&=\frac{3}{2}e^{i\frac{2\pi}{3}}(q_xi+q_y)\end{aligned} \tag{A.8}$$

Substituting Eq.A.8 in Eq. A.3, we see the form of the Hamiltonian is exactly like that of the Dirac equation with $m = 0$. Diagonalising the Hamiltonian yields,

$$E_{p_z} = \pm\frac{3t}{2}\sqrt{q_x^2 + q_y^2} = \pm\frac{3t}{2}|q| \tag{A.9}$$

which is an equation of a cone. Hence the term Dirac-cone.

The σ-bands can be calculated using the method described in the book *Physical properties of carbon nanotubes*[189]. We have calculated the matrix elements for each of the matrix elements,

$$H_{11} = \left\langle 2s^A \right| H \left| 2s^B \right\rangle = H_{ss}[e^{\frac{iak_x}{\sqrt{3}}} + 2e^{\frac{-iak_x}{2\sqrt{3}}}\cos\left(\frac{ak_y}{2}\right)]$$

$$H_{12} = \left\langle 2s^A \right| H \left| 2p_x^B \right\rangle = H_{sp}[-e^{\frac{iak_x}{\sqrt{3}}} + e^{-\frac{iak_x}{2\sqrt{3}}}\cos\left(\frac{ak_y}{2}\right)]$$

$$H_{13} = \left\langle 2s^A \right| H \left| 2p_y^B \right\rangle = -\sqrt{3}iH_{sp}[e^{-\frac{iak_x}{2\sqrt{3}}}\sin\left(\frac{ak_y}{2}\right)]$$

$$H_{21} = \left\langle 2p_x^A \right| H \left| 2s^B \right\rangle = H_{sp}[e^{\frac{iak_x}{\sqrt{3}}} - e^{-\frac{-iak_x}{2\sqrt{3}}}\cos\left(\frac{ak_y}{2}\right)]$$

$$H_{22} = \left\langle 2p_x^A \right| H \left| 2p_x^B \right\rangle =$$

$$H_\sigma[-e^{\frac{iak_x}{\sqrt{3}}} - \frac{1}{2}e^{-\frac{iak_x}{2\sqrt{3}}}\cos\left(\frac{ak_y}{2}\right)] - \frac{3}{2}H_\pi[e^{-\frac{iak_x}{2\sqrt{3}}}\cos\left(\frac{ak_y}{2}\right)]$$

$$H_{23} = \left\langle 2p_x^A \right| H \left| 2s^B \right\rangle = \frac{\sqrt{3}i}{2}(H_\sigma + H_\pi)[e^{\frac{iak_x}{\sqrt{3}}} - e^{-\frac{-iak_x}{2\sqrt{3}}}\cos\left(\frac{ak_y}{2}\right)]$$

$$H_{31} = \left\langle 2p_y^A \right| H \left| 2s^B \right\rangle = -\sqrt{3}iH_{sp}[e^{-\frac{iak_x}{2\sqrt{3}}}\sin\left(\frac{ak_y}{2}\right)]$$

$$H_{32} = \left\langle 2p_y^A \right| H \left| 2p_x^B \right\rangle = \frac{\sqrt{3}i}{2}(H_\sigma + H_\pi)[e^{-\frac{iak_x}{2\sqrt{3}}}\sin\left(\frac{ak_y}{2}\right)]$$

$$H_{33} = \left\langle 2p_y^A \right| H \left| 2p_y^B \right\rangle = H_\pi[e^{\frac{iak_x}{\sqrt{3}}} + \frac{1}{2}e^{\frac{-iak_x}{2\sqrt{3}}}\cos\left(\frac{ak_y}{2}\right)] - H_\sigma\frac{3}{2}[e^{\frac{-iak_x}{2\sqrt{3}}}\cos\left(\frac{ak_y}{2}\right)]$$

Appendix B

Derivation of Mott Formula (Referred in Equation 2.93)

In this section, we derive the Mott Formula by using the Sommerfeld expansion around the Fermi energy. For any smoothly varying function of ϵ, say $H(\epsilon)$, the Sommerfeld expansion is given by,

$$\begin{aligned}\int_{-\infty}^{\infty} \frac{H(\epsilon)}{e^{\beta(\epsilon-\mu)}+1} d\epsilon &= \int_{-\infty}^{\mu} H(\epsilon)d\epsilon + \frac{\pi^2}{6}k_B^2T^2H^{'}(\mu) + \mathcal{O}\left(\frac{k_B^4T^4}{\mu^4}\right) + \cdots \\ &= \int_{-\infty}^{\infty} H(\epsilon)f(\epsilon)d\epsilon \end{aligned} \tag{B.1}$$

here $\mathcal{O}$ refers to the limiting behavior of higher even orders and f is the Fermi-Dirac distribution function. It must be noted that the function $H(\epsilon)$ should vanish at, $\epsilon \to -\infty$. The definition of the thermoelectric linearized Seebeck coefficient is expressed as, $\sigma S = v$ [31]. We have shown in section 2.91 that the velocity of the band electron is expressed as $v = \frac{1}{eT}\int \sigma(\epsilon)(\epsilon-\mu)\frac{\partial f}{\partial \epsilon}d\epsilon$. To make the velocity term look like Eq. B.1, we use the following algebraic trick. We integrate $\int_{-\infty}^{\infty} f(\epsilon)H(\epsilon)d\epsilon$ by parts,

$$\int_{-\infty}^{\infty} f(\epsilon)H(\epsilon)d\epsilon = \Big[f(\epsilon)G(\epsilon)\Big]\Big|_0^{\infty} - \int_{-\infty}^{\infty} f'(\epsilon)G(\epsilon)d\epsilon \tag{B.2}$$

Where $G(\epsilon)$ is the derivative of $H(\epsilon)$. Since the Fermi-Dirac function vanishes at the limits, the first term in the above expression vanishes. Therefore, Eq. B.2

becomes,

$$\int_{-\infty}^{\infty} f(\epsilon)H(\epsilon)d\epsilon = -\int_{-\infty}^{\infty} f'(\epsilon)G(\epsilon)d\epsilon \tag{B.3}$$

With $H(\epsilon) = \sigma(\epsilon)(\epsilon - \mu)$, $\therefore$ $G(\epsilon) = \sigma^{'}(\epsilon)(\epsilon - \mu) + \sigma(\epsilon)$. Using Eq.B.3, the velocity expression becomes,

$$\begin{aligned} \sigma S = v &= \frac{1}{eT}\int \sigma(\epsilon)(\epsilon - \mu)f^{'}(\epsilon)d\epsilon \\ &= -\frac{1}{eT}\int [\sigma^{'}(\epsilon)(\epsilon - \mu) + \sigma(\epsilon)]f(\epsilon)d\epsilon \end{aligned} \tag{B.4}$$

We now expand the conductivity term as a Taylor series around the Fermi energy, $\sigma(\epsilon) = \sum_0^\infty \frac{1}{m!}\left[\frac{d^m\sigma}{d\epsilon^m}\right]\Big|_\mu (\epsilon - \mu)^m$,

$$\sigma(\epsilon) = \sigma(\mu) + \sigma^{'}(\epsilon)(\epsilon - \mu) + \mathcal{O}(\epsilon - \mu)^2 \tag{B.5}$$

The chemical potential at the Fermi energy is zero. Therefore the first term in Eq.B.5 vanishes. If we truncate the expansion to the second term, the conductivity becomes

$$\sigma(\epsilon) = \sigma^{'}(\epsilon)(\epsilon - \mu) \tag{B.6}$$

Substituting Eq. B.6 in Eq. B.4, we get,

$$\sigma S = -\frac{2}{eT}\int \sigma(\epsilon)f(\epsilon)d\epsilon \tag{B.7}$$

Eq. B.7 is now in the form of Eq. B.1. Therefore,

$$\sigma S = -\frac{2}{eT}\left[\int \sigma(\epsilon)d\epsilon + \frac{\pi^2}{6}k_B^2T^2\sigma^{'}(\epsilon)\Big|_\mu\right] \tag{B.8}$$

The first term vanishes becomes the conductivity vanishes at the limits of the integral. Therefore, Eq. B.8 yields the Mott Formula,

$$S = -\frac{\pi^2k_B^2T}{3e}\frac{\sigma'(\epsilon)}{\sigma(\epsilon)}\Big|_\mu = -\frac{\pi^2k_B^2T}{3e}\frac{d(\ln\sigma(\epsilon))}{d\epsilon}\Big|_\mu \tag{B.9}$$

Appendix C

Derivation of irreducible representations (Referred in Chapter 4)

We define the reducible representation (Γ_{red}) by placing three vectors on each atom in the unit cell which will obey the following rules when operated by a symmetry transformation.

(a) If a vector is not moved (reversed) by an operation, it contributes 1 (-1) to χ.

(b) If a vector is moved to a new location by an operation, it contributes 0 to χ.

where χ is the character in the reducible representation. Our reducible representations (Γ_{red}) are shown in the column before every new point group representation in table C.1. Using the reduction formula, $a_i = \frac{1}{g}\sum \chi_R \chi_{IR}$, where a_i is the number of times an irreducible representation contributes to the reducible representation, g is the total number of symmetry operations for a particular point group and χ_R (χ_{IR}) is the corresponding character in the reducible (irreducible) representation, we derive the irreducible representations.

Since the basis play an important role in identifying if the Raman or Infrared modes are active or not, one must understand how the basis can be used to derive

Table C.1: The point group representation for SLBN, BLBN, 5LBN and Bulk-*h*BN at the Γ point in the BZ. The irreducible representation is obtained from the reducible representation Γ^{X}_{red} of the system X using the reduction formula.

D_{6h}	E	$2C_6$	$2C_3$	C_2	$3C_2^{'}$	$3C_2^{''}$	i	$2S_6$	$2S_3$	σ_h	$3\sigma_v$	$3\sigma_d$	Basis
A_{2u}	1	1	1	1	-1	-1	-1	-1	-1	-1	1	1	z
B_{1g}	1	-1	1	-1	1	-1	1	1	-1	-1	-1	1	$yz(3x^2-y^2)$
B_{2g}	1	-1	1	-1	-1	1	1	1	-1	-1	1	-1	$xz(x^2-3y^2)$
E_{2g}	2	-1	-1	2	0	0	2	-1	-1	2	0	0	$\{x^2-y^2, xy\}$
E_{1u}	2	1	-1	-2	0	0	-2	1	-1	2	0	0	$\{x, y\}$
$\Gamma^{bulk-hBN}_{red}$	12	0	0	0	0	-4	0	-8	0	4	4	0	
Γ^{SLBN}_{red}	6	0	0	0	-2	0	0	-4	0	2	0	2	
D_{3d}	E		$2C_3$		$3C_2^{'}$		i		$2S_6$		$3\sigma_d$		
A_{2u}	1		1		-1		-1		-1		1		z
A_{1g}	1		1		1		1		1		1		z^2
E_g	2		-1		0		2		-1		0		$\{xz, yz\}$
E_u	2		-1		0		-2		1		0		$\{x, y\}$
Γ^{BLBN}_{red}	12		0		4		0		0		0		
D_{3h}	E		$2C_3$		$3C_2^{'}$		σ_h		$2S_3$		$3\sigma_v$		
$A_1^{'}$	1		1		1		1		1		1		z^2
$A_2^{''}$	1		1		-1		1		1		-1		z
$E^{'}$	2		-1		0		2		-1		0		$\{x, y\}$
$E^{''}$	2		-1		0		-2		1		0		$\{xz, yz\}$
Γ^{5LBN}_{red}	30		0		10		2		-4		-2		

the character table. Here we derive the characters for three reproducible representation from their respective basis. The Mulliken symbol for the representations are defined as follows. All one-dimensional representations are designated with either A or B, two-dimensional as E, three dimensionals as T, four as G, five as H and so one. The subscripts are defined as follows. (i) A one-dimensional irreducible representation which are symmetric with respect to rotation by $\frac{2\pi}{n}$ about the principal C_n axis are designated A which those which are antisymmetric are designated by B. (ii) Subscript 1 if the irreducible representation is symmetric with respect to rotation about a C_2 axis perpendicular to the C_n axis and 2 if it is antisymmetric. (iii) The prime superscript and double prime are given to irreducible representations which are respectively symmetric and antisymmetric with respect to σ_h. (iv) Groups which have center of inversion, the subscript g (*gerade*) and u (*ungerade*) are given to irreducible that are symmetric and antisymmetric with respect to inversion.

Example 1: Group D_{6h}; Symmetry operation:C_2, Mulliken symbol:E_{2g}: Since the symmetry operation corresponds to a rotation of 180 in the plane of the

sheets, θ = 180° and the rotation matrix becomes, $\begin{pmatrix} -1 & 0 \\ 0 & -1 \end{pmatrix}$ The basis for E_{2g} is written as $\{x^2 - y^2, xy\}$, therefore another coordinate would transform as

$$\begin{pmatrix} x^{'} \\ y^{'} \end{pmatrix} = \begin{pmatrix} -1 & 0 \\ 0 & -1 \end{pmatrix} \begin{pmatrix} x \\ y \end{pmatrix} \tag{C.1}$$

which yields,

$$\begin{aligned} x^{'} = -x \;\&\; y^{'} = -y \\ \therefore x^{'2} - y^{'2} = (-x)^2 - (-y)^2 = x^2 - y^2 \\ \&\; x^{'}y^{'} = (-x)(-y) = xy \end{aligned} \tag{C.2}$$

Eq. C.2 can be written as,

$$\begin{pmatrix} x^{'} - y^{'} \\ x^{'}y^{'} \end{pmatrix} = \begin{pmatrix} 1 & 0 \\ 0 & 1 \end{pmatrix} \begin{pmatrix} x^2 - y^2 \\ xy \end{pmatrix} \tag{C.3}$$

The character is defined as the traces of the box diagonal matrices. Therefore, the character is 2.

Example 2: Group D_{6h}; Symmetry operation:C_2, Mulliken symbol:E_{2u}: The basis is given by $\{x, y\}$. With θ = 180°, the transformation matrix corresponding to $\{x, y\} \Rightarrow \{x^{'}, y^{'}\}$ can be easily seen to be Eq. C. The trace is therefore -2.

Example 3: Group D_{3h}; Symmetry operation:C_3, Mulliken symbol:$E^{'}$: The basis is given by $\{x, y\}$. With θ = 120°, the transformation matrix corresponding to $\{x, y\} \Rightarrow \{x^{'}, y^{'}\}$ can shown to be,

$$\begin{pmatrix} x^{'} \\ y^{'} \end{pmatrix} = \begin{pmatrix} -\frac{1}{2} & -\frac{\sqrt{3}}{2} \\ \frac{\sqrt{3}}{2} & -\frac{1}{2} \end{pmatrix} \begin{pmatrix} x \\ y \end{pmatrix} \tag{C.4}$$

The character is therefore -1.

Bibliography

[1] A.K. Geim and K.S. Novoselov. The rise of graphene. *Nature Materials*, 6:183, 2007.

[2] Pulickel Ajayan, Philip Kim, and Kaustav Banerjee. Two-dimensional van der waals materials. *Physics Today*, 69:38, 2016.

[3] Md. Sajibul Alam Bhuyan, Md. Nizam Uddin, Md. Maksudul Islam, Ferdaushi Alam Bipasha, and Sayed Shafayat Hossain. Synthesis of graphene. *International Nano letters*, 6:65, 2016.

[4] A.K. Geim and I.V. Grigorieva. Van der waals heterostructures. *Nature*, 499:419, 2013.

[5] K. I. Bolotin, K. J. Sikes, J. Hone, H. L. Stormer, and P. Kim. Temperature-dependent transport in suspended graphene. *Physical Review Letters*, 101:096802, 2008.

[6] S. V. Morozov, K. S. Novoselov, M. I. Katsnelson, F. Schedin, D. C. Elias, J. A. Jaszczak, and A. K. Geim. Giant intrinsic carrier mobilities in graphene and its bilayer. *Phys. Rev. Lett.*, 100:016602, 2008.

[7] Y. W. Tan, Y. Zhang, K. Bolotin, Y. Zhao, S. Adam, E. H. Hwang, S. Das Sarma, H. L. Stormer, and P. Kim. Measurement of scattering rate and minimum conductivity in graphene. *Phys. Rev. Lett.*, 99:246803, 2007.

[8] Y.M. Zuev, W. Chang, and P. Kim. Thermoelectric and magnetothermoelectric transport measurements of graphene. *Physical Review Letters*, 102:096807, 2009.

[9] E. McCann and M. Koshino. The electronic properties of bilayer graphene. *Rep. Prog. Phys.*, 76:056503, 2013.

[10] D. K. Efetov and P. Kim. Controlling electron-phonon interactions in graphene at ultrahigh carrier densities. *Phys. Rev. Lett.*, 105:256805, 2010.

[11] Kunal S. Mali, John Greenwood, Jinne Adisoejoso, Roald Phillipson, and Steven De Feyter. Nanostructuring graphene for controlled and reproducible functionalization. *Nanoscale*, 7:1566, 2015.

[12] B. Muchharla, A. Pathak, Z. Liu, L. Song, T. Jayasekera, S. Kar, R. Vajtai, L. Balicas, P.M. Ajayan, S. Talapatra, and N. Ali. Tunable electronics in large-area atomic layers of boron-nitrogen-carbon. *Nano Lett.*, 13:3476, 2013.

[13] Z. Liu, L. Ma, G. Shi, W. Zhou, Y. Gong, S. Lei, X. Yang, J. Zhang, J. Yu, K.P.Hackenberg, A. Babakhani, J.C. Idrobo, R. Vajtai, J. Lou, and P.M. Ajayan. In-plane heterostructures of graphene and hexagonal boron nitride with controlled domain sizes. *Nature Nanotech*, 8:119, 2013.

[14] L. Ci, L. Song, C. Jin, D. Jariwala, D. Wu, Y. Li, A. Srivastava, Z. F. Wang, K. Storr, L. Balicas, F. Liu, and P. M. Ajayan. Atomic layers of hybridized boron nitride and graphene domains. *Nature Mater*, 9:430, 2010.

[15] Chun-Chung Chen, Zhen Li, Li Shi, and Stephen B. Cronin. Thermoelectric transport across graphene/hexagonal boron nitride/graphene heterostructures. *Nano Research*, 8:666, 2015.

[16] D. R. Hamann, M. Schluter, and C. Chiang. Norm-conserving pseudopotentials. *Phys. Rev. Lett*, 43:1494, 1979.

[17] D. Vanderbilt. Soft self-consistent pseudopotentials in a generalized eigenvalue formalism. *Phys. Rev. B*, 41:7892, 1990.

[18] Fernando de Juan, Antonio Politano, Gennaro Chiarello, and Herbert A.Fertig. Symmetries and selection rules in the measurement of the phonon spectrum of graphene and related materials. *Carbon*, 85:225, 2015.

[19] T. M. G. Mohiuddin, A. Lombardo, R. R. Nair, A. Bonetti, G. Savini, R. Jalil, N. Bonini, D. M. Basko, C. Galiotis, N. Marzari, K. S. Novoselov, A. K. Geim, and A. C. Ferrari. Uniaxial strain in graphene by raman spectroscopy:g peak splitting, grüneisen parameters, and sample orientation. *Physical Review B*, 79:205433, 2009.

[20] Michael Thompson Pettes, Insun Jo, Zhen Yao, and Li Shi. Influence of polymeric residue on the thermal conductivity of suspended bilayer graphene. *Nano Lett.*, 11:1195, 2011.

[21] Xiangfan Xu, Luiz F.C. Pereira, Yu Wang, Jing Wu, Kaiwen Zhang, Xiangming Zhao, Sukang Bae, Cong Tinh Bui, Rongguo Xie, John T.L. Thong, Byung Hee Hong, Kian Ping Loh, Davide Donadio, Baowen Li, and Barbaros Özyilmaz. Length-dependent thermal conductivity in suspended single-layer graphene. *Nature Communications*, 5:3689, 2014.

[22] Ransell D'Souza and Sugata Mukherjee. First-principles study of the electrical and lattice thermal transport in monolayer and bilayer graphene. *Phys. Rev. B*, 95:085435, 2017.

[23] Hongyang Li, Hao Ying, Xiangping Chen, Denis L. Nika, Alexandr I. Cocemasov, Weiwei Cai, Alexander A. Balandin, and Shanshan Chen. Thermal conductivity of twisted bilayer graphene. *Nanoscale*, 6:13402, 2014.

[24] Yuki Anno, Yuki Imakita, Kuniharu Takei, Seiji Akita, and Takayuki Arie. Enhancement of graphene thermoelectric performance through defect engineering. *2D Mater.*, 4:025019, 2017.

[25] J. Serrano, A. Bosak, R. Arenal, M. Krisch, K. Watanabe, T. Taniguchi, H. Kanda, A. Rubio, and L. Wirtz. Vibrational properties of hexagonal

boron nitride: Inelastic x-ray scattering and ab initio calculations. *Phys. Rev. Lett.*, 98:095503, 2007.

[26] E. K. Sichel, R. E. Miller, M. S. Abrahams, and C. J. Buiocchi. Heat capacity and thermal conductivity of hexagonal pyrolytic boron nitride. *Phys. Rev. B*, 13:4607, 1976.

[27] Insun Jo, Michael Thompson Pettes, Jaehyun Kim, Kenji Watanabe, Takashi Taniguchi, Zhen Yao, and Li Shi. Thermal conductivity and phonon transport in suspended few-layer hexagonal boron nitride. *Nano Research*, 13:550, 2013.

[28] Chengru Wang, Jie Guo, Lan Dong, Adili Aiyiti, Xiangfan Xu, and Baowen Li. Superior thermal conductivity in suspended bilayer hexagonal boron nitride. *Sci. Rep.*, 6:25334, 2016.

[29] A. Kinaci, J. B. Haskins, C. Sevik, and Tahir Cagin. Thermal conductivity of BN-C nanostructures. *Phys. Rev. B*, 86:115410, 2012.

[30] M. Bernardi, M. Palummo, and J.C. Grossman. Optoelectronic properties in monolayers of hybridized graphene and hexagonal boron nitride. *Phys. Rev. Lett*, 108:226805, 2012.

[31] G. K. H. Madsen and D. J. Singh. Boltztrap. a code for calculating band-structure dependent quantities. *Computer Physics Communication*, 175:67, 2006.

[32] R.P. Feynman. There's plenty of room at the bottom. *Eng. Sci.*, 61:22, 1960.

[33] R. F. Curl. Dawn of the fullerenes: Conjecture and experiment (nobel lecture). *Angew. Chem. Int. Ed. Engl.*, 36:1566, 1997.

[34] H. Kroto. Symmetry, space, stars, and c 60 (nobel lecture). *Angew. Chem. Int. Ed. Engl.*, 36:1578, 1997.

[35] R. E. Smalley. Discovering the fullerenes (nobel lecture). *Angew. Chem. Int. Ed. Engl.*, 36:1594, 1997.

[36] A. K. Geim. Random walk to graphene (nobel lecture). *Angew. Chem. Int. Ed. Engl.*, 50:6966, 2011.

[37] K. S. Novoselov. Graphene: Materials in the flatland (nobel lecture). *Angew. Chem. Int. Ed. Engl.*, 50:7002, 2011.

[38] H. P. Boehm, R. Setton, and E. Stumpp. Nomenclature and terminology of graphite intercalation compounds. *Pure and Applied Chemistry*, 66:1893, 1994.

[39] R. Mas-Ballesté, C. Gómez-Navarro, J. Gómez-Herrero, and Félix Zamora. 2d materials: to graphene and beyond. *Nanoscale*, 3:20, 2011.

[40] J. Wang, F. Ma, and M. Sun. Graphene, hexagonal boron nitride, and their heterostructures: properties and applications. *RSC Adv.*, 7:16801, 2017.

[41] K. S. Novoselov, A. K. Geim, S. V. Morozov, D. Jiang, Y. Zhang, S. V. Dubonos, I. V. Grigorieva, and A. A. Firsov. Electric field effect in atomically thin carbon films. *Science*, 306:666, 2004.

[42] A. H. Castro Neto, F. Guinea, N. M. R. Peres, K. S. Novoselov, and A. K. Geim. The electronic properties of graphene. *Rev. Mod. Phys.*, 81:109, 2009.

[43] Gianluca Giovannetti, Petr A. Khomyakov, Geert Brocks, Paul J. Kelly, and Jeroen van den Brink. Substrate-induced band gap in graphene on hexagonal boron nitride: Ab initio density functional calculations. *Phys. Rev. B*, 76:073103, 2007.

[44] K. S. Novoselov, A. K. Geim, S. V. Morozov, D. Jiang, M. I. Katsnelson, I. V. Grigorieva, S. V. Dubonos, and A. A. Firsov. Two-dimensional gas of massless dirac fermions in graphene. *Nature*, 438:197, 2005.

[45] Yuanbo Zhang, Yan-Wen Tan, Horst L. Stormer, and Philip Kim. Experimental observation of the quantum hall effect and berry's phase in graphene. *Nature*, 438:201, 2005.

[46] P. R. Wallace. The band theory of graphite. *Phys. Rev.*, 71:622, 1947.

[47] Letian Dou, Andrew B. Wong, Yi Yu, Minliang Lai, Nikolay Kornienko, Samuel W. Eaton, Anthony Fu, Connor G. Bischak, Jie Ma, Tina Ding, Naomi S. Ginsberg, Lin-Wang Wang, A. Paul Alivisatos, and Peidong Yang. Atomically thin two-dimensional organic-inorganic hybrid perovskites. *Science*, 349:1518, 2015.

[48] C. R. Dean, A.F.Young, I.Meric, C.Lee, L.Wang, S.Sorgenfrei, K.Watanabe, T.Taniguchi, P. Kim, K.L.Shepard, and J. Hone. Boron nitride substrates for high-quality graphene electronics. *Nature Nanotech.*, 5:722, 2010.

[49] K. S. Novoselov, E. McCann, S. V. Morozov, V. I. Fal'ko, M. I. Katsnelson, U. Zeitler, D. Jiang, F. Schedin, and A. K. Geim. Unconventional quantum hall effect and berry's phase of 2π in bilayer graphene. *Nature Physics*, 2:177, 2006.

[50] Taisuke Ohta, Aaron Bostwick, Thomas Seyller, Karsten Horn, and Eli Rotenberg. Controlling the electronic structure of bilayer graphene. *Science*, 313:951, 2006.

[51] Suchismita Ghosh, Wenzhong Bao, Denis L. Nika, Samia Subrina, Evghenii P. Pokatilov, Chun Ning Lau, and Alexander A. Balandin. Dimensional crossover of thermal transport in few-layer graphene. *Nature Materials*, 9:555, 2010.

[52] Alexander A. Balandin. Thermal properties of graphene and nanostructured carbon materials. *Nature Materials*, 10:569, 2011.

[53] M. Neek-Amal and F. M. Peeters. Nanoindentation of a circular sheet of bilayer graphene. *Phys. Rev. B*, 81:235421, 2010.

[54] Y.Y.Zhang, C.M.Wang, Y.Cheng, and Y.Xiang. Mechanical properties of bilayer graphene sheets coupled by sp^3 bonding. *Carbon*, 49:4511, 2011.

[55] R. R. Nair, P. Blake, A. N. Grigorenko, K. S. Novoselov, T. J. Booth, T. Stauber, N. M. R. Peres, and A. K. Geim. Fine structure constant defines visual transparency of graphene. *Science*, 320:5881, 2008.

[56] J. Scott Bunch, Scott S. Verbridge, Jonathan, S. Alden, Arend, M. van der Zande, Jeevak M. Parpia, Harold G. Craighead, and Paul L. McEuen. Impermeable atomic membranes from graphene sheets. *Science*, 8:2458, 2008.

[57] D. C. Elias, R. R. Nair, T. M. G. Mohiuddin, S. V. Morozov, P. Blake, M. P. Halsall, A. C. Ferrari, and D. W. Boukhvalov. Control of graphene's properties by reversible hydrogenation: Evidence for graphane. *Science*, 323:610, 2009.

[58] Sukang Bae, Hyeongkeun Kim, Youngbin Lee, Xiangfan Xu, Jae-Sung Park, Yi Zheng, Jayakumar Balakrishnan, Tian Lei, Hye Ri Kim, Young Il Song, Young-Jin Kim, Kwang S. Kim, Jong-Hyun Ahn Barbaros Özyilmaz, Byung Hee Hong, and Sumio Iijima. Roll-to-roll production of 30-inch graphene films for transparent electrodes. *Nature Nanotechnology*, 5:574, 2010.

[59] Fengnian Xia, Damon B. Farmer, Yu ming Lin, and Phaedon Avouris. Graphene field-effect transistors with high on/off current ratio and large transport band gap at room temperature. *Nano Lett.*, 10:715, 2010.

[60] Chang-Ran Wang, Wen-Sen Lu, Lei Hao, Wei-Li Lee, Ting-Kuo Lee, Feng Lin, I-Chun Cheng, and Jian-Zhang Chen. Enhanced thermoelectric power in dual-gated bilayer graphene. *Phys. Rev. Lett.*, 107:186602, 2011.

[61] Jun Yan, M-H. Kim, J. A. Elle, A. B. Sushkov, G. S. Jenkins, H. M. Milchberg, M. S. Fuhrer, and H. D. Drew. Dual-gated bilayer graphene hot-electron bolometer. *Nature Nanotechnology*, 7:472, 2012.

[62] K. Sugawara, K. Kanetani, T. Sato, and T. Takahashi. Fabrication of li-intercalated bilayer graphene. *AIP Advances*, 1:022103, 2011.

[63] Kohei Kanetani, Katsuaki Sugawara, Takafumi Sato, Ryota Shimizu, Katsuya Iwaya, Taro Hitosugi, and Takashi Takahashi. Ca intercalated bilayer graphene as a thinnest limit of superconducting $c_6$ca. *PNAS*, 109:19610, 2012.

[64] Lei Gong, Robert J. Young, Ian A. Kinloch, Ibtsam Riaz, Rashid Jalil, and Kostya S. Novoselov. Optimizing the reinforcement of polymer-based nanocomposites by graphene. *ACS Nano*, 6:2086, 2012.

[65] Robert J.Young, Ian A.Kinloch, LeiGong, and Kostya S.Novoselov. The mechanics of graphene nanocomposites: A review. *Composites Science and Technology*, 72:1459, 2012.

[66] Edward McCann and Vladimir I. Fal'ko. Landau-level degeneracy and quantum hall effect in a graphite bilayer. *Phys. Rev. Lett.*, 96:086805, 2006.

[67] F. Guinea, A. H. Castro Neto, and N. M. R. Peres. Electronic states and landau levels in graphene stacks. *Phys. Rev. B*, 73:245426, 2006.

[68] Augustinus (Stijn) M. Goossens, Stefanie C. M. Driessen, Tim A. Baart, Kenji Watanabe, Takashi Taniguchi, and Lieven M. K. Vandersypen. Gate-defined confinement in bilayer graphene-hexagonal boron nitride hybrid devices. *Nano Lett.*, 12:4656, 2012.

[69] Hugen Yan, Xuesong Li, Bhupesh Chandra, George Tulevski, Yanqing Wu, Marcus Freitag, Wenjuan Zhu, Phaedon Avouris, and Fengnian Xia. Tunable infrared plasmonic devices using graphene/insulator stacks. *Nature Nanotechnology*, 7:330, 2012.

[70] J.H. Chen, C. Jang, S. Adam, M. S. Fuhrer, E. D. Williams, and M. Ishigami. Charged-impurity scattering in graphene. *Nature Physics*, 4:377, 2008.

[71] K. Nomura and A. H. MacDonald. Quantum hall ferromagnetism in graphene. *Physical Review Letters*, 96:256602, 2006.

[72] E. H. Hwang S. Adam and S. Das Sarma. Carrier transport in two-dimensional graphene layers. *Physical Review Letters*, 98:096802, 2007.

[73] E.H. Hwang and S. Das Sarma. Acoustic phonon scattering limited carrier mobility in two-dimensional extrinsic graphene. *Phys. Rev. B*, 77:115449, 2008.

[74] F. T. Vasko and V. Ryzhii. Voltage and temperature dependencies of conductivity in gated graphene. *Phys. Rev. B*, 76:233404, 2007.

[75] T. Stauber, N. M. R. Peres, and F. Guinea. Electronic transport in graphene: A semiclassical approach including midgap states. *Phys. Rev. B*, 76:205423, 2007.

[76] Jian-Hao Chen, Chaun Jang, Shudong Xiao, Masa Ishigami, and Michael S. Fuhrer. Intrinsic and extrinsic performance limits of graphene devices on sio$_2$. *Nature Nanotechnology*, 3:206, 2008.

[77] F. Guinea, M. I. Katsnelson, and M. A. H. Vozmediano. Midgap states and charge inhomogeneities in corrugated graphene. *Phys. Rev. B*, 77:075422, 2008.

[78] J. Martin, N. Akerman, G. Ulbricht, T. Lohmann, J. H. Smet, K. von Klitzing, and A. Yacoby. Observation of electron–hole puddles in graphene using a scanning single-electron transistor. *Nature Physics*, 4:144, 2008.

[79] K.I.Bolotin, K.J.Sikes, Z.Jiang, M.Klima, G.Fudenberg, J.Hone, P.Kim, and H.L.Stormer. Obsehigh electron mobility in suspended graphenervation of electron–hole puddles in graphene using a scanning single-electron transistor. *Solid State Communications*, 146:351, 2008.

[80] Sugata Mukherjee and T. P. Kaloni. Electronic properties of boron- and nitrogen-doped graphene: a first principles study. *J Nanopart Res*, 14:1059, 2012.

[81] M. Morscher, M. Corso, T. Greber, and J. Osterwalder. Formation of single layer *h*-BN on Pd(1 1 1). *Surf. Sci.*, 600:3280, 2006.

[82] A. Goriachko, Y. He, M. Knapp, H. Over, M. Corso, T. Brugger, S. Berner, J. Osterwalder, and T. Greber. Self-assembly of a hexagonal boron nitride nanomesh on Ru(0001). *Langmuir*, 23:2928, 2007.

[83] A. Geim. Graphene: status and prospects. *Science*, 324:1530, 2009.

[84] L. S. Panchakarla, K. S. Subrahmanyam, S. K. Saha, A. Govindaraj, H. R. Krishnamurthy, U. V. Waghmare, and C. N. R. Rao. Synthesis, structure, and properties of boron- and nitrogen- doped graphene. *Adv. Mater*, 21:4726, 2009.

[85] M.P. Levendorf, C.J. Kim, L. Brown, P.Y. Huang, R.W. Havener, D.A. Muller, and J. Park. Graphene and boron nitride lateral heterostructures for atomically thin circuitry. *Nature*, 488:627, 2012.

[86] EJ Kan, X Wu, Z Li, XC Zeng, J Yang, and JG Hou. Half-metallicity in hybrid bcn nanoribbons. *J Chem Phys*, 129:084712, 2008.

[87] Yi Ding, Yanli Wang, and Jun Ni. Electronic properties of graphene nanoribbons embedded in boron nitride sheets. *Applied Physics Letters*, 95:123105, 2009.

[88] Sudipta Dutta, Arun K. Manna, and Swapan K. Pati. Intrinsic half-metallicity in modified graphene nanoribbons. *Physical Review Letters*, 102:096601, 2009.

[89] J. M. Pruneda. Origin of half-semimetallicity induced at interfaces of C-BN heterostructures. *Physical Review B*, 81:161409(R), 2010.

[90] Somnath Bhowmick, Abhishek K. Singh, and Boris I. Yakobson. Quantum dots and nanoroads of graphene embedded in hexagonal boron nitride. *The Journal of Physical Chemistry C*, 115:9889, 2011.

[91] Yuanyue Liu, Somnath Bhowmick, and Boris I. Yakobson. BN white graphene with "colorful" edges: The energies and morphology. *Nano Letter*, 11:3113, 2011.

[92] Yabo Gao, Yanfeng Zhang, Pengcheng Chen, Yuanchang Li, Mengxi Liu, Teng Gao, Donglin Ma, Yubin Chen, Zhihai Cheng, Xiaohui Qiu, Wenhui Duan, and Zhongfan Liu. Toward single-layer uniform hexagonal boron nitride–graphene patchworks with zigzag linking edges. *Nano Letters*, 13:3439, 2013.

[93] Gang Hee Han, Julio A. Rodrıguez-Manzo, Chan-Woo Lee, Nicholas J. Kybert, Mitchell B. Lerner, Zhengqing John Qi, Eric N. Dattoli, Andrew M. Rappe, Marija Drndic, and A. T. Charlie Johnson. Continuous growth of hexagonal graphene and boron nitride in-plane heterostructures by atmospheric pressure chemical vapor deposition. *ACS Nano*, 7:10129, 2013.

[94] Lei Liu, Jewook Park, David A. Siegel, Kevin F. McCarty, Kendal W. Clark, Wan Deng, Leonardo Basile, Juan Carlos Idrobo, An-Ping Li, and Gong Gu. Heteroepitaxial growth of two-dimensional hexagonal boron nitride templated by graphene edges. *Science*, 343:163, 2014.

[95] Yuan Liu, Nathan O. Weiss, Xidong Duan, Hung-Chieh Cheng, Yu Huang, and Xiangfeng Duan. Van der waals heterostructures and devices. *Nature Reviews Materials*, 1:16042, 2016.

[96] A. Majumdar. Thermoelectricity in semiconductor nanostructures. *Science*, 303:777, 2004.

[97] M. Zebarjadi, K. Esfarjani, M. S. Dresselhaus, Z. F. Ren, and G. Chen. Perspectives on thermoelectrics: from fundamentals to device applications. *Energy Environ. Sci.*, 5:5147, 2012.

[98] David G. Cahill, Paul V. Braun, Gang Chen, David R. Clarke, Shanhui Fan, Kenneth E. Goodson, Pawel Keblinski, William P. King, Gerald D. Mahan, Arun Majumdar, Humphrey J. Maris, Simon R. Phillpot, Eric Pop, and Li Shi. Nanoscale thermal transport. ii. 2003–2012. *Applied Physics Reviews*, 1:011305, 2014.

[99] G. Fiori, A. Betti, S. Bruzzone, and G. Iannaccone. Lateral graphene hbcn heterostructures as a platform for fully two-dimensional transistors. *ACS Nano*, 6:2642, 2012.

[100] L. Ci, L. Song, C. Jin, D. Jariwala, D. Wu, A. Srivastava Y. Li, Z. F. Wang, K. Storr, L. Balicasa, F. Liu, and P. M. Ajayan. Atomic layers of hybridized boron nitride and graphene domains. *Nature Material*, 9:430, 2010.

[101] A. Sciambi, M. Pelliccione, M. P. Lilly, S. R. Bank, A. C. Gossard, L. N. Pfeiffer, K. W. West, and D. Goldhaber-Gordon. Vertical field effect transistor based on wave-function extension. *Phys. Rev. B*, 84:085301, 2011.

[102] W. Mehr, J. C. Scheytt, J. Dabrowski, G. Lippert, Y.-H. Xie, M. C. Lemme, M. Ostling, and G. Lupina. Vertical graphene base transistor. *IEEE Electron Device Lett.*, 33:691, 2012.

[103] Xiaoliang Zhong, Rodrigo G. Amorim, Ralph H. Scheicher, Ravindra Pandey, and Shashi P. Karna. Electronic structure and quantum transport properties of trilayers formed from graphene and boron nitride. *Nanoscale*, 4:5490, 2012.

[104] Kaike Yang, Yuanping Chen, Roberto D'Agosta, Yuee Xie, Jianxin Zhong, and Angel Rubio. Enhanced thermoelectric properties in hybrid graphene/boron nitride nanoribbons. *Phys. Rev. B*, 86:045425, 2012.

[105] A. Kinaci, J. B. Haskins, and T. Cagin. On calculation of thermal conductivity from einstein relation in equilibrium molecular dynamics. *J. Chem. Phys.*, 137:014106, 2012.

[106] L. Britnell, R. V. Gorbachev, R. Jalil, B. D. Belle, F. Schedin, A. Mishchenko, T. Georgiou, M. I. Katsnelson, L. Eaves, S. V. Morozov, N. M. R. Peres, J. Leist, A. K. Geim, K. S. Novoselov, and L. A. Ponomarenko. Field-effect tunneling transistor based on vertical graphene heterostructures. *Science*, 335:947, 2012.

[107] I. Jo, I. K. Hsu, Y. J. Lee, M. M. Sadeghi, S Kim, S Cronin, E Tutuc, S K Banerjee, Z Yao, and L Shi. Low-frequency acoustic phonon temperature distribution in electrically biased graphene. *Nano Lett*, 11:85, 2011.

[108] E. Pop, V. Varshney, and A. K. Roy. Thermal properties of graphene: Fundamentals and applications. *MRS Bulletin*, 37:1273, 2012.

[109] P. Hohenberg and W. Kohn. Inhomogeneous electron gas. *Phys. Rev.*, 136:B864, 1964.

[110] W. Kohn. Nobel lecture: Electronic structure of matter-wave functions and density functionals. *Rev. of Modern Physics*, 71:1253, 1999.

[111] W. Kohn and L.J. Sham. Self-consistent equations include exchange and correlation effects. *Physical Review*, 140:A1133, 1965.

[112] M. Born and R. Oppenheimer. Zur quantentheorie der molekeln. *Annalen der Physik*, 84:457, 1927.

[113] M. Born and K. Huang. *Dynamical Theory of Crystal Lattices*. Oxford University Press, 1954.

[114] Wolfram Koch and Max C. Holthausen. *A Chemist's Guide to Density Functional Theory*. Wiley-VCH, 2001.

[115] Attila Szabo and Neil S. Ostlund. *Modern Quantum Chemistry: Introduction to Advanced Electronic Structure Theory*. McGraw-Hill, 1989.

[116] R. O. Jones and O. Gunnarsson. The density functional formalism, its applications and prospects. *Annalen der Physik*, 61:689, 1989.

[117] N. David Mermin. Thermal properties of the inhomogeneous electron gas. *Phys. Rev.*, 137:A1441, 1965.

[118] Erich Runge and E. K. U. Gross. Density-functional theory for time-dependent systems. *Phys. Rev. Lett.*, 52:997, 1984.

[119] T. Koopmans. Über die zuordnung von wellenfunktionen und eigenwerten zu den einzelnen elektronen eines atoms. *Physica*, 1:104, 1934.

[120] J. F. Janak. Proof that $\frac{\delta e}{\delta n_i} = \varepsilon$ in density-functional theory. *Phys. Rev. B*, 18:7165, 1978.

[121] P. A. M. Dirac. Note on exchange phenomena in the thomas atom. *Mathematical Proceedings of the Cambridge Philosophical Society*, 26:376, 1930.

[122] D. M. Ceperley and B. J. Alder. Ground state of the electron gas by a stochastic method. *Phys. Rev. Lett.*, 45:566, 1980.

[123] L. Wilk S. H. Vosko and M. Nusair. Accurate spin-dependent electron liquid correlation energies for local spin density calculations: a critical analysis. *Can. J. Phys.*, 58:1200, 1980.

[124] J. P. Perdew and Alex Zunger. Self-interaction correction to density-functional approximations for many-electron systems. *Phys. Rev. B*, 23:5048, 1981.

[125] Lee A. Cole and J. P. Perdew. Calculated electron affinities of the elements. *Phys. Rev. A*, 25:1265, 1982.

[126] John P. Perdew and Yue Wang. Accurate and simple analytic representation of the electron-gas correlation energy. *Phys. Rev. B*, 45:13244, 1992.

[127] K. Capelle. A bird's-eye view of density-functional theory. *Brazilian Journal of Physics*, 36:1318, 2006.

[128] J. P. Perdew, K. Burke, and M. Ernzerhof. Generalized gradient approximation made simple. *Phys. Rev. Lett.*, 77:3865, 1996.

[129] A. D. Becke. Density-functional exchange-energy approximation with correct asymptotic behavior. *Phys. Rev. A*, 38:3098, 1988.

[130] J. P. Perdew. Electronic structure of solids. volume 51, page 11. Akademie Verlag, Berlin, 1991.

[131] W. Lee, C. Yang, and R. G. Parr. Development of the colle-salvetti correlation-energy formula into a functional of the electron density. *Phys. Rev. B*, 37:785, 1988.

[132] John P. Perdew. Density-functional approximation for the correlation energy of the inhomogeneous electron gas. *Phys. Rev. B*, 34:7406, 1986.

[133] H. J. Monkhorst and J. D. Pack. Special points for brillouin-zone integrations. *Phys. Rev. B*, 13:5188, 1976.

[134] N. Troullier and J. L. Martins. Efficient pseudopotentials for plane-wave calculations. *Phys. Rev. B*, 43:1993, 1991.

[135] G. P. Kerker. Efficient pseudopotentials for plane-wave calculations. *J. Phys. C*, 13:L189, 1980.

[136] David Vanderbilt. Optimally smooth norm-conserving pseudopotentials. *Phys. Rev. B*, 32:1985, 1985.

[137] S. Goedecker, M. Teter, and J. Hutter. Separable dual-space gaussian pseudopotentials. *Phys. Rev. B*, 54:1703, 1996.

[138] Stefano Baroni, Paolo Giannozzi, and Andrea Testa. Green's-function approach to linear response in solids. *Phys. Rev. Lett.*, 58:1861, 1987.

[139] Paolo Giannozzi, Stefano Baroni, Nicola Bonini, Matteo Calandra, Roberto Car, Carlo Cavazzoni, Davide Ceresoli, Guido L Chiarotti, Matteo Cococcioni, Ismaila Dabo, Andrea Dal Corso, Stefano de Gironcoli, Stefano Fabris, Guido Fratesi, Ralph Gebauer, Uwe Gerstmann, Christos Gougoussis, Anton Kokalj, Michele Lazzeri, Layla Martin-Samos, Nicola Marzari, Francesco Mauri, Riccardo Mazzarello, Stefano Paolini, Alfredo Pasquarello, Lorenzo Paulatto, Carlo Sbraccia, Sandro Scandolo, Gabriele Sclauzero, Ari P Seitsonen, Alexander Smogunov, Paolo Umari, and Renata M Wentzcovitch. Quantum espresso: a modular and open-source software project for quantum simulations of materials. *J. Phys. Condens. Matter*, 21:395502, 2009.

[140] X. Gonze, J.M. Beuken, R. Caracas F. Detraux, M. Fuchs, G.M. Rignanese, L. Sindic, M. Verstraete, G. Zerah, F. Jollet, M. Torrent, A. Roy, M. Mikami, Ph. Ghosez, J.Y. Raty, and D.C. Allan. Green's-function approach to linear response in solids. *Computational Materials Science*, 25:478, 2002.

[141] G. Kresse and J. Furthmüller. Efficient iterative schemes for ab initio total-energy calculations using a plane-wave basis set. *Phys. Rev. B*, 54:11169, 1996.

[142] Xavier Andrade, Joseba Alberdi-Rodriguez, David A Strubbe, Micael J T Oliveira, Fernando Nogueira, Alberto Castro, Javier Muguerza, Agustin Arruabarrena, Steven G Louie, and Alán Aspuru-Guzik. Time-dependent

density-functional theory in massively parallel computer architectures: the octopus project. *J. Phys. Condens. Matter*, 24:233202, 2012.

[143] M D Segall, Philip J D Lindan, M J Probert, C J Pickard, P J Hasnip, S J Clark, and M C Payne. First-principles simulation: ideas, illustrations and the castep code. *J. Phys. Condens. Matter*, 14:2717, 2002.

[144] R Caracas and X Gonze. First-principle study of materials involved in incommensurate transitions. *Zeitschrift für Kristallographie-Crystalline Materials*, 220:511, 2005.

[145] R. M. Sternheimer. Electronic polarizabilities of ions from the hartree-fock wave functions. *Phys. Rev.*, 96:951, 1954.

[146] X. Gonze and J.P. Vigneron. First-principles responses of solids to atomic displacements and homogeneous electric fields: Implementation of a conjugate-gradient algorithm. *Phys. Rev. B*, 55:10337, 1997.

[147] X. Gonze and J.P. Vigneron. Density-functional approach to nonlinear-response coefficients of solids. *Phys. Rev. B*, 39:13120, 1989.

[148] L. Boltzmann. Weitere studien über das wärmegleichgewicht unter gas-molekülen. *Sitzungs-Berichte Akad. Wiss., Wien part II*, 66:275, 1872.

[149] M. Cutler and N. F. Mott. Observation of anderson localization in an electron gas. *Physical Review*, 181:1336, 1969.

[150] D. L. Nika, E. P. Pokatilov, A. S. Askerov, and A. A. Balandin. Phonon thermal conduction in graphene: Role of umklapp and edge roughness scattering. *Phys. Rev. B*, 79:155413, 2009.

[151] L. Lindsay and D. A. Broido. Enhanced thermal conductivity and isotope effect in single-layer hexagonal boron nitride. *Phys. Rev. B*, 84:155421, 2011.

[152] Wu Li, Jesús Carrete, Nebil A. Katcho, and Natalio Mingo. ShengBTE: a solver of the Boltzmann transport equation for phonons. *Comp. Phys. Commun.*, 185:1747, 2014.

[153] A. J. Minnich, J. A. Johnson, A. J. Schmidt, K. Esfarjani, M. S. Dresselhaus, K. A. Nelson, and G. Chen. Thermal conductivity spectroscopy technique to measure phonon mean free paths. *Phys. Rev. Lett.*, 107:095901, 2011.

[154] K. T. Regner, Z. Su D. P. Sellan, C. H. Amon, A. J. H. McGaughey, and J. A. Malen. Broadband phonon mean free path contributions to thermal conductivity measured using frequency domain thermoreflectance. *Nat. Comm.*, 4:1640, 2013.

[155] J. A. Johnson, A. A. Maznev, J. Cuffe, J. K. Eliason, A. J. Minnich, T. Kehoe, C. M. Sotomayor Torres, G. Chen, and K. A. Nelson. Direct measurement of room-temperature nondiffusive thermal transport over micron distances in a silicon membrane. *Phys. Rev. Lett.*, 110:025901, 2013.

[156] Joseph Callaway. Model for lattice thermal conductivity at low temperatures. *Physical review*, 113:1046, 1959.

[157] P. G. Klemens. Thermal conductivity and lattice vibrational modes. In F. Seitz and D. Turnbull, editors, *Solid State Physics: Advances in Research and Applications*, volume 7, page 1. Academic, New York, 1958.

[158] D. L. Nika, E. P. Pokatilov, A. S. Askerov, and A. A. Balandin. Phonon thermal conduction in graphene: Role of umklapp and edge roughness scattering. *Phys. Rev. B*, 79:155413, 2009.

[159] P. G. Klemens and D. F. Pedraza. Thermal conductivity of graphite in the basal plane. *Carbon*, 32:735, 1994.

[160] Yulu Shen, Guofeng Xie, Xiaolin Wei, Kaiwang Zhang, Minghua Tang, Jianxin Zhong, Gang Zhang, and Yong Wei Zhang. Size and boundary scattering controlled contribution of spectral phonons to the thermal conductivity in graphene ribbons. *Appl. Phys. Lett.*, 115:063507, 2014.

[161] P. Anees, M. C. Valsakumar, and B. K. Panigrahi. Effect of strong phonon-phonon coupling on the temperature dependent structural stability and

frequency shift of 2d hexagonal boron nitride. *Phys. Chem. Chem. Phys.*, 18:2672, 2016.

[162] N. W. Ashcroft and N. D. Mermin. *Solid State Physics*. Holt, Reinehart and Winston, New York, 1976.

[163] A. Matthiessen and C. Vogt. Ueber den einfluss der temperatur auf die elektrische leitungsfähigkeit der legirungen. *Ann. Phys., Lpzg*, 122:19, 1864.

[164] D. Marx and J. Hutter. *AB INITIO* molecular dynamics: Theory and implementation. *Modern methods and algorithms of quantum chemistry*, 1:301, 2000.

[165] M. P. Allen and D. J. Tildesley. *Computer simulation of liquids*. Oxford University Press, 1989.

[166] D. Frenkel and B. Smit. *Understanding molecular simulation: from algorithms to applications*. Academic Press, 2001.

[167] Bo Liu, Julia A Baimova, Chilla D Reddy, Adrian Wing-Keung Law, Sergey V Dmitriev, Hong Wu, and Kun Zhou. Interfacial thermal conductance of a silicene/graphene bilayer heterostructure and the effect of hydrogenation. *ACS applied materials and interfaces*, 6:18180, 2013.

[168] M. Omini and A. Sparavigna. Beyond the isotropic-model approximation in the theory of thermal conductivity. *Phys. Rev. B*, 53:9064, 1996.

[169] Ryogo Kubo. Statistical-mechanical theory of irreversible processes. i. general theory and simple applications to magnetic and conduction problems. *J. Phys. Soc. Jpn.*, 12:570, 1957.

[170] Ryogo Kubo, Mario Yokota, and Sadao Nakajima. Statistical-mechanical theory of irreversible processes. ii. response to thermal disturbance. *J. Phys. Soc. Jpn.*, 12:570, 1957.

[171] Nicholas Metropolis, Arianna W. Rosenbluth, and Marshall N. Rosenbluth. Equation of state calculations by fast computing machines. *J. Phys. Chem. C*, 21:1087, 1953.

[172] L. A. Ponomarenko, R. Yang, T. M. Mohiuddin, M. I. Katsnelson, K. S. Novoselov, S. V. Morozov, A. A. Zhukov, F. Schedin, E. W. Hill, and A. K. Geim. Effect of a high-κ environment on charge carrier mobility in graphene. *Phys. Rev. Lett.*, 102:206603, 2009.

[173] Joseph G. Checkelsky and N. P. Ong. Thermopower and nernst effect in graphene in a magnetic field. *Phys. Rev. B*, 80:081413, 2009.

[174] Seung Geol Nam, Dong Keun Ki, and Hu Jong Lee. Thermoelectric transport of massive dirac fermions in bilayer graphene. *Physical Review B*, 82:245416, 2010.

[175] Fereshte Ghahari, Hong-Yi Xie, Takashi Taniguchi, Kenji Watanabe, Matthew S. Foster, and Philip Kim. Enhanced thermoelectric power in graphene: Violation of the mott relation by inelastic scattering. *Phys. Rev. Lett.*, 116:136802, 2016.

[176] Jia An Yan, W. Y. Ruan, and M. Y. Chou. Phonon dispersions and vibrational properties of monolayer, bilayer, and trilayer graphene: Density-functional perturbation theory. *Phys. Rev. B*, 77:125401, 2008.

[177] B. D. Kong, S. Paul, M. Buongiorno Nardelli, and K. W. Kim. First-principles analysis of lattice thermal conductivity in monolayer and bilayer graphene. *Phys. Rev. B*, 80:033406, 2009.

[178] Zhen Yao, Charles L. Kane, and Cees Dekker. High-field electrical transport in single-wall carbon nanotubes. *Phys. Rev. Lett.*, 84:2941, 2000.

[179] J. Maultzsch, S. Reich, C. Thomsen, H. Requardt, and P. Ordejón. Phonon dispersion in graphite. *Phys. Rev. Lett.*, 92:075501, 2004.

[180] Philip B. Allen. Improved callaway model for lattice thermal conductivity. *Phys. Rev. B*, 88:144302, 2013.

[181] Jinlong Ma and Wu Liand Xiaobing Luo. Examining the callaway model for lattice thermal conductivity. *Physical Review B*, 90:035203, 2014.

[182] S. Mei, L. N. Maurer, Z. Aksamija, and I. Knezevic. Full-dispersion monte carlo simulation of phonon transport in micron-sized graphene nanoribbons. *Journ. of Appl. Phys.*, 116:164307, 2014.

[183] Arnab K. Majee and Zlatan Aksamija. Length divergence of the lattice thermal conductivity in suspended graphene nanoribbons. *Phys. Rev. B*, 93:235423, 2016.

[184] Yangyu Guo and Moran Wang. Heat transport in two-dimensional materials by directly solving the phonon boltzmann equation under callaway's dual relaxation model. *Phys. Rev. B*, 96:134312, 2017.

[185] L. Lindsay, Wu Li, Jesus Carrete, Natalio Mingo, D. A. Broido, and T. L. Reinecke. Phonon thermal transport in strained and unstrained graphene from first principles. *Phys. Rev. B*, 89:155426, 2014.

[186] Giorgia Fugallo, Andrea Cepellotti, Lorenzo Paulatto, Michele Lazzeri, Nicola Marzari, and Francesco Mauri. Thermal conductivity of graphene and graphite: Collective excitations and mean free paths. *Nano Lett.*, 14:6109, 2014.

[187] Carlos A. Polanco and Lucas Lindsay. *Ab initio* phonon point defect scattering and thermal transport in graphene. *Phys. Rev. B*, 97:014303, 2018.

[188] L. Lindsay, D. A. Broido, and Natalio Mingo. Flexural phonons and thermal transport in multilayer graphene and graphite. *Phys. Rev. B*, 83:235428, 2011.

[189] G. Saito, G Dresselhaus, and M. S. Dresselhaus. *Physical Properties of Carbon Nanotubes*. Imperial College Press, London, 1998.

[190] V. W. Scarola and G. D. Mahan. Phonon drag effect in single-walled carbon nanotubes. *Phys. Rev. B*, 66:205405, 2002.

[191] F. Bloch. Zum elektrischen widerstandsgesetz bei tiefen temperaturen. *Zeitschrift für Physik*, 59:208, 1930.

[192] Michael S. Fuhrer. Viewpoint: Textbook physics from a cutting-edge material. *Physics*, 3:106, 2010.

[193] S. Das Sarma, Shaffique Adam, E. H. Hwang, and Enrico Rossi. Electronic transport in two-dimensional graphene. *Reviews of Modern Physics*, 83:407, 2011.

[194] R. D'Souza and S. Mukherjee. First principles calculation of thermoelectric parameters of monolayer- and bilayer-graphene and heterostructures of graphene and *h*-BN. *Journal of Physics: Conference Series*, 759:012040, 2016.

[195] Thomas Garm Pedersen and Jesper Goor Pedersen. Self-consistent tight-binding model of b and n doping in graphene. *Phys. Rev. B*, 87:155433, 2013.

[196] Byoung Seo Lee and Joon Sik Lee. Thermal conductivity reduction in graphene with silicon impurity. *Applied Physics A*, 121:1193, 2015.

[197] Elaheh K. Goharshadia and Sayyed Jalil Mahdizadeha. Thermal conductivity and heat transport properties of nitrogen-doped graphene. *Journal of Molecular Graphics and Modelling*, 62:74, 2015.

[198] Eric Pop, Vikas Varshney, and Ajit K. Roy. Thermal properties of graphene: Fundamentals and applications. *MRS Bulletin*, 37:1273, 2012.

[199] N. Kumar, K. Moses, K. Pramoda, S. N. Shirodkar, A. K. Mishra, U. V. Waghmare, A. Sundaresana, and C. N. R. Rao. Borocarbonitrides, $B_xC_yN_z$. *J. Mater. Chem. A*, 81:109, 2013.

[200] Ransell D'Souza and Sugata Mukherjee. Electronic structure, phase stability and resistivity of hybrid hexagonal $C_x(BN)_{1-x}$ two-dimensional nanomaterial a first-principles study. *Physica E*, 69:138, 2015.

[201] Hongki Min, Bhagawan Sahu, Sanjay K. Banerjee, and A. H. MacDonald. *Ab initio* theory of gate induced gaps in graphene bilayers. *Phys. Rev. B*, 75:155115, 2007.

[202] Eduardo V. Castro, K. S. Novoselov, S. V. Morozov, N. M. R. Peres, J. M. B. Lopes dos Santos, Johan Nilsson, F. Guinea, A. K. Geim, and A. H. Castro Neto. Biased bilayer graphene: Semiconductor with a gap tunable by the electric field effect. *Phys. Rev. Lett.*, 99:216802, 2007.

[203] Kin Fai Mak, Chun Hung Lui, Jie Shan, and Tony F. Heinz. Observation of an electric-field-induced band gap in bilayer graphene by infrared spectroscopy. *Phys. Rev. Lett.*, 102:256405, 2009.

[204] Ransell D'Souza and Sugata Mukherjee. Thermoelectric transport in graphene/*h*-BN/graphene heterostructures: A computational study. *Physica E*, 81:96, 2016.

[205] Fernando de Juan, Antonio Politano, Gennaro Chiarello, and Herbert A. Fertig. Symmetries and selection rules in the measurement of the phonon spectrum of graphene and related materials. *Carbon*, 85:225, 2015.

[206] Nicolas Mounet and Nicola Marzari. First-principles determination of the structural, vibrational and thermodynamic properties of diamond, graphite, and derivatives. *Physical Review B*, 71:205214, 2005.

[207] Hartmut Zabel. Phonons in layered compounds. *J. Phys:Condens. Matter*, 13:7679, 2001.

[208] D. A. Broido, A. Ward, and N. Mingo. Lattice thermal conductivity of silicon from empirical interatomic potentials. *Physical Review B*, 72:014308, 2005.

[209] Yongqing Cai, Jinghua Lan, Gang Zhang, and Yong Wei Zhang. Lattice vibrational modes and phonon thermal conductivity of monolayer mos_2. *Physical Review B*, 89:035438, 2014.

[210] J. H. Seol, I. Jo, A. L. Moore, L. Lindsay, Z. H. Aitken, M. T. Pettes, X. Li, Z. Yao, R. Huang, D. Broido, N. Mingo, R. S. Ruoff, and L. Shi. Two-dimensional phonon transport in supported graphene. *Science*, 328:213, 2010.

[211] Shanshan Chen, Arden L. Moore, Weiwei Cai, Ji Won Suk, Jinho An, Columbia Mishra, Charles Amos, Carl W. Magnuson, Junyong Kang, Li Shi, and Rodney S. Ruoff. Raman measurements of thermal transport in suspended monolayer graphene of variable sizes in vacuum and gaseous environments. *ACS Nano*, 5:321, 2011.

[212] Shanshan Chen, Qingzhi Wu, Columbia Mishra, Junyong Kang, Hengji Zhang, Kyeongjae Cho, Weiwei Cai, Alexander A. Balandin, and Rodney S. Ruoff. Thermal conductivity of isotopically modified graphene. *Nature materials*, 11:203, 2012.

[213] Alexander A. Balandin, Suchismita Ghosh, Wenzhong Bao, Irene Calizo, Desalegne Teweldebrhan, Feng Miao, and Chun Ning Lau. Superior thermal conductivity of single-layer graphene. *Nano Lett*, 8:902, 2008.

[214] S. Ghosh, I. Calizo, D. Teweldebrhan, E. P. Pokatilov, D. L. Nika, A. A. Balandin, W. Bao, F. Miao, and C. N. Lau. Extremely high thermal conductivity of graphene: Prospects for thermal management applications in nanoelectronic circuits. *Appl. Phys. Lett.*, 92:151911, 2008.

[215] Weiwei Cai, Arden L. Moore, Xuesong Li Yanwu Zhu, Shanshan Chen, Li Shi, and Rodney S. Ruoff. Thermal transport in suspended and supported monolayer graphene grown by chemical vapor deposition. *Nano Lett.*, 10:1645, 2010.

[216] Luis A. Jauregui, Yanan Yue, Anton N. Sidorov, Jiuning Hu, Qingkai Yu, Gabriel Lopez, Romaneh Jalilian, Daniel K. Benjamin, Derek A. Delkd, Wei Wu, Zhihong Liu, Xinwei Wang, Zhigang Jiang, Xiulin Ruan, Jiming Bao, Steven S. Pei, and Yong P. Chen. Thermal transport in graphene nanostructures: Experiments and simulations. *ECS Trans.*, 28:73, 2010.

[217] Yee Kan Koh, Myung Ho Bae, David G. Cahill, and Eric Pop. Heat conduction across monolayer and few-layer graphenes. *Nano Lett.*, 10:4363, 2010.

[218] Claire Berger, Zhimin Song, Xuebin Li, Xiaosong Wu, Nate Brown, Cêcile Naud, Didier Mayou, Tianbo Li, Joanna Hass, Alexei N. Marchenkov,

Edward H. Conrad, Phillip N. First, and Walt A. de Heer. Electronic confinement and coherence in patterned epitaxial graphene. *Science*, 312:1191, 2006.

[219] Xiao-Yong Fang, Xiao-Xia Yu, Hong-Mei Zheng, Hai-Bo Jin, Li Wang, and Mao-Sheng Cao. Temperature- and thickness-dependent electrical conductivity of few-layer graphene and graphene nanosheets. *Phys. Lett. A*, 379:2245, 2015.

[220] Paulo T. Araujo, Mauricio Terrones, and Mildred S. Dresselhaus. Defects and impurities in graphene-like materials. *Mater. Today*, 15:98, 2012.

[221] M.M. Lucchese, F. Stavale, E.H. Martins Ferreira, C. Vilani, M.V.O. Moutinho, Rodrigo B.Capaz, C.A. Achete, and A.Jorio. Quantifying ion-induced defects and raman relaxation length in graphene. *Carbon*, 48:1592, 2010.

[222] Ado Jorio, Mildred S. Dresselhaus, Riichiro Saito, and Gene Dresselhaus. *Raman Spectroscopy in Graphene Related Systems*. Wiley, Weinheim, 2011.

[223] S. Mukherjee and T. P. Kaloni. Electronic properties of boron- and nitrogen-doped graphene: a first principles study. *Journal of Nanoparticles Research*, 14:1059, 2012.

[224] Ransell D'Souza, Sugata Mukherjee, and Tanusri Saha-Dasgupta. Influence of interface geometry on phase stability and bandgap engineering in boron nitride substituted graphene: A combined first-principles and monte carlo study. *Journal of Alloys and Compounds*, 708:437, 2017.

[225] D. L. Nika, E. P. Pokatilov, and A. A. Balandin. Theoretical description of thermal transport in graphene: The issues of phonon cut-off frequencies and polarization branches. *Physica Status Solidi B*, 248:2609, 2011.

[226] L. Lindsay, D. A. Broido, and Natalio Mingo. Flexural phonons and thermal transport in graphene. *Phys. Rev. B*, 82:115427, 2010.

[227] L. Lindsay, D. A. Broido, and Natalio Mingo. Diameter dependence of carbon nanotube thermal conductivity and extension to the graphene limit. *Phys. Rev. B*, 82:161402, 2010.

[228] Micheline Roufosse and P. G. Klemens. Thermal conductivity of complex dielectric crystals. *Phys. Rev. B*, 7:5379, 1973.

[229] S. Grimme, S. Ehrlich, and L. Goerigk. Effect of the damping function in dispersion corrected density functional theory. *J. Comp. Chem.*, 32:1456, 2011.

[230] Andre M. Rappe, Karin M. Rabe, Efthimios Kaxiras, and J. D. Joannopoulos. Optimized pseudopotentials. *Phys. Rev. B*, 41:1227, 1990.

[231] Jesús Carrete, Wu Li, Lucas Lindsay, David A. Broido, Luis J. Gallego, and Natalio Mingo. Physically founded phonon dispersions of fewlayer materials and the case of borophene. *Materials Research Letters*, 4:204, 2016.

[232] G. Kern, G. Kresse, and J. Hafner. *Ab initio* calculation of the lattice dynamics and phase diagram of boron nitride. *Phys. Rev. B*, 59:8551, 1999.

[233] P. H. Tan, W. P. Han, W. J. Zhao, Z. H. Wu, K. Chang, H. Wang, Y. F. Wang, N. Bonini, N. Marzari, N. Pugno, G. Savini, A. Lombardo, and A. C. Ferrari. The shear mode of multi-layer graphene. *Nature materials*, 11:294, 2012.

[234] R. J. Nemanich, S. A. Solin, and R. M. Marti. Light scattering study of boron nitride microcrystals. *Physical Review B*, 23:6348, 1981.

[235] R. Geick, C. H. Perry, and G. Rupprecht. Normal modes in hexagonal boron nitride. *Phys. Rev.*, 146:543, 1966.

[236] S. Reich, A. C. Ferrari, R. Arenal, A. Loiseau, I. Bello, and J. Robertson. Resonant raman scattering in cubic and hexagonal boron nitride. *Phys. Rev. B*, 71:205201, 2005.

[237] Ramon Cuscó, Bernard Gil, Guillaume Cassabois, and Luis Artús. Temperature dependence of raman-active phonons and anharmonic interactions in layered hexagonal BN. *Phys. Rev. B*, 94:155435, 2016.

[238] K. Esfarjani, G. Chen, and H. T. Stokes. Heat transport in silicon from first-principles calculations. *Phys. Rev. B*, 84:085204, 2011.

[239] J. A. Sanjurjo, E. Lopez-Cruz, P. Vogl, and M. Cardona. Dependence on volume of the phonon frequencies and the ir effective charges of several iii-v semiconductors. *Phys. Rev. B*, 28:4579, 1983.

[240] Youdi Kuang, Lucas Lindsay, Sanqiang Shi, Xinjiang Wang, and Baoling Huang. Thermal conductivity of graphene mediated by strain and size. *International Journal of Heat and Mass Transfer*, 101:772, 2016.

[241] A. Alofi and G. P. Srivastava. Thermal conductivity of graphene and graphite. *Phys. Rev. B*, 87:115421, 2013.

[242] Z. Aksamija and I. Knezevic. Lattice thermal conductivity of graphene nanoribbons: Anisotropy and edge roughness scattering. *Applied Physics Letters*, 98:141919, 2011.

[243] D. L. Nika and A. A. Balandin. Two-dimensional phonon transport in graphene. *J. Phys.: Condens. Matter*, 24:233203, 2012.

[244] Zhiyong Wei, Juekuan Yang, Kedong Bi, and Yunfei Chen. Mode dependent lattice thermal conductivity of single layer graphene. *Journal of Applied Physics*, 116:153503, 2014.

[245] L. Lindsay and D. A. Broido. Theory of thermal transport in multilayer hexagonal boron nitride and nanotubes. *Phys. Rev. B*, 85:035436, 2012.

[246] M. S. Green. Markoff random processes and the statistical mechanics of time-dependent phenomena. ii. irreversible processes in fluids. *J. Chem. Phys*, 22:398, 1954.

[247] R. Kubo. Statistical-mechanical theory of irreversible processes. i. general theory and simple applications to magnetic and conduction problems. *J. Phys. Soc. Jpn.*, 12:570, 1957.

[248] S. Grimme, J. Antony, S. Ehrlich, and S. Krieg. A consistent and accurate ab initio parametrization of density functional dispersion correction (dft-d) for the 94 elements H-Pu. *J. Chem. Phys.*, 132:154104, 2010.

[249] T. P. Kaloni and S. Mukherjee. Comparative study of electronic properties of graphite and hexagonal boron nitride (*h*-BN) using pseudopotential plane wave method. *Modern Physics Letters B*, 25:1855, 2011.

[250] S. Plimpton. Fast parallel algorithms for short-range molecular dynamics. *J Comp Phys*, 117:1–19, 1995. We have used the latest release of the code LAMMPS (March 2015 version) in our MD simulations.

[251] Bohayra Mortazavi, Luiz Felipe C. Pereira, Jin-Wu Jiang, and Timon Rabczuk. Modelling heat conduction in polycrystalline hexagonal boron-nitride films. *Scientific Reports*, 5:13228, 2015.

[252] Tao Ouyang, Yuanping Chen, Yuee Xie, Kaike Yang, Zhigang Bao, and Jianxin Zhong. Thermal transport in hexagonal boron nitride nanoribbons. *Nanotechnology*, 21:245701, 2010.

[253] Zhizhou Yu, M. L. Hu, C. X. Zhang, C. Y. He, L. Z. Sun, and Jianxin Zhong. Transport properties of hybrid zigzag graphene and boron nitride nanoribbons. *J of Physical Chemistry C*, 115:10836, 2011.

[254] Qing Peng and Suvranu De. Tunable band gaps of mono-layer hexagonal BNC heterostructures. *Physica E*, 44:1662, 2012.

[255] M. Kan, J. Zhou, Q. Wang, Q. Sun, and P. Jena. Tuning the band gap and magnetic properties of BN sheets impregnated with graphene flakes. *Phys. Rev. B*, 84:205412, 2011.

[256] W. R. L. Lambrecht and B. Segall. nomalous band-gap behavior and phase stability of c-BN-diamond alloys. *Phys. Rev. B*, 47:9289, 1993.

[257] J. Neugebauer and C. G. Van de Walle. Electronic structure and phase stability of $GaAs_{1-x}N_x$ alloys. *Phys. Rev. B*, 51:10568, 1995.

[258] B. T. Liou, S. H. Yen, and Y. K. Kuo. Vegard's law deviation in band gap and bowing parameter of $Al_xIn_{1-x}N$. *Applied Physics A*, 81:651, 2005.

[259] Jochen Heyd, Gustavo E. Scuseria, and Matthias Ernzerhof. Hybrid functionals based on a screened coulomb potential. *J Chem Phys*, 118:8207, 2003.

[260] Lars Hedin. New method for calculating the one-particle green's function with application to the electron-gas problem. *Phys Rev*, 139:A796, 1965.

[261] N. W. Ashcroft and N.D. Mermin. *Solid State Physics*. Holt, Reinhart and Winston, New York, 1976.

[262] Sharmila N. Shirodkar, Umesh V. Waghmare, Timothy S. Fisherb, and Ricardo Grau-Crespo. Engineering the electronic bandgaps and band edge positions in carbon-substituted 2d boron nitride: a first-principles investigation. *Physical Chemistry Chemical Physics*, 17:13547, 2015.

[263] Koretaka Yuge. Phase stability of boron carbon nitride in a heterographene structure: A first-principles study. *Phys. Rev. B*, 79:144109, 2009.

[264] Young-Woo Son, Marvin L. Cohen, and Steven G. Louie. Energy gaps in graphene nanoribbons. *Phys. Rev. Lett.*, 97:216803, 2006.

[265] Jun Zhu, Sumanta Bhandary, Biplab Sanyal, and Henrik Ottosson. Interpolation of atomically thin hexagonal boron nitride and graphene: Electronic structure and thermodynamic stability in terms of all-carbon conjugated paths and aromatic hexagons. *J. Phys. Chem. C*, 115:10264, 2011.

[266] Jiong Lu, Kai Zhang, Xin Feng Liu, Han Zhang, Tze Chien Sum, Antonio H. Castro Neto, and Kian Ping Loh. Order-disorder transition in a two-dimensional boron-carbon-nitride alloy. *Nature Communications*, 4:2681, 2013.

[267] K. Durczewski and M. Ausloos. Nontrivial behavior of the thermoelectric power: Electron-electron versus electron-phonon scattering. *Phys. Rev. B*, 97:5303, 2000.

[268] Maedeh Zahedifar and Peter Kratzer. Band structure and thermoelectric properties of half-heusler semiconductors from many-body perturbation theory. *Phys. Rev. B*, 97:035204, 2018.

[269] Yang Lu and Jing Guo. Thermal transport in grain boundary of graphene by non-equilibrium green's function approach. *Appl. Phys. Lett.*, 101:043112, 2012.

[270] Yong Xu, Xiaobin Chen, Jian-Sheng Wang, Bing-Lin Gu, and Wenhui Duan. Thermal transport in graphene junctions and quantum dots. *Phys. Rev. B*, 81:195425, 2010.

[271] Jian-Sheng Wang, Bijay Kumar Agarwalla, Huanan Li, and Juzar Thingna. Nonequilibrium green's function method for quantum thermal transport. *Front. Phys*, 9:673, 2014.

[272] Roger Willet, Helen Place, and Michael Middleton. Crystal structures of three new copper(11) halide layered perovskites: Structural, crystallographic, and magnetic correlations. *Jour. Am. Chem. Soc.*, 110:8639, 1988.